# Quantum purity and symmetry control of single-photon sources based on semiconductor quantum dots

Hélène Ollivier

université
PARIS-SACLAY

# Quantum purity and symmetry control of single-photon sources based on semiconductor quantum dots

## Pureté quantique et contrôle de symétrie de sources de photons uniques basées sur des boîtes quantiques semiconductrices

**Thèse de doctorat de l'Université Paris-Saclay**

École doctorale n° 572, ondes et matière (EDOM)
Spécialité de doctorat: physique
Unité de recherche: Université Paris-Saclay, CNRS, Centre de Nanosciences et de Nanotechnologies, 91120, Palaiseau, France.
Référent: : Faculté des sciences d'Orsay

**Thèse présentée et soutenue à Paris-Saclay, le 16 juillet 2021, par**

**Hélène OLLIVIER**

### Composition du Jury

| | |
|---|---|
| **Rosa Tualle-Brouri**<br>Professeur, IOGS, Université Paris-Saclay | Présidente |
| **Carole Diederichs**<br>Maître de conférence, Sorbonne Université | Rapportrice |
| **Jan Suffczyński**<br>Dr hab., University of Warsaw | Rapporteur |
| **Jean-Michel Gérard**<br>Ingénieur de recherche, CEA Grenoble | Examinateur |
| **Rinaldo Trotta**<br>Professeur, Université La Sapienza de Rome | Examinateur |

### Direction de la thèse

| | |
|---|---|
| **Pascale Senellart-Mardon**<br>Directrice de Recherche, Centre de Nanosciences et de Nanotechnologies | Directrice |

Thèse de doctorat

NNT: 2021UPASP054

# Remerciements

Mes quatre années de thèse ont été ponctuées de rencontres et interactions avec de nombreuses personnes que je voudrais remercier ici.

Tout d'abord, je tiens à témoigner ma reconnaissance au jury pour avoir accepté de lire et corriger mon manuscrit et d'assister à ma soutenance. Ensuite, je voudrais remercier chaleureusement Pascale Senellart dont les qualités scientifiques et humaines ont été très importantes au cours de cette thèse. Depuis le début elle m'a impressionnée par le débit de ses idées et sa capacité de travail. Son enthousiasme et sa compréhensivité en toutes circonstances ont été capitaux pour moi. Je candidaterai pour travailler de nouveau avec elle si notre rêve de laboratoire d'optique quantique en Bretagne se réalise un jour !

Merci au directeur du C2N Giancarlo Faini ainsi qu'à toute l'équipe administrative.

Je remercie Olivier Krebs pour son amabilité, toutes les discussions théoriques qu'il est toujours disposé à entretenir, et pour tous les prêts de matériel très fréquents en période de manipulation au laboratoire. Merci à Loïc Lanco et Daniel Lanzilloti-Kimura, pour les discussions intéressantes et leur sympathie. Merci à Christoph Simon pour sa participation à nos projets. Merci à Carlos et Juan qui m'ont encadrée au début de ma thèse, beaucoup appris sur les manips, et avec qui j'ai passé de bons moments, au labo ou en-dehors. Encore merci pour les petites attentions comme le livre de Barbijaputa et la bouteille de pisco. Je dois beaucoup à Sarah dont le sérieux et la constante et communicative bonne humeur sont des atouts fantastiques pour l'équipe, et rendent le travail avec elle vraiment agréable. Je souhaite à tout le monde d'avoir des collègues enthousiastes comme Elham et Ilse, entre les prouesses artistiques de la première et l'entrain effréné de la deuxième sur "Walk of Life". Merci encore à elles pour la super baby shower organisée en l'honneur de Sophie. Merci à Nathan, avec qui j'ai beaucoup apprécié de passer du temps au labo (et en en-dehors) bien qu'il éteigne mon ordinateur quand je travaille à distance. Merci à tous ceux qui ont croisé ma route, même brièvement, pendant cette thèse : Guillaume, avec qui nos avis divergents ont donné lieu à des débats intéressants, Jovana, elle aussi férue de crochet, Lise, avec qui les remplissages de bidons d'azote devenaient moins ennuyeux, Anis, stagiaire très volontaire, et Lorenzo, qui finissait sa thèse quand j'arrivais et qui m'a montré ce qu'était une belle soutenance.

Un grand merci à Martin, qui est toujours disposé à aider sans compter, et dont le calme et la prévenance sont précieux. Merci à Priya pour sa bienveillance et sa participation au projet de contrôle du dédoublement de structure fine. Merci à Anne pour sa sympathie, et pour avoir gardé Eustache quand je partais en conférence. Merci à Omar et Fabrice pour leur gentillesse. Merci à Clément pour sa constante bienveillance et son calme apaisant, les conversations le midi ou entre deux aller-retours au labo. Ce fut un grand plaisir de partager ton bureau. Merci à Marie, pour sa positivité et son rire communicatif, et son soutien en

toutes circonstances. Merci à Paul pour son soutien, son éternelle bonne humeur et pour avoir été un boute-en-train en matière de sorties, pique-niques, galettes des rois et séjour au Grau-du-Roi. Je maintiens cependant que Nelle n'est pas mieux qu'Eustache. Merci à Florian pour son aide au labo, sa jovialité, ses blagues et tous les bons moments partagés.

Merci à la super équipe des polaritons, Titta et Valentin mes anciens co-bureaux, mais aussi Nicolas et Philippe (et sa fille Margot pour nous avoir prêté ses petits vêtements), Jacqueline et Sylvain. Ils ont été disponibles pour des discussions, prêt de matériel et ont grandement participé à la bonne ambiance du groupe.

Merci à Abdou, pour la fabrication des échantillons et sa participation au projet de contrôle du dédoublement de structure fine, ainsi que pour toutes les discussions chaleureuses. Merci à Aristide pour son aide précieuse apportée en salle blanche, sur la machine de mesures sous pointes entre autres. Merci également à lui, à Isabelle Sagnes et à Niccolo Somaschi pour la confection des échantillons, sans quoi aucun des résultats de cette thèse n'aurait vu le jour. Merci au reste de l'équipe très sympathique de Quandela pour leur aide et collaboration, Valérian, Alexandre, Petr. Je remercie en outre les membres de l'atelier pour leur conception de pièces sur mesure pour certaines expériences.

J'adresse une grande reconnaissance à l'équipe pédagogique d'optique de l'IUT d'Orsay avec qui j'ai eu le plaisir de travailler pour ma mission d'enseignement (et au-delà), en particulier Loïc Rondin, Grégory Gredat, Fabien Legrand, Théodore Nicolas et Guilhem Madiot.

Je tiens à témoigner toute ma gratitude à mes proches amis, Catherine et Liêm, toujours aux aguets pour voler à mon secours dans les moments ardus, et enthousiastes pour garder Sophie et préparer une sortie ou une bouffe. Merci aussi à Clémence, Camille et Guénolé, à Maxime et Chloé, à Julie.

Je voudrais remercier affectueusement mes parents Florence et Yvonnick Ollivier (qui furent mes enseignants de physique-chimie au lycée !) pour m'avoir soutenue et encouragée ces 28 dernières années. Merci infiniment pour avoir jonglé pendant plusieurs mois entre leur travail et la garde de petite Sophie, qu'ils ont patiemment chouchoutée pendant que je rédigeais. Merci d'avoir pris soin de moi quand j'en avais besoin. Merci à ma Mamie Anne-Marie Riou pour son soutien et son intérêt, ainsi que pour les heures quotidiennes passées à surveiller et occuper Sophie quand Papa et Maman travaillaient. Merci à Tata et Tonton, Huguette et Yves Rouxel, pour avoir pris le relais un moment. Merci à mon Papy Jacques Riou de m'avoir toujours poussée à être curieuse et qui serait sûrement fier de moi. Merci à toute ma famille pour m'avoir toujours appuyée, encouragée et demandé des nouvelles. Merci à Eustache et Cannelle pour leur précieux soutien félin, et à Fanny et Moche pour leur précieux soutien canin.

Merci à ma petite Sophie qui illumine ma vie depuis plus d'un an par ses (sou)rires et ses câlins. Enfin, merci à Stephen, pour toute l'aide qu'il m'a apportée, merci pour tous les bons moments que l'on passe ensemble et merci de m'avoir donné la plus merveilleuse des petites perles. Merci pour tout.

# Synthèse

Les technologies quantiques promettent d'importantes améliorations dans plusieurs domaines scientifiques et commerciaux, en particulier dans les domaines des communications, des mesures et de l'informatique. Comme pour les technologies quantiques, la lumière joue un rôle clé, en tant que porteur naturel d'information sur de longues distances. Différentes saveurs de lumière quantique sont explorées dans ce contexte. Pendant cette thèse, nous avons étudié des sources de lumière quantique basées sur des boîtes quantiques semiconductrices. Ces dernières décennies, diverses technologies ont été développées et améliorées au Centre de Nanosciences et Nanotechnologies pour fabriquer de façon fiable des sources de photons uniques basées sur des boîtes quantiques semiconductrices. Notre approche est de graver des cavités en forme de micropilier autour de boîtes quantiques pré-sélectionnées, en utilisant la procédure de lithographie *in situ*. Les propriétés de ces sources de photons uniques sont constamment optimisées pour leur utilisation dans des applications quantiques. La source idéale devrait produire des photons uniques de façon cadencée, avec une efficacité et une indiscernabilité proches de l'unité.

Dans cette thèse, on décrit dans un premier temps la majorité des principes physiques fondamentaux qui gouvernent la génération de lumière à partir de boîtes quantiques semiconductrices. Nous introduisons les différentes transitions optiques (des excitons constitués d'une paire électron-trou, ou des trions, qui contiennent une charge supplémentaire) et les règles de sélection. Par exemple, les excitons présentent deux vecteurs propres qui sont usuellement séparés par une quantité appelée le dédoublement de structure fine. Nous discutons comment une cavité peut être utilisée pour accélérer l'émission spontanée et collecter efficacement les photons générés. Nous étudions comment les propriétés des photons uniques dépendent de la nature de la transition qui les génère. En particulier, nous explorons l'influence sur le profil temporel du paquet d'onde, la pureté quantique, l'indiscernabilité et le taux de photons maximum atteignable. Nous présentons aussi une étude comparative de quinze sources de photons uniques pour démontrer la reproducibilité de leurs performances et la robustesse de leur procédé de fabrication.

De façon à mesurer l'indiscernabilité des photons uniques, il est d'usage d'utiliser l'interférométrie de Hong-Ou-Mandel puisque la visibilité des interférences dans cette expérience est liée à l'indisernabilité des photons uniques. En revanche, la pureté des photons uniques influence ces interférences. Par conséquent, les scientifiques de la communauté corrigent habituellement la visibilité des interférences par une quantité qui dépend de la pureté des photons uniques. Cependant, jusqu'à présent, cette connexion ne prenait pas en compte l'origine de la pureté imparfaite des photons uniques. Dans cette thèse, nous

présentons un modèle qui donne le facteur de correction adéquat selon cette origine. Nous appliquons ensuite ce modèle à des sources imparfaites que nous réalisons artificiellement à partir de sources presque idéales auxquelles nous ajoutons du bruit. Finalement, nous identifions l'origine du bruit dans le cas de nos sources afin de déduire l'indiscernabilité des photons uniques.

Enfin, contrôler le dédoublement de structure fine est une aptitude prometteuse pour générer des qubits encodés en fréquence ou des paires de photons intriqués. Nous proposons une nouvelle méthode pour contrôler le dédoublement de structure fine compatible avec l'insertion d'une boîte quantique dans une cavité en forme de micropilier. Elle est basée sur l'utilisation de trois sources de tension que l'on utilise pour contrôler le champ électrique en trois dimensions à la position de la boîte quantique. Nous présentons la démonstration expérimentale du contrôle du dédoublement de structure fine de deux différentes boîtes quantiques sur deux échantillons différents, ainsi que des résultats théoriques de simulations réalisées avec COMSOL, qui permettent de comprendre le fonctionnement de la méthode.

# Abstract

Quantum technologies promise important improvements in several scientific and commercial domains, especially in the fields of communications, sensing and computing. Like in classical technologies, light plays a key role, as a natural carrier of information on long distances. Different flavours of quantum light are explored in this context. During this thesis, we studied quantum light sources based on semiconductor quantum dots. Over the past decades, various technologies have been developed and improved at the Center for Nanosciences and Nanotechnologies to reliably fabricate efficient single-photon sources based on semiconductor quantum dots. Our approach is to etch micropillar cavities around pre-selected quantum dots making use of the in-situ lithography procedure. The properties of these single-photon sources are constantly optimized for use in quantum applications. The ideal source should produce single photons in a clocked manner, with near-unity efficiency and indistinguishability.

In this thesis, we first describe most of the fundamental physics principles which govern the generation of light from semiconductor quantum dots. We introduce the different optical transitions (excitons made of an electron-hole pair, or trions, that have an extra charge) and their selection rules. For example, excitons show two eigenstates that are usually separated by a quantity called the fine structure splitting (FSS). We discuss how a cavity can be used to enhance the spontaneous emission and efficiently collect the generated photons. We study how the properties of the single photons depend on the nature of the transition that generates them. In particular, we explore the influence on the temporal wavepacket profile, the single-photon purity, the indistinguishability and the maximum reachable photon rate. We also present a benchmarking of fifteen single-photon sources to demonstrate their performance reproducibility and the robustness of the fabrication process.

In order to measure the indistinguishability of single-photons, it is common to use Hong-Ou-Mandel interferometry since the visibility of interferences in such an experiment is linked to the single-photon indistinguishability. However, the single-photon purity influences these interferences. Consequently, scientists from the community commonly "correct" the interference visibility by a quantity that depends on the single-photon purity. However, so far, this connection did not take into account the origin of the imperfect single-photon purity. In this thesis, we present a model that gives the proper correction factor to use depending on this origin. We then apply this model to imperfect sources that we emulate from near-ideal sources to which we add noise. Finally, we identify the origin of the noise in our sources to deduce their single-photon indistinguishability.

Finally, controlling the excitonic fine structure splitting is a promising feature to generate

qubits encoded in frequency or entangled photon pairs. We propose a new method to control the fine structure splitting compatible with the insertion of the QD in a micropillar cavity. It is based on three remote voltage knobs used to control the electric field in three dimensions at the position of the dot. We present the experimental demonstration of the fine structure splitting tuning on two different quantum dots from two different samples, as well as theoretical results obtained from COMSOL simulations that allow comprehending the device operation.

# Abbreviations

FWHM = Full Width at Half Maximum
FSS= Fine Structure Splitting
HOM = Hong Ou Mandel
HWP = Half Waveplate
MBE = Molecular Beam Epitaxy
MHB = Mixed Holes Basis
PBS = Polarizing Beam Splitter
QD = Quantum Dot
QWP = Quarter Waveplate
SLM = Spatial Light Modulator
SPDC = Spontaneous Parametric Down-Conversion

# Contents

# Introduction

In 1900, Lord Kelvin claimed, in a lecture he gave at the Royal Institution of Great Britain [1], that there were two mysteries left in physics. He referred to them as "dark clouds". The first one was embodied by the Michelson-Morley experiment, which led Kelvin to say "I am afraid we must still regard Cloud No. I as very dense". The clearing of this cloud led to the development of the theory of relativity. Cloud No. II, "which has obscured the brilliance of the molecular theory of heat and light during the last quarter of the nineteenth century", was what Paul Ehrenfest called "the ultraviolet catastrophe". It refers to the divergence between the experimental observations on the black-body radiation at short wavelengths and the Rayleigh-Jeans model. Planck derived an expression admitting that the electromagnetic field is absorbed and emitted by discrete packets of energy, proportional to its frequency. The proportionality factor was named after him as "Planck's constant", $h$. He never really believed in this assumption, describing his derivation as an "act of desperation" [2] and he tried to explain it by classical arguments. Other physicists understood the physical insight provided by Planck, especially Einstein, who embraced and developed the concept of the photon. With that new idea, Einstein was able to explain the photoelectric effect, for which he was awarded the Nobel Prize in 1921.

Quantum mechanics has been expansively investigated since then, and it gave rise to plenty of applications. Many of them come from the field of light-matter interaction, such as lasers [3] and magnetic resonance imaging for example. Scientists and engineers are now working towards taking advantage of the quantum behaviour of light and matter to develop quantum computing, quantum communication and quantum sensing.

A quantum computer is based on manipulating quantum bits (qubits), which are two-level systems that can be in any coherent superposition of two states, instead of the usual 0 and 1 bits we are used to in classical computation. It should allow for the preparation and measurement of a large number of qubits, with logic gates to implement algorithms. A quantum computer could require way less resources in time and memory space than a classical one [4]. It would allow solving problems that are either hard or impossible to solve with a classical computer. A quantum computer is expected to solve massive quantum systems that could never be solved on a classical computer. A quantum computer could also simulate quantum systems [5] in a more efficient way than a classical computer. For example, quantum simulation might allow for the discovery of new chemical processes, which are based on quantum evolution of a large number of particles. This may include the discovery of a new way to generate ammonia. That molecule, which is commonly used as a fertilizer, is today produced through the Haber-Bosch process, requiring high temperatures and pressures, consuming up

to 2% of the world's energy [6]. We know there is a more energy-efficient way to synthetize ammonia, since the enzyme nitrogenase does it under ambient conditions [7]. Other applications involve finances [8] and machine learning [9] among many others. All these applications are the origin for a strong enthusiasm towards future quantum technologies and involvement of many research groups and already established companies. It is also leading to the emergence of multiple start-up companies all over the world to participate in this global effort. We recently witnessed the beginning of a "quantum computing race" towards the demonstration of "quantum computing supremacy" or rather "quantum computational advantage". Google claimed in 2019 [10], that they had implemented a quantum algorithm on a superconductor based quantum machine, taking 200 seconds instead of $10,000$ years on the most powerful classical supercalculator. However, the task they performed with their quantum computer was claimed to be solvable by a classical one within 2.5 days by IBM. In December 2020, the team of Jian-Wei Pan in Hefei, China performed a boson-sampling computation with 50 squeezed states [11]. The experiment itself took about $10^{14}$ less time than the one it would take on a classical supercomputer (200 seconds instead of 2.5 billion years). The demonstrated computations do not yet appear particularly useful, but both works represent an important milestone for quantum computing. Although there would be many benefits for having quantum algorithms that can vastly outperform classical algorithms, quantum computing may also undermine encryption protocols that are designed around computational complexity. Indeed, a quantum computer that would be powerful enough to implement Shor's algorithm [12], and determine the prime factors of large numbers in a short enough time, could break RSA cryptography, a public-key cryptosystem used to keep emails and online transactions confidential. Although such perspective is not within reach in the near future considering the current status of the technological developments, strategies are already explored to counter this threat.

One way to ensure that communication is secure against a future quantum computer is to implement quantum cryptographic protocols [13]. This can be accomplished by transmitting quantum information from one place to another in order to generate a secure key to encrypt information. A well-known example of such a scheme is the BB84 protocol [14]. However, long-distance quantum cryptography requires a quantum network to transmit quantum information. This involves the transfer of the state of a qubit from one place to another, using the principles of superposition and entanglement of states [15]. Quantum information can then be used to implement long-distance quantum encryption protocols. Setting up a quantum network would require quantum communication between quantum nodes, forming the basis of a quantum internet [16–18]. For that purpose, it may be necessary to build quantum repeaters [19], quantum satellites for free-space transmission [20] and low-loss fiber optics engineering to overcome losses for long distance communication. Quantum networks would also allow for more fundamental applications such as testing Bell's inequalities [21–23], or quantum gravity [24].

Finally, another field of application of quantum technologies is quantum sensing, which comprises quantum metrology and uses quantum measurements to reach higher precision than classical measurements [25, 26]. Quantum sensing covers a wide range of measurable quantities [27]. For example, quantum imaging is being investigated to exceed the capacities of classical imaging and get a lower shot noise [28].

In order to conceive a quantum computer or a quantum network, one needs to find ways to prepare qubits, to store them, to transfer their information, to measure them and to implement logic gates with them. Different approaches are being explored for these purposes, such as atoms [29] or trapped ions [30, 31], two approaches that can implement quantum gates with high fidelity. Another set of candidates, integrated in the solid-state, such as superconducting qubits [32], nitrogen-vacancy centers in diamond or semiconductor quantum dots are more compact, and more promising for scalability. NV centers in diamond are promising candidates for sensing for instance, since they have a very long spin coherence time ($\simeq$ ms) and can be used at room temperature [33]. It is likely that a successful quantum computer or quantum network architecture will be a hybrid system [34], based on a combination of these different approaches to take advantage of the assets of each platform.

Given that photons can interact with most of the systems mentioned above, they would be adapted to carry information from one local quantum platform to another. In that context, single photons should ideally be emitted on-demand (so only when they are triggered) and at a high rate to increase the speed of operations. For some applications, they also need to be identical i.e. in a pure quantum state. Single-photon sources can also be used to construct entangled photonic states [35] that are useful for applications such as linear optical computing [36] and all-optical repeaters [37].

Several types of single-photon sources have been developed to date. The most common one is spontaneous parametric down-conversion (SPDC) sources. They are based on the generation of two photons in a non-linear crystal by frequency down-conversion of an excitation laser pulse. They are said to be "heralded" because one photon detected on one output heralds the presence of another on the other output. A considerable advantage of these sources is that they can be operated at room temperature. However, they do not lead to a true single photon generation, there is always the possibility to obtain more than one photon, a possibility that increases linearly with the source efficiency. This intrinsic drawback is being overcome by exploring multiplexing strategies [38]. Another way to generate single photons that has been explored for more than two decades is based on the long-known ability of atoms to emit one photon at a time [39]. This approach has led to the generation of single-photon emission with single atoms [40], as well as NV centers [41, 42], molecules [43, 44], or quantum dots [45]. In this thesis, we study semiconductor quantum dots [46], nanostructures that confine charge carriers in three dimensions.

Over the last two decades, semiconductor quantum dots have become interesting systems for quantum technologies, able to generate single photons or other quantum states of light [47–49], as well as store information in electron or hole spins that are considered as stationary qubits [50]. We focus on the single-photon generation aspect of semiconductor quantum dots. The first demonstration of single-photon generation with quantum dots was reported in 2000 [45]. Semiconductor quantum dots are also the only known type of solid-state emitter that can emit on-demand entangled photon pairs [51], which was proposed in 2000 [52] and first demonstrated in 2006 [53]. They are thus promising systems to implement quantum relays [54–56] and quantum repeaters based on the Shapiro Lloyd scheme [57]. When located in the

bulk material, semiconductor quantum dots emit isotropically which reduces the photon rate in the collected direction. But like for any atom, placing a cavity around them enhances the light emission in one direction via the Purcell effect. This was demonstrated with quantum dots in 1998 [58], and applied specifically to the generation of single photons in 2002 [59]. Quantum dots can also be coupled to waveguides [60, 61] or plasmonic resonators [62]. In terms of generation of entangled photon pairs, ultrabright sources of entangled photon pairs were fabricated in my team, using semiconductor QDs embedded into coupled microcavities [48]. The best entangled photon source to date was demonstrated in 2019 [63].

In order to work towards large-scale quantum operations, it is necessary to reproducibly fabricate single-photon sources. This is why methods allowing for coupling deterministically a QD with a cavity are developed. The first one was carried out in 2005 [64, 65] where the QD was coupled to a photonic crystal cavity. In 2008 my group invented a way to couple QDs to microcavities where it is possible to fabricate several devices at once on a given sample of semiconductor wafer [66]. Ultrabright single-photon sources were obtained by coupling QDs to nanowires [61] or to micropillars [67]. Indistinguishable photons were obtained from a QD single photon source under resonant excitation since 2013 [68, 69]. When I joined the C2N team, the state of the art was set by the near-ideal single-photon sources obtained by the fabrication methods developed in the group before my arrival [70]. The first applications with these sources were carried out during my PhD including several experiments of Boson sampling, with 3 photons with a source of our group sent to the group of Pr. Andrew White [71], then with 5, 7 and 20 photons by the group of Jian-Wei Pan [72–74] with similar devices fabricated in the university of Wurzburg. Our group also realized the first interfacing of a QD single-photon source with a photonic chip and performed a three-photon interference. This was done with the groups of Pr. Fabio Sciarrino (Rome) and Pr. Roberto Osellame (Milan) with a reconfigurable photonic chip on glass [75]. More recently, our single-photon sources were used to generate 4-photon linear cluster states in collaboration with the group of Pr. Hagai Eisenberg (Jerusalem) [35].

This thesis details the results I have obtained for my graduate studies with the group of Pr. Pascale Senellart in the Photonics Department at the Centre for Nanosciences and Nanotechnologies (C2N). My work started in 2017 in Marcoussis and ended in Palaiseau - which means that I experienced the adventure of moving an experimental laboratory at the end of 2018. The C2N is known for its large and efficient cleanroom facilities, where semiconductors nanoprocessing is mastered at the best level. Moreover, our team developed the know-how to fabricate components in large numbers using the *in situ* lithography technique that allows us to precisely position a single quantum dot in a cavity.

My PhD project was centered on two main topics: better understanding the physics determining the single-photon source performances and develop new tools to control the quantum dot energy levels. I conducted an in-depth study of the single-photon sources' performances to understand the various physical phenomena that impose limits on them and on their reproducibility. We took advantage of the deterministic fabrication techniques to benchmark many sources and we propose different ways to overcome these limits and fabricate identical sources of highly indistinguishable photons. I also revisited the usual characterization tools, such as

the Hong-Ou-Mandel interference, that is routinely used to determine the indistinguishability of the emitted single photon. Finally, we proposed a new method to control the QD symmetry that is at the core of the generation of entangled photon pairs.

This manuscript is structured as the following:

- In Chapter 1, I introduce the fundamentals of single-photon emission from semiconductor quantum dots in cavities. We discuss the various optical transitions and the subtle physics that govern their polarization. I present the basics of light-matter interaction and briefly describe the experimental techniques and the figures of merit used to characterize single-photon sources.

- In Chapter 2, I investigate the reproducibility of our single-photon sources technology and the robustness in terms of performance. I discuss how the source operation and performances differ when based on a neutral or charged quantum dot and discuss performance reproducibility. These results have been published in ACS Photonics in 2020 [76].

- In Chapter 3, I revisit a critical tool used to characterize single-photon sources: the HOM interference. Over the course of this thesis, we realized that the HOM interference can allow accessing the true single-photon indistinguishability, even for a source that presents a residual probability of emitting more than one photon. A theoretical framework was developed by Dr. S. Wein in the team of Pr. C. Simon that we tested experimentally. We then applied this method to our single-photon sources. These results were published in Physical Review Letter in 2021 [77].

- In Chapter 4, we present a new method to control the symmetry governing the optical selection rules of a quantum dot exciton. Such control is highly sought after for the generation of entangled photon pairs, but could also be used for other purposes. Our method relies on the remote application of an electric potential and is fully compatible with the insertion of quantum dots in micropillar cavities for efficient photon extraction. The content of this latter chapter gave rise to a patent and an article is under preparation.

Finally, the last chapter of this manuscript summarizes the main results obtained during this thesis and drafts future studies and challenges.

# Chapter 1

# Fundamentals of single-photon sources based on quantum dots in micropillar cavities

Quantum dots (QDs) are semiconductor nanostructures that allow a confinement of carriers in three dimensions. In this manuscript, we specifically study III-V InGaAs/GaAs naturally grown QDs that have shown state-of-the-art performances for quantum technologies. When excited with a light of high enough frequency, the QD experiences a transition of an electron from the valence to the conduction band. When returning to its initial state, the QD emits a photon of equal energy to the transition. This concept is the basis for using semiconductor QDs as a single-photon source [45]. In this chapter, we present the fundamentals of single-photon sources based on QDs embedded in micropillar cavities. In a first section we focus on the physics of the QD itself, its growth and optical transitions. Some of these optical selection rules arise from asymmetries in the QD carrier wavefunctions that are at the core of Chapter 4 where we present a new way to control them. Next, we discuss the basics of spontaneous emission control for a QD coupled to a cavity. Finally, we present the metrics and experimental tools used to study and characterize our single-photon sources. These first sections set the ground for what will follow in Chapter 2 where we study the optical properties governing the single-photon source performances and benchmark fifteen sources. We further use these tools and definitions in Chapter 3 to revisit the HOM interference of imperfect single-photon sources.

## 1.1 Quantum dots as artificial atoms

### 1.1.1 Growth of self-assembled quantum dots

In this thesis we study self-assembled QDs made of indium gallium arsenide (InGaAs) and gallium arsenide (GaAs). The semiconductor nanostructures are grown by stacking layers of atoms by molecular beam epitaxy (MBE). The first material deposited in the process is GaAs, which forms the host material. The next step is to deposit indium arsenide InAs. The first layer of InAs, called the *wetting layer*, is a thin quantum well. GaAs and InAs present the same crystal structure but different lattice constants: the mismatch is about 7%. Hence, when

the InAs that is deposited on top of the GaAs becomes thicker than about 1.7 monolayers [78], it energetically favors the formation of nano-islands because it reduces the strain energy in the crystal. This is called the Stranski-Krastanov transition [79]. These islands appear at random positions on the sample and show random sizes, as illustrated in figure 1.1. More layers of GaAs are then deposited on top of the InAs to enclose the QDs.

The bandgap of InAs ($\simeq$ 0.35 eV at 300 K) is lower than that of GaAs ($\simeq$ 1.42 eV at 300 K) [80] so that the embedded islands create a three-dimensional (3D) confinement potential for the charge carriers. This confinement leads to a discretization of the electronic energy levels, forming a QD with behaviours similar to those of a natural atom, as first evidenced in 1994 [78]. Over the years, QDs have been referred to as *artificial atoms*, although they are made of about $10^4$ atoms.

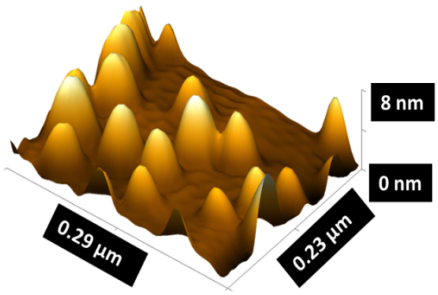


Figure 1.1: Atomic force microscope image of the surface of a QD InAs layer. Image extracted from [81].

After GaAs regrowth, Ga/In interdiffusion takes place so that the QD material is a InGaAs alloy. The InGaAs nano-islands present flat lenses shapes with a height of about 3 nm in the growth direction ($z$) and a diameter of 10 to 20 nm in the ($xy$) plane. The wetting layer is a 2-dimensional quantum well with a bandgap of 1.45 eV at 10K, which corresponds to a wavelength of 855 nm [82]. The QDs studied in this manuscript confine the carriers in 3 dimensions, with an energy difference between the ground state and the first excited state of about 1.34 eV at 10K, which corresponds to a wavelength around 925 nm.

The QDs density can be tuned from about $10\,\mu m^{-2}$ to $500\,\mu m^{-2}$ [82–84] and are usually a bit asymmetric in the ($xy$) plane. In this PhD work, the samples are annealed at a temperature between 850 and 950 °C after growth, leading to further interdiffusion of InAs and GaAs in the QDs. This reduces the difference of energy between the bulk and the nano-island. The annealing also leads to a more homogeneous energy distribution and an overall larger QD size [85].

### 1.1.2 Energy levels

The electronic wavefunction $\Psi(\mathbf{r})$ in a crystal lattice can be approximated using Bloch's theorem, which states that the eigenfunctions are formed by a product of a plane wave $e^{i\mathbf{k}.\mathbf{r}}$ and a periodic function $u(\mathbf{r})$ with translation symmetry dictated by the lattice structure. Hence

$\Psi(\mathbf{r})$ is constructed from a superposition of eigenfunctions

$$\psi_n(\mathbf{r}, \mathbf{k}) = u_n(\mathbf{r})e^{i\mathbf{k}\cdot\mathbf{r}} \tag{1.1}$$

The orthogonal periodic functions $u_n$ satisfy $u_n(\mathbf{r}) = u_n(\mathbf{r} + \mathbf{T})$, where $\mathbf{T}$ is a primitive translation vector of the lattice and the index $n$ labels the band constructed from the molecular orbitals of a unit cell [86].

The growth of the QD introduces a potential well that modifies the electronic wavefunction. Since the well is spatially much larger than the periodicity of $u_n(\mathbf{r})$, then for small $\mathbf{k}$ (near the $\Gamma$ point), $u_n(\mathbf{r})$ varies fast compared to $e^{i\mathbf{k}\cdot\mathbf{r}}$ with respect to $\mathbf{r}$. Thus, the electronic wavefunction can be obtained by quantizing the plane-wave component $e^{i\mathbf{k}\cdot\mathbf{r}}$ while leaving $u_n(\mathbf{r})$ unperturbed. This leads to QD eigenfunctions near the $\Gamma$ point in the form of

$$\psi_{n,\mathbf{k}}(\mathbf{r}) = u_n(\mathbf{r})\phi_{\mathbf{k}}(\mathbf{r}), \tag{1.2}$$

where $u_n$ is dictated by the material band structure and the quantized QD envelope function $\phi_{\mathbf{k}}(\mathbf{r})$ is dictated by the dot shape.

Since GaAs and InAs have different bandgaps, as represented on the energy diagram in figure 1.2, electrons and holes can be trapped in the corresponding potential well. In an extreme simplified picture, we can approximate a QD as a 3D infinite potential well and obtain a first approximation for the envelop functions $\phi_{\mathbf{k}}$ of electrons and holes. In the effective mass approximation, this simplified model gives the energy between the excited states and the fundamental state as [87]:

$$E_{e,h} = \frac{\hbar^2\pi^2}{2m^*_{e,h}}\left(\frac{n_x^2}{L_x^2} + \frac{n_y^2}{L_y^2} + \frac{n_z^2}{L_z^2}\right) \tag{1.3}$$

where $n_x, n_y, n_z$ are strictly positive integers labeling the quantization of $\mathbf{k}$ in each Cartesian direction, $m_e$ (resp. $m_h$) is the effective mass of the electron (resp. of the hole) and $L_x$, $L_y$ and $L_z$ are the dimensions of the well along $x$, $y$ and $z$ respectively. This 3D confinement gives rise to 'shells' for the electron and the hole labeled $s$-shell, $p$-shell, and so on, analogous to atomic physics.

In our case, the QDs are mostly flat in the $(xy)$ plane and have a very small height, which entails that there is only one accessible energy level in the $z$ direction ($n_z = 1$). Moreover, the recombination time of an excited state corresponding to $n_{x,y} > 1$ at 10 K is much slower ($\simeq 1$ ns) than the thermalization of high-energy carriers to the lowest-energy state ($< 50$ ps). In the following, we will be mostly interested in the optical recombination of single QDs brought to their first excited state either by direct excitation or through non-resonant excitation followed by rapid relaxation. Therefore we will only consider the ground state and first excited state of the in-plane quantization to explain the transitions studied in this thesis.

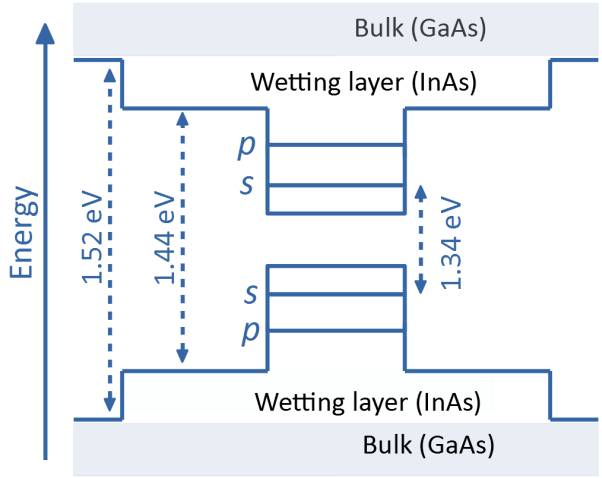


Figure 1.2: Sketch of the energy structure of a quantum dot. The energy gap for the wetting layer and GaAs are also indicated. Here, $s$ and $p$ label the shell arising from the 3D confinement of the slowly-varying component of the electronic wavefunction.

### 1.1.3 Occupancy of a quantum dot

The properties of the single-photons emitted by a QD depend strongly on the optical transition. In this section, I present the different accessible states for the QD, and relate them to the different chapters of the thesis where I explore their properties in the context of single-photon emission.

#### Different accessible states

The energy levels of the QD can be filled in different ways, as shown in figure 1.3. When they contain an electron-hole pair, the corresponding state is often called *exciton* ($X$) although the Coulomb interaction of the electron and hole is a perturbation. When there is an extra hole (resp. electron) in the valence (resp. conduction) band, the transition is a positive (resp. negative) charged exciton, also called trion, written $X^+$ (resp. $X^-$). Most charged exciton transitions studied in this thesis are $X^+$ transitions and will be referred to as *trions* unless stated otherwise. Finally, QDs can also contain two electrons and two holes, in which case the transition is called *biexciton* ($XX$). In this case, because of the Coulomb interaction between the carriers, the energy of the biexciton is not exactly equal to twice the energy of the exciton. For all these possible transitions, the recombination of an electron and a hole give rise to the emission of a photon. The polarization of the emitted photon is governed by the optical selection rules that we will discuss in section 1.2.

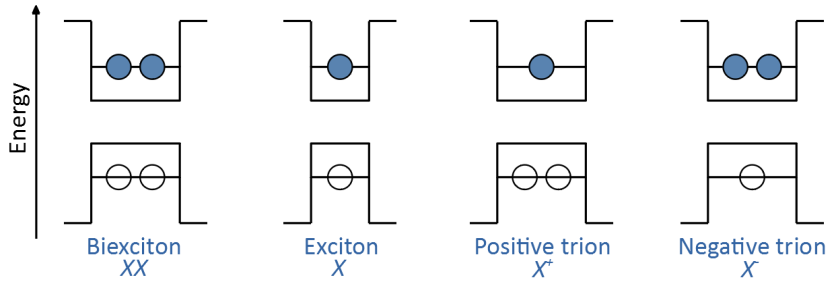


Figure 1.3: Accessible first excited states of a QD.

Using $n-i-p$ diode structures, it is possible to control the occupancy of a QD [88, 89]. In order to study the spin of trions, a 20 nm-thick $Ga_{0.1}Al_{0.9}As$ barrier can be added above the QD layer on the $p$-doped side in order to increase the hole capture time inside the QD [90]. By creating an electron-hole pair in the QD with an additional laser, we can then trap a hole since the electron quickly escapes whereas the hole can not, as shown in figure 1.4 [91]. It is even possible to have several extra charges, in which case we talk about $X^{2+}$, $X^{2-}$, etc.

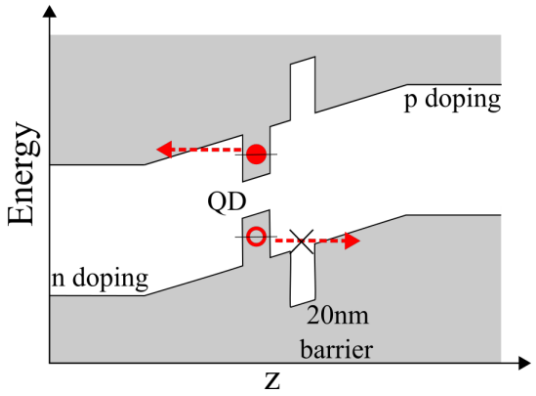


Figure 1.4: Schematic of a doping structure allowing to trap a hole in a QD: a tunneling barrier reduces the hole tunneling rate. Extracted from [91].

Excitons and trions optical transitions can both be used to generate single photons. When the trion decays, the systems ends up in a state made of a single charge, which has a spin and so can be used as a stationary qubit [92]. The generation of single photons using trions and excitons is discussed in Chapter 2.

Biexcitons can be used to generate entangled photon pairs via the radiative cascade $XX \rightarrow X \rightarrow$ ground state. For that purpose, the excitonic wavefunction must have a specific level of symmetry. This mechanism is the initial motivation for Chapter 4 of this thesis.

### 1.1.4 Hole energy levels

Every possible configuration of occupancy of the QD previously described contains a hole. This brings up a more detailed discussion about the hole energy levels, since they influence the properties of the emitted photons when this hole recombines with an electron.

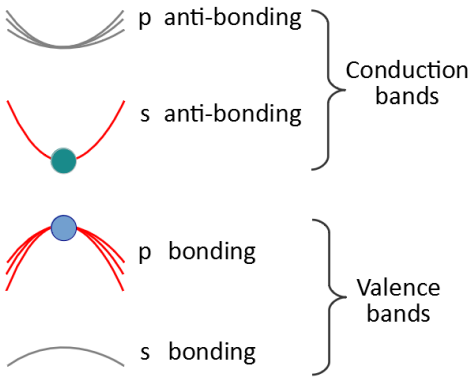


Figure 1.5: Schematic of the conduction and valence bands in the zincblende structure. Here, $s$ and $p$ label the bands composed of molecular orbitals described by the fast-varying component of the electronic wavefunction.

Let us consider an exciton in a QD and restrict ourselves to the highest occupied and lowest unoccupied levels. Figure 1.5 presents the bulk valence and conduction bands for a semiconductor with a zincblende structure such as GaAs and InAs. Each band from the diagram corresponds to a given index $n$ of the periodic component of the QD electronic wavefunction $u_n(\mathbf{r})$ formed from the molecular orbitals of the lattice unit cell [86] (referred to as $s$, $p$, $d$, etc., not to be confused with the shells introduced previously). As we can see on the figure, the electron is in an $s$ antibonding orbital of the conduction band and so its orbital angular momentum $L_e$ is equal to 0, with only one projection $m_l^- = 0$. Its spin is equal to 1/2 and so it also has two possible states corresponding to the two projections of its spin along the $z$ axis: $m_s^- = 1/2$ and $-1/2$. We can also see that the hole is in a $p$ bonding orbital of the valence band and so its orbital angular momentum $L_h$ is equal to 1, giving rise to three possible projections: $m_l^+ = -1$; 0 or $-1$. Its spin is also 1/2, with two projections $m_s^+ = 1/2$ and $-1/2$. The electron has 2 possible states while the hole has 6 and so the total number of accessible states for an exciton is $2 \times 6 = 12$.

Let us first focus on the states of the hole. The six accessible states are represented in figure 1.6.

| Total angular momentum projection | $-3/2$ | $-1/2$ | $-1/2$ | $+1/2$ | $+1/2$ | $+3/2$ |
|---|---|---|---|---|---|---|
| $\lvert m_l^+, m_s^+ \rangle$ | $\lvert -1, -1/2 \rangle$ | $\lvert -1, +1/2 \rangle$ | $\lvert 0, -1/2 \rangle$ | $\lvert 0, +1/2 \rangle$ | $\lvert +1, -1/2 \rangle$ | $\lvert +1, +1/2 \rangle$ |

Figure 1.6: Possible states for the hole of the exciton (tensor basis).

Following rules for the addition of angular momenta, the total angular momentum takes two possible values ($|1/2 + 1 = 3/2|$ or $|1/2 - 1| = 1/2$). The eigenstates for the hole in the coupled basis are actually combinations of the six states constituting the tensor basis

$|m_l^+, m_s^+\rangle$. They are written as follows:

$$\begin{array}{lll} |-1;-1/2\rangle & -\frac{1}{\sqrt{3}}|0;-1/2\rangle + \sqrt{\frac{2}{3}}|-1;+1/2\rangle & \sqrt{\frac{2}{3}}|0;-1/2\rangle + \frac{1}{\sqrt{3}}|-1;+1/2\rangle \\ -|+1;+1/2\rangle & -\frac{1}{\sqrt{3}}|0;+1/2\rangle - \sqrt{\frac{2}{3}}|+1;-1/2\rangle & \sqrt{\frac{2}{3}}|0;+1/2\rangle - \frac{1}{\sqrt{3}}|+1;-1/2\rangle \end{array} \tag{1.4}$$

When we introduce the notations $|\Uparrow\rangle$ for $|m_s^+ = +1/2\rangle$, $|\Downarrow\rangle$ for $|m_s^+ = -1/2\rangle$, and $\frac{|X \pm iY\rangle}{\sqrt{2}}$ for $|m_l^+ = \pm 1\rangle$, we retrieve the states given in reference [93], shown in table 1.1. The corresponding energy diagram is plotted in figure 1.7.

| Expression | Name | Notation |
|---|---|---|
| $\frac{1}{\sqrt{2}}\|(X-iY)\Downarrow\rangle$ | Heavy hole $hh$ | $\|-3/2\rangle$ |
| $-\frac{1}{\sqrt{3}}\|Z\Downarrow\rangle + \frac{1}{\sqrt{3}}\|(X-iY)\Uparrow\rangle$ | Split-off $so$ | |
| $\sqrt{\frac{2}{3}}\|Z\Downarrow\rangle + \frac{1}{\sqrt{6}}\|(X-iY)\Uparrow\rangle$ | Light hole $lh$ | $\|-1/2\rangle$ |
| $-\frac{1}{\sqrt{3}}\|Z\Uparrow\rangle - \frac{1}{\sqrt{3}}\|(X+iY)\Downarrow\rangle$ | Split-off $so$ | |
| $\sqrt{\frac{2}{3}}\|Z\Uparrow\rangle - \frac{1}{\sqrt{6}}\|(X+iY)\Downarrow\rangle$ | Light hole $lh$ | $\|+1/2\rangle$ |
| $-\frac{1}{\sqrt{2}}\|(X+iY)\Uparrow\rangle$ | Heavy hole $hh$ | $\|+3/2\rangle$ |

Table 1.1: Eigenstates for the hole.

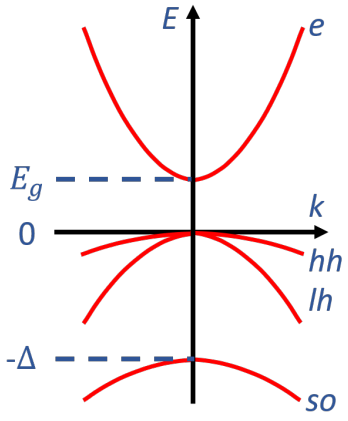


Figure 1.7: Schematic of zincblende bands in the presence of spin-orbit coupling. $E_g$ is the gap energy and $\Delta$ the spin-orbit splitting.

The spin-orbit coupling results in a degeneracy lifting leading to a band called the "split-off" band. The energy difference $\Delta$ is big enough to not consider any mixing with the split-off band (in the few hundreds meV range). This band structure describes the bulk crystal where light holes and heavy holes are degenerate at $\mathbf{k}=\mathbf{0}$. The strain between the InGaAs and GaAs layers actually entails a deformation that induces a large splitting between the heavy and light hole bands [94]. Furthermore, when considering the QD confinement, the difference in effective masses further splits those bands. In the end, the splitting between heavy and light holes bands is on the order of 50 meV at $\mathbf{k}=\mathbf{0}$.

### 1.1.5 Excitonic case: exchange Hamiltonian

We consider now that the hole described so far is trapped with an electron in the QD. These two particles are coupled by a direct Coulomb interaction, making them attract each other

because they have opposite charges. If there is no extra charge involved, namely if the dot is occupied by an exciton and not a trion, the hole and the electron are also coupled by a Coulomb exchange interaction. This interaction is commonly split into two terms, namely the short-range and the long-range exchange interactions [95]. The long-range part originates from the interaction between dipoles located in different bulk unit cells [96], and is sometimes neglected for solid-state QDs because its effect is screened by the bulk dielectric tensor [97]. In the following, we neglect the long-range interaction, but the concepts would stay similar even if we were to take it into account. The spin Hamiltonian for the short-range part of the electron-hole exchange interaction of an exciton is given by [98]:

$$\hat{H}_{\text{exch.}} = -\sum_{i=x,y,z} \left(a_{\text{i}} J_{h,i} S_{e,i} + b_{\text{i}} J_{h,i}^3 S_{e,i}\right) \tag{1.5}$$

with $J_h$ the spin of the hole, $S_{\text{e}}$ the spin of the electron and $a_{\text{i}}$ and $b_{\text{i}}$ the spin coupling constants along each axis [99].

Using the electron spin matrices and heavy holes total angular momentum matrices, given by:

$$S_x = \frac{1}{2}\begin{pmatrix} 0 & 1 \\ 1 & 0 \end{pmatrix} \qquad S_y = \frac{1}{2i}\begin{pmatrix} 0 & 1 \\ -1 & 0 \end{pmatrix} \qquad S_z = \frac{1}{2}\begin{pmatrix} 1 & 0 \\ 0 & -1 \end{pmatrix} \tag{1.6}$$

$$J_x = \frac{1}{2}\begin{pmatrix} 0 & \sqrt{3} & 0 & 0 \\ \sqrt{3} & 0 & 2 & 0 \\ 0 & 2 & 0 & \sqrt{3} \\ 0 & 0 & \sqrt{3} & 0 \end{pmatrix} \quad J_y = \frac{1}{2i}\begin{pmatrix} 0 & \sqrt{3} & 0 & 0 \\ -\sqrt{3} & 0 & 2 & 0 \\ 0 & -2 & 0 & \sqrt{3} \\ 0 & 0 & -\sqrt{3} & 0 \end{pmatrix} \tag{1.7}$$

$$J_z = \begin{pmatrix} 3/2 & 0 & 0 & 0 \\ 0 & 1/2 & 0 & 0 \\ 0 & 0 & -1/2 & 0 \\ 0 & 0 & 0 & -3/2 \end{pmatrix}$$

In the basis $\{|+\frac{3}{2},+\frac{1}{2}\rangle, |+\frac{3}{2},-\frac{1}{2}\rangle, |+\frac{1}{2},+\frac{1}{2}\rangle, |+\frac{1}{2},-\frac{1}{2}\rangle, |-\frac{1}{2},+\frac{1}{2}\rangle, |-\frac{1}{2},-\frac{1}{2}\rangle, |-\frac{3}{2},+\frac{1}{2}\rangle, |-\frac{3}{2},-\frac{1}{2}\rangle\}$, we get:

$$\hat{H}_{\text{exch.}} = \begin{pmatrix} \delta_0 & 0 & 0 & \delta_3 & 0 & 0 & 0 & -\delta_2 \\ 0 & -\delta_0 & \delta_4 & 0 & 0 & 0 & -\delta_1 & 0 \\ 0 & \delta_4 & \delta_7 & 0 & 0 & \delta_5 & 0 & 0 \\ \delta_3 & 0 & 0 & -\delta_7 & \delta_6 & 0 & 0 & 0 \\ 0 & 0 & 0 & \delta_6 & -\delta_7 & 0 & 0 & \delta_3 \\ 0 & 0 & \delta_5 & 0 & 0 & \delta_7 & \delta_4 & 0 \\ 0 & -\delta_1 & 0 & 0 & 0 & \delta_4 & -\delta_0 & 0 \\ -\delta_2 & 0 & 0 & 0 & \delta_3 & 0 & 0 & \delta_0 \end{pmatrix} \tag{1.8}$$

where the couplings $\delta_k$, $k \in \{1, ..., 7\}$ are defined as follows:

$$\delta_0 = -3/4(a_z + 9/4b_z) \qquad \delta_4 = -\frac{\sqrt{3}}{4}(a_x + a_y + \frac{7}{4}(b_x + b_y))$$

$$\delta_1 = \frac{3}{8}(b_x - b_y) \qquad \delta_5 = -\frac{1}{2}(a_x - a_y + \frac{5}{2}(b_x - b_y))$$

$$\delta_2 = \frac{3}{8}(b_x + b_y) \qquad \delta_6 = -\frac{1}{2}(a_x + a_y) + \frac{5}{2}(b_x + b_y))$$

$$\delta_3 = -\frac{\sqrt{3}}{4}(a_x - a_y + \frac{7}{4}(b_x - b_y)) \qquad \delta_7 = -\frac{1}{4}(a_z + \frac{1}{4}b_z)$$

The exchange Hamiltonian is not sufficient to describe the band structure, especially to consider for heavy/light hole splitting or mixing. For that purpose, we also take into account the Luttinger-Kohn Hamiltonian [100, 101], which governs the behaviour of holes bands. It was derived from the $\mathbf{k}\cdot\mathbf{p}$ method using Bloch wavefunctions and is given in the basis $\{|3/2, 3/2\rangle, |3/2, 1/2\rangle, |3/2, -1/2\rangle, |3/2, -3/2\rangle\}$ by:

$$\hat{H}_{\text{LK}} = \begin{pmatrix} P+Q & -S & R & 0 \\ -S^* & P-Q & 0 & R \\ R^* & 0 & P-Q & S \\ 0 & R^* & S^* & P+Q \end{pmatrix} \tag{1.9}$$

where $P$, $Q$, $R$ and $S$ are parameters that depend on the coupling between the bands, and also on strain tensors if we take them into account through the Bir-Pikus term [102]. In the basis $\{|+\frac{3}{2}, +\frac{1}{2}\rangle, |+\frac{3}{2}, -\frac{1}{2}\rangle, |+\frac{1}{2}, +\frac{1}{2}\rangle, |+\frac{1}{2}, -\frac{1}{2}\rangle, |-\frac{1}{2}, +\frac{1}{2}\rangle, |-\frac{1}{2}, -\frac{1}{2}\rangle, |-\frac{3}{2}, +\frac{1}{2}\rangle, |-\frac{3}{2}, -\frac{1}{2}\rangle\}$, the expression of these two Hamiltonians $\hat{H}_{\text{exch.}}$ and $\hat{H}_{\text{LK}}$ combined into one is:

$$\hat{H}_{\text{exch.+LK}} = \begin{pmatrix} \delta_0+P+Q & 0 & -S & \delta_3 & R & 0 & 0 & -\delta_2 \\ 0 & -\delta_0+P+Q & \delta_4 & -S & 0 & R & -\delta_1 & 0 \\ -S^* & \delta_4 & \delta_7+P-Q & 0 & 0 & \delta_5 & R & 0 \\ \delta_3 & -S^* & 0 & -\delta_7+P-Q & \delta_6 & 0 & 0 & R \\ R^* & 0 & 0 & \delta_6 & -\delta_7+P-Q & 0 & S & \delta_3 \\ 0 & R^* & \delta_5 & 0 & 0 & \delta_7+P-Q & \delta_4 & S \\ 0 & -\delta_1 & R^* & 0 & S^* & \delta_4 & -\delta_0+P+Q & 0 \\ -\delta_2 & 0 & 0 & R^* & \delta_3 & S^* & 0 & \delta_0+P+Q \end{pmatrix} \tag{1.10}$$

The heavy holes and light holes are split by $\Delta_{lh} = |2Q|$. In practice, this value is on the order of magnitude of tenths of meV, and the heavy hole band is the closest in energy to the conduction band (see figure 1.7), so we can neglect the light holes, under the condition that there is no mixing of light holes and heavy holes (i.e. $S = R = 0$). This mixing effect will be developed later.

### Restriction to heavy holes

The total angular momentum component along the $z$ axis (growth axis) is given by $J_{h,z} = \pm 3/2$ for the heavy holes and $S_{e,z} = \pm 1/2$ for the electrons. Therefore, there are four possible combinations to give excitonic states:

$$
\begin{aligned}
|\psi_{\mathrm{HH}}^{+1}\rangle &= \left|\frac{3}{2},+\frac{3}{2}\right\rangle_{\text{hole}} \otimes \left|-\frac{1}{2}\right\rangle_{\text{electron}} & |\psi_{\mathrm{HH}}^{+2}\rangle &= \left|\frac{3}{2},+\frac{3}{2}\right\rangle_{\text{hole}} \otimes \left|+\frac{1}{2}\right\rangle_{\text{electron}} \\
|\psi_{\mathrm{HH}}^{-1}\rangle &= \left|\frac{3}{2},-\frac{3}{2}\right\rangle_{\text{hole}} \otimes \left|+\frac{1}{2}\right\rangle_{\text{electron}} & |\psi_{\mathrm{HH}}^{-2}\rangle &= \left|\frac{3}{2},-\frac{3}{2}\right\rangle_{\text{hole}} \otimes \left|-\frac{1}{2}\right\rangle_{\text{electron}}
\end{aligned}
\tag{1.11}
$$

These states are characterized by their angular momentum projections $M = S_{e,z} + J_{h,z}$. When the electron and the hole of these states recombine, the system is left in its ground state that has a zero angular momentum. Then, the states with $M = \pm 2$ are not optically active since light matter interaction conserves the angular momentum. They are thus called dark excitons while the states with $M = \pm 1$ are called bright excitons.

In the basis $(|\psi_{\mathrm{HH}}^{+2}\rangle, |\psi_{\mathrm{HH}}^{+1}\rangle, |\psi_{\mathrm{HH}}^{-1}\rangle, |\psi_{\mathrm{HH}}^{-2}\rangle)$, the Hamiltonian (1.8) is reduced to:

$$
\hat{H}_{\text{exch.+LK, HH}} = \begin{pmatrix}
\delta_0+P+Q & 0 & 0 & -\delta_2 \\
0 & -\delta_0+P-Q & -\delta_1 & 0 \\
0 & -\delta_1 & -\delta_0+P-Q & 0 \\
-\delta_2 & 0 & 0 & \delta_0+P+Q
\end{pmatrix}
\tag{1.12}
$$

The diagonal terms of this Hamiltonian show that there is a splitting between the bright and dark states, equal to $2\delta_0$. The off-diagonal terms $\delta_2$ show a mixing and splitting of the dark states. Finally, the off-diagonal terms $\delta_1$ imply a mixing and splitting of the bright states in the case where the in-plane rotational symmetry is broken, that is when $b_x \neq b_y$. In terms of symmetry, this means that the $D_{2d}$ symmetry is reduced to $C_{2v}$ (corresponding to one $C_2$ axis and 2 $\sigma_v$ planes, see figure A.1(c) in Appendix A). This splitting of the bright states is called the *fine structure splitting* (FSS) [103].

### Synthesis

All these considerations are synthetized in the diagram shown in figure 1.8.

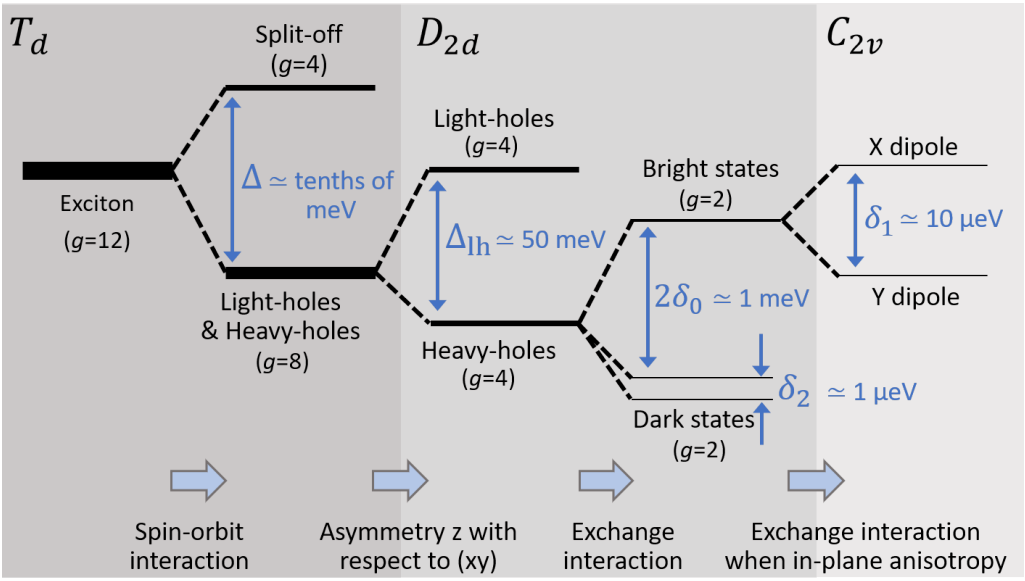


Figure 1.8: Diagram summarizing the accessible states for an exciton and their degeneracies $g$ (proportional to the thickness of the levels on the schematic).

In our samples, the fine structure splitting is usually on the order of 0 to 20 μeV. We will see in Chapter 2 how the fine structure splitting influences the QD emission. There are different ways to control the FSS that have been explored to allow for various applications. This topic will be developed in Chapter 4.

## 1.2 Optical selection rules

Polarization is a very important property of light, especially in the context of quantum operations, since it is commonly used as a measured and encoded quantity. In QDs like in atoms in general, the polarization of the emitted light depends on the states involved in the recombination, following optical selection rules. In this section, we discuss the polarization of single photons emitted from exciton and trion-based sources, that will be a central topic of Chapter 2. I will also use the fundamentals presented here for the optical selection rules of biexcitonic radiative cascades in Chapter 4.

The optical selection rules in the dipole approximation are given by the dipole vector operator $\hat{\mathbf{d}} = \sum_i q_i \hat{\mathbf{r}}_i$, where $q_i$ is the charge of particle $i$ and $\hat{\mathbf{r}}_i$ is its position operator. In the semi-classical approximation where we treat the field classically, the optical coupling between an initial $|i\rangle$ and final $|f\rangle$ state is given by $|\mathbf{d}_{if} \cdot \mathbf{p}_l|^2$, where $\mathbf{d}_{if} = \langle f|\hat{\mathbf{d}}|i\rangle$ is the transition dipole moment vector and $\mathbf{p}_l$ is one of two orthogonal polarization unit vectors in the plane of the QD. In the Bloch function approximation and for interband transitions, the selection rules and emission polarization are governed by the change in band occupancy and the overlap of the envelope functions $\mathbf{d}_{if} \simeq \langle u_{f,n'}|\hat{\mathbf{d}}|u_{i,n}\rangle \langle \phi_f|\phi_i\rangle$. Here, we consider $s$ states of the envelope function of both the electron and hole. Then, we focus only on the first term that determines whether or not a QD optical transition is allowed and also its emission polarization properties.

First, we define a quantum basis vectors for all the bright exciton states: we do not restrict the discussion to the heavy holes. We thus consider heavy holes and light holes with an angular momentum projection $M = \pm 1$:

$$|\psi_{\text{ground}}\rangle = |g\rangle$$

$$|\psi^{+1}_{\text{HH}}\rangle = \left|\tfrac{3}{2}, +\tfrac{3}{2}\right\rangle_{\text{hole}} \otimes \left|-\tfrac{1}{2}\right\rangle_{\text{electron}} \qquad |\psi^{+1}_{\text{LH}}\rangle = \left|\tfrac{3}{2}, +\tfrac{1}{2}\right\rangle_{\text{hole}} \otimes \left|+\tfrac{1}{2}\right\rangle_{\text{electron}}$$

$$|\psi^{-1}_{\text{LH}}\rangle = \left|\tfrac{3}{2}, -\tfrac{1}{2}\right\rangle_{\text{hole}} \otimes \left|-\tfrac{1}{2}\right\rangle_{\text{electron}} \qquad |\psi^{-1}_{\text{HH}}\rangle = \left|\tfrac{3}{2}, -\tfrac{3}{2}\right\rangle_{\text{hole}} \otimes \left|+\tfrac{1}{2}\right\rangle_{\text{electron}}$$

We know that states that have an angular momentum projection $M = \pm 1$ give rise to circularly polarized photons when decaying to the ground state [104]. Left or right polarization depends on the sign of $M$. Right circular arises from the recombination of $|\psi^{+1}_{\text{LH}}\rangle$ and $|\psi^{+1}_{\text{HH}}\rangle$, and left circular from the recombination of $|\psi^{-1}_{\text{LH}}\rangle$ and $|\psi^{-1}_{\text{HH}}\rangle$. The optical dipole vector operator is given by the outer tensor product of the initial and final states multiplied by their dipole moment vector giving rise to emission. Under its matrix form, in the basis $\{|\psi_{\text{ground}}\rangle, |\psi^{+1}_{\text{HH}}\rangle, |\psi^{+1}_{\text{LH}}\rangle, |\psi^{-1}_{\text{LH}}\rangle, |\psi^{-1}_{\text{HH}}\rangle\}$, it is given by:

$$\hat{\mathbf{d}} \simeq d \begin{pmatrix} \mathbf{0} & \boldsymbol{\sigma}^+ & \boldsymbol{\sigma}^+ & \boldsymbol{\sigma}^- & \boldsymbol{\sigma}^- \\ \boldsymbol{\sigma}^- & \mathbf{0} & \mathbf{0} & \mathbf{0} & \mathbf{0} \\ \boldsymbol{\sigma}^- & \mathbf{0} & \mathbf{0} & \mathbf{0} & \mathbf{0} \\ \boldsymbol{\sigma}^+ & \mathbf{0} & \mathbf{0} & \mathbf{0} & \mathbf{0} \\ \boldsymbol{\sigma}^+ & \mathbf{0} & \mathbf{0} & \mathbf{0} & \mathbf{0} \end{pmatrix} \tag{1.13}$$

where $d$ is the dipole magnitude and $\boldsymbol{\sigma}^{\pm}$ are unit vectors giving rise to circular polarization. For simplicity, we assume that the dipole magnitude for each optically-allowed transition is roughly equal. In reality, the envelope functions for heavy and light holes may differ leading to different dipole magnitudes. However, such a case does not alter the following discussion.

From now on, to compute the polarization vector of any transition from an initial state to the ground state, we just evaluate the element of the dipole operator. For example, we recover a $\boldsymbol{\sigma}^+$ polarization when computing $\langle\psi_{\text{ground}}|\,\hat{\mathbf{d}}\,|\psi^{+1}_{\text{HH}}\rangle$.

### 1.2.1 Polarization emitted by excitons in absence of FSS or by trions

In this section, we aim at determining the polarization emitted when an electron hole pair recombines in the case of an exciton showing a zero FSS. We will see that the same polarization arises from the recombination of an electron-hole pair from a trion.

We focus on the bright states of the exciton and restrict Hamiltonian (1.10) to the basis: $\{|\psi^{+1}_{\text{HH}}\rangle, |\psi^{+1}_{\text{LH}}\rangle, |\psi^{-1}_{\text{LH}}\rangle, |\psi^{-1}_{\text{HH}}\rangle\}$, corresponding to the combinations giving an angular momentum projection of $M = \pm 1$. In this basis, the exciton Hamiltonian is written:

$$\hat{H}_{\text{exch.+LK, Br. St.}} = \begin{pmatrix} -\delta_0 + P + Q & \delta_4 & R & -\delta_1 \\ \delta_4 & \delta_7 + P - Q & \delta_5 & R \\ R^* & \delta_5 & \delta_7 + P - Q & \delta_4 \\ -\delta_1 & R^* & \delta_4 & -\delta_0 + P + Q \end{pmatrix} \tag{1.14}$$

In this section, we suppose that there is no fine structure splitting ($\delta_1 = 0$), and that the hole states are purely heavy ($R = 0$ and $\delta_4 = 0$). In that case, the eigenvectors of matrix (1.14) are:

$$\begin{array}{ll} |\psi_{\mathrm{HH}}^{+1}\rangle & \frac{1}{\sqrt{2}}(-|\psi_{\mathrm{LH}}^{+1}\rangle + |\psi_{\mathrm{LH}}^{-1}\rangle) \\ |\psi_{\mathrm{HH}}^{-1}\rangle & \frac{1}{\sqrt{2}}(|\psi_{\mathrm{LH}}^{+1}\rangle + |\psi_{\mathrm{LH}}^{-1}\rangle) \end{array}$$

The two eigenstates on the left contain purely heavy holes, whereas the two eigenstates on the right contain mixtures of light holes. We are interested in the emission from the two eigenstates of the left, since they correspond to the lowest-energy excited states.

In the case of a trion, one of the charges (either the hole for a positive trion or the electron for a negative trion) is paired with the exciton. This pairing must satisfy the Pauli exclusion principle. For example, in the case of a negative trion, we cannot have $|\psi_{\mathrm{HH}}^{+1}\rangle\,|-\frac{1}{2}\rangle_{\mathrm{electron}}$ because this implies the state has two spin-down electrons occupying the $s$ band. Hence, the two lowest-energy excited states of the trion are $|\psi_{\mathrm{HH}}^{+1}\rangle\,|+\frac{1}{2}\rangle_{\mathrm{electron}}$ and $|\psi_{\mathrm{HH}}^{-1}\rangle\,|-\frac{1}{2}\rangle_{\mathrm{electron}}$. The corresponding ground states are then simply $|\psi_{\mathrm{ground}}\rangle\,|+\frac{1}{2}\rangle_{\mathrm{electron}}$ and $|\psi_{\mathrm{ground}}\rangle\,|-\frac{1}{2}\rangle_{\mathrm{electron}}$. This pairing of spins prohibits the exchange interaction in the excited state [105]. Thus, due to spin-conservation, the polarization selection rules of the degenerate negative trion are also dictated by the recombination of the heavy-hole eigenstates $|\psi_{\mathrm{HH}}^{+1}\rangle$ or $|\psi_{\mathrm{HH}}^{-1}\rangle$.

In both cases, excitons with no FSS or trions, the light-matter interaction governed by the optical dipole vector operator (1.13) gives that the emitted polarizations are:

$$\begin{aligned} \langle\psi_{\mathrm{ground}}|\,\hat{\mathbf{d}}\,|\psi_{\mathrm{HH}}^{+1}\rangle &= d\boldsymbol{\sigma}^{+} \\ \langle\psi_{\mathrm{ground}}|\,\hat{\mathbf{d}}\,|\psi_{\mathrm{HH}}^{-1}\rangle &= d\boldsymbol{\sigma}^{-} \end{aligned} \tag{1.15}$$

We can visualize the polarizations in polar plots as the one below in figure 1.9(a), that corresponds to the polarizations $\boldsymbol{\sigma}^{+}$ and $\boldsymbol{\sigma}^{-}$.

### 1.2.2 Polarization emitted by excitons in presence of FSS

In that case, we set $\delta_4 = 0$ and $\delta_1 \neq 0$. The eigenvectors of matrix (1.14) are:

$$\begin{array}{ll} \frac{1}{\sqrt{2}}(|\psi_{\mathrm{HH}}^{+1}\rangle + |\psi_{\mathrm{HH}}^{-1}\rangle) & \frac{1}{\sqrt{2}}(-|\psi_{\mathrm{LH}}^{+1}\rangle + |\psi_{\mathrm{LH}}^{-1}\rangle) \\ \frac{1}{\sqrt{2}}(-|\psi_{\mathrm{HH}}^{+1}\rangle + |\psi_{\mathrm{HH}}^{-1}\rangle) & \frac{1}{\sqrt{2}}(|\psi_{\mathrm{LH}}^{+1}\rangle + |\psi_{\mathrm{LH}}^{-1}\rangle) \end{array} \tag{1.16}$$

The two eigenstates on the right are the same mixtures of light holes as previously. Here again, the ones we are interested in are the two eigenstates on the left, since they are combinations of excitons that correspond to the lowest-energy excited states.

The optical dipole vector operator (1.13) gives that the emitted polarizations are:

$$\begin{aligned}\frac{1}{\sqrt{2}}\langle\psi_{\text{ground}}|\,\hat{\mathbf{d}}(|\psi_{\text{HH}}^{+1}\rangle+|\psi_{\text{HH}}^{-1}\rangle)&=\frac{d}{\sqrt{2}}(\boldsymbol{\sigma}^{+}+\boldsymbol{\sigma}^{-})\\ \frac{1}{\sqrt{2}}\langle\psi_{\text{ground}}|\,\hat{\mathbf{d}}(-|\psi_{\text{HH}}^{+1}\rangle+|\psi_{\text{HH}}^{-1}\rangle)&=\frac{d}{\sqrt{2}}(-\boldsymbol{\sigma}^{+}+\boldsymbol{\sigma}^{-})\end{aligned} \tag{1.17}$$

These polarizations correspond to two orthogonal linear polarizations illustrated in figure 1.9.

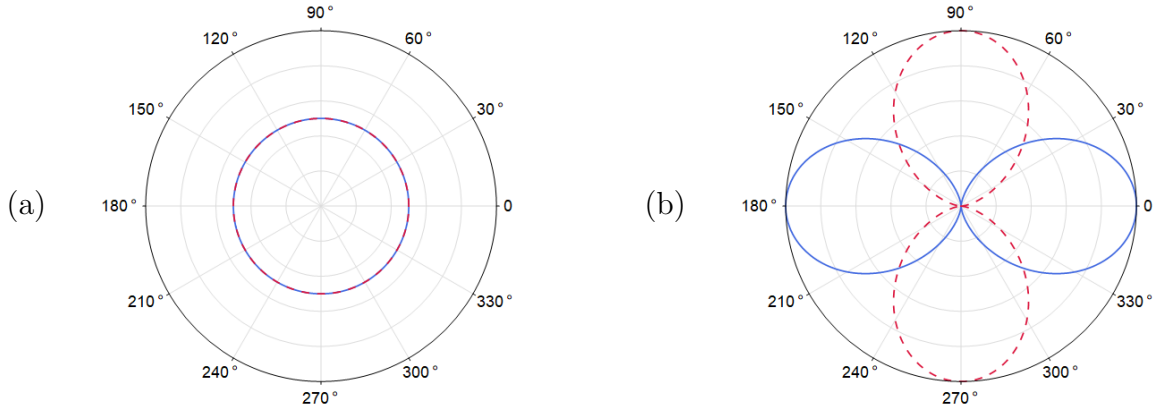


Figure 1.9: (a) Intensity of emission (in units of dipole magnitude $d$) along a linear polarization in polar coordinates, for the recombination of an exciton made of an electron and a purely heavy hole and a zero fine structure splitting $\delta_1 = 0$. The two eigenstates recombinations give rise to perfectly circularly polarized light, in opposite directions (since they have $+1$ and $-1$ angular momenta). (b) Same for a non-zero fine structure splitting $\delta_1 \neq 0$. The fact that the lines go through zero shows that the emission is perfectly linearly polarized: the two eigenstates recombinations give rise to perfectly linear and orthogonally polarized light.

In practice, the polarizations emitted by trions are not always perfectly circular: they sometimes show some ellipticity. Also, polarizations emitted by excitons showing a non-zero FSS are not always orthogonal, as we will observe experimentally in Chapter 2. This comes from the heavy-light hole mixing, as we will see in the next section.

### 1.2.3 Polarization emitted by trions in presence of heavy/light hole mixing

In the previous section, we explored the case where the energy eigenstates are composed of electron spin states and pure heavy holes. However, in some cases, a mixing can occur between the heavy holes and the light holes. This heavy/light hole mixing appears through the non-diagonal terms of the Luttinger-Kohn Hamiltonian (1.9) through the coefficients $R$ and $S$.

It has been shown that these terms are non-zero when the QD presents an in-plane shape anisotropy and when its major axis does not align with any of the cristallographic axes of the semiconductor [106]. It can also arise from strain anisotropy [102]. In either case, a heavy/light hole mixing occurs. Then, one can write the states of the lowest-energy holes (the

ones recombining with the electrons to give a photon), as the following:

$$|\phi_{\mathrm{H}}^{\pm}\rangle = \frac{1}{\sqrt{1+\beta^2}}\left(|\pm 3/2\rangle - \beta e^{\pm 2i\theta_s}\,|\mp 1/2\rangle\right) \tag{1.18}$$

where $\beta^2/(1+\beta^2)$ is the probability for the hole to be light. If the mixing arises from strain, then $\beta = \rho_s/\Delta_{lh}$ in the approximation of weak valence-band mixing ($\rho_s \ll \Delta_{lh}$), where $\theta_s$ is the strain orientation and the quantity $\rho_s$ is the strain coupling amplitude [102]. For the electron-hole pair, the state can then be written:

$$|\psi_{\mathrm{H}}^{\pm}\rangle = \frac{1}{\sqrt{1+\beta^2}}\left(|\psi_{\mathrm{HH}}^{\pm 1}\rangle - \beta e^{\pm 2i\theta_s}\,|\psi_{\mathrm{LH}}^{\mp 1}\rangle\right) \tag{1.19}$$

The optical dipole vector operator (1.13) gives that the emitted polarizations are:

$$\begin{aligned}
\langle\psi_{\mathrm{ground}}|\,\hat{\mathbf{d}}\,|\psi_{\mathrm{H}}^{+}\rangle &= \frac{d}{\sqrt{2}}(\boldsymbol{\sigma}^{+} - \beta e^{2i\theta_s}\boldsymbol{\sigma}^{-}) \\
\langle\psi_{\mathrm{ground}}|\,\hat{\mathbf{d}}\,|\psi_{\mathrm{H}}^{-}\rangle &= \frac{d}{\sqrt{2}}(\boldsymbol{\sigma}^{-} - \beta e^{-2i\theta_s}\boldsymbol{\sigma}^{+})
\end{aligned} \tag{1.20}$$

These two polarizations correspond to two elliptical counter-rotating polarizations. The recombination of electrons with light hole states $|\pm 1/2\rangle$ gives photon polarization that is opposite to the one rising from a recombination of electrons with heavy hole states $|\pm 3/2\rangle$. The corresponding polar plots are presented in figure 1.10.

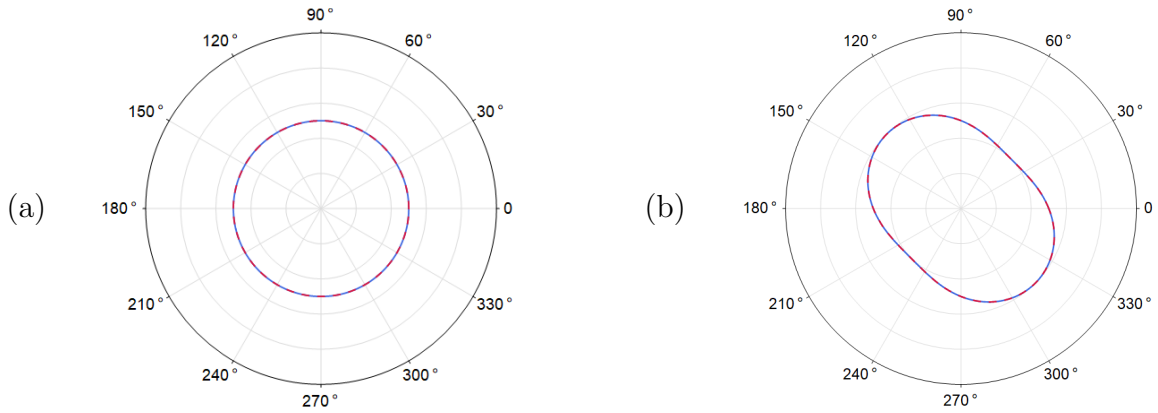


Figure 1.10: Intensity of the emission (in units of dipole magnitude $d$) along a linear polarization in polar coordinates, for the recombination of an electron with (a) a purely heavy hole ($\beta = 0$). The emission is perfectly circularly polarized, as for an exciton without FSS. (b) a mixed heavy/light hole state $|\phi_{\mathrm{H}}^{+}\rangle$ ($\beta = 0.2$). The emission is not perfectly circularly polarized anymore but elliptical: it contains a degree of linear polarization.

### 1.2.4 Polarization emitted by excitons with FSS and heavy/light hole mixing

To take into account the fine structure splitting in the presence of heavy/light hole mixing, we write the Hamiltonian in the mixed holes basis (MHB) $\{|\psi_{\mathrm{H}}^{+}\rangle, |\psi_{\mathrm{H}}^{-}\rangle\}$, with $|\psi_{\mathrm{H}}^{\pm}\rangle$ defined

in equation (1.19). The exchange Hamiltonian has the same expression as in the other basis, with an extra phase:

$$\hat{H}_{\text{exch., MHB}} = \begin{pmatrix} \delta'_0 & \delta'_1 e^{2i\theta'_d} \\ \delta'_1 e^{-2i\theta'_d} & \delta'_0 \end{pmatrix} \tag{1.21}$$

where $\delta'_0$ and $\delta'_1$ are not necessarily equal to $\delta_0$ and $\delta_1$ respectively because they include contributions from splitting and mixing between the light hole components of $|\psi^{\pm}_{\text{H}}\rangle$. The quantity $\theta'_d$ depends primarily on the dot shape orientation $\theta_d$ [102] but can also be influenced by the strain orientation $\theta_s$ due to the hole mixing. Hence, the polarization selection rules can be influenced by the subtle interplay between strain and shape anisotropy [102]. The eigenstates of this matrix are:

$$\begin{aligned} |X\rangle &= \frac{1}{\sqrt{2}}(e^{2i\theta'_d}\,|\psi^{+}_{\text{H}}\rangle + |\psi^{-}_{\text{H}}\rangle) \\ |Y\rangle &= \frac{1}{\sqrt{2}}(-e^{2i\theta'_d}\,|\psi^{+}_{\text{H}}\rangle + |\psi^{-}_{\text{H}}\rangle) \end{aligned} \tag{1.22}$$

After replacing $|\psi^{+}_{\text{H}}\rangle$ and $|\psi^{-}_{\text{H}}\rangle$ by their complex expressions given in equation (1.19), we get:

$$\begin{aligned} |X\rangle &= \frac{1}{\sqrt{2(1+\beta^2)}}\left(e^{2i\theta'_d}\,|\psi^{+1}_{\text{HH}}\rangle - \beta e^{-2i\theta_s}\,|\psi^{+1}_{\text{LH}}\rangle - \beta e^{2i(\theta'_d+\theta_s)}\,|\psi^{-1}_{\text{LH}}\rangle + |\psi^{-1}_{\text{HH}}\rangle\right) \\ |Y\rangle &= \frac{1}{\sqrt{2(1+\beta^2)}}\left(-e^{2i\theta'_d}\,|\psi^{+1}_{\text{HH}}\rangle - \beta e^{-2i\theta_s}\,|\psi^{+1}_{\text{LH}}\rangle + \beta e^{2i(\theta'_d+\theta_s)}\,|\psi^{-1}_{\text{LH}}\rangle + |\psi^{-1}_{\text{HH}}\rangle\right) \end{aligned} \tag{1.23}$$

The optical dipole vector operator (1.13) gives that the emitted polarizations are:

$$\begin{aligned} \langle\psi_{\text{ground}}|\,\hat{\mathbf{d}}\,|X\rangle &= \frac{d}{\sqrt{2(1+\beta^2)}}\left(\boldsymbol{\sigma}^{+}(e^{2i\theta'_d} - \beta e^{-2i\theta_s}) - \boldsymbol{\sigma}^{-}(\beta e^{2i(\theta_s+\theta'_d)} - 1)\right) \\ \langle\psi_{\text{ground}}|\,\hat{\mathbf{d}}\,|Y\rangle &= \frac{d}{\sqrt{2(1+\beta^2)}}\left(-\boldsymbol{\sigma}^{+}(e^{2i\theta'_d} + \beta e^{-2i\theta_s}) + \boldsymbol{\sigma}^{-}(\beta e^{2i(\theta_s+\theta'_d)} + 1)\right) \end{aligned} \tag{1.24}$$

These two polarizations are linear and not perfectly orthogonal. The corresponding polar plots are presented in figure 1.11.

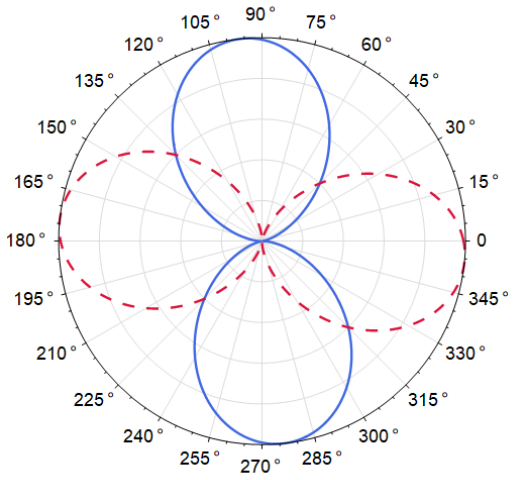


Figure 1.11: Intensity of the emission (in units of dipole magnitude $d$) along a linear polarization in polar coordinates, for the recombination of an exciton that are made of an electron and a mixed heavy/light hole. The emission is still perfectly linearly polarized, but the polarizations of the two dipoles are no longer orthogonal.

A mixing between the light and heavy holes arises from non-diagonal terms in the Luttinger-Kohn Hamiltonian. These terms are large when the in-plane anisotropy of the QD is large or when there is an anisotropic relaxation of strains in the QD plane, which contributes to the non-diagonal terms through the Bir-Pikus term [102]. In our case, the elastic constants tensor is very symmetric for InAs which is cubic. Thus if there are non-negligible non-diagonal terms in the Luttinger-Kohn Hamiltonian, it is most likely due to an in-plane anisotropy of the QD. Furthermore, our QDs are annealed, which relaxes the strains and makes them more symmetric than before the annealing. Hence these effects should be relatively weak when present.

## 1.3 Light-matter interaction

In this section, we further describe light-matter interaction phenomena at the core of our studies. An excited QD can spontaneously emit a single photon with near unity efficiency, but in all directions of space. To counter this issue, spontaneous emission can be controlled to ensure that a QD emits in a well defined mode of the electromagnetic field. This can be done by coupling the QD to a cavity [107]. In the first two subsections, we explore spontaneous emission and its enhancement by a cavity using Fermi's golden rule. We then discuss how to deterministically prepare the QD in the excited state by introducing the Jaynes-Cummings model to describe the coherent control of the QD using optical pulses.

### 1.3.1 Spontaneous emission in the bulk

We describe in this subsection the spontaneous emission rate by the QD in a bulk material [3, 108]. This gives us a reference for the spontaneous emission rate when the QD environment is

not engineered to enhance the emission in a particular mode. We consider a two-level system located in a dielectric material, such as GaAs in our samples, at position $\mathbf{r} = \mathbf{0}$. The two-level system has been brought to its excited state by optical excitation. Once the excitation laser is off, the state of the electromagnetic field around the artificial atom is vacuum. The phenomenon of spontaneous emission populates a state of the electromagnetic field with a photon with a wavevector $\mathbf{k}$ and polarization $\mathbf{p}$ and leaves the two-level system in its ground state. Such situation can be described using perturbation theory in the framework of Fermi's golden rule, that allows to calculate the transition rate from an initial state $|i\rangle$ to a final state $|f\rangle$ given by [109]:

$$\Gamma_{i\to f} = \frac{2\pi}{\hbar} |\langle f| \hat{H}_{\text{pert.}} |i\rangle|^2 \delta(E_\text{f} - E_\text{i}) \tag{1.25}$$

where $\hat{H}_{\text{pert.}}$ is the perturbation undergone by the system.

Here the initial state is $|i\rangle = |e, 0\rangle$ (an artificial atom in its excited state, and no photon) and the final state can be $|f\rangle = |g, \{\mathbf{k}, \mathbf{p}\}\rangle$ (the artificial atom in its ground state and a photon in any mode of the continuum). $E_\text{i} = E_\text{e} - E_\text{g}$ is the difference in energy between the excited and the ground states. We sum over all the possible final states to obtain the total spontaneous emission rate $\Gamma_\text{sp}^\text{bulk}$.

In the dipole approximation, the perturbation Hamiltonian is given by:

$$\hat{H}_\text{pert} = -\hat{\mathbf{d}} \cdot \hat{\mathbf{E}} \tag{1.26}$$

where $\hat{\mathbf{d}}$ is the dipole and $\hat{\mathbf{E}}$ the electric field operators in the second quantization framework, expressed as:

$$\hat{\mathbf{E}}(\mathbf{r}, t) = \sum_{\mathbf{k},\mathbf{p}} i\sqrt{\frac{\hbar\omega}{2\underline{\varepsilon}(\omega)V}}\mathbf{p}(\hat{a}_{\mathbf{k},\mathbf{p}} e^{i\mathbf{k}.\mathbf{r}} - \hat{a}^\dagger_{\mathbf{k},\mathbf{p}} e^{-i\mathbf{k}.\mathbf{r}}) \tag{1.27}$$

where $\hat{a}_{\mathbf{k},\mathbf{p}}$ and $\hat{a}^\dagger_{\mathbf{k},\mathbf{p}}$ are respectively the annihilation and the creation operators in the mode $\{\mathbf{k}, \mathbf{p}\}$. $\underline{\varepsilon}(\omega)$ is the dielectric permittivity of the medium and is equal to $\underline{n}^2\varepsilon_0$. The quantization volume is written $V = L^3$.

We then obtain:

$$\begin{aligned}\Gamma_{i\to f} &= \frac{2\pi}{\hbar} \left| -\langle g, \mathbf{k}, \mathbf{p}| \hat{\mathbf{d}} \cdot \hat{\mathbf{E}} |e, 0\rangle \right|^2 \delta(E_\text{f} - E_\text{i}) \\ &= \frac{2\pi}{\hbar} \frac{E_\text{f}}{2|\underline{n}|^2\varepsilon_0 V} d^2 |\mathbf{e}_z \cdot \mathbf{p}|^2 \delta(E_\text{f} - E_\text{i})\end{aligned} \tag{1.28}$$

where $d = |\langle g| \hat{\mathbf{d}} |e\rangle|$, $E_\text{f} = \hbar\omega$, and $\mathbf{e}_z$ is a unitary vector aligned along the dipole direction.

For GaAs at 930 nm, the index real and imaginary parts values are respectively $\text{Re}(\underline{n}) = 3,5$ and $\text{Im}(\underline{n}) \simeq 0$. We then assume that $|\underline{n}|^2 \simeq \text{Re}(\underline{n})^2$ and write $\text{Re}(\underline{n}) = n$.

We can also explicit the term $|\mathbf{e}_z \cdot \mathbf{p}|^2$. Each wavevector $\mathbf{k}$ has two possible orthogonal states of polarization, $\mathbf{p}_1$ and $\mathbf{p}_2$, but we can always choose them so that one of them (say

$\mathbf{p}_1$) is orthogonal to the dipole oriented along $\mathbf{e}_z$. Then its contribution to the emitted field is zero, as shown in figure 1.12. Hence, we take into account only the contribution from $\mathbf{p}_2$, which is $|\mathbf{e}_z \cdot \mathbf{p}|^2 = \sin^2\theta$ where $\theta$ is the angle between the dipole $\mathbf{d}$ and the wavevector $\mathbf{k}$.

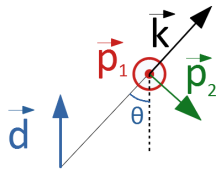


Figure 1.12: Schematic showing how only one of the two possible polarization states (here called $\mathbf{p}_2$) can be considered for each wavevector (see text).

The total spontaneous emission rate is given by the integral, over all the accessible energies and solid angles, of $\Gamma_{i\to f}$ weighted by the density of states $\rho(\Omega, E)$ defined as:

$$\mathrm{d}N = \rho(\Omega, E)\mathrm{d}E\mathrm{d}\Omega \tag{1.29}$$

where $\mathrm{d}N$ is the number of states with energy in the range $[E, E+\mathrm{d}E]$ and whose wavevector points into the solid angle $\mathrm{d}\Omega$.

The corresponding volume in the wavevectors space is equal to $\mathrm{d}^3k = k^2\mathrm{d}k\mathrm{d}\Omega$, with $\mathrm{d}\Omega = \sin\theta\mathrm{d}\theta\mathrm{d}\phi$, see figure 1.13.

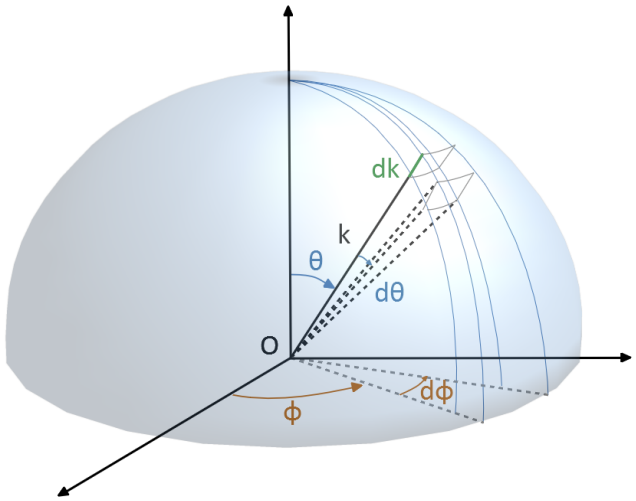


Figure 1.13: Schematic of the elementary integration volume.

We obtain the density of states, or electromagnetic modes, in 3D by choosing a quantization volume notated $L^3$. With $E = \hbar\omega = \hbar\frac{kc}{n}$, we obtain $\mathrm{d}^3k = \frac{n^3E^2}{(\hbar c)^3}\mathrm{d}E\mathrm{d}\Omega$. We then divide this volume by the volume of a single mode $(2\pi/L)^3$ to obtain the number of modes in $\mathrm{d}^3k$. Then:

$$\mathrm{d}N = \left(\frac{L}{2\pi}\right)^3 \frac{n^3E^2}{(\hbar c)^3}\mathrm{d}E\mathrm{d}\Omega \tag{1.30}$$

from which we deduce the density of modes:

$$\rho(\Omega, E) = \left(\frac{L}{2\pi}\right)^3 \frac{n^3 E^2}{(\hbar c)^3} \tag{1.31}$$

We can sum over the final states and obtain the total emission rate in an homogeneous medium of refractive index $n$:

$$\Gamma_{\mathrm{sp}}^{\mathrm{bulk}} = \int_{\mathcal{D}_{\mathrm{f}}} \Gamma_{i\to f} dN = \iint \Gamma_{i\to f} \rho(\Omega, E_{\mathrm{f}}) \mathrm{d}E_{\mathrm{f}} \mathrm{d}\Omega \tag{1.32}$$

where $\mathcal{D}_{\mathrm{f}}$ is the domain of final states. Replacing the different terms, one gets:

$$\Gamma_{\mathrm{sp}}^{\mathrm{bulk}} = \int_{E_{\mathrm{f}}\in\mathcal{D}_{\mathrm{f}}} \iint_{\Omega} \frac{2\pi}{\hbar} \frac{E_{\mathrm{f}}}{2n^2\varepsilon_0 V} d^2 \sin^2\theta \delta(E_{\mathrm{f}} - E_{\mathrm{i}}) \left(\frac{L}{2\pi}\right)^3 \frac{n^3 E_{\mathrm{f}}^2}{(\hbar c)^3} \mathrm{d}E_{\mathrm{f}} \sin\theta \mathrm{d}\theta \mathrm{d}\phi \tag{1.33}$$

and so

$$\Gamma_{\mathrm{sp}}^{\mathrm{bulk}} = \frac{2\pi}{\hbar} \frac{E_{\mathrm{i}}}{2n^2\varepsilon_0} d^2 \frac{8\pi}{3} \left(\frac{1}{2\pi}\right)^3 \frac{n^3 E_{\mathrm{i}}^2}{(\hbar c)^3} = \frac{d^2 n E_{\mathrm{i}}^3}{3\varepsilon_0 \pi \hbar^4 c^3} \tag{1.34}$$

Knowing that $E_{\mathrm{i}} = E_{\mathrm{e}} - E_{\mathrm{g}} = \hbar\omega_0$, we finally obtain:

$$\Gamma_{\mathrm{sp}}^{\mathrm{bulk}} = \frac{n\omega_0^3 d^2}{3\pi\varepsilon_0 \hbar c^3} \tag{1.35}$$

with $\omega_0$ being the resonance frequency of the two-level system transition. The radiative lifetime of the exciton in the bulk is given by $T = (\Gamma_{\mathrm{sp}}^{\mathrm{bulk}})^{-1}$. The order of magnitude of this value when the QD is in a GaAs bulk is about 1 ns. Note that we get $\Gamma_{\mathrm{sp}}^{\mathrm{bulk}} = n\Gamma_0$ with $\Gamma_0$ being the spontaneous emission rate in vacuum. Expression (1.35) was derived assuming a point dipole in a continuous homogeneous medium.

### 1.3.2 Spontaneous emission in a cavity: the Purcell effect

The emission rate we just calculated corresponds to a quasi-isotropic emission in the bulk. It has been shown that the fraction of photons one can actually collect from a source built from a single InGaAs QD in bulk GaAs is lower than 1% [61]. This value can be increased [110] by taking advantage of cavity quantum electrodynamics that makes it possible to collect the emission into a well defined and oriented mode of the electromagnetic field. In this section, we derive the emission rate of an emitter placed into a cavity [111], in order to then be able to compare it to the spontaneous emission by the same atom in the bulk material described in the previous subsection. The enhancement of spontaneous emission by a cavity is called the *Purcell effect* [112].

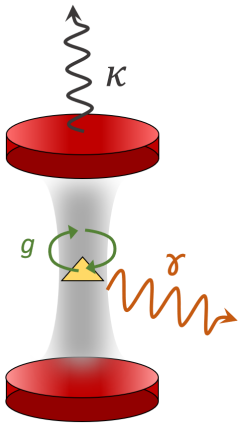


Figure 1.14: QD-cavity coupling parameters involved: $\gamma$ is the QD spontaneous emission rate derived earlier ($\Gamma_{\text{sp}}^{\text{bulk}}$), $\kappa$ is the cavity mode damping rate and $g$ is the coupling between the QD and the cavity mode.

The different parameters involved in the QD-cavity system are shown in figure 1.14. The QD spontaneous decay rate $\gamma$ was derived in 1.3.1 as $\Gamma_{\text{sp}}^{\text{bulk}}$, $g$ is the atom-field coupling, and $\kappa$ is the cavity damping rate. We can define two regimes for the cavity's behaviour: the *bad-cavity* (resp. *good-cavity*) *regime* corresponds to $R \ll \kappa$ (resp. $R \gg \kappa$) where [113]

$$R = \frac{4g^2(\kappa + \gamma)}{(\kappa + \gamma)^2 + 4\delta^2} \tag{1.36}$$

is the effective rate of population transfer between the QD and the cavity mode, where $\delta$ is the QD-cavity detuning. Typically in the samples studied in this thesis, we have $\hbar g \simeq 17\,\mu\text{eV}$, $\hbar\kappa \simeq 500\,\mu\text{eV}$ and $\hbar\gamma \simeq 0.6\,\mu\text{eV}$. Hence we have $\kappa \gg \gamma$. In addition, under resonant or quasi-resonant operation, we have that $\kappa^2 \gg \delta^2$. Thus $R \simeq 4g^2/\kappa$ and then the condition $R \ll \kappa$ ($\Leftrightarrow R/\kappa \ll 1$) effectively reduces to requiring $g \ll \kappa$. From the above quantities, we can see that our samples are far into the bad-cavity regime since $17\,\mu\text{eV} \ll 500\,\mu\text{eV}$.

Since the device operates in the bad cavity limit ($g \ll \kappa$), the spontaneous emission from the QD is irreversible (the photons quickly escape from the cavity). Thus, here again we can apply Fermi's golden rule (recall equation (1.25)).

The density of electromagnetic modes coupled to the atom is modified when the atom is placed into a cavity compared to when it is in the bulk. For an ideal cavity with no losses, the mode density along the direction of quantization becomes discretized into a series of infinitely narrow resonances with a separation dictated by the cavity geometry. However, a cavity with losses will instead have a mode density given by a series of resonances with Lorentzian shapes [114], each with a FWHM given by the damping rate of that resonance. We can assume the cavity resonance $\omega_c$ nearest to the QD resonance $\omega_0$ has a width $\kappa$ that is much smaller than the spectral separation between other cavity resonances. In this case, since the QD resonance is much narrower than the cavity resonance ($\gamma \ll \kappa$), the QD will only couple to one cavity resonance $\omega_c$. Then, since the mode density $\rho_{\text{cav,1D}}(\omega)$ has to respect the

normalization condition:

$$\int_0^\infty \rho_{\mathrm{cav,1D}}(\omega) d(\hbar\omega) = 1, \tag{1.37}$$

the density of modes coupled to the QD, within the condition that $\kappa \ll \omega_c$, is:

$$\rho_{\mathrm{cav,1D}}(\omega) = \frac{2}{\pi\hbar\kappa} \frac{\kappa^2}{4(\omega - \omega_c)^2 + \kappa^2}. \tag{1.38}$$

In practice, the cavity is a three-dimensional object that affects the density of modes in all directions. However, to simplify the description, we consider that the total density of modes can be separated into a sum of the density of modes of the bulk and the density of modes of the cavity. This approximation is commonly done for micropillar cavities where no clear modification of the spontaneous emission has been observed for a QD in a pillar detuned from the cavity mode with respect to QDs in bulk [58]. Using equation (1.28) and integrating over all the possible final states, we can express this idea mathematically by the following expression:

$$\rho(\omega_\mathrm{f}) = \rho_{\mathrm{bulk}}(\omega_\mathrm{f}) + \delta(\Omega - \Omega_{\text{cav axis}}) \rho_{\mathrm{cav,1D}}(\omega_\mathrm{f}) \tag{1.39}$$

with $\Omega_{\text{cav axis}}$ the direction of the emission in the cavity.

The total decay rate of the QD is then given by:

$$\begin{aligned} \Gamma = \Gamma_{\mathrm{sp}}^{\mathrm{bulk}} + \int_{E_\mathrm{f} \in \mathcal{D}_\mathrm{f}} \int_\Omega \frac{2\pi}{\hbar} \frac{E_\mathrm{f}}{2n^2\varepsilon_0 V} d^2 \sin^2\theta \delta(E_\mathrm{f} - E_\mathrm{i}) \delta(\Omega - \Omega_{\text{cav axis}}) \\ \times \frac{2}{\pi\hbar\kappa} \frac{\kappa^2}{4(E_\mathrm{f}/\hbar - \omega_c)^2 + \kappa^2} \mathrm{d}E_\mathrm{f} \mathrm{d}\Omega, \end{aligned} \tag{1.40}$$

where $E_i = \omega_0/\hbar$. By evaluating Eq. (1.40), we obtain

$$\Gamma = \Gamma_{\mathrm{sp}}^{\mathrm{bulk}} + \frac{2\omega_0 d^2 \sin^2\theta}{n^2\hbar\varepsilon_0 V} \frac{\kappa}{\kappa^2 + 4(\omega_0 - \omega_\mathrm{c})^2} \tag{1.41}$$

At perfect resonance between the atom and the cavity ($\omega_\mathrm{c} - \omega_0 = \delta = 0$) and assuming that the dipole is oriented to maximize the light-matter coupling ($\theta = \pi/2$), the rate of emission is $\Gamma = \Gamma_{\mathrm{sp}}^{\mathrm{bulk}} + \Gamma_{\mathrm{sp}}^{\mathrm{cavity}}$ where

$$\Gamma_{\mathrm{sp}}^{\mathrm{cavity}} = \frac{2Qd^2}{n^2\hbar\varepsilon_0 V}, \tag{1.42}$$

and where $Q = \omega_c/\kappa$ is the cavity quality factor.

We define the Purcell factor by the ratio between the spontaneous emission rate from an emitter in a cavity and the spontaneous emission rate from the same emitter in the bulk:

$$F_\mathrm{P} = \frac{\Gamma_{\mathrm{sp}}^{\mathrm{cavity}}}{\Gamma_{\mathrm{sp}}^{\mathrm{bulk}}} \tag{1.43}$$

Substituting (1.35) and (1.42) into (1.43), we get:

$$F_\mathrm{P} = 6\pi \frac{Qc^3}{n^3\omega_0^3 V} = \frac{3}{4\pi^2} \frac{Q(\lambda/n)^3}{V} \tag{1.44}$$

where $\omega_0/c$ is equal to $2\pi/\lambda$. The Purcell enhancement is proportional to the ratio $Q/V$ which means that the higher the $Q$-factor is, or the smaller the mode volume of the cavity is, the more the emission is accelerated into the cavity mode.

We can also define the *mode coupling* $\beta$ as the fraction of photons emitted by the QD into the cavity:

$$\beta = \frac{\Gamma_{\text{sp}}^{\text{cavity}}}{\Gamma_{\text{sp}}^{\text{bulk}} + \Gamma_{\text{sp}}^{\text{cavity}}} = \frac{F_{\text{P}}}{F_{\text{P}} + 1} \tag{1.45}$$

This expression highlights that the higher the Purcell factor is, the closer to 1 is the fraction of photons emitted into the cavity mode.

### 1.3.3 Jaynes-Cummings model and the semi-classical approximation

To observe spontaneous emission of indistinguishable single photons from our QD-cavity device, it is necessary to deterministically prepare the QD in the excited state [68]. This can be done by applying a coherent pulse to the cavity, which in-turn excites the QD. In the bad-cavity regime, if the timescale of the pulse is much faster than the Purcell-enhanced lifetime of the QD, then we can approximate the excitation dynamics by neglecting the QD decay. In addition, if the timescale of the pulse is much slower than the cavity lifetime, the cavity mode amplitude becomes proportional to the incident coherent state amplitude. This allows us to also neglect the cavity losses and instead treat the excitation dynamics as a simple coherent interaction between a two-level system and a single electromagnetic mode.

The Jaynes-Cummings model describes the coupling between a two-level system and a single electromagnetic mode [115, 116]. It is primarily used to capture the dynamics of a QD in a high Q factor cavity, close to the strong coupling regime. However, in this section, we present it to introduce the semi-classical approximation for a coherently-driven two-level system. The Jaynes-Cummings model is also used in Chapter 2 to describe the coherent dynamics of sources based on excitons coupled to a micropillar cavity.

#### Derivation of the Jaynes-Cummings Hamiltonian

The total Hamiltonian of the coupled light-matter system is written:

$$\hat{H} = \hat{H}_{\text{A}} + \hat{H}_{\text{F}} + \hat{H}_{\text{AF}} \tag{1.46}$$

where $\hat{H}_{\text{A}}$ accounts for the atom, $\hat{H}_{\text{F}}$ for the field and $\hat{H}_{\text{AF}}$ for the interaction between the two. Their respective expressions are:

$$\hat{H}_{\text{A}} = \hbar\omega_0 \left|e\right\rangle \left\langle e\right| \tag{1.47}$$

with $|g\rangle$ the ground state, $|e\rangle$ the excited state and $\omega_0$ the atomic transition frequency,

$$\hat{H}_{\text{F}} = \hbar\omega \left(\hat{a}^\dagger \hat{a} + \frac{1}{2}\right) \tag{1.48}$$

with $\omega$ the cavity resonance frequency corresponding to a single mode, and

$$\hat{H}_{\mathrm{AF}} = -\hat{\mathbf{d}} \cdot \hat{\mathbf{E}} \tag{1.49}$$

just like in equation (1.26).

The dipole operator can be written $\hat{\mathbf{d}} = \langle \mathrm{e}| \hat{\mathbf{d}} |\mathrm{g}\rangle (|\mathrm{g}\rangle \langle \mathrm{e}| + |\mathrm{e}\rangle \langle \mathrm{g}|)$ since $\langle \mathrm{e}| \hat{\mathbf{d}} |\mathrm{e}\rangle = \langle \mathrm{g}| \hat{\mathbf{d}} |\mathrm{g}\rangle = \mathbf{0}$ (by parity considerations). Then:

$$\hat{\mathbf{d}} = \mathbf{d}_{\mathrm{ge}}(\hat{\sigma} + \hat{\sigma}^\dagger) \tag{1.50}$$

where $\hat{\sigma} = |\mathrm{g}\rangle \langle \mathrm{e}|$ and $\hat{\sigma}^\dagger = |\mathrm{e}\rangle \langle \mathrm{g}|$ are the atomic lowering operator and raising operator respectively, and $\mathbf{d}_{\mathrm{ge}} = \langle \mathrm{e}| \hat{\mathbf{d}} |\mathrm{g}\rangle$ is the dipole moment of the atomic transition.
As before, in the second quantization framework, the electric field mode of the cavity is written:

$$\hat{\mathbf{E}}(\mathbf{r}) = \sqrt{\frac{\hbar\omega}{2n^2\varepsilon_0 V}}(\mathbf{f}(\mathbf{r})\hat{a} + \mathbf{f}^*(\mathbf{r})\hat{a}^\dagger) \tag{1.51}$$

where $\mathbf{f}(\mathbf{r})$ is the normalized spatial mode profile. Let $\mathbf{r}_0$ be the position of the QD with dipole $\hat{\mathbf{d}}$. We define the phase reference of $\hat{\mathbf{E}}$ so that $\mathbf{f}(\mathbf{r}_0)$ is real. Then:

$$\hat{\mathbf{E}}(\mathbf{r}_0) = \sqrt{\frac{\hbar\omega}{2n^2\varepsilon_0 V}}\mathbf{f}(\mathbf{r}_0)(\hat{a} + \hat{a}^\dagger) \tag{1.52}$$

The interaction Hamiltonian becomes:

$$\begin{aligned} \hat{H}_{\mathrm{AF}} &= \sqrt{\frac{\hbar\omega}{2n^2\varepsilon_0 V}}\mathbf{d}_{\mathrm{ge}} \cdot \mathbf{f}(\mathbf{r}_0)(\hat{\sigma} + \hat{\sigma}^\dagger)(\hat{a} + \hat{a}^\dagger) \\ &= \hbar g(\hat{\sigma} + \hat{\sigma}^\dagger)(\hat{a} + \hat{a}^\dagger) \end{aligned} \tag{1.53}$$

where we defined the atom-field coupling energy as:

$$\hbar g = \sqrt{\frac{\hbar\omega}{2n^2\varepsilon_0 V}}\mathbf{d}_{\mathrm{ge}} \cdot \mathbf{f}(\mathbf{r}_0) \tag{1.54}$$

The quantity $g$ is the atom-field coupling defined in the previous subsection. We assume now that the QD is at the field maximum so that $\mathbf{f}(\mathbf{r}_0) = \mathbf{e}$ where $\mathbf{e}$ is a real unit vector. Then $\mathbf{d}_{\mathrm{ge}}.\mathbf{f}(\mathbf{r}_0) = |\mathbf{d}_{\mathrm{ge}}| \cos\vartheta$, where $\vartheta$ is angle between the dipole $\mathbf{d}_{\mathrm{ge}}$ and polarization of the cavity mode $\mathbf{e}$. When $\mathbf{d}_{\mathrm{ge}}$ and $\mathbf{e}$ are parallel, $\vartheta = 0$ and:

$$\hbar g = d\sqrt{\frac{\hbar\omega}{2n^2\varepsilon_0 V}} \tag{1.55}$$

When $g \ll \omega$, the terms $\hat{\sigma}^\dagger\hat{a}^\dagger$ and $\hat{\sigma}\hat{a}$ do not conserve energy since they would correspond to the emission of a photon as the atom goes from the ground state to the excited state, and to the absorption of a photon as the atom goes from the excited state to the ground state respectively. From a more mathematical perspective, we can use the following reasoning. In the free-field case, the operators $\hat{a}$ and $\hat{a}^\dagger$ evolve as:

$$\hat{a}(t) = \hat{a}(0)e^{-i\omega t} \qquad\qquad \hat{a}^\dagger(t) = \hat{a}^\dagger(0)e^{i\omega t} \tag{1.56}$$

Similarly, for the free-atomic case:

$$\hat{\sigma}(t) = \hat{\sigma}(0)e^{-i\omega_0 t} \qquad \hat{\sigma}^\dagger(t) = \hat{\sigma}^\dagger(0)e^{i\omega_0 t} \tag{1.57}$$

Then we have

$$\hat{\sigma}\hat{a} \propto e^{-i(\omega+\omega_0)t} \qquad \hat{\sigma}\hat{a}^\dagger \propto e^{-i(\omega_0-\omega)t} \qquad \hat{\sigma}^\dagger\hat{a} \propto e^{i(\omega_0-\omega)t} \qquad \hat{\sigma}^\dagger\hat{a}^\dagger \propto e^{i(\omega+\omega_0)t} \tag{1.58}$$

For $|\omega-\omega_0| \ll \omega+\omega_0$, the first and last terms vary much faster than the two others. Then their contribution would average to zero when integrating over time. Using that approximation, called *rotating wave approximation*, the interaction Hamiltonian can then be written:

$$\hat{H}_{\mathrm{AF}} = \hbar g(\hat{\sigma}\hat{a}^\dagger + \hat{\sigma}^\dagger\hat{a}) \tag{1.59}$$

and the total Hamiltonian is:

$$\hat{H} = \hat{H}_{\mathrm{A}} + \hat{H}_{\mathrm{F}} + \hat{H}_{\mathrm{AF}} = \hbar\omega_0\hat{\sigma}^\dagger\hat{\sigma} + \hbar\omega\hat{a}^\dagger\hat{a} + \hbar g(\hat{\sigma}\hat{a}^\dagger + \hat{\sigma}^\dagger\hat{a}) \tag{1.60}$$

This Hamiltonian defines the Jaynes-Cummings model, which corresponds to an atom interacting with a single and nearly resonant optical mode, within the rotating wave approximation, ignoring any dissipation process such as spontaneous emission or any input or output from the cavity [117].

**Dynamics of a QD excited by a laser pulse**

We use the Jaynes-Cummings model, and from equation (1.60), we move into the rotating frame of mode $\hat{a}$. The Hamiltonian becomes:

$$\hat{H} = \hbar\Delta\hat{\sigma}^\dagger\hat{\sigma} + \hbar g(\hat{\sigma}\hat{a}^\dagger + \hat{\sigma}^\dagger\hat{a}) \tag{1.61}$$

where $\Delta = \omega_0 - \omega$ is the detuning between the field frequency $\omega$ and the natural oscillation frequency of the atomic dipole $\omega_0$. We populate the cavity with laser pulses, that are coherent states of light and that in turn excite the QD. Assuming that these coherent states of light are intense ($|\alpha|^2 \gg 1$) so that it is not affected by the state of the QD, we can write the full system state as:

$$|\psi(t)\rangle = |\phi(t)\rangle_{\mathrm{A}} |\alpha\rangle_{\mathrm{F}} \tag{1.62}$$

where $|\alpha\rangle$ is a coherent state. This leads to the semi-classical Hamiltonian describing the evolution of the two-level system:

$$\hat{H}_{\mathrm{A}} = \langle\alpha|\hat{H}|\alpha\rangle = \hbar\Delta\hat{\sigma}^\dagger\hat{\sigma} + \hbar g(\hat{\sigma}\alpha^* + \hat{\sigma}^\dagger\alpha) \tag{1.63}$$

We choose that $\alpha$ is real and let $\Omega_R = 2g\alpha$ be the Rabi frequency, that quantifies the strength of the light-matter interaction. On resonance ($\Delta = 0$), the atom Hamiltonian is then equal to:

$$\hat{H}_{\mathrm{A}} = \frac{\hbar\Omega_R}{2}(\hat{\sigma} + \hat{\sigma}^\dagger) = \frac{\hbar\Omega_R}{2}\hat{\sigma}_x \qquad \text{with} \qquad \hat{\sigma}_x = \begin{pmatrix} 0 & 1 \\ 1 & 0 \end{pmatrix} \tag{1.64}$$

We can now solve the Schrödinger equation:

$$\partial_t |\phi(t)\rangle = -\frac{i\Omega_R}{2}\hat{\sigma}_x |\phi(t)\rangle \tag{1.65}$$

The solution has the form:

$$|\phi(t)\rangle = e^{-i\frac{\Omega_R}{2}\hat{\sigma}_x t}\,|\phi(0)\rangle = \begin{pmatrix} \cos\frac{\Omega_R}{2}t & -i\sin\frac{\Omega_R}{2}t \\ -i\sin\frac{\Omega_R}{2}t & \cos\frac{\Omega_R}{2}t \end{pmatrix} |\phi(0)\rangle = \hat{U}(t)\,|\phi(0)\rangle \tag{1.66}$$

where $\hat{U}(t)$ is the unitary transformation governing the state evolution. If the atom is initially in the state $|\mathrm{g}\rangle$ coupled to a resonant field, the populations in the two levels $|\mathrm{g}\rangle$ and $|\mathrm{e}\rangle$ are given by:

$$P_\mathrm{e} = \left| \begin{pmatrix} 1 & 0 \end{pmatrix} \hat{U}(t) \begin{pmatrix} 1 \\ 0 \end{pmatrix} \right|^2 = \sin^2\left(\frac{\Omega_R}{2}t\right) \tag{1.67}$$

$$P_\mathrm{g} = \left| \begin{pmatrix} 0 & 1 \end{pmatrix} \hat{U}(t) \begin{pmatrix} 0 \\ 1 \end{pmatrix} \right|^2 = \cos^2\left(\frac{\Omega_R}{2}t\right) \tag{1.68}$$

Finally

$$P_\mathrm{e} = \frac{1}{2}\left[1 - \cos(\Omega_R t)\right] \tag{1.69}$$

$$P_\mathrm{g} = \frac{1}{2}\left[1 + \cos(\Omega_R t)\right] \tag{1.70}$$

There is an oscillation in the populations between the two states $|\mathrm{g}\rangle$ and $|\mathrm{e}\rangle$, at an angular frequency $\Omega_R = 2\hbar g\alpha$, called the Rabi frequency. Note that the coherent state amplitude varies with time in the case of a pulsed laser excitation.

## 1.4 Description of our QD-cavity devices

### 1.4.1 Structures under study

In the context of this thesis, we study two-level systems in our InGaAs QDs artificial atoms coupled to micropillar cavities as illustrated in figure 1.15(a). The devices are made from a planar cavity made of 34 pairs of $\lambda/(4n)$ thick GaAs/AlGaAs layers ($\lambda$ being the QD emission wavelength and $n$ the material index of the layer), a $\lambda/n$ thick layer of GaAs which constitutes the cavity *spacer* and 16 other pairs of $\lambda/(4n)$ thick GaAs/AlGaAs layers. The layer of InAs QDs is vertically located at the center of the spacer. The top and bottom layers act as distributed Bragg reflectors (DBRs) and allow for a vertical confinement of the electromagnetic field. The pillar cavity is etched vertically from the top from this planar sample to obtain a 3D optical confinement. The field is confined vertically by the two DBRs and the vertical edges of the micropillar confine the field horizontally like in an optical fiber. Finally, the cavity is a cylinder with a 13 µm height and a few micrometers wide, depending on the sample and its purpose. In the $(xy)$ plane, the QD should lie at the maximum of the cavity electric field, which for a circular pillar fundamental mode corresponds to its center. In the vertical direction $z$, the QD is also located at the antinode of the planar cavity mode.

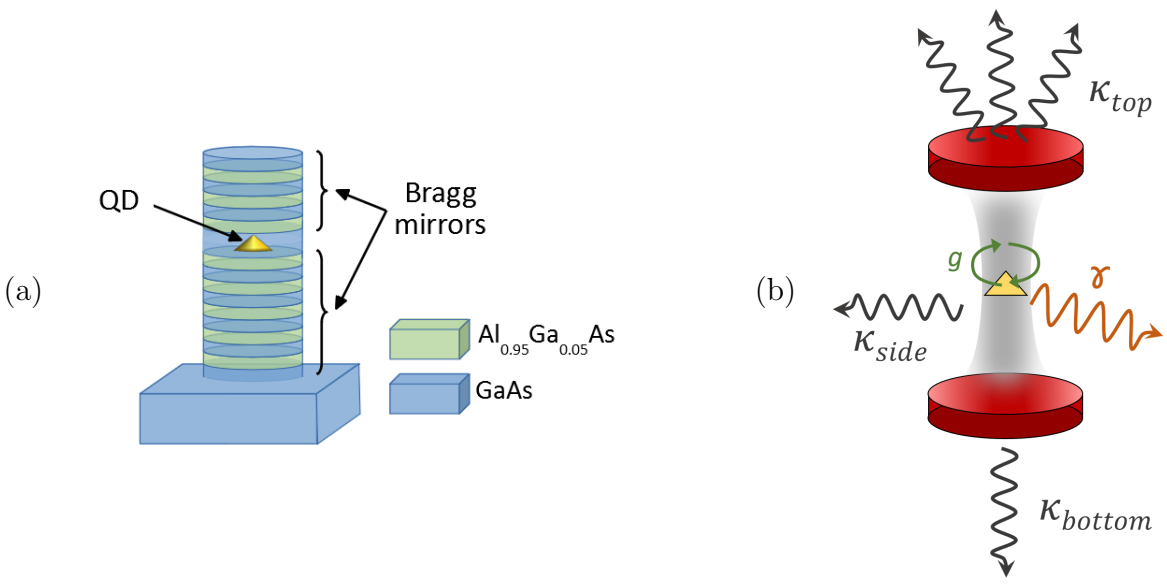


Figure 1.15: (a) Sketch of QD-micropillar cavity device. (b) QD-cavity coupling: various channels for the cavity mode damping (see text).

The different parameters involved in the QD-cavity system (spontaneous decay rate $\gamma$, atom-field coupling $g$ and cavity damping rate $\kappa = \kappa_{\text{top}} + \kappa_{\text{side}} + \kappa_{\text{bottom}}$) are recalled in figure 1.15(b). Here, instead of considering the total cavity damping rate $\kappa$ as in figure 1.14, we consider the various channels for a photon to escape outside the cavity: from the top ($\kappa_{\text{top}}$), the side ($\kappa_{\text{side}}$), the bottom ($\kappa_{\text{bottom}}$). Only the fraction escaping from the top can be collected to obtain a bright single-photon source. The micropillar is not perfectly circular and therefore the cavity itself presents a small anisotropy leading to two nearly-degenerate linearly polarized fundamental cavity modes. The energy difference typically amounts to 30-70 µeV which is smaller than the cavity spectral linewidth of $\kappa$ =200-500 µeV.

### 1.4.2 Deterministic QD-cavity assembling: *in situ* lithography

Quantum dots grow at random positions, but the light-matter coupling is optimized when the QD is at the maximum of the cavity mode electromagnetic field. Before the development of deterministic techniques to couple QDs to cavities, it was necessary to randomly build devices and explore large numbers of sources in order to find one with good characteristics. The cryogenic *in situ* lithography technique [66] allows to position the pillar center within 50 nm of the QD and to adjust the pillar cavity diameter to ensure the spectral resonance between the QD and the cavity lines. This technique was developed in our group in 2008. I briefly present its principle.

#### Spatial matching

We recall that prior to this *in situ* lithography step, the sample is made of a planar cavity with a layer of QDs in the middle of the $\lambda/n$ thick GaAs spacer. The planar cavity is spin-coated with an optical photo-resist, and set up on a motorized platform, that can be moved

in all three directions of space. The sample is placed in a cryostat at around 7 K where an optical lithography is performed while monitoring the QD emission properties. A red laser ($\lambda_r \simeq 830$ nm) is used to non-resonantly excite the QDs in the sample. The photoluminescence (PL) signal obtained is detected in a spectrometer equiped with a camera. When a QD with the desired wavelength is detected, the sample is then moved around the position of this QD, to get a scan of PL. This signal presents a spatial Gaussian shape with a FWHM of about 1 µm, and the QD can then be positioned at the maximum of PL, with an accuracy of ±50 nm. Once the location is determined, a green laser ($\lambda_g \simeq 530$ nm) is switched on to expose the photo-resist, which creates a circular mask later used to define the micropillar cavity. That way, we ensure that the QD is positioned at the maximum of the pillar fundamental mode.

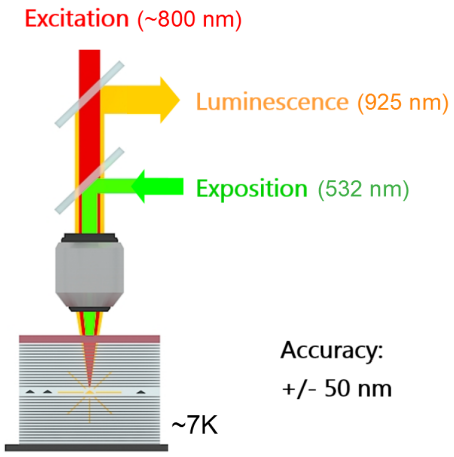


Figure 1.16: Schematic of the *in situ* lithography technique.

**Spectral matching**

The next important point is to have a spectral matching between the QD transition and the micropillar fundamental mode. The wavelength of the cavity is determined by its radius. In the first implementation of the lithography, we used the fact that a longer exposure and a higher power of the green laser resulted in a larger radius of the mask defining the micropillar. The resist exposure time was adjusted to obtain the desired pillar diameter.

After these two steps, the sample is brought back to room temperature. The photo-resist is developed and used to obtain a hard mask for the etching of the planar cavity into micropillar cavities.

### 1.4.3 Electrical control of the QD wavelength

The *in situ* lithography technique was improved over time and since 2014 [118], it is possible to write an arbitrary pattern in the resist centered on the QD. This is especially useful to implement an electrical control of the device. Indeed, the rough spectral matching obtained with the *in situ* lithography process can be finely tuned by using an electrical control of the QD transition wavelength through the confined Stark effect. For that purpose, each pillar

is now connected through 1D ridges to a circular frame and a large mesa structure where electrical contacts are defined, as shown in figure 1.17.

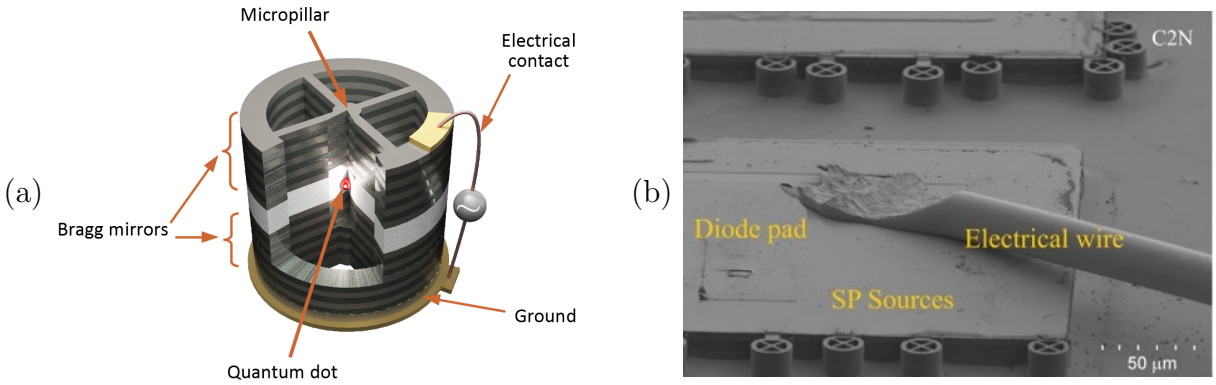


Figure 1.17: (a) Schematic of an electrically controlled device. Figure taken from [119]. (b) SEM image of one of the samples under study in this thesis: each wheel-shaped structure represents a single microcavity coupled to a single QD transition.

The semiconductor layering is doped to obtain a p-i-n-type band structure, and allows us to apply a bias voltage to the QD. This can be used to fine-tune the QD-cavity resonance after fabrication via the Stark effect [118]. Applying a voltage also strongly reduces the charge noise in the etched pillar samples. The particular geometry chosen to apply the bias plays a key role in the new approach proposed in Chapter 4 to control the QD FSS.

All the concepts presented above, together with the endeavour to optimize the performance of our devices, culminated in 2016 with the demonstration of a near-optimal solid-state source of indistinguishable single photons [70]. Since then, our devices have been used in many quantum optics applications both by our group and our collaborators, such as boson sampling [71], single-photon filtering [120] and tomography of QD-induced polarization rotation [119]. More recently, they have been used to create path-entangled two-photon states [121], generate photon-number superposition states [47] and construct linear cluster states [35]. In the next section we present the experimental techniques used to characterize our devices.

## 1.5 Experimental techniques: excitation, collection and characterization

In this section, we briefly describe the experimental techniques that we use to operate the sources and collect the single photons. Then, we define the different figures of merit that are commonly used in the community to characterize single-photon sources.

### 1.5.1 Excitation and collection of the single photons

The wavelength-tunable excitation lasers available in our lab are a Mira laser (from Coherent) and a Tsunami laser (from Spectra-Physics), with repetition rates around 81 MHz. We control the pulse duration by shaping the laser pulses using a 4-f filter, depicted in figure 1.18. The

pulse is spectrally dispersed using a diffraction grating, and a narrow portion is selected using a slit in order to obtain a pulse with a duration varying from 3 ps up to 25 ps. To achieve even longer pulses, it is possible to use an etalon to filter an even narrower portion of the laser spectrum. This technique is used in Chapter 3, where durations up to 80 ps are achieved.

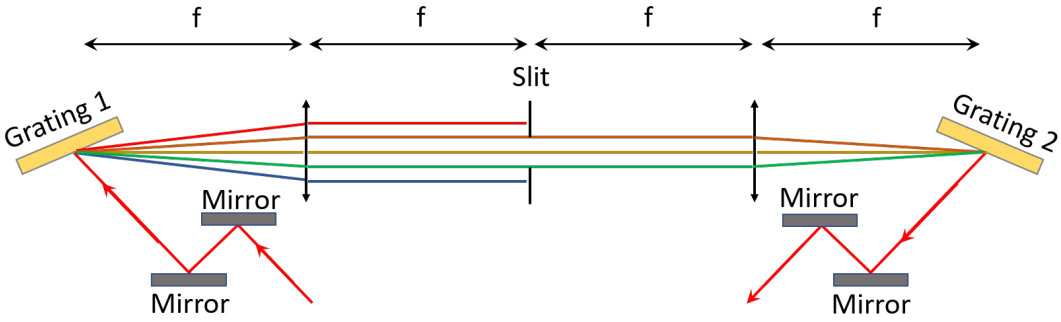


Figure 1.18: Experimental setup used to shape the laser pulses based on a 4-f optical system.

Contrarily to non-resonant excitation schemes, resonant excitation of the QDs enables one to reach near-unity indistinguishability by deterministically bringing the QD to its excited state [68, 70, 122]. In order to excite the QDs resonantly, we reject the reflected excitation pulse by filtering in polarization. The principle of the experimental setup to excite the QD and collect the single photons from the devices is shown in figure 1.19.

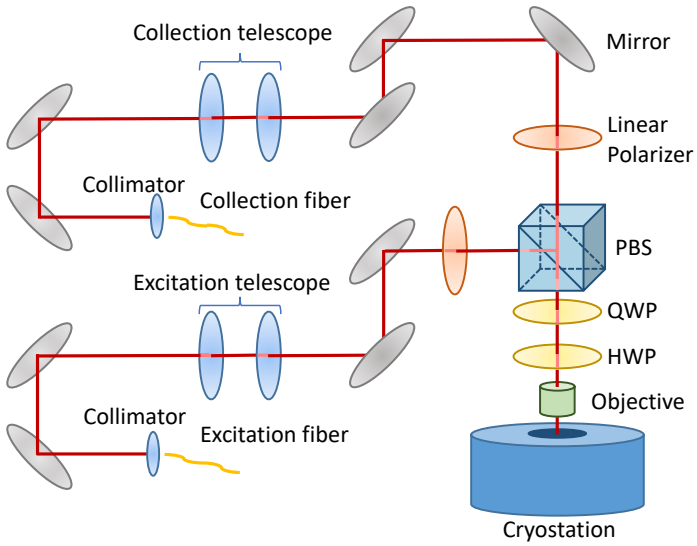


Figure 1.19: Schematic of the optical setup used for resonant excitation of the QD devices. The collection is crossed polarized to the excitation line. PBS: polarizing beam splitter, QWP: quarter waveplate, HWP: half waveplate.

After choosing its wavelength and shaping its pulse, the excitation laser beam enters the setup through a single-mode fiber; then a first telescope optimizes the spatial overlap of the beam with the fundamental mode of the micropillar [66, 123]. An input polarizer sets the

polarization along the reflection axis of a polarizing beam splitter (PBS). The beam is sent through a 0.45 NA objective to a low vibration cryostat where the sample is cooled down to 7 K. The QD emission is collected in the transmission mode of the PBS, orthogonal to the input polarization. A half waveplate (HWP) and a quarter waveplate (QWP) are used together to control the linear polarization sent on the cavity and to correct for any polarization ellipticities. The laser reflected by the cavity is sent back into the excitation path. In the collection path, a second polarizer improves laser extinction and a second telescope adjusts the single-photon beam diameter to match the collection fiber mode. The collected signal is then sent either into our spectrometer from Horiba, that allows for a spectral resolution corresponding to 75 pixels per nanometer, or into superconducting nanowire single-photon detectors (SNSPDs), that show a jitter time of about 50 ps at the full width at half maximum.

We present in figure 1.20 an example of spectrum of the light collected via this setup from one of our sources. A single emission line appears over the full spectrum with a linewidth of $18.5 \pm 0.3$ pm limited by the apparatus spectral resolution.

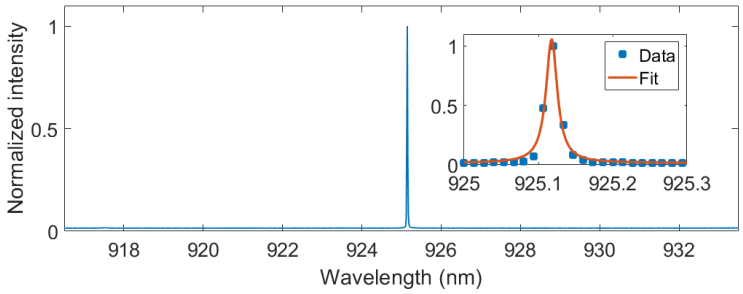


Figure 1.20: Example of spectrum acquired on one of our sources with the experimental setup described in this section. The inset is a zoom on the QD emission line data and a fit by a Lorentzian function of FWHM equal to $18.5 \pm 0.3$ pm.

### 1.5.2 Coherent control of a QD

Coherently controlling the QD allows for the deterministic preparation of the QD excited state, leading to the generation of indistinguishable photons [68]. The coherent excitation of QDs was theoretically described in section 1.3.3 making use of the Jaynes-Cummings model. We can observe the derived Rabi oscillations (see equations (1.68) and (1.70)) by measuring the countrate of emitted single photons while varying the excitation power in the pulsed regime. The Rabi oscillation occurs during the excitation laser pulse. When the pulse ends, the system returns to the ground state within a given decay time, emitting a photon with a probability that is proportional to the probability for the system to be in the excited state. This latter probability, given by equation (1.67), shows a dependence on $\sin^2(\Omega_R t)$. The Rabi frequency $\Omega_R$ is proportional to the electric field amplitude [3], and so to the square root of the excitation pulse power $P$. Thus, the QD emission oscillates with a phase $\Omega_R \tau_P$ (with $\tau_P$ the pulse duration) that is proportional to $\sqrt{P}$. Such a power measurement is shown in figure 1.21, for which the pulse duration was set to $\tau_P = 40$ ps. The highest countrate of single photons from the QD is obtained for $\Omega_R \tau_p \simeq \pi$. In that situation, the probability of excitation approaches 1. We call this condition as $\pi$-pulse excitation. Note that the contrast

of the oscillation quickly decreases with the power. This is due to the Purcell-enhanced spontaneous emission [124] that was not taken into account in the model discussed in section 1.3.3, but is non negligible on the timescale of the 40 ps pulses.

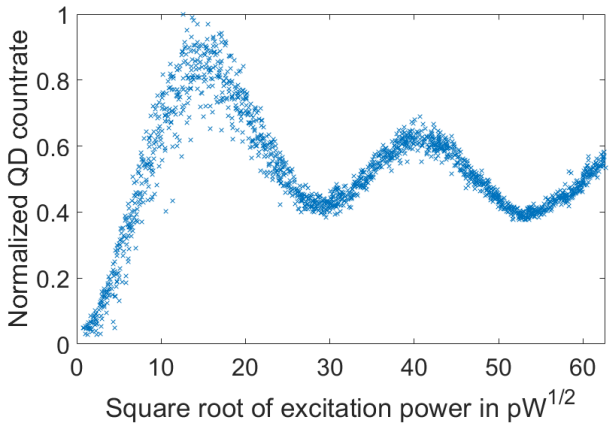


Figure 1.21: QD emission as a function of the square root of the power of excitation laser. The pulse duration is set to 40 ps for the whole measurement. We define the $\pi$-pulse as the power leading to the first maximum of emission intensity.

### 1.5.3 Temporal wavepacket profile

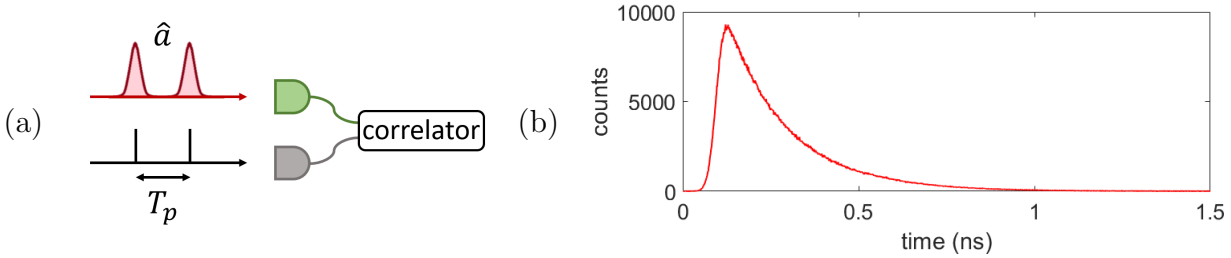


Figure 1.22: (a) Experimental setup to determine the temporal wavepacket profile of the emitted photons. (b) Typical measured temporal profile.

The temporal wavepacket profile gives information about the distribution in time of the photons emitted by the QD. It is measured by connecting the output single-mode fiber from the setup to a single-photon detector, itself connected to a correlator as shown in figure 1.22(a). The clock from the laser is sent to the correlator as well, giving a time reference at the repetition rate of the laser (81 MHz, which corresponds to a pulse period of $T_p \simeq 12$ ns). We then obtain a histogram representing the probability of photon arrival as a function of the arrival time after the clock signal. An example is shown in figure 1.22(b).

In terms of quantum operators, the temporal wavepacket profile is characterized by the average photon number detected per unit of time, written $N(t) = \langle \hat{N}(t) \rangle = \langle \hat{a}^\dagger(t)\hat{a}(t) \rangle$ where $\hat{a}(t)$ and $\hat{a}^\dagger(t)$ are the propagating modes annihilation and creation operators respectively, in units of $\sqrt{\text{Hz}}$ and the expectation is taken for the quantum state of light produced by

the QD. Note that here and everywhere in this section, we use the notation $\hat{a}(t)$ to describe the continuum of propagating mode outside of the cavity in the time basis. This is not to be confused with the stationary cavity mode $\hat{a}$ used to describe the Jaynes-Cummings Hamiltonian in section 1.3.3.

### 1.5.4 Brightness

The efficiency of a single-photon source determines the speed of optical computation [125], the rate of quantum communications [126] and the sensitivity in quantum sensing [127]. It is then important to define universal quantities to compare the different single-photon source technologies, quantify progress and identify the remaining challenges.

In the pulsed regime, the relevant value to characterize the efficiency of the source is the average number of photons produced by the device after applying one excitation pulse, also called *brightness*. In terms of quantum operators, this is the average number of photons $\mu = \int N(t)dt$ from the source, where the integral is taken over one period of device excitation. This can also be written in terms of the probability $p_n$ of obtaining $n$ photons: $\mu = \sum_n np_n$.

In practice, the average number of photons is degraded by transmission losses incurred after emission but before collection into an optical fiber. The average number of photons $\mathcal{B}_{\text{smf}}$ collected at the output of the single-mode fiber is the relevant figure for experiments exploiting single photons. This is measured by connecting single-photon detectors to the collection fiber (see figure 1.23) and then dividing the detection rate by the pulsed excitation repetition rate [46] and correcting for the detector efficiency. Because the fibered brightness $\mathcal{B}_{\text{smf}}$ depends on losses that are independent of the single-photon source quality, it is still useful to estimate the brightness from the source in order to compare different devices. To do this, we can correct the value $\mathcal{B}_{\text{smf}}$ by the global efficiency of our setup (transmission and output coupling), which is approximately 40% in the present work, to obtain the *first lens brightness* $\mathcal{B}$. This is the average number of photons entering into the collection objective per excitation pulse.

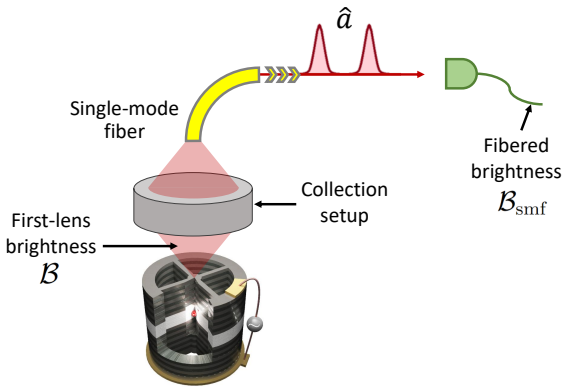


Figure 1.23: Experimental setup to measure the brightness of a source.

If the probability for the source to produce more than one photon per excitation is small, then $\mathcal{B} \simeq p_1$ provides a good estimate of the *single-photon* brightness at the first lens $\mathcal{B}_s$. We

will discuss more about how to more accurately estimate $\mathcal{B}_s$ from $\mathcal{B}$ in the following section.

The single-photon first lens brightness of our sources is governed by the product of multiple factors:

$$\mathcal{B}_s = \beta \eta_{\text{top}} p_{\text{QD}} \eta_{\text{pol}}. \tag{1.71}$$

The first factor $\beta$ is the ratio $F_p/(F_p+1)$ which is the probability for the photon to be emitted in the cavity mode, as described in section 1.3.2. We refer to the second factor $\eta_{\text{top}}$ as the *extraction efficiency*, which is the proportion of photons that are extracted from the top of the pillar, over the whole cavity emission: $\eta_{\text{top}} = \kappa_{\text{top}}/\kappa$ (see figure 1.15(b)). It is reduced when photons are lost through the edges, through the bottom or through the arms of the device. The third factor $p_{\text{QD}}$ is the occupation probability of the QD which is a combination of the excitation probability discussed in section 1.5.2 and the probability of staying in a given charge state. This latter probability can be different from 1 when the QD oscillates between two optical transitions (blinking). Finally, $\eta_{\text{pol}}$ is the *degree of linear polarization* and participates in the brightness since the photons collected via the setup described in section 1.5.1 filters the light from the pillar in polarization. Then, any light that is not linearly polarized, or that is linearly polarized but not parallel to the PBS angle, is rejected. We will detail in Chapter 2 all these factors, their impact on the brightness of the sources and how they could be improved.

### 1.5.5 Single-photon purity

Another important figure of merit is the single-photon purity. This quantity is used to characterize the probability to obtain no more than one photon per pulsed excitation of the source. It is measured using a Hanbury Brown and Twiss interferometer. The output beam from the setup is sent into a beam splitter. The two outputs from this beam splitter are then monitored by single-photon detectors, as shown in figure 1.24(a).

(a)

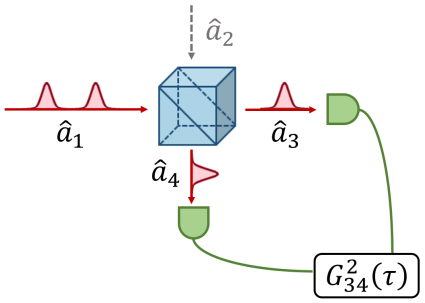


(b)

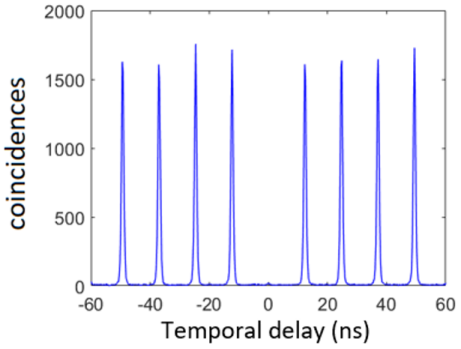


Figure 1.24: (a) Hanbury Brown and Twiss interferometer. (b) Typical second-order correlation histogram $G^{(2)}_{34}(\tau)$ as a function of the delay between two detectors' clicks.

A typical second-order correlation histogram characterizing the single-photon purity is presented in figure 1.24(b). The peak at zero time delay on the obtained histogram is non-zero when there is a non-zero probability for one excitation pulse to give two or more photons. The expression of the plotted quantity is described by:

$$G^{(2)}_{34}(\tau) = \int G^{(2)}_{34}(t,\tau)dt \tag{1.72}$$

where the integral is taken over one period of excitation, and where $G_{34}^{(2)}$ is called the unnormalized second order correlation function. Its expression is:

$$G_{34}^{(2)}(t,\tau) = \langle \hat{a}_3^\dagger(t)\hat{a}_4^\dagger(t+\tau)\hat{a}_4(t+\tau)\hat{a}_3(t)\rangle \tag{1.73}$$

where the modes are represented in figure 1.24(a). For a perfectly balanced beam-splitter, the input modes $\hat{a}_1$ and $\hat{a}_2$ and the output modes $\hat{a}_3$ and $\hat{a}_4$ are linked by the relation:

$$\begin{pmatrix}\hat{a}_3(t)\\ \hat{a}_4(t)\end{pmatrix} = \frac{1}{\sqrt{2}}\begin{pmatrix}1 & -1\\ 1 & 1\end{pmatrix}\begin{pmatrix}\hat{a}_1(t)\\ \hat{a}_2(t)\end{pmatrix} \tag{1.74}$$

Here $\hat{a}_1$ is in the vacuum state. Consequently, we have that:

$$G_{34}^{(2)}(t,\tau) = \frac{1}{4}\langle \hat{a}_1^\dagger(t)\hat{a}_1^\dagger(t+\tau)\hat{a}_1(t+\tau)\hat{a}_1(t)\rangle = \frac{1}{4}G_{11}^{(2)}(t,\tau) \tag{1.75}$$

We see that measuring $G_{34}^{(2)}(\tau)$ then gives us access to the autocorrelation of our emission $G_{11}^{(2)}(t,\tau)$.

We quantify the single-photon purity by $1-g^{(2)}$ where $g^{(2)}$ is the normalized second-order correlation and which is given by the integrated coincidences around zero delay normalized by the area of the side-band peaks:

$$g^{(2)} = \frac{A_0}{A_{\text{uncorr}}} \tag{1.76}$$

with $A_0$ the area of the central peak of the interferogram, and $A_{\text{uncorr}}$ the average area of the uncorrelated peaks.

In terms of correlation functions, these peak areas are given by:

$$\begin{aligned} A_0 &= \int_{\tau\simeq 0} G_{34}^{(2)}(\tau)d\tau = \frac{1}{4}\int_{\tau\simeq 0} G_{11}^{(2)}(\tau)d\tau = \frac{1}{4}\iint_{\tau\simeq 0} G_{11}^{(2)}(t,\tau)dtd\tau \\ A_{\text{uncorr}} &= \int_{\tau\simeq T_p} G_{34}^{(2)}(\tau)d\tau = \frac{1}{4}\int_{\tau\simeq T_p} G_{11}^{(2)}(\tau)d\tau = \frac{1}{4}\iint_{\tau\simeq T_p} G_{11}^{(2)}(t,\tau)dtd\tau \end{aligned} \tag{1.77}$$

For the case of $A_{\text{uncorr}}$, the time $\tau \simeq T_p$ is much larger than the photon lifetime and so we can assume the pulses are uncorrelated. This allows us to separate the intensity correlation by:

$$\begin{aligned} \iint_{\tau\simeq T_p} G_{11}^{(2)}(t,\tau)dtd\tau &= \iint_{\tau\simeq T_p} \langle \hat{a}_1^\dagger(t)\hat{a}_1^\dagger(t+\tau)\hat{a}_1(t+\tau)\hat{a}_1(t)\rangle dtd\tau \\ &= \iint_{\tau\simeq T_p} \langle \hat{a}_1^\dagger(t)\hat{a}_1(t)\rangle\langle \hat{a}_1^\dagger(t+\tau)\hat{a}_1(t+\tau)\rangle dtd\tau = \mu^2 \end{aligned} \tag{1.78}$$

So, finally [128]:

$$g^{(2)} = \frac{1}{\mu^2}\iint G_{11}^{(2)}(t,\tau)dtd\tau \tag{1.79}$$

The example in figure 1.24(b) corresponds to $g^{(2)} = 0.0237 \pm 0.0004$.

Similar to the average photon number $\mu$, we can also write the integrated intensity correlation $g^{(2)}$ in terms of the photon number probabilities $p_n$ using the well-known [129] relation:

$$g^{(2)} = \frac{1}{\mu^2} \sum_n n(n-1)p_n. \tag{1.80}$$

From this relation we can see that, if the probability for more than two photons to be emitted is small, then $g^{(2)}$ is well-approximated by $g^{(2)} \simeq 2p_2/\mu^2$. In this same regime, the average photon number is approximated by $\mu \simeq p_1 + 2p_2$. Hence, we can then get a more accurate estimate of the single-photon first lens brightness using the simple correction:

$$\mathcal{B}_s \simeq \mathcal{B} - \mathcal{B}^2 g^{(2)}. \tag{1.81}$$

However, this correction is very small for the values reported in this thesis, typically less than 1% of $\mathcal{B}$.

### 1.5.6 Indistinguishability

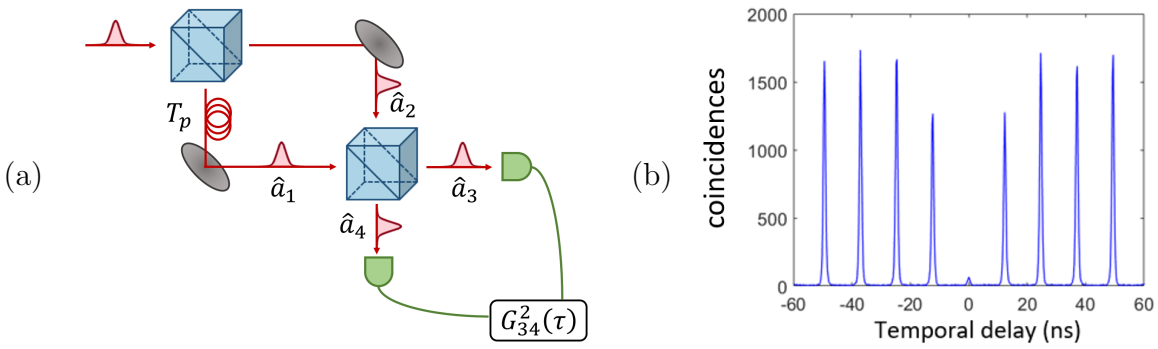


Figure 1.25: (a) Hong-Ou-Mandel interferometer. (b) Typical second-order correlation measured in a Hong-Ou-Mandel two-photon interference experiment. The peaks at ±12 ns present a reduced area because of the unbalanced Mach-Zehnder configuration.

To implement logical gates between single photons, it is important that the generated photons are identical, or indistinguishable. This allows exploiting the quantum interference to obtain probabilistic gates as introduced in the KLM scheme [130]. The indistinguishability of successively emitted photons is quantified by the mean wavepacket overlap $M$ between a wavepacket emitted from a given excitation pulse and the one emitted from another excitation pulse. In terms of quantum operators, its expression is the following:

$$M = \frac{1}{\mu^2} \iint |G^{(1)}(t,\tau)|^2 dt d\tau \tag{1.82}$$

where $G^{(1)}(t,\tau)$ is the first order correlation function, defined as $\langle \hat{a}^\dagger(t+\tau)\hat{a}(t)\rangle$.

The photons produced by the source are temporally separated by a duration $T_p \simeq 12$ ns. To measure their mean wavepacket overlap $M$, we first split the stream of photons into two

paths using a beam splitter. We then delay one path by $T_p$ and then input both paths into a second beam splitter. With a probability 1/4, two photons from successive pulses arrive simultaneously on the BS and interfere, providing information about their wavepacket overlap [70, 131]. The experimental setup is shown in figure 1.25(a).

The measurement is based on the Hong-Ou-Mandel effect [132] which occurs when two indistinguishable photons arrive at two different inputs from a beam-splitter. The quantum character of the light leads to a coalescence of the photons, in other words they leave the beam splitter through the same output. To explain it simply we can take the example of two single photons in the same plane wave mode described by $|\psi\rangle = \hat{a}_1^\dagger \hat{a}_2^\dagger |00\rangle_{12}$ arriving at a beam splitter. Relation 1.74 gives that:

$$\begin{aligned} \psi &= \frac{1}{2}\left((\hat{a}_3^\dagger)_t + (\hat{a}_4^\dagger)_r\right)\left(-(\hat{a}_3^\dagger)_r + (\hat{a}_4^\dagger)_t\right)|00\rangle_{34} \\ &= \frac{1}{2}(|2_{tr}0\rangle + |1_t 1_t\rangle - |1_r 1_r\rangle + |02_{rt}\rangle), \end{aligned} \tag{1.83}$$

where the indices $r$ and $t$ hold for *reflected* and *transmitted* respectively. When the photons are indistinguishable, we have $|1_t 1_t\rangle = |1_r 1_r\rangle$ so these two possible outcomes cancel out and we are left only with situations where the two photons bunch.

The two outputs of the interferometer are monitored by single-photon detectors linked to a correlator, and a typical histogram characterizing the photons indistinguishability is shown in figure 1.25(b). If the two photons show any distinguishability, they have a non-zero probability to entail coincidences (simultaneous "clicks" on the detectors). This increases the area of the central peak on the interferogram. The HOM visibility is $V_{\mathrm{HOM}} = 1 - 2A_0/A_{\mathrm{uncorr}}$ where $A_0/A_{\mathrm{uncorr}}$ is the ratio of coincidences to the uncorrelated peaks.

The example in figure 1.25(b) corresponds to $V_{\mathrm{HOM}} = 0.895 \pm 0.002$.

As for the single-photon purity, we can describe this measurement in terms of mode operators and correlation functions. The measured quantity is, here again:

$$G_{34}^{(2)}(\tau) = \int \langle \hat{a}_3(t)\hat{a}_4(t+\tau)\hat{a}_4(t+\tau)\hat{a}_3(t)\rangle dt \tag{1.84}$$

We now use the methods presented in reference [133], to obtain the indistinguishability from cross-correlations of the input states of the HOM beam-splitter.

To link the input state to the measured quantity $G_{34}^{(2)}(\tau)$, we again use the beam splitter relations. However this time, $\hat{a}_2$ is not in the vacuum state. We use relation (1.74) and inject the expressions of $\hat{a}_3$ and $\hat{a}_4$ as a function of $\hat{a}_1$ and $\hat{a}_2$ in the definition of $G_{34}^{(2)}(t,\tau)$. By considering a separable input state ($\hat{\rho}_{12}(t) = \hat{\rho}_1^\dagger(t) \otimes \hat{\rho}_2(t)$), we can split the averages: for example $\langle \hat{a}_1^\dagger(t)\hat{a}_2^\dagger(t+\tau)\hat{a}_1(t)\hat{a}_2(t+\tau)\rangle = \langle \hat{a}_1^\dagger(t)\hat{a}_1(t)\rangle\langle \hat{a}_2^\dagger(t+\tau)\hat{a}_2(t+\tau)\rangle$. This assumption is valid so long as the photons are not initially correlated, which is the usual case when the excitation pulses are further separated in time than the lifetime of the source ($T \ll 1/\gamma$), or if the photons arrive from independent sources.
Furthermore, we assume that the sources emitting into $\hat{a}_1$ and $\hat{a}_2$ are driven with a $\pi$-pulse

and show a very low $g^{(2)}$ so that the single-photon coherence in the photon number basis is almost zero [1]. Then, we neglect the terms $\langle \hat{a}_{1,2}(t)\rangle$, $\langle \hat{a}_{1,2}(t+\tau)\rangle$, $\langle \hat{a}^\dagger_{1,2}(t)\rangle$ and $\langle \hat{a}^\dagger_{1,2}(t+\tau)\rangle$. There is also no two-photon coherence, so the terms $\langle \hat{a}^\dagger_1(t)\hat{a}^\dagger_1(t+\tau)\rangle\langle \hat{a}_2(t+\tau)\hat{a}_2(t)\rangle$ and $\langle \hat{a}_1(t+\tau)\hat{a}_1(t)\rangle\langle \hat{a}^\dagger_2(t+\tau)\hat{a}^\dagger_2(t)\rangle$ vanish as well. Then expression 1.72 reduces to:

$$\begin{aligned}4G^{(2)}_{34}(t,\tau) = &\langle \hat{a}^\dagger_1(t)\hat{a}^\dagger_1(t+\tau)\hat{a}_1(t+\tau)\hat{a}_1(t)\rangle - \langle \hat{a}^\dagger_1(t)\hat{a}_1(t+\tau)\rangle\langle \hat{a}^\dagger_2(t+\tau)\hat{a}_2(t)\rangle \\ &+ \langle \hat{a}^\dagger_1(t)\hat{a}_1(t)\rangle\langle \hat{a}^\dagger_2(t+\tau)\hat{a}_2(t+\tau)\rangle + \langle \hat{a}^\dagger_1(t+\tau)\hat{a}_1(t+\tau)\rangle\langle \hat{a}^\dagger_2(t)\hat{a}_2(t)\rangle \\ &- \langle \hat{a}^\dagger_1(t+\tau)\hat{a}_1(t)\rangle\langle \hat{a}^\dagger_2(t)\hat{a}_2(t+\tau)\rangle + \langle \hat{a}^\dagger_2(t)\hat{a}^\dagger_2(t+\tau)\hat{a}_2(t+\tau)\hat{a}_2(t)\rangle\end{aligned} \tag{1.85}$$

The second and fifth terms of equation (1.85) are conjugates:

$$\begin{aligned}&- \langle \hat{a}^\dagger_1(t)\hat{a}_1(t+\tau)\rangle\langle \hat{a}^\dagger_2(t+\tau)\hat{a}_2(t)\rangle - \langle \hat{a}^\dagger_1(t+\tau)\hat{a}_1(t)\rangle\langle \hat{a}^\dagger_2(t)\hat{a}_2(t+\tau)\rangle \\ &= -2\mathrm{Re}\left(\langle \hat{a}^\dagger_1(t)\hat{a}_1(t+\tau)\rangle\langle \hat{a}^\dagger_2(t+\tau)\hat{a}_2(t)\rangle\right) = -2\mathrm{Re}\left(\langle \hat{a}^\dagger_1(t)\hat{a}_1(t+\tau)\rangle\langle \hat{a}^\dagger_2(t)\hat{a}_2(t+\tau)\rangle^*\right)\end{aligned} \tag{1.86}$$

Similarly to $g^{(2)}$ for the case of the single-photon purity (see equation (1.76)), we define $g^{(2)}_{\mathrm{HOM}}$ as [133]:

$$g^{(2)}_{\mathrm{HOM}} = \frac{\int_{t=0}^{\infty}\int_{\tau,0} G^{(2)}_{34}(t,\tau)dtd\tau}{\int_{t=0}^{\infty}\int_{\tau,n} G^{(2)}_{34}(t,\tau)dtd\tau} \tag{1.87}$$

In the numerator, integral in $\tau$ is taken over the $0^{\mathrm{th}}$ peak of the interferogram, whereas in the denominator this integral is taken over any $n^{\mathrm{th}}$ uncorrelated peak where $n$ is an integer strictly larger than 1.

The numerator of 1.87 is:

$$\int_{t=0}^{\infty}\int_{\tau,0} G^{(2)}_{34}(t,\tau) = \frac{1}{4}\left(\mu_1^2 g_1^{(2)} + \mu_2^2 g_2^{(2)} + 2\mu_1\mu_2 - 2\mu_1\mu_2 M_{12}\right) \tag{1.88}$$

and the denominator is:

$$\int_{t=0}^{\infty}\int_{\tau,n} G^{(2)}_{34}(t,\tau) = \frac{1}{4}\left(\mu_1^2 + \mu_2^2 + 2\mu_1\mu_2\right) = \frac{1}{4}(\mu_1+\mu_2)^2 \tag{1.89}$$

where we have introduced:

- $g_1^{(2)}$ and $g_2^{(2)}$ the integrated second-order intensity auto-correlation function of modes $\hat{a}_1$ and $\hat{a}_2$:

$$g_i^{(2)} = \frac{1}{\mu_i^2}\iint \langle \hat{a}^\dagger_i(t)\hat{a}^\dagger_i(t')\hat{a}_i(t')\hat{a}_i(t)\rangle dtdt' \tag{1.90}$$

  which was already introduced in equation (1.79), and where $\mu_1$ and $\mu_2$ are the time-integrated mean photon numbers, given by

$$\mu_i = \int \langle \hat{a}^\dagger_i(t)\hat{a}_i(t)\rangle dt \tag{1.91}$$

[1] Note that when exciting with a pulse area lower than $\pi$, it was shown in reference [47] that the single-photon wavepackets present a vacuum component with a coherence in the photon number basis.

- The mean wavepacket overlap between modes $\hat{a}_i$ and $\hat{a}_j$:

$$M_{ij} = \frac{1}{\mu_i \mu_j} \iint \mathrm{Re}\left( \langle \hat{a}_i^\dagger(t') \hat{a}_i(t) \rangle \langle \hat{a}_j^\dagger(t') \hat{a}_j(t) \rangle^* \right) dt dt' \tag{1.92}$$

The separation in time between pulses $T_p$ being much larger than the photon lifetime, we can consider that the correlation between fields at times $t$ and $t + T_p$ is zero like we did for equation (1.78). This is why $M_{12}$ appears in the numerator (where $\tau$ is taken over the $0^{\text{th}}$ peak), and not in the denominator (where $\tau$ is taken over another peak). For the same reason, in the denominator, $\langle \hat{a}_i^\dagger(t) \hat{a}_j^\dagger(t+\tau) \hat{a}_j(t+\tau) \hat{a}_i(t) \rangle \to \langle \hat{a}_i^\dagger(t) \hat{a}_i(t) \rangle \langle \hat{a}_j^\dagger(t+\tau) \hat{a}_j(t+\tau) \rangle$ when $\tau$ is of the order of magnitude of $T_p$ or more. It then gives $\mu_1 \mu_2$ after integration. In a nutshell, in this section we make the assumption that there is no correlation between photons from successive pulses.

We introduce $\bar{g}^{(2)}$, which is the weighted average of $g_1^{(2)}$ and $g_2^{(2)}$ by the ratio of $\mu_1$ and $\mu_2$:

$$\bar{g}^{(2)} = \frac{1}{2} \left( \frac{\mu_1}{\mu_2} g_1^{(2)} + \frac{\mu_2}{\mu_1} g_2^{(2)} \right) \tag{1.93}$$

Finally:

$$g_{\text{HOM}}^{(2)} = \frac{1 - M_{12} + \bar{g}^{(2)}}{(\mu_1 + \mu_2)^2 / 2\mu_1 \mu_2} \tag{1.94}$$

The interference visibility, defined by $V_{\text{HOM}} = 1 - 2g_{\text{HOM}}^{(2)}$, is given by:

$$V_{\text{HOM}} = 1 - \frac{1 - M_{12} + \bar{g}^{(2)}}{(\mu_1 + \mu_2)^2 / 4\mu_1 \mu_2} \tag{1.95}$$

If the interference is balanced, then $\mu_1 = \mu_2$ and $V_{\text{HOM}} = M_{12} - (g_1^{(2)} + g_2^{(2)})/2$ can be used to solve for the mean wavepacket overlap $M_{12}$. If both fields are in the same state, which would be the case for a usual HOM interference characterizing our sources (see figure 1.25(a)), the visibility reduces to the following correction factor:

$$V_{\text{HOM}} = M - g^{(2)} \tag{1.96}$$

where $M = M_{12} = M_{11} = M_{22}$ and $g^{(2)} = g_1^{(2)} = g_2^{(2)}$.
This relation is valid for any two unentangled and identical input states.

When the beam splitter used to implement the HOM interference measurement is not perfectly $50:50$, relation (1.74) becomes:

$$\begin{pmatrix} \hat{a}_3(t) \\ \hat{a}_4(t) \end{pmatrix} = \begin{pmatrix} \cos\alpha & -\sin\alpha \\ \sin\alpha & \cos\alpha \end{pmatrix} \begin{pmatrix} \hat{a}_1(t) \\ \hat{a}_2(t) \end{pmatrix} \tag{1.97}$$

In that case, relation (1.96) becomes:

$$V_{\text{HOM}} = 4RT(M + 1 - g^{(2)}) - 1 \tag{1.98}$$

where $R = \sin^2\alpha$ and $T = \cos^2\alpha$ are the reflection and transmission coefficients of the beam splitter respectively.

**To sum up**

In this chapter, we have introduced the fundamentals of single-photon emission from semiconductor QDs in cavities. We have described the various optical transitions and their optical selection rules, that are key features to understand the operation of the single-photon sources studied in this thesis. We have detailed the subtle physics that govern the polarization of the emitted photon and how the quantum dot reduced symmetry plays a key role in it. We have then recalled the basics of light-matter interaction to describe the spontaneous emission control exploited in this thesis to obtain efficient single-photon sources and to coherently control the quantum dot excitation. Finally, we have briefly described the experimental techniques adopted during this work and introduced the various figures of merit to characterize single-photon sources.

# Chapter 2

# Trions and excitons as single-photon sources: operation and reproducibility

High-quality single-photon sources are needed for quantum technologies: we need them to show high brightness, good single-photon purity and high indistinguishability. These characteristics are defined in Chapter 1. A high brightness ensures that quantum operations can be performed at a high rate while a good single-photon purity and indistinguishability allow for high fidelity and reliability of these operations. Several groups in the QD community have achieved the fabrication of single-photon sources with state-of-the-art performances [61, 134–136]. However, another important feature that single-photon sources should provide is reproducibility, to allow for future scalability. When quantum dots form during growth on an etched substrate, they show inhomogeneous spectral resonances spanning 2 to 30 meV [137–140]. In the case of a planar substrate, they appear at random positions on the samples. Most high-performance sources rely on fabrication techniques where the spatial and spectral matching of the QD-cavity coupling is not fully controlled. In that case, finding a source showing a high QD-cavity coupling requires an exploration among a large number of devices - sometimes in the thousands. This is not a feasible protocol for scalability, since the QD-cavity coupling determines the source brightness, its spectral bandwidth through the Purcell effect [112], and its degree of indistinguishability [141, 142]. More recently, several groups have developed techniques to precisely position the QD in a photonic structure [143–145], but only a few of them [70, 146] report the performance of more than one or two devices. To maximize the possibilities of our semiconductor QDs for single-photon generation, we need to study a large number of devices and understand the underlying physics.

The performance of the source depends on the precise QD transition on which it operates and on the cavity properties. In this chapter, we first discuss the physics that determines the source performance. The cavity birefringence imposes important constraints on the source operation that we first discuss in section 2.1. Each source type is based on one of the two different optical transitions described in section 1.1.3: the charged exciton (trion) or the neutral exciton. In the context of single-photon generation, the trion-based sources are simpler than the exciton-based sources. For this reason, I will first describe the case of the trion in section 2.2 and then describe the case of the exciton in section 2.3. This analysis shows the importance of properly identifying the QD transition. We then propose a new technique for

identifying these optical transitions, based on their different behaviours when rotating the excitation laser polarization. In section 2.5, we address the question of large-scale production of identical single-photons by benchmarking fifteen of our sources from different samples, showing their performance reproducibility. These sources were fabricated using the *in situ* cryogenic photolithography technique [66], presented in 1.4.2, and studied in our group over several months. Finally, we outline the remaining challenges for larger scale fabrication of identical sources.

## 2.1 Constraints imposed by the cavity birefringence

### 2.1.1 Position of the problem

The micropillar cavities in which the QDs are embedded do not show perfect cylindrical symmetry. This is due to the etching step that is always slightly anisotropic: the [110] and [1−10] directions of GaAs are not equivalent because of the chemical bounds' orientations. The micropillars thus present two perpendicular eigenaxes, that are associated with polarization orientations labelled $H$ and $V$ [147]. We use the experimental configuration where the single photons are collected (presented in figure 1.19 from chapter 1) in a cross-polarization with respect to the laser polarization. I define the $H_{\text{coll}}$ axis as the collection orientation of the PBS, which makes a 90° angle with the excitation polarization axis $V_{\text{exc}}$. These vectors orientations are summarized in figure 2.1.

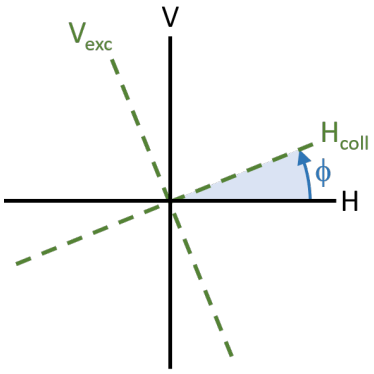


Figure 2.1: Polarization directions: cavity axes $V$ and $H$ and polarization of the excitation and collection $V_{\text{exc}}$ and $H_{\text{coll}}$, respectively.

Let us consider now that a QD is embedded into the cavity, and is excited with a laser with the aim of producing single photons. For $\phi \neq 0$, we experimentally observe that part of the excitation pulse is thus collected in the cross-polarized collection path, which severely degrades the quality of the light emitted by the source, especially in terms of single-photon purity and indistinguishability. This comes from the cavity birefringences which effectively act as a waveplate as soon as $\phi \neq 0$. In the following, we call "cavity-rotated light" the portion of laser light that is collected in the cross-polarized collection path.

To avoid collecting cavity-rotated light from the excitation pulse, and instead collect only the emission from the QD, it is thus necessary to align the excitation polarization $V_{\text{exc}}$ with the cavity polarization $V$. A pulsed excitation of the cavity mode aligned with $V$ will in turn excite the QD optical transition corresponding to that polarization. Then, if the cavity dissipates much faster than the QD, the remaining light in the $V$-polarized mode of the cavity, that has not been absorbed by the QD, will quickly dissipate and not be collected or affect the emission dynamics of the QD.

Since the cavity and its birefringence have an effect on the characteristics of the light collected from the sample in a cross-polarized configuration, we first provide a theoretical

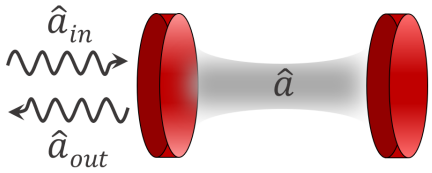


Figure 2.2: Representation of the cavity with the input and output modes, $\langle \hat{a}_{\text{in}} \rangle$ and $\langle \hat{a}_{\text{out}} \rangle$ respectively.

description for it.

### 2.1.2 Theoretical description of the cavity

The classical equation of motion for a cavity mode amplitude $\langle \hat{a}(t) \rangle$ is [148, 149]:

$$\frac{d\langle \hat{a}(t) \rangle}{dt} = -i\omega_c \langle \hat{a}(t) \rangle - \frac{\kappa}{2} \langle \hat{a}(t) \rangle - \sqrt{\eta_{\text{top}}\kappa} \langle \hat{a}_{\text{in}}(t) \rangle \tag{2.1}$$

where $\omega_c$ is the central cavity frequency, $\eta_{\text{top}}\kappa$ is the coupling rate between the cavity mode and the collection mode with $\kappa$ being the Lorentzian FWHM of the cavity mode. The quantity $\eta_{\text{top}}$ alone represents the proportion of light that is emitted upwards into the collection mode, over the total emitted light. It accounts for the absorption by the material, scattering in the arms of the device or emission towards the bottom of the pillar. In the devices studied in this manuscript, $\eta_{\text{top}}$ is approximately equal to $80 - 90\%$ [123]. The first term of equation (2.1), including $\omega_c$, corresponds to the classical oscillator dynamics. The second term $(\kappa/2)\langle \hat{a}(t) \rangle$ leads to the damping of the cavity field amplitude with a rate $\kappa/2$. Finally, the term $-\sqrt{\eta_{\text{top}}\kappa}\langle \hat{a}_{\text{in}}(t) \rangle$ takes into account the input (driving amplitude) incident on the cavity. A diagram of the cavity is represented in figure 2.2. The output mode is given by the input-output relation:

$$\langle \hat{a}_{\text{out}}(t) \rangle = \langle \hat{a}_{\text{in}}(t) \rangle + \sqrt{\eta_{\text{top}}\kappa} \langle \hat{a}(t) \rangle \tag{2.2}$$

Let us solve these equations for a plane-wave input of frequency $\omega$. To do so, we take the Fourier transform of the equation of motion. Then, the Fourier transform of $d\langle \hat{a}(t) \rangle / dt$ is $-i\omega \langle \hat{a}(\omega) \rangle$. For simplicity, we chose the same notation $\hat{a}$ for the Fourier-transformed amplitude and for the time-dependent one. The differential equation (2.1) becomes:

$$-i\omega \langle \hat{a}(\omega) \rangle = -i\omega_c \langle \hat{a}(\omega) \rangle - \frac{\kappa}{2} \langle \hat{a}(\omega) \rangle - \sqrt{\eta_{\text{top}}\kappa} \langle \hat{a}_{\text{in}}(\omega) \rangle \tag{2.3}$$

By dividing equation (2.2) by $\langle \hat{a}_{\text{in}}(t) \rangle$ and introducing the amplitude reflection coefficient $r(\omega) = \langle \hat{a}_{\text{out}}(\omega) \rangle / \langle \hat{a}_{\text{in}}(\omega) \rangle$, we get that $\langle \hat{a}(\omega) \rangle = \langle \hat{a}_{\text{in}}(\omega) \rangle (r-1)/\sqrt{\eta_{\text{top}}\kappa}$. By injecting this in equation (2.3), we get:

$$\begin{aligned} r(\omega) &= 1 - \frac{2\eta_{\text{top}}\kappa}{\kappa - 2i\omega + 2i\omega_c} \\ \text{or } r(\delta) &= 1 + \frac{2i\eta_{\text{top}}\kappa}{2\delta - i\kappa} \end{aligned} \tag{2.4}$$

where $\delta = \omega_c - \omega$ is the cavity-probe detuning. The real and imaginary parts of the reflection coefficient as a function of $\delta/\kappa$ are plotted in figure 2.3(a).

The squared modulus of the reflection coefficient $|r(\delta)|^2$ is shown in figure 2.3(b).

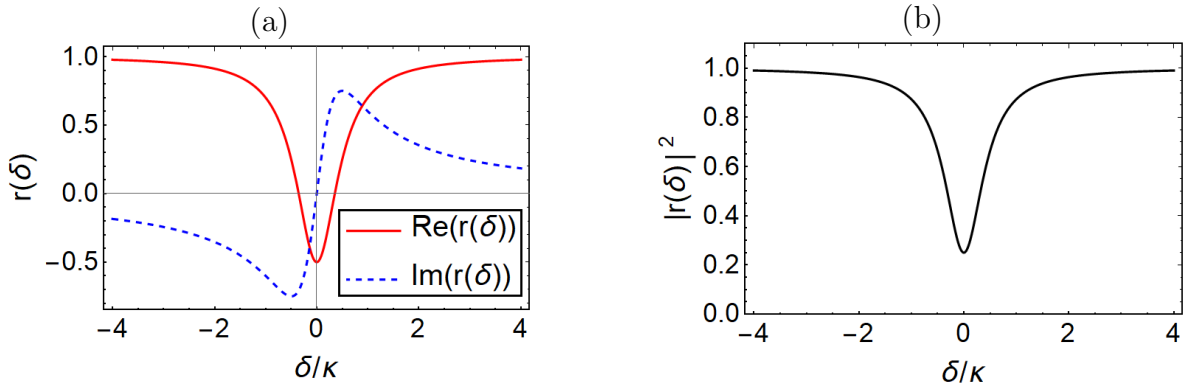


Figure 2.3: (a) Reflection coefficient real (red solid line) and imaginary (dashed blue line) parts, as a function of the cavity-probe detuning $\delta$, for $\eta_{\text{top}} = 75\%$. (b) Squared modulus of the reflection coefficient of the cavity, as a function of the cavity-probe detuning $\delta$, for $\eta_{\text{top}} = 75\%$. The value of $\eta_{\text{top}}$ governs the amplitude of the dip while the value of $\kappa$ governs its width.

We see next how one can experimentally obtain the curve from figure 2.3(b) and extract some cavity parameters.

### 2.1.3 Reflectivity measurement

To obtain the cavities' parameters, it is usual to realize a reflectivity measurement. This is done by exciting the pillar with a continuous wave laser and scanning across the cavity modes frequencies, or with a wide spectrum pulsed laser. The two methods are equivalent, although in the second case it is necessary to normalize the reflectivity spectrum by the excitation laser spectrum. The experimental setup is presented in figure 2.4.

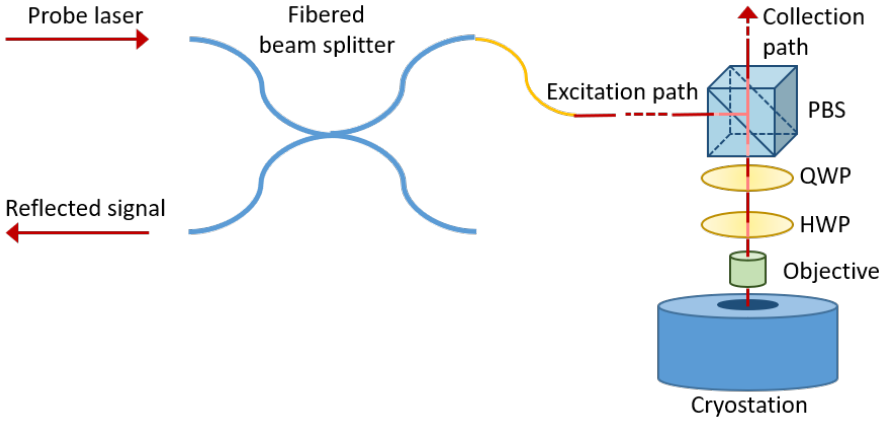


Figure 2.4: Experimental setup for the measurement of the reflected light.

By looking at the signal from the collection path in a spectrometer, we can turn the HWP and the QWP to extinguish the cavity-rotated light. We then know that the ex-

citation polarization is aligned with $H$ or $V$. In that configuration, the reflectivity spectrum gives the characteristics of the corresponding cavity mode only. To get the parameters of the other cavity mode, we need to rotate the HWP by 45° and look at the reflectivity spectrum again. As an example, we present reflectivity spectra for the two cavity modes of one of our micropillars, in figure 2.5. Panels 1(a) and 1(b) correspond to the normalized intensity of the laser (in orange) and the intensity reflected by the cavity (in blue), for modes $H$ and $V$ respectively. For both sets H and V, the reflected intensity divided by the laser intensity is shown on panels 2(a) and 2(b) respectively, together with a Lorentzian fit. It corresponds to the theoretical figure 2.3(b). We extract the following parameters: $\mathrm{FWHM}_h = 0.358 \pm 0.013$ nm and $\lambda_h = 924.551 \pm 0.004$ nm from panel 2(a), and $\mathrm{FWHM}_v = 0.347 \pm 0.014$ nm and $\lambda_v = 924.500 \pm 0.004$ nm from panel 2(b). In units of energy, these correspond to $\hbar\omega_h = 1.341949 \pm 0.000006$ eV, $\hbar\kappa_h = 520 \pm 22\,\mu$eV, $\hbar\omega_v = 1.342024 \pm 0.000006$ eV and $\hbar\kappa_v = 504 \pm 20\,\mu$eV. The splitting between the two cavity modes energies is equal to $\Delta_c = 74 \pm 8\,\mu$eV, well below the cavity linewidth.

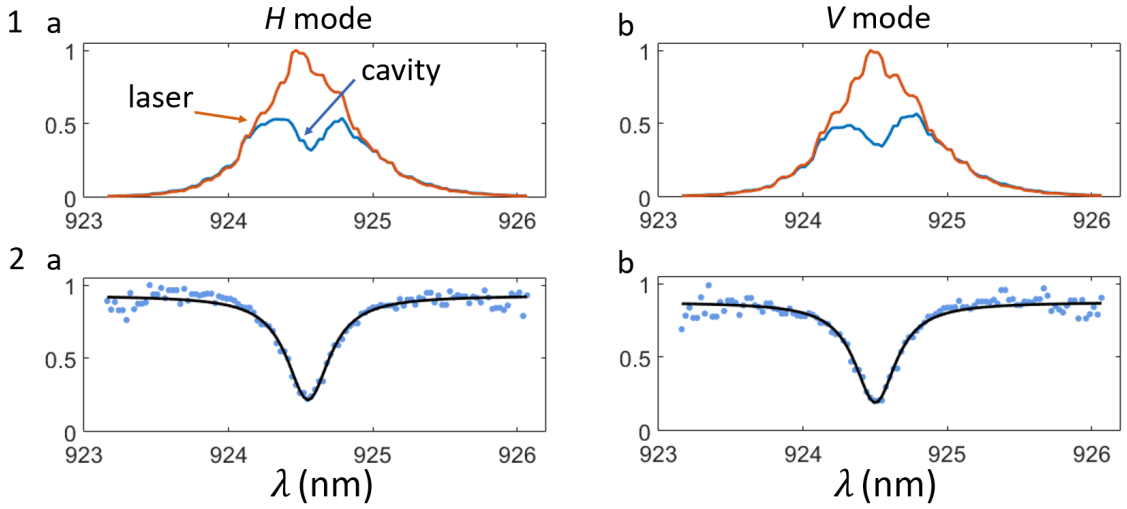


Figure 2.5: Normalized intensity of the laser pulse (orange solid line) of duration 2 ps corresponding to a 0.66 nm width in wavelength, and intensity of the signal reflected by the cavity (blue solid line) for the mode aligned with $H$ (resp. $V$) of the cavity in panel 1(a) (resp. 1(b)). For both sets of data, the reflected intensity is divided by the input intensity (blue data points) and fit with a Lorentzian function. The result is displayed on panels 2(a) and 2(b).

### 2.1.4 Cavity-rotated light

Now let us suppose that we have an input polarization $V_{\mathrm{exc}} \neq V$ (see figure 2.1). We can then define an input vector aligned with this polarization, with coordinates $(-\sin\phi, \cos\phi)$ (along the $H$ and $V$ axes respectively). Each polarization undergoes a transformation according to the reflection coefficient for that mode. Since the $H$ and $V$ polarizations of the cavity modes are orthogonal, their equations of motion are not coupled, and we can write the output

polarization vector as follows:

$$\mathbf{v}_{\text{out}} = \begin{pmatrix} -\sin\phi \left(-1 \quad + \dfrac{4i\delta_h}{2i\delta_h + \kappa_h}\right) \\ \cos\phi \left(-1 \quad + \dfrac{4i\delta_v}{2i\delta_v + \kappa_v}\right) \end{pmatrix} \tag{2.5}$$

Finally, to get the collected amplitude, we filter by the orthogonal polarization $H_{\text{coll}}$, namely take the scalar product of $\mathbf{v}_{\text{out}}$ with the vector of coordinates $(\cos\phi, \sin\phi)$. We obtain the following expression for the collected amplitude:

$$\begin{pmatrix} \cos\phi \\ \sin\phi \end{pmatrix} \cdot \mathbf{v}_{\text{out}} = \frac{i(\delta_v\kappa_h - \delta_h\kappa_v)}{(\kappa_h/2 + i\delta_h)(\kappa_v/2 + i\delta_v)} \sin(2\phi) \tag{2.6}$$

The different detunings involved are sketched in figure 2.6(a): $\delta_h$ (resp. $\delta_v$) is the detuning between the probe frequency of the exciting laser $\omega_p$ and the $h$ mode (resp. $v$ mode) of the cavity. We introduce the frequency detuning $\Delta_p$ between the laser of frequency $\omega_p$ and the mean cavity frequency $(\omega_h + \omega_v)/2$, and the cavity splitting $\Delta_c = \delta_v - \delta_h$. Figure 2.6(b) shows the intensity collected as a function of frequency detuning $\Delta_p$ and cross-polarization HWP angle $\phi$. The intensity for $\Delta_p = 0$ is presented in figure 2.6(c). If $V_{\text{exc}}$ does not align with the cavity polarization $V$, namely if $\phi \neq 0°[90°]$, the cavity is excited in a superposition state of the $H$ and $V$ polarization states of the cavity. If these two modes are not degenerate, then the light in the cavity experiences a rotation of polarization, or birefringence. Such polarization rotation has been recently used in the team of Loïc Lanco to measure the cavity coupling accurately [123]. Over time after the excitation, the cavity-rotated light is reflected off the cavity in a polarization that is not perfectly parallel to its initial polarization, so not completely orthogonal to the collected polarization $H_{\text{coll}}$. When we set $\kappa_h = \kappa_v$ and $\Delta_c = 0$, the 2D map from figure 2.6(b) is uniformly zero.

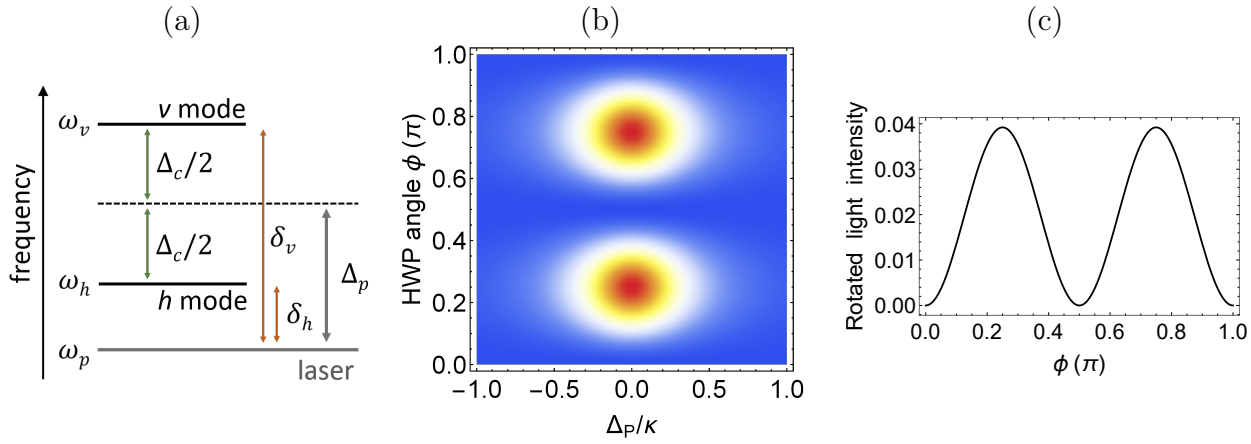


Figure 2.6: (a) Diagram showing the different parameters: $\delta_h$, $\delta_v$, $\Delta_p$, $\Delta_c$. $\omega_p$ is the probe frequency of the exciting laser. (b) Theoretical map of the cavity-rotated light intensity for the following set of parameters: $\kappa_h = \kappa_v = \kappa$ and $\Delta_c = 0.1\kappa$. (c) Intensity of the light reflected by the cavity as a function of the excitation polarization angle, for a probe laser frequency half-way between the cavity mode resonances corresponding to $H$ and $V$ .

Note that measuring a map of the intensity of the cavity-rotated light such as shown in figure 2.6(b) does not allow us to extract precisely the parameters of the cavities (central wavelength or width). The light collected is a superposition of both modes of the cavity, and these modes are not resolved enough to allow for a reliable fit.

We focus now on what happens if a QD is coupled to such a birefringent cavity. We have seen in Chapter 1 that there are several possible occupancies for QDs depending on its charge state. We first focus on the case of the trion.

## 2.2 Trion-based sources

Trions are composed of an electron-hole pair with an extra charge. Once the electron-hole pair radiatively decays, one charge is left, and its spin can be used as a stationary qubit. In this section, I will talk about the characteristics of trions in the context of single-photon generation, especially when embedded into a cavity and operated under resonant excitation in a cross-polarization configuration.

### 2.2.1 Operation in crossed polarization

For the devices studied in this thesis, the trions are usually positively charged, since we set a barrier reducing the hole tunneling rate [91], as shown in figure 1.4.

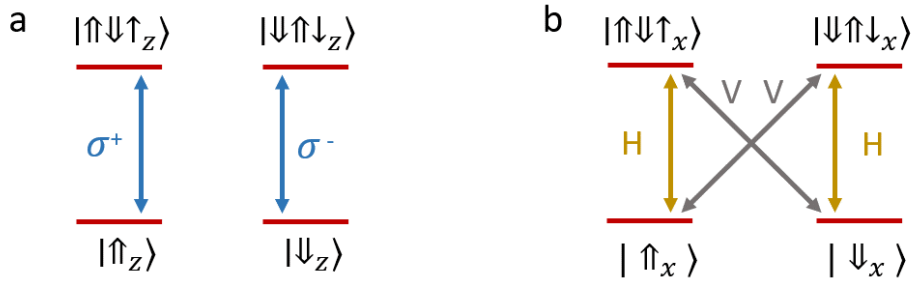


Figure 2.7: Panel (a) is a schematic of the energy levels and optical selection rules for a single-photon source based on a positive trion. Panel (b) shows them with spin projections expressed along an in-plane axis $x$ (without magnetic field).

In the case of a positive trion, the system ground state is composed of two energy levels of the hole spin state $|\Uparrow_z\rangle$ and $|\Downarrow_z\rangle$, which we define with a vertical quantization axis $z$. The excited trion states $|\Uparrow\Downarrow\uparrow_z\rangle$ and $|\Downarrow\Uparrow\downarrow_z\rangle$ correspond to two holes with opposite spin states and one electron. The optical selection rules governing the transitions are summarized in the energy diagram in figure 2.7(a). Similar rules apply in the case of a negative trion.

In the absence of an in-plane magnetic field, the two possible ground states $|\Uparrow_z\rangle$ and $|\Downarrow_z\rangle$ are degenerate, as are the two possible excited states $|\Uparrow\Downarrow\uparrow_z\rangle$ and $|\Downarrow\Uparrow\downarrow_z\rangle$. In that case, the

states and optical transition rules can be written in another basis. For example, we define:

$$\begin{aligned} |\Uparrow_x\rangle &= \frac{1}{\sqrt{2}}(|\Uparrow_z\rangle + |\Downarrow_z\rangle) \\ |\Downarrow_x\rangle &= \frac{1}{\sqrt{2}}(|\Uparrow_z\rangle - |\Downarrow_z\rangle) \end{aligned} \tag{2.7}$$

and similar expressions for the excited states $|\Uparrow\Downarrow\uparrow_x\rangle$ and $|\Downarrow\Uparrow\downarrow_x\rangle$. These excited states are then connected to the ground states $|\Uparrow_x\rangle$ and $|\Downarrow_x\rangle$ by linearly polarized optical transitions:

$$\begin{aligned} |H\rangle &= \frac{1}{\sqrt{2}}(|\sigma^+\rangle + |\sigma^-\rangle) \\ |V\rangle &= \frac{-i}{\sqrt{2}}(|\sigma^+\rangle - |\sigma^-\rangle) \end{aligned} \tag{2.8}$$

The subsequent optical selection rules in that new basis are shown in figure 2.7(b).

In the absence of spin initialization, namely when the hole spin is in a mixture of spin up and down states, a $V_{\text{exc}}$-polarized optical excitation populates both trion states. If the cavity is not too asymmetric, each of these excited states radiates $H_{\text{coll}}$-polarized light with a probability of 50%, for any value of $\phi$.

The expression of the source brightness is given in section 1.5.4. The maximum brightness one can extract from a trion in a cross-polarization setup would then be equal to one half of $\beta\eta_{\text{top}}$ multiplied by the probability of occupation $(P(|\Uparrow\Downarrow\uparrow_x\rangle) + P(|\Downarrow\Uparrow\downarrow_x\rangle))$.

### 2.2.2 Temporal wavepacket profile

The trion emission takes place in crossed polarization as soon as the excited state is populated. This happens on the excitation pulse timescale. The illustrated selection rules lead to the generation of single-photon wavepackets with a mono-exponential decay, where the rise time is governed by the excitation pulse length and the decay time by the Purcell-enhanced spontaneous emission rate.

Figure 2.8 shows the emission dynamics of a trion-based single-photon source. It is obtained by sending the collected signal from the collection setup into a superconducting nanowire single-photon detector (with a given finite response), connected to an autocorrelator as well as the laser clock as a synchronization entry, as described in section 1.5.3. The emission intensity shows a short rise time followed by a mono-exponential decay.

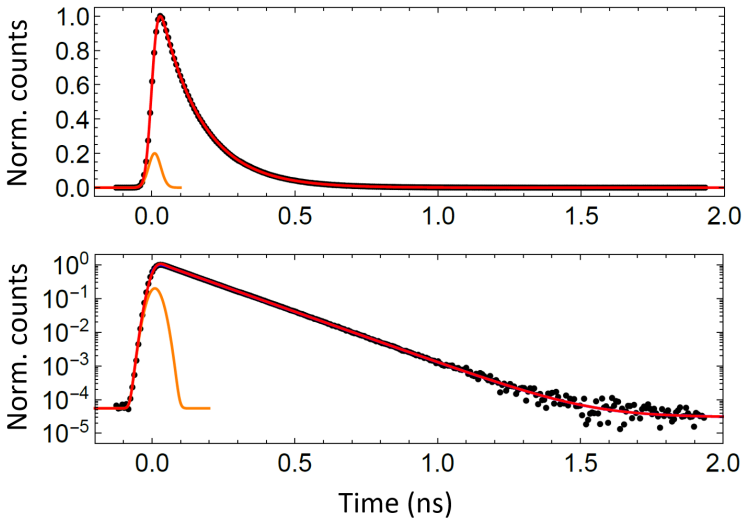


Figure 2.8: Time evolution of the emission for a source based on a trion, plotted linearly in the upper panel and logarithmically in the lower one. The black points are the experimental data, the red curves are the fits to the theoretical models for total intensity. The orange curve presents the expected 15 ps FWHM Gaussian laser pulse, as measured by our detectors with a finite temporal jitter of $\sim 40$ ps.

The data (black points in figure 2.8) is fit using a mono-exponential decay, convolved with a Gaussian function, to account for the finite detector response:

$$f(t) = \alpha e^{-\Gamma t} * e^{-t^2/(2\sigma^2)} \tag{2.9}$$

where $t > 0$, $\sigma = \frac{\text{FWHM}}{2\sqrt{2ln2}}$ is the Gaussian standard deviation and $\alpha$ is a free amplitude parameter that depends on the integration time of the histogram. The fit gives a value of $164.9 \pm 0.9$ ps for the decay time, and a FWHM of 46 ps for the Gaussian to be in agreement with the measured rise time. This last value shows that the rise time is limited by the detector response, since the excitation pulse was much faster (about 15 ps), while the finite detector response is roughly 40 ps.

## 2.3 Exciton-based sources

We now turn to the more complex situation where a neutral QD is coupled to the cavity.

An exciton can be modelled by a three-level system: it comprises a single ground state $|g\rangle$ and the two intrisic exciton eigenstates - hereafter labelled $|x\rangle$ and $|y\rangle$ - leading to an emission in the corresponding linear polarizations $X$ and $Y$. The two exciton states show a fine-structure splitting (FSS) $\Delta_{\text{FSS}} = E_y - E_x = \hbar\omega_{xy}$ presented in section 1.1.4.

The neutral exciton states of the QDs are coupled to the two orthogonal polarization modes of the micropillar cavity. In the present section, we use the following notations, drawn in figure 2.9: $\theta$ is the angle going from the $x$ dipole of the exciton to the $H$ polarization

orientation and $\phi$ is still the angle going from the $H$ polarization orientation to the collection mode orientation, aligned along $H_{\text{coll}}$. $\theta$ is random since we have no control over it in the growth process. We will also use the notation $h$ (resp. $v$) which is used to designate the index of the cavity mode with $H$-polarization (resp. $V$-polarization).

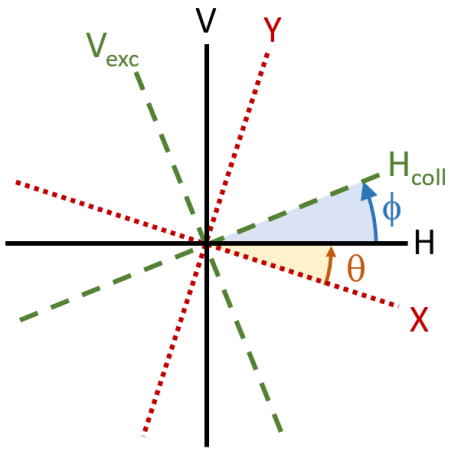


Figure 2.9: Polarization directions: cavity axes V and H, exciton axes X and Y and polarization of the excitation and collection $V_{\text{exc}}$ and $H_{\text{coll}}$, respectively.

### 2.3.1 Theoretical description of an exciton-based SPS

The model presented in this section was developed in the frame of a collaboration between our group and Dr. Stephen Wein from the group of Pr. Christoph Simon (University of Calgary).

#### Hamiltonian

The exciton-based sources can be modeled by two dipoles of a three-level system coupled to two harmonic oscillators, corresponding to the $h$ and $v$ optical modes of the cavity, via Jaynes-Cummings interactions (see section 1.3.3). This gives rise to a Hamiltonian with four Jaynes-Cummings interaction terms between each combination of dipole and cavity mode:

$$\frac{1}{\hbar}\hat{H} = \delta_x \hat{x}^\dagger \hat{x} + \delta_y \hat{y}^\dagger \hat{y} + \delta_h \hat{h}^\dagger \hat{h} + \delta_v \hat{v}^\dagger \hat{v} + g_{xh}(\hat{x}^\dagger \hat{h} + \hat{x}\hat{h}^\dagger) + g_{xv}(\hat{x}^\dagger \hat{v} + \hat{x}\hat{v}^\dagger) + g_{yh}(\hat{y}^\dagger \hat{h} + \hat{y}\hat{h}^\dagger) + g_{yv}(\hat{y}^\dagger \hat{v} + \hat{y}\hat{v}^\dagger) \tag{2.10}$$

as written in the $x$–$y$ linear dipole basis of the QD where $\hat{h}$ and $\hat{v}$ are the photon annihilation operators of the horizontally and vertically polarized cavity modes, respectively, with detunings $\delta_h$ and $\delta_v$ from the QD exciton transition. The QD is written in its eigenbasis of $|x\rangle$ and $|y\rangle$ with a fine-structure splitting defined as $\hbar\omega_{xy} = 2\hbar\delta_y = -2\hbar\delta_x$ and a ground state $|0\rangle$, as shown in figure 2.10. The QD operators are defined as $\hat{x} = |0\rangle\langle x|$ and $\hat{y} = |0\rangle\langle y|$. The cavity bosonic operators follow $\hat{h}|n\rangle = \sqrt{n}|n-1\rangle$ and $\hat{v}|n\rangle = \sqrt{n}|n-1\rangle$ and $\delta_h$ and $\delta_v$ are the cavity-probe detunings of the cavity modes. Note that for the sake of succinctness, we use $\hat{x}^\dagger$ and $\hat{y}^\dagger$ to represent the QD raising operators. They should not be confused with harmonic oscillator creation operators or position operators.

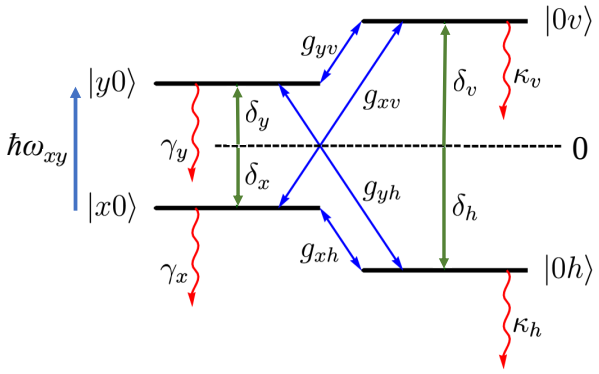


Figure 2.10: Energy level diagram for the exciton states coupled to two orthogonal cavity modes where we define the zero-energy reference such that $\delta_y = -\delta_x$ and where $\hbar\omega_{xy} = 2\hbar\delta_y = -2\hbar\delta_x$ is the FSS. Arrows pointing down indicate negative detunings. The diagram also includes the cavity mode detunings $\delta_h$ and $\delta_v$; the four Jaynes-Cummings interaction rates $g_{xh}$, $g_{yh}$, $g_{xv}$, and $g_{yv}$; and finally the dissipation rates from $|x0\rangle$, $|y0\rangle$, $|0h\rangle$ and $|0v\rangle$: $\gamma_x$, $\gamma_y$, $\kappa_h$ and $\kappa_v$ respectively. These coefficients are taken into account in the model through the Markovian master equation presented later.

The cavity-QD interaction arises from an electric dipole approximation, where the couplings are given by equation (1.54). Let $\theta_{ij}$ be the angle between the dipole $\mathbf{d}_i$ and the electric field $\mathbf{E}_j$.

$$g_{ij} = \mathbf{d}_i.\mathbf{E}_j = |\mathbf{d}_i| \cos\theta_{ij} \sqrt{\frac{\omega_j}{2\hbar n^2 \varepsilon_0 V_j}}, \tag{2.11}$$

where $i \in \{x, y\}$, $j \in \{h, v\}$, with the notations introduced in section 1.3.1. Using the orthogonality of the $x$–$y$ and $h$–$v$ axes, all the $\theta_{ij}$ can be expressed as a function of $\theta_{xh}$, that is simply equal to $\theta$, shown in figure 2.9. Then the cavity couplings are given by

$$g_{xh} = g_h \cos\theta, \qquad g_{xv} = -g_v \sin\theta, \qquad g_{yh} = g_h \sin\theta, \quad \text{and} \quad g_{yv} = g_v \cos\theta, \tag{2.12}$$

where $g_j = d\sqrt{\omega_j/(2\hbar n^2 \epsilon_0 V_j)}$ and $d = |\mathbf{d}_x| = |\mathbf{d}_y|$ (with $j \in \{h, v\}$). This last assumption means that the two transitions have the same oscillator strength, which is not exactly the case, but they are often quite similar. Although we will use these assumptions on the relationship between cavity coupling rates to simplify our solutions, we will still use the former notation during the majority of the derivations.

### Single-excitation approximation

In order to analytically solve the dynamics of QD-based single-photon sources, it is useful to use the so-called "single-excitation approximation". This approximation consists in considering that there is at most one "excitation" in the system, which could be held in the QD or the cavity, or any superposition of these. In other words, it is accurate so long as the energy of the system is equal to or less than one quantum $\hbar\omega$ above the ground state energy, where $\omega \simeq \omega_{\text{QD}} \simeq \omega_{\text{cav}}$. It is a common assumption used to derive the standard Purcell factor [113, 150]. Here, it allows us to model the emission dynamics of the system, which can capture its

basic characteristics in terms of intensity profile and brightness under certain conditions that we will detail below.

In section 1.4, we have seen that under some conditions, $R_j \simeq 4g_j^2/\kappa_j$ where $j \in \{h, v\}$. These conditions are that $\kappa \gg \gamma$ (which is the case for our samples typical values) and that $\kappa^2 \gg \delta^2$, which is the case when we use resonant or quasi-resonant excitation. We recall that for the samples we studied in this thesis, the different parameters are $\hbar g_j \simeq 17\,\mu\text{eV}$, $\hbar\kappa_j \simeq 500\,\mu\text{eV}$ and $\hbar\gamma \simeq 0.6\,\mu\text{eV}$. These parameters mean that our samples are within the bad-cavity regime since $\kappa_j \gg R_j$.

We assume that our system is initially constituted by the QD in its ground state with no photons in the cavity. If one of the cavity modes (say $V$) is excited with a laser pulse, the cavity mode will quickly be populated with $n$ photons. Thus, during the excitation pulse, the populated cavity mode will increase the cavity-QD coupling to $\sim \sqrt{n+1}g_v$. This allows the pulse to quickly excite the QD. The timescale of the QD decay, defined as $1/(R_j + \gamma)$, is approximately equal to 230 ps, which is very long compared to the timescale of the cavity mode decay ($1/\kappa_j \simeq 1.3$ ps). Thus, when the pulse finishes, the cavity population decays rapidly whereas the QD remains almost fully excited. In this situation, the single-excitation approximation is accurate and the emitted single photon is dominated by the decay dynamics occuring when the QD goes from its excited state to its ground state. Although I have illustrated each of these steps discretely, in reality they all overlap. In particular, the QD will begin being excited as soon as the cavity mode is populated with 1 photon and will only finish being excited once the cavity has fully decayed. In addition, the above scenario is valid only when the excitation laser pulse duration is much smaller than $1/(R_j + \gamma)$ so that excitation and emission can be separated into two distinct timescales. It is mostly the case in our experiments since we use durations up to 15 ps, which is very small compared to 230 ps.

In that single-excitation approximation, the subspace available to the evolving state is then: $\{|g00\rangle, |x00\rangle, |y00\rangle, |g10\rangle, |g01\rangle\}$ where we have dropped the commas for the sake of clarity. From now on, since we are in the single-excitation approximation, we can restrict our notation to (in the same order): $\{|00\rangle, |x0\rangle, |y0\rangle, |0h\rangle, |0v\rangle\}$. These states correspond to :

$$\begin{aligned}
|00\rangle \equiv |g00\rangle = |g00\rangle \quad &\leftrightarrow \text{ ground state of the total system (QD and cavity),} \\
|x0\rangle \equiv |x00\rangle = \hat{x}^\dagger |g00\rangle \quad &\leftrightarrow \text{ one quantum of energy in the } x \text{ dipole of the QD,} \\
|y0\rangle \equiv |y00\rangle = \hat{y}^\dagger |g00\rangle \quad &\leftrightarrow \text{ one quantum of energy in the } y \text{ dipole of the QD,} \\
|0h\rangle \equiv |g10\rangle = \hat{h}^\dagger |g00\rangle \quad &\leftrightarrow \text{ one quantum of energy in the } h \text{ axis of the cavity,} \\
|0v\rangle \equiv |g01\rangle = \hat{v}^\dagger |g00\rangle \quad &\leftrightarrow \text{ one quantum of energy in the } v \text{ axis of the cavity.}
\end{aligned} \tag{2.13}$$

Without the single-excitation approximation, the available Hilbert space would be $\{|000\rangle, |x00\rangle, |y00\rangle, |010\rangle, |001\rangle, |x10\rangle, |y10\rangle, |x01\rangle, |y01\rangle, ...\}$, where we could have more than one quantum of energy in the system at once.

In the single-excitation approximation, the Hamiltonian (2.10) can then be written in the

matrix formalism, in the basis $\{|00\rangle, |x0\rangle, |y0\rangle, |0h\rangle, |0v\rangle\}$, as follows:

$$\hat{H} = \hbar \begin{pmatrix} 0 & 0 & 0 & 0 & 0 \\ 0 & \delta_x & 0 & g_{xh} & g_{xv} \\ 0 & 0 & \delta_y & g_{yh} & g_{yv} \\ 0 & g_{xh} & g_{yh} & \delta_h & 0 \\ 0 & g_{xv} & g_{yv} & 0 & \delta_v \end{pmatrix} \tag{2.14}$$

Note that without the single-excitation approximation, the Hamiltonian would be a matrix of infinite dimension. See Figure 2.10 for an energy level diagram of this Hamiltonian in the basis truncated to a single excitation.

### Including dissipation: master equation

The dissipation of the QD and cavity modes, schematically represented in figure 2.10, can be included formally using a Markovian master equation approach [151]:

$$\frac{d}{dt}\hat{\rho}(t) = -\frac{i}{\hbar}\left[\hat{H}, \hat{\rho}(t)\right] + \gamma_x \mathcal{D}(\hat{x})\hat{\rho}(t) + \gamma_y \mathcal{D}(\hat{y})\hat{\rho}(t) + \kappa_h \mathcal{D}(\hat{h})\hat{\rho}(t) + \kappa_v \mathcal{D}(\hat{v})\hat{\rho}(t) \tag{2.15}$$

where $\mathcal{D}(\hat{A})\hat{\rho} = \hat{A}\hat{\rho}\hat{A}^\dagger - \left\{\hat{A}^\dagger\hat{A}, \hat{\rho}\right\}/2$ for the cavity-QD system density operator $\hat{\rho}$ and a general system operator $\hat{A}$. The curly brackets represent the anti-commutator, such that $\left\{\hat{A}^\dagger\hat{A}, \hat{\rho}\right\} = \hat{A}^\dagger\hat{A}\hat{\rho} + \hat{\rho}\hat{A}^\dagger\hat{A}$. The term $\left\{\hat{A}^\dagger\hat{A}, \hat{\rho}\right\}$ is responsible for causing the amplitude damping, or decoherence, of the excited state. That is, it is responsible for reducing the probability of finding the state in the excited state corresponding to $\hat{A}^\dagger\hat{A}$. This reduction in probability is perfectly compensated by the term $\hat{A}\hat{\rho}\hat{A}^\dagger$, which is responsible for causing the system to 'jump' to the ground state so that the trace of $\hat{\rho}$ is preserved.
The rates $\gamma_x$ and $\gamma_y$ correspond to the decay rate of the QD exciton states in the bulk, including both radiative and potential non-radiative components.

### Effective non-Hermitian Hamiltonian

Let us consider that the QD is excited at a time preceding $t = 0$, with a $\pi$-pulse excitation. In that case, the initial state does not include coherence with the state $|00\rangle$. In addition, the master equation (2.15) can never generate coherence between the ground state $|00\rangle$ and any other state since it only models the passive system emission. Therefore, $\langle 00|\,\rho(t)\,|\Phi\rangle = 0$ for $|\Phi\rangle$ in $\{|x0\rangle, |y0\rangle, |0h\rangle, |0v\rangle\}$ at all times $t \geq 0$. In other words, the ground state $|00\rangle$ can only ever incoherently collect population from the 4 decaying excited states. As a result, the only nonzero density matrix element associated with $|00\rangle$ is the population $\langle 00|\,\rho(t)\,|00\rangle$, which is fully described by the evolution of the excited states by $1 - \sum_{|\Phi\rangle}\langle\Phi|\,\rho(t)\,|\Phi\rangle$. That is, the ground state evolution is superfluous since it can be solely obtained by accounting for what population is missing from the excited states. It is then possible to describe the evolution of the full system with an effective non-Hermitian Hamiltonian [152], that includes all the terms that govern only the evolution of the subspace $\{|x0\rangle, |y0\rangle, |0h\rangle, |0v\rangle\}$. We can obtain this Hamiltonian by rearranging the master equation (2.15), including the amplitude damping part $\left\{\hat{A}^\dagger\hat{A}, \hat{\rho}\right\}$ of the dissipative operator $\mathcal{D}(\hat{A})$ into the effective Hamiltonian.

$$\frac{d}{dt}\hat{\rho}(t) = -\frac{i}{\hbar}\left[\hat{\mathcal{H}}\hat{\rho} - \hat{\rho}\hat{\mathcal{H}}^{\dagger}\right] + \gamma_x \hat{x}\hat{\rho}\hat{x}^{\dagger} + \gamma_y \hat{y}\hat{\rho}\hat{y}^{\dagger} + \kappa_h \hat{h}\hat{\rho}\hat{h}^{\dagger} + \kappa_v \hat{v}\hat{\rho}\hat{v}^{\dagger} \tag{2.16}$$

where

$$\hat{\mathcal{H}} = \hat{H} - \frac{i\hbar}{2}\left(\gamma_x \hat{x}^{\dagger}\hat{x} + \gamma_y \hat{y}^{\dagger}\hat{y} + \kappa_h \hat{h}^{\dagger}\hat{h} + \kappa_v \hat{v}^{\dagger}\hat{v}\right). \tag{2.17}$$

This way of writing the master equation is equal to equation (2.15). In this form, we can see that the evolution of the subspace $\{|x0\rangle, |y0\rangle, |0h\rangle, |0v\rangle\}$ is fully governed by the non-Hermitian Hamiltonian $\hat{\mathcal{H}}$. The remaining terms in equation (2.16) serve only to connect the subspace $\{|x0\rangle, |y0\rangle, |0h\rangle, |0v\rangle\}$ to the ground state $|00\rangle$.

In the matrix formalism, $\hat{\mathcal{H}}$ is written as follows in the subspace $\{|x0\rangle, |y0\rangle, |0h\rangle, |0v\rangle\}$:

$$\hat{\mathcal{H}} = \hbar \begin{pmatrix} \delta_x - \frac{i}{2}\gamma_x & 0 & g_{xh} & g_{xv} \\ 0 & \delta_y - \frac{i}{2}\gamma_y & g_{yh} & g_{yv} \\ g_{xh} & g_{yh} & \delta_h - \frac{i}{2}\kappa_h & 0 \\ g_{xv} & g_{yv} & 0 & \delta_v - \frac{i}{2}\kappa_v \end{pmatrix}. \tag{2.18}$$

In the end, by analyzing only the time dynamics of the non-Hermitian Schrödinger equation

$$\frac{d}{dt}|\psi(t)\rangle = -\frac{i}{\hbar}\hat{\mathcal{H}}|\psi(t)\rangle, \tag{2.19}$$

we can obtain the dynamics of the intensity of the photons emitted by the QD into the cavity.

### Initial state

To collect only the emission from the QD, and no cavity-rotated light from the excitation pulse, as explained in section 2.1.1, we align the excitation polarization along one of the cavity polarization, say $V$ (that is $\phi = 0$). We can then approximate the initial state of the excited system to be the $|v0\rangle$ state, where $|v0\rangle = -\sin\theta\,|x0\rangle + \cos\theta\,|y0\rangle$ and $|h0\rangle = \cos\theta\,|x0\rangle + \sin\theta\,|y0\rangle$ represent the excited state of the QD dipoles that are aligned parallel to $V$ and $H$, respectively. These states correspond to one quantum of energy in a superposition of $x$ and $y$ dipoles of the QD. They should not be confused with $|0v\rangle$ and $|0h\rangle$, which are the states of the system corresponding to the QD in the ground state and one photon in the cavity with a polarization $V$ or $H$, respectively.

### Change of basis

To obtain a simplified solution for $|\psi(t)\rangle$, we apply the relations of equation (2.12) and assume $\gamma_x = \gamma_y = \gamma$. Then, we write the non-Hermitian Hamiltonian in the $\{|h0\rangle, |v0\rangle\}$ basis of the QD defined above.

In the basis $\{|h0\rangle, |v0\rangle, |0h\rangle, |0v\rangle\}$, the matrix $\hat{\mathcal{H}}$ becomes

$$\hat{\mathcal{H}} = \frac{\hbar}{2} \begin{pmatrix} -\omega_{xy}\cos 2\theta - i\gamma & \omega_{xy}\sin 2\theta & 2g_h & 0 \\ \omega_{xy}\sin 2\theta & \omega_{xy}\cos 2\theta - i\gamma & 0 & 2g_v \\ 2g_h & 0 & 2\delta_h - i\kappa_h & 0 \\ 0 & 2g_v & 0 & 2\delta_v - i\kappa_v \end{pmatrix}. \tag{2.20}$$

Here we clearly see that the $|v0\rangle$ state of the QD only couples to the $|0v\rangle$ state of the cavity, and likewise for the $h$-polarization. However, because $|v0\rangle$ and $|h0\rangle$ are not energy eigenstates of the QD, they are coupled by the fine-structure splitting term $\omega_{xy} \sin 2\theta$. The energy diagram of the exciton can then be represented as in figure 2.11.

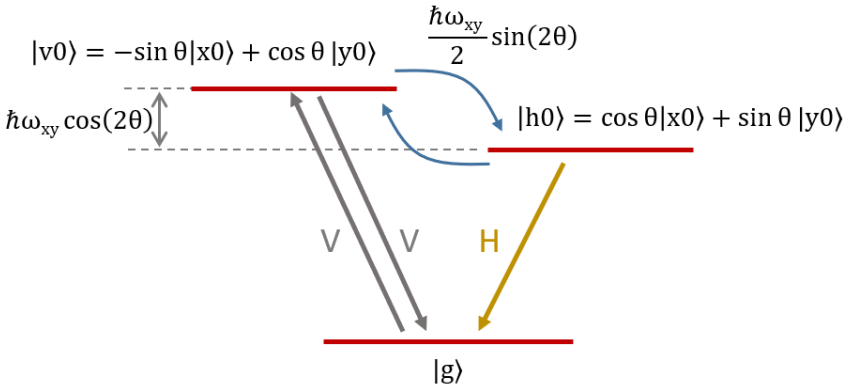


Figure 2.11: Schematic of the energy levels and optical selection rules for a single-photon source based on an exciton shown in the cavity polarization basis when $\phi = 0$. This diagram illustrates the $\{|h0\rangle, |v0\rangle\}$ basis of the exciton, which is not an energy eigenbasis. Thus the blue arrows represent the off-diagonal elements and the gray double arrow represents the difference in diagonal elements of the exciton Hamiltonian in the $\{|h0\rangle, |v0\rangle\}$ basis (the top left $2 \times 2$ matrix in (2.20)).

We can already comprehend why there is light from the QD coming out of the cavity collected in the cross-polarization configuration. The coupling between the $|v0\rangle$ and $|h0\rangle$ states of the exciton, which is proportional to the FSS, entails an oscillation of population between those states (provided that $\theta \neq 0$). Then, when the photon is emitted by the QD, it has a time-evolving probability of being $H$-polarized.

On the other hand, if the FSS coupling was zero, the photons emitted by the QD would be polarized in the same way as the exciting light, and then would be rejected by the PBS in the collection setup. Also, if the FSS coupling was non zero but we were to excite the exciton with a light polarized along $|x0\rangle$ or $|y0\rangle$ (which would be the case if $\theta = 0°[90°]$), no signal would be collected in crossed polarization either.

In the end, this behaviour where there is an exchange of population between the two exciton eigenstates in time is similar to the cavity birefringence described in section 2.1, this time driven by the emitter birefringence. Effectively, we align the excitation polarization so that $\phi = 0$ to not get any cavity-rotated light. If the QD and cavity do not have degenerate axes ($\theta \neq 0$), we then get light 'rotated' by the QD.

### Adiabatic elimination

To obtain an effective non-Hermitian Hamiltonian just for the QD states, we can 'adiabatically eliminate' [150] the cavity state amplitudes by imposing $\langle 0h|\dot{\psi}\rangle = \langle 0v|\dot{\psi}\rangle = 0$. In physical

terms, this approximation makes the assumption that dissipative rates $\kappa_h$ and $\kappa_v$ are much larger than the coupling rate $g$ so that the probability of having a photon in a cavity mode $h$ or $v$ is proportional to the probability of the QD being in the corresponding state $|h0\rangle$ or $|v0\rangle$, respectively. We are allowed to apply this adiabatic elimination only if the cavity is not initially populated, which is the case since we approximate the initial state to be $|v0\rangle$ here. Using the Schrödinger equation, we find the following proportionality relations:

$$\begin{aligned} \langle 0h|\psi\rangle &= -\frac{2g_h}{2\delta_h - i\kappa_h}\langle h0|\psi\rangle\,, \\ \langle 0v|\psi\rangle &= -\frac{2g_v}{2\delta_v - i\kappa_v}\langle v0|\psi\rangle\,. \end{aligned} \tag{2.21}$$

By substituting these relations back into the equations of motion for $|h0\rangle$ and $|v0\rangle$, we find that the effective non-Hermitian Hamiltonian governing the evolution of the QD is

$$\hat{\mathcal{H}}_{\text{eff}} = \frac{\hbar}{2}\begin{pmatrix} -\omega_{xy}\cos 2\theta - 2\Delta_h - i(\gamma + R_h) & \omega_{xy}\sin 2\theta \\ \omega_{xy}\sin 2\theta & \omega_{xy}\cos 2\theta - 2\Delta_v - i(\gamma + R_v) \end{pmatrix}, \tag{2.22}$$

where $\Delta_h = R_h\delta_h/\kappa_h$ and $\Delta_v = R_v\delta_v/\kappa_v$ are the cavity-induced Lamb shifts with $R_h = 4g_h^2/\kappa_h(1 + 4\delta_h^2/\kappa_h^2)^{-1}$ and $R_v = 4g_v^2/\kappa_v(1 + 4\delta_v^2/\kappa_v^2)^{-1}$. These quantities $R_j$ with $j \in \{h, v\}$ are the enhancements of the QD decay rate due to the Purcell effect, introduced in section 1.4 (equation (1.36) with $\gamma \ll \kappa_j$). Finally, $\theta$ is the angle between the QD $x$-dipole axis and the cavity $h$ polarization. Recall that this effective Hamiltonian reduced to the QD states is only valid so long as $\kappa_h$ and $\kappa_v$ dominate the system rates. Hence, this adiabatic elimination is only valid so long as the system is far in the bad-cavity regime ($g_h \ll \kappa_h$ and $g_v \ll \kappa_v$), and the initial state is within the QD subspace $\{|h0\rangle, |v0\rangle\}$.

### 2.3.2 Temporal wavepacket profile

The evolution of the initial QD state $|\psi(0)\rangle = |v0\rangle$ can now be solved exactly by diagonalizing the $2 \times 2$ effective non-Hermitian Hamiltonian. The population in $|h0\rangle$ is given by

$$\begin{aligned} |\langle h0|\psi(t)\rangle|^2 &= |\langle h0|\, e^{-it\hat{\mathcal{H}}_{\text{eff}}}\, |v0\rangle|^2 \\ &= \frac{\omega_{xy}^2}{2}\left(\frac{\cosh(\Omega_i t) - \cos(\Omega_r t)}{\Omega_r^2 + \Omega_i^2}\right)\sin^2(2\theta)e^{-\Gamma t}, \end{aligned} \tag{2.23}$$

where $\Gamma = \gamma + (R_h + R_v)/2$ is the Purcell-enhanced decay rate and

$$\Omega_r + i\Omega_i = \sqrt{\lambda^2 + \omega_{xy}^2 + 2\lambda\omega_{xy}\cos(2\theta)}, \tag{2.24}$$

where $\Omega_r$ and $\Omega_i$ are real numbers, and where $\lambda = (\Delta_h - \Delta_v) + i(R_h - R_v)/2$. The complex parameter $\lambda$ captures possible asymmetry of the couplings between the QD and the cavity modes: $\lambda$ is non-zero when the QD is closer in energy to one cavity mode than to the other (namely $\delta_h \neq \delta_v$) and/or when the cavity axes show different linewidths ($\kappa_h \neq \kappa_v$). The different configurations giving a non-zero $\lambda$ are sketched in figure 2.12. The value $\Omega_r$ is the frequency of oscillation in the emission intensity. Under most conditions, $\Omega_r$ is nearly equal to the FSS of the exciton states (see below).

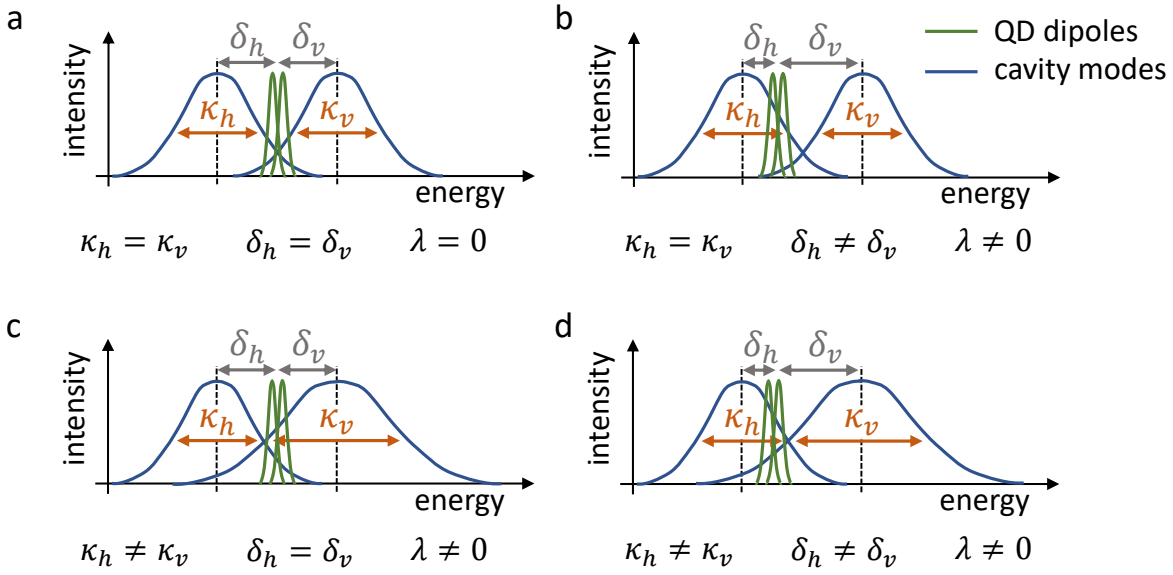


Figure 2.12: Schematics of the different configurations where $\lambda$ is zero (top left panel, where $\kappa_h = \kappa_v$ and $\delta_h = \delta_v$) or non-zero (panels (b) where $\kappa_h = \kappa_v$ and $\delta_h \neq \delta_v$, (c) where $\kappa_h \neq \kappa_v$ and $\delta_h = \delta_v$ and (d) where $\kappa_h \neq \kappa_v$ and $\delta_h \neq \delta_v$). The green (resp. blue) curves represent the QD dipoles (resp. the cavity modes).

From equation (2.21), the cavity population $\langle \hat{h}^\dagger \hat{h} \rangle$ is proportional to the population in the QD excited state, by a factor $|2g_h/(2\delta_h - i\kappa_h)|^2 = R_h/\kappa_h$. Hence, the emitted single photon's intensity will have the temporal shape given by

$$\begin{aligned} \langle \hat{h}^\dagger \hat{h} \rangle &= \frac{R_h}{\kappa_h} |\langle h0|\psi(t)\rangle|^2 \\ &= \frac{R_h}{\kappa_h} \frac{\omega_{xy}^2}{2} \left( \frac{\cosh(\Omega_i t) - \cos(\Omega_r t)}{\Omega_r^2 + \Omega_i^2} \right) \sin^2(2\theta) e^{-\Gamma t}. \end{aligned} \tag{2.25}$$

In the particular case where the Purcell effect induced by each cavity mode is nearly equal $R_h \approx R_v \approx R$ and the cavity modes are nearly degenerate $\delta_h \approx \delta_v \approx 0$ so that $|\lambda| \ll |\omega_{xy}|$, then $\Omega_i \approx 0$ and $\Omega_r \approx \omega_{xy}$, and the emission intensity simply becomes

$$\langle \hat{h}^\dagger \hat{h} \rangle = \frac{R}{2\kappa_h} (1 - \cos(\omega_{xy} t)) \sin^2(2\theta) e^{-\Gamma t} \tag{2.26}$$

where $\Gamma = \gamma + R = \gamma(1 + F_\mathrm{p})$ is the Purcell-enhanced decay rate of the QD and $R = 4g^2/\kappa = \gamma F_\mathrm{p}$ is the emission rate via the cavity mode.

This model explains important features. The initial exciton state has no overlap with the collection mode at $t = 0$. Thus the single-photon emission along $H_\mathrm{coll}$ is delayed from the excitation, with a timescale inversely proportional to the FSS. While both components of the excited state decay with the total decay rate $\Gamma$, the emission in the $H_\mathrm{coll}$ polarization is modulated in time by the oscillation induced by $\hbar\omega_{xy}$. In the limit where $\hbar\omega_{xy} \to 0$, we find that no emission from an exciton in the cross-polarized collection mode is expected.

An example of measured decay dynamics of an exciton is shown in figure 2.13. For visualization purposes, I did not set the angle $\phi$ perfectly equal to zero for these data, so that some cavity-rotated light is measured (see subsection 2.1.1). Hence, we detect both the laser pulse rotated by the cavity and the exciton emission dynamics to compare the relative timescales. The maximum of the single-photon emission is delayed by approximately 200 ps from the laser excitation pulse. The overall exponential decay is governed by the Purcell-enhanced spontaneous emission rate, and is also modulated by the phase dependence of the frequency components $|x0\rangle$ and $|y0\rangle$ at the rate $\omega_{xy}$. The experimental observations are accurately reproduced by equation (2.26) using the parameters $\tau = 1/\Gamma = 252\pm3$ ps and $\hbar\omega_{xy} = 8.58\pm0.03\,\mu$eV. The reduced contrast in the oscillations observed in the lifetime curve (the fact that it does not go to zero in the dips) was found to be consistent with a finite gaussian detector response time with a full width at half maximum (FWHM) of 53 ps (very similar to the one obtained with the trion lifetime fit) which also dominated the observed width of the 15 ps Gaussian excitation pulse.

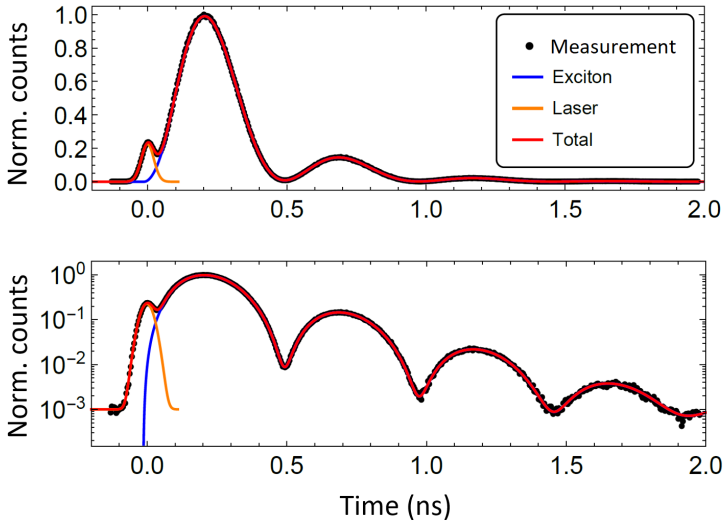


Figure 2.13: Time evolution of the emission for a source based on an exciton, plotted linearly in the upper panel and logarithmically in the lower one. The black points are the experimental data. The blue curve is the calculated temporal profile for an exciton (equation (2.26)) after taking into account the timing response of the detector and the orange curve is the contribution from the laser. The red curves are the total intensities.

Note however that if $|\lambda|$ is not very small compared to $|\omega_{xy}|$, the temporal profile of the emitted single-photons might not be described by equation (2.26) anymore. In our case, the $H$ and $V$ cavity parameters usually slightly differ (see figure 2.5). To get an idea of the effect of this difference, I used expression 2.23 to plot in figure 2.14 the temporal profile of the emission from a QD for which $\lambda = 0$ (a QD which energy is half-way between the two mode energies of the cavity, that have equal energy linewidths), to compare with one corresponding to our measured parameters orders of magnitude. We can conclude that in figure 2.13, although the reduction of the contrast of the oscillations is probably also affected by this phenomenon, the detector response clearly dominates this effect.

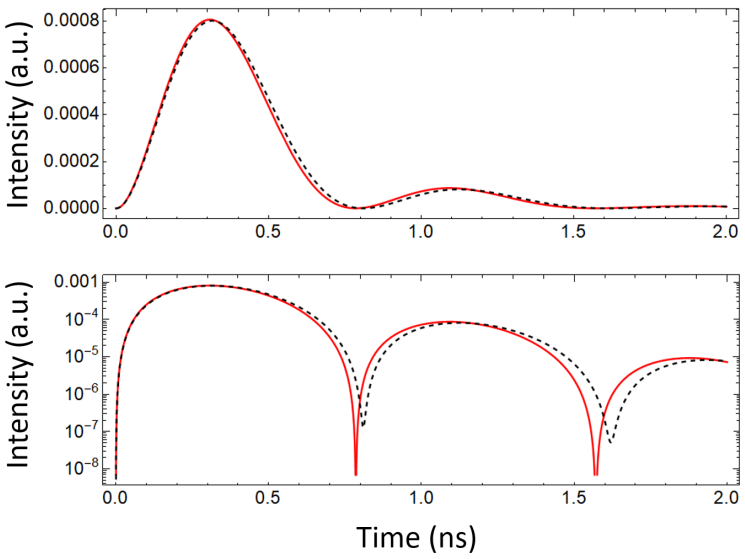


Figure 2.14: Comparison of the temporal profiles of the emission from a QD coupled in the same way to both modes of the cavity, namely when $\lambda = 0$ (solid red line), and from one being coupled in different ways to the two modes of the cavity, namely when $\lambda \neq 0$ (dashed black line). The upper panel shows a linear scale while the lower one is logarithmic. For the case $\lambda = 0$, the parameters in units of energy are: $\kappa_h = \kappa_v = 515\,\mu\text{eV}$, $g_h = g_v = 17\,\mu\text{eV}$, and $\delta_h = \delta_v = 0$. For the case where $\lambda \neq 0$, $\kappa_h = 505\,\mu\text{eV}$, $\kappa_v = 525\,\mu\text{eV}$, $g_h = g_v = 17\,\mu\text{eV}$, $\delta_h = -\,40\,\mu\text{eV}$ and $\delta_v = 40\,\mu\text{eV}$. For both cases, $\omega = 8\,\mu\text{eV}$, $\gamma = 0.5\,\mu\text{eV}$ and $\theta = 22.5°$.

### 2.3.3 Brightness from an exciton in the bad-cavity regime

A quantity we are interested in is the emission brightness $\mathcal{B}$, as defined in section 1.5.4. The brighter a source is, the higher the rate at which quantum operations or experiments can be implemented is. Under resonant excitation, the physics described above in case of an exciton sets an upper limit to this brightness.

The brightness emitted from the collected mode of the cavity, that we note $\hat{h}_{\text{out}}$, is given by the integrated average photon number in that mode. It is equal to $\int_0^\infty \langle \hat{h}^\dagger_{\text{out}}(t)\hat{h}_{\text{out}}(t)\rangle\, dt$. Since we assume $\langle \hat{h}_{\text{in}}(t)\rangle = 0$ during decay, we have from the input-output relation (2.2) that $\langle \hat{h}^\dagger_{\text{out}}(t)\hat{h}_{\text{out}}(t)\rangle = \eta_{\text{top}}\kappa_h \langle \hat{h}^\dagger(t)\hat{h}(t)\rangle$. Hence, the brightness is $\mathcal{B} = \eta_{\text{top}}\kappa_h \int_0^\infty \langle \hat{h}^\dagger(t)\hat{h}(t)\rangle\, dt$ where $\int_0^\infty \langle \hat{h}^\dagger(t)\hat{h}(t)\rangle\, dt$ is the cavity population given in equation (2.25) (or in equation (2.26) in the case that $\lambda \ll$FSS). We obtain:

$$\mathcal{B} = \frac{R}{2}\eta_{\text{top}} \int_0^\infty (1 - \cos(\omega_{xy}t)) \sin^2(2\theta) e^{-\Gamma t} dt \tag{2.27}$$

The analytical result is:

$$\mathcal{B} = \frac{1}{2}\eta_{\text{top}} \frac{R}{R+\gamma} \frac{\omega_{xy}^2}{(R+\gamma)^2 + \omega_{xy}^2} \sin^2(2\theta) \tag{2.28}$$

We recognize $\beta = R/(R+\gamma)$ and $\eta_{\text{top}}$ from the definition of the brightness given in section 1.5.4. We have not considered the reduction of efficiency related to $p_{\text{QD}}$, that leaves us with

$\eta_{\text{pol}} = \frac{1}{2}\frac{\omega_{xy}^2}{(R+\gamma)^2+\omega_{xy}^2}\sin^2(2\theta)$.

The maximum of $\mathcal{B}$ is equal to 1/2 and is obtained when the following four conditions are all satisfied: when $\omega_{xy} \gg R+\gamma$, $R/\gamma$ (the Purcell factor) is big, $\theta$ is equal to 45° and $\eta_{\text{top}} = 100\%$.
This means that the brightness is limited to 1/2 in the bad-cavity regime, which is defined by $R \ll \kappa_h, \kappa_v$ [113], in a cross-polarization setup.

If we take values (in units of energy) that correspond to our situation, for example $\omega_{xy}$ =8 µeV as in the case of figure 2.13, $g$ =17 µeV, $\kappa$ =500 µeV, $\gamma$ =0.6 µeV and $\eta_{\text{top}} \simeq 80-90\%$ the conditions to reach $\mathcal{B} = 1/2$ mentioned above are not fulfilled. The brightness in that case is equal to approximately 30% (in the case where $\theta = 45°$).

We have seen earlier that our systems operate in the bad-cavity regime. But if the parameters turned out to be such that we are not as far into the bad-cavity regime, for example if $\kappa$ is smaller, then the brightness can slightly exceed 1/2 and the maximum is equal to 9/16. The demonstration of this result is developed in Appendix B.

## 2.4 Rotated emission identification method

As shown before, the nature of the optical transition does not only control the temporal profile but also determines the brightness of the sources. It is therefore important to develop tools to identify the transition.

### 2.4.1 Motivation

Advanced equipment is required to observe the exciton FSS splitting. It can be done by means of high resolution spectral analysis, which we use in Chapter 4, and that consists in rotating the excitation polarization and measuring the wavelength of the emitted light with a high spectral resolution system. This gives a sinusoidal behaviour and the wavelengths of the minima and maxima correspond to the wavelength of the two dipoles. Another method is to measure the emission dynamics with high temporal resolution, as shown in figure 2.13. In this section, we propose another simple identification tool based on the polarization-dependent optical selection rules. Thanks to this method, we are able to immediately determine the nature of the transition we are studying in the lab, just using a standard resolution spectrometer.

### 2.4.2 Characterization using cavity-rotated light

The brightness of each source is determined both by the nature of the transition and, in the case of excitons, the orientation of the cavity axes with respect to the QD dipoles, which arises randomly during the growth process. In this context, it is useful to analyze the emission collected in cross-polarization when turning the excitation polarization $V_{\text{exc}}$ by an angle $\phi$ with respect to the cavity axes, recall figure 2.9. For $\phi = 0$, the excitation is parallel to the $V$ cavity axis and only the spectrally narrow emission arising from the QD is collected in the $H$-mode, which corresponds to the configuration used for the source operation. However, when $\phi$ is

different from 0° or 90°, we can see a broader line, as shown in figure 2.15 for an exciton and a trion. This is the cavity-rotated light, presented in 2.1. From an experimental point of view, to vary $\phi$ and obtain figure 2.15, we turn the HWP after the PBS by an angle $\phi/2$ in the experimental setup described in section 1.5.1. To be able to visualize the cavity-induced light rotation, we use 3 ps laser pulses, which are broader and filtered by the cavity mode. This gives a result that is qualitatively similar to what would be obtained by scanning a narrow band laser as calculated in figure 2.6. The emission of the cavity-rotated light is maximal for around $\phi = 45°$ and 135° [123].

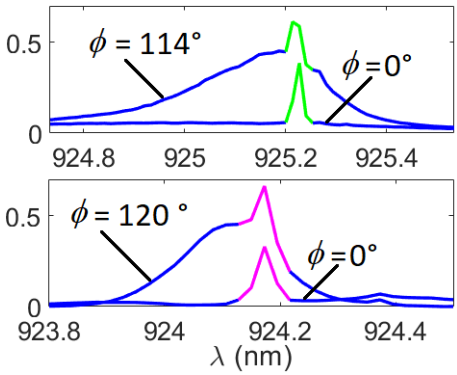


Figure 2.15: Spectra obtained for different values of the polarization angle of the excitation $\phi$, illustrating the cavity birefringence contribution. The upper (lower) panel corresponds to an exciton (a trion), with the narrower signal from the QD highlighted in green (pink). In both panels, the broader blue curve is the cavity-rotated light.

### Case of a trion

The selection rules illustrated in figure 2.7 can be rewritten in any two-orthogonal linear polarization basis, and the amplitude of the QD emission in the polarization orthogonal to the excitation is independent of the orientation of the excitation.

### Case of an exciton

In this section, we use the effective non-Hermitian Hamiltonian (2.22) again, describing the evolution of the exciton. If the initial state is not equal to $|v0\rangle$ as in section 2.3.2, but to $|v_{\text{exc}}0\rangle$ instead, meaning that the excitation laser polarization makes an angle $\phi$ with the $|0v\rangle$ cavity axis, then the QD contribution to the collection will be given by the population in $|h_{\text{coll}}0\rangle$, that is:

$$|\langle h_{\text{coll}}0|\psi(t)\rangle|^2 = |\langle h_{\text{coll}}0|\, e^{-it\hat{\mathcal{H}}_{\text{eff}}}\, |v_{\text{exc}}0\rangle|^2 \tag{2.29}$$

For the sake of simplicity, we consider already that the coupling of the QD to both cavity modes is symmetric, meaning that $R_h = R_v = R$ and $\delta_h = \delta_v = \delta$ (case (a) in figure 2.12). The effective non-Hermitian Hamiltonian (2.22) reduces then to:

$$\hat{\mathcal{H}}_{\text{eff}} = -\frac{1}{2}(2\Delta + i(\gamma + R))\hat{I} - \frac{\omega_{xy}}{2}\hat{P}(-\theta)\hat{\sigma}_z\hat{P}(\theta) \tag{2.30}$$

where

$$\hat{P}(\theta) = \begin{pmatrix} \cos\theta & -\sin\theta \\ \sin\theta & \cos\theta \end{pmatrix} \quad \text{and} \quad \hat{\sigma}_z = \begin{pmatrix} 1 & 0 \\ 0 & -1 \end{pmatrix} \tag{2.31}$$

are a rotation matrix by an angle $\theta$ and the $z$ Pauli matrix respectively.

Since $\hat{P}(-\theta)\hat{P}(\theta) = \hat{I}$, we have:

$$\hat{\mathcal{H}}_{\text{eff}} = \hat{P}(-\theta)\left[-\left(\Delta + \frac{i}{2}(\gamma + R)\right)\hat{I} - \frac{\omega_{xy}}{2}\hat{\sigma}_z\right]\hat{P}(\theta) \tag{2.32}$$

We notice that $\hat{\mathcal{H}}_{xy} = -\left(\Delta + \frac{i}{2}(\gamma + R)\right)\hat{I} - \frac{\omega_{xy}}{2}\hat{\sigma}_z$, which is the effective Hamiltonian in the $x - y$ basis, is diagonal.

Also, we have (see figure 2.9):

$$\begin{cases} |h_{\text{coll}}0\rangle &= \cos(\theta+\phi)\,|x0\rangle + \sin(\theta+\phi)\,|y0\rangle \\ |v_{\text{exc}}0\rangle &= -\sin(\theta+\phi)\,|x0\rangle + \cos(\theta+\phi)\,|y0\rangle \end{cases} \tag{2.33}$$

We can now expand equation (2.29), knowing that $\langle x0|\, e^{-it\hat{\mathcal{H}}_{\text{eff}}}\,|y0\rangle = \langle y0|\, e^{-it\hat{\mathcal{H}}_{\text{eff}}}\,|x0\rangle = 0$, since $\hat{\mathcal{H}}_{\text{eff}}$ is diagonal in the $x - y$ basis.

$$\begin{aligned} \langle h_{\text{coll}}0|\, e^{-it\hat{\mathcal{H}}_{\text{eff}}}\,|v_{\text{exc}}0\rangle = &-\cos(\theta+\phi)\sin(\theta+\phi)\,\langle x0|\, e^{-it\hat{\mathcal{H}}_{xy}}\,|x0\rangle \\ &+\cos(\theta+\phi)\sin(\theta+\phi)\,\langle y0|\, e^{-it\hat{\mathcal{H}}_{xy}}\,|y0\rangle \end{aligned} \tag{2.34}$$

Finally:

$$|\,\langle h_{\text{coll}}0|\, e^{-it\hat{\mathcal{H}}_{\text{eff}}}\,|v_{\text{exc}}0\rangle\,|^2 = \sin^2(2(\theta+\phi))\sin^2\left(\frac{\omega_{xy}t}{2}\right)e^{-(\gamma+R)t} \tag{2.35}$$

This equation is equivalent to equation (2.26), but now the emission from the exciton is proportional to the sine squared of $2(\theta+\phi)$ instead of $2\theta$. It is then minimal if the excitation polarization is aligned with an axis of the exciton. The signal from the exciton is maximal if the sum $\theta + \phi$ is equal to 45°. So, to maximize the emission one needs to excite the QD with a polarization that is half way between the two excitonic axes, but this does not coincide, *a priori*, with the orientation of $H$ or $V$, that are the excitation polarization orientations needed to get no cavity-rotated light along with the single photons from the device. The ideal case for the use of an exciton would then to get control of the relative axes orientation of the cavity and QD, and then be able to set it at 45°.

### 2.4.3 Experimental results

We now turn to experimental observations, one based on a trion and one based on an exciton. By turning the half-waveplate angle, we vary the angle $\phi$ of the linear polarization with which the QD gets excited, relatively to one of the cavity axes.

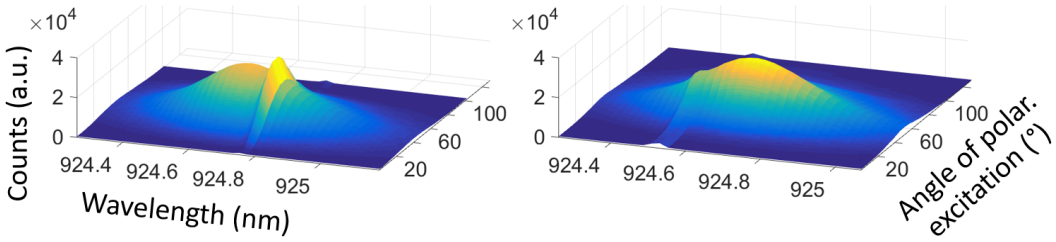


Figure 2.16: Emission spectra measured as a function of $\phi$ for two devices: an exciton on the left panel and a trion on the right one.

Figure 2.16 shows the spectra obtained by continuously rotating the HWP, as a function of $\phi$. The broader emission lines correspond to the cavity birefringence signal, the narrower lines to the QD emission. We already notice that on the left panel, the intensity coming from the QD varies with $\phi$, while it barely varies on the right panel.

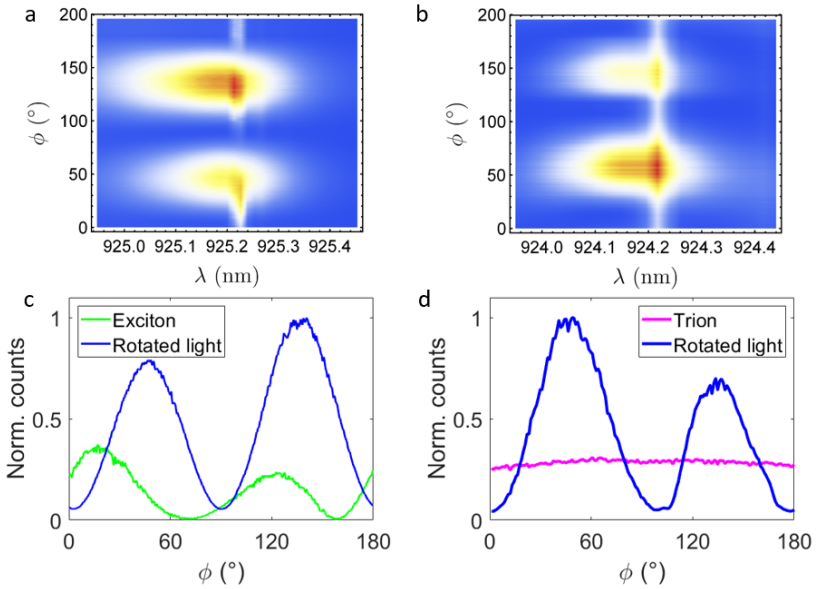


Figure 2.17: (a,b) Emission spectra measured as a function of $\phi$ for two devices: an exciton (a) and a trion (b). The broader emission lines correspond to the cavity birefringence signal, the narrower lines to the QD emission. (c) and (d) Peak intensity of the rotated light (blue) and the QD emission (green, pink) as a function of the angle $\phi$. The rotated light curve in panels (c,d) are the maximum of the broader peak in panels (a) and (b) respectively, determined by neglecting points surrounding the QD resonance. The QD trends are then estimated by taking the maximum of the narrow QD resonance and subtracting the interpolated value of the rotated light.

Figure 2.17(a) shows the emission spectra measured for the exciton, as a function of $\phi$. The fact that the cavity-rotated light spectrum is a bit more stretched on one side than on the other could be explained by different cavity linewidths ($\kappa_h \neq \kappa_v$). To show this, figure 2.18 represents the same map as in figure 2.6(b) but with different parameters, especially $\kappa_v \neq \kappa_h$.

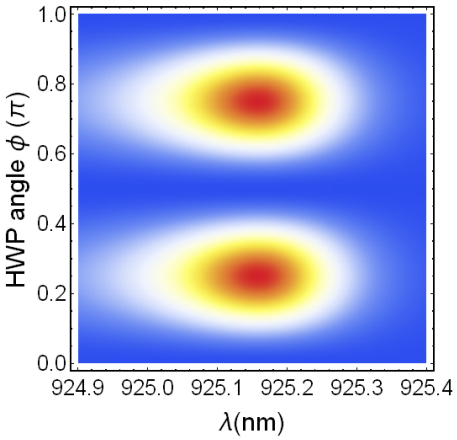


Figure 2.18: Theoretical map obtained in the same way as figure 2.6(b), with the following set of parameters: $\hbar\kappa_h = \hbar\kappa$ =500 µeV, $\hbar\kappa_v = 1.1\hbar\kappa$ =550 µeV, $\Delta_c = 0.1\kappa$, and $(\lambda_1 + \lambda_2)/2 =$ 925.2 nm. Here the intensity is plotted as a function of the wavelength on the horizontal axis, to make the comparison with the experimental figures 2.17(a) and (b) easier.

Figure 2.17(c) presents the intensity of the cavity-rotated light and the QD emission (from figure 2.17(a)) as a function of $\phi$. The emission intensity arising from the exciton resembles the squared sinusoidal dependance on $\phi$ predicted by equation (2.35). A laser polarized along one of the exciton axes $X$ or $Y$ ($\phi + \theta = 90°$ or $0°$) excites an eigenstate of the system and no emission takes place in the orthogonal polarization. The emission of the exciton thus depends on the angle between the incident polarization and the exciton axes ($\theta+\phi$). This measurement also allows to estimate $\theta$ by taking the difference between emission peaks or dips of the exciton and the rotated light. For the exciton-based device in figure 2.17, this angle is estimated to be $\theta \simeq -22° \pm 6°$. The observed deviations from the expected squared sinusoidal trends may indicate some non-orthogonality of the QD dipole axes, which can be explained by phenomena presented in subsection 1.2, or a slight misalignment when turning the HWP. Figure 2.17(b) and (d) show the same experiment and analysis on a trion-based source. The rotated light arising from the cavity has a similar squared sinusoidal dependence but the trion emission is roughly independent of $\phi$, which is consistent with the explanation from section 2.4.2.

In the end, we have shown that we can easily identify the studied transition (exciton or charged state). When turning the HWP, if the intensity of the light emitted from the QD stays constant, we can deduce that we are observing a charged state. On the contrary, if the intensity of the light shows a sinusoidal dependence on the HWP angle, then we know that we are observing an exciton. The technique also allows identifying the various important angles defining $H$, $V$, $X$ and $Y$. We now use this identification technique to study 15 sources and investigate how the source performances depend on the QD state.

## 2.5 Performance: benchmarking of sources

The structure of the sources reported here [70] are described in subsection 1.1.1. They have been designed following the *in situ* process, presented in section 1.4.2. More specifically, the layering comprises 14 (28) GaAs/AlAs Bragg pairs in the top (bottom) mirror. A 20 nm-thick

$Ga_{0.1}Al_{0.9}As$ barrier, positioned 10 nm above the QD layer, is used to increase the hole capture time inside the QD [90] as mentioned in subsection 1.1.3.
The experimental setup is still the one described in 1.5.1. Using this cross-polarization configuration, the source operation relies on the ability of the QD optical transition to generate light in a polarization orthogonal to the excitation. In this section, we show that following the optical transition under consideration (exciton or trion), the performance of a single-photon source is significantly different due to the substantial differences in the emission process, that were described in the previous section.

### 2.5.1 Presentation of the devices

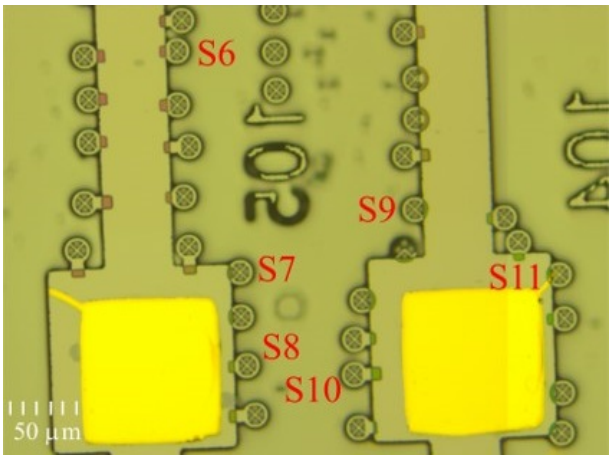


Figure 2.19: Optical microscope image of a sample under study. Labels refer to the source numbering used hereafter in the benchmarking.

We report sources from five samples (labelled from A to E) fabricated from the same 2-inch wafer grown by MBE, allowing to process QDs with similar properties even before selection. Each sample contains 15 to 30 sources. Only a few sources were investigated on samples A to C and all sources were investigated on samples D and E. Among the studied sources, we selected those giving a first lens brightness (see subsection 1.5.4) greater than 5%. For samples D and E, 6 and 4 sources passed this criteria respectively, corresponding to 20 to 25% of sources per sample. In total, fifteen sources were selected. The labels in figure 2.19 show the corresponding sources for sample D.

### 2.5.2 Measurement protocol

The sources are operated under resonant excitation in order to obtain the highest degree of quantum purity. For each source, we determine the voltage maximizing the brightness and then measure not only the figures of merit defining each source performance (single-photon purity, indistinguishability and brightness), but also the emission wavelength and temporal profile, that are critical characteristics for large-scale fabrication of identical sources.

All figures of merit are reported using $\pi$-pulse excitation [153] with 15 ps pulses at a repetition rate of 81 MHz. See Appendix C for $g^{(2)}$ and HOM histograms for each source. The characteristics of a given source in different figures have been measured under the same conditions.

### 2.5.3 Results and interpretation

We now present the main quantum properties of the fifteen selected devices.

#### Emission wavelength

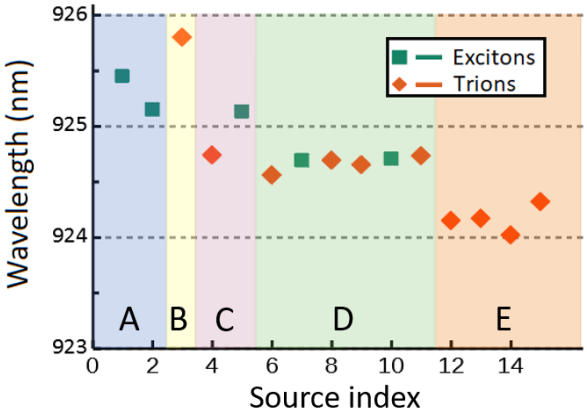


Figure 2.20: QD emission wavelength, measured when the sources were tuned for maximum brightness. The green squares represent sources based on excitons; the orange diamonds sources based on trions.

The source operation wavelength is a key parameter for scalability. The typical inhomogeneous broadening of the InGaAs QDs spectrum is around 30 nm. However, this variation is reduced when we implement the *in situ* lithography since we select QDs in a small spectral range and fabricate pillars with the correct diameter to match the QD resonance, as described in section 1.4.2. Figure 2.20 shows the QD emission wavelength at maximal brightness. We observe an average wavelength of 924.7 nm with a standard deviation of 0.5 nm. The operation wavelength of each device has been stable after more than 10 cooling cycles over their lifetime of 3 years. The samples studied come from different locations of the same wafer. When considering sources from a given sample, which means from the same area of the original wafer, the standard deviation is substantially reduced with 0.06 nm for sample D and 0.12 nm for sample E, showing the high degree of control provided by the *in situ* lithography. The fact that the average wavelength of the QDs varies from one location of the initial wafer to another comes from the epitaxial growth process implemented in the C2N cleanroom. The different molecular beams come with different angles with respect to the wafer. Thus, although we make the wafer spin to homogenize the thickness of the different component layers across it, the wafer is not perfectly invariant by translation in the plane. In industrial epitaxy growth systems, the fabrication process would increase the yield of sources operating at the same

wavelength.

The QD wavelengths reported in figure 2.20 were not optimized with the aim of getting a high wavelength homogeneity but to have the maximum brightness. We could have reached a higher spectral homogeneity by shifting the QD wavelength using the Stark tuning. With modest applied voltages it is easy to tune the QD wavelength on the order of 0.1 nm. Tuning the QD wavelength by about 0.06 nm would only lead to a small reduction to the brightness since the typical spectral width of the cavity is about 0.2 nm.

**Single-photon purity**

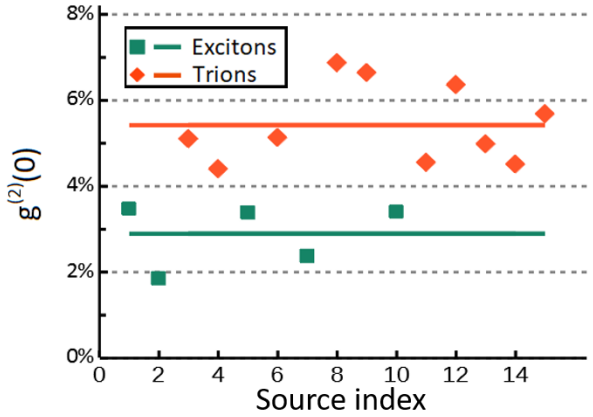


Figure 2.21: Second-order correlation values $g^{(2)}(0)$, characterizing the single-photon purity, measured when the sources were tuned for maximum brightness. The green squares represent sources based on excitons; the orange diamonds sources based on trions. The horizontal solid lines show the mean value for each type of source. The excitons present an average $g^{(2)}(0)$ of $2.89 \pm 0.74\%$ and the trions present an average $g^{(2)}(0)$ of $5.42 \pm 0.92\%$.

Figure 2.21 shows the $g^{(2)}(0)$ values of the sources, with an average of $4.6 \pm 1.5\%$. The principle of that measurement is described in section 1.5.5. We note that the single-photon purity $(1-g^{(2)}(0))$ is systematically higher for excitons than for trion sources. This can be understood by comparing the different emission processes for each source type in cross-polarization (shown in figure 2.8 and figure 2.13). Since the emission from the exciton through the $H$ mode of the cavity is delayed compared to the excitation pulse, the probability that the QD gets re-excited afterwards is low because the excitation pulse is over. In the case of a trion, the emission process in cross-polarization begins on the same timescale as the pulse and so there is a higher probability of re-excitation of the transition within the same excitation pulse, leading to the emission of a second photon [47, 154]. We will study this more in detail in Chapter 3.

### Indistinguishability


Figure 2.22: Measured visibility V of the photons (smaller points) and single-photon indistinguishability $M_s$, measured when the sources were tuned for maximum brightness. The green squares represent sources based on excitons; the orange diamonds sources based on trions. The horizontal solid lines show the mean value of indistinguishability for each type of source.

Figure 2.22 shows the visibility of the HOM interference between two consecutive single photons emitted with a 12 ns delay, as well as the single-photon indistinguishability. The description of the setup used to measure the visibility is given in section 1.5.6, as well as the definition of the interference visibility and total mean wavepacket overlap. The single-photon indistinguishability is computed from the visibility following the formula $M_s = (V + g^{(2)}(0))/(1 - g^{(2)}(0))$ [77]. We will detail the full justification for this expression in Chapter 3. The quantity $M_s$ is limited by inherent decoherence processes of the emitter rather than non-zero $g^{(2)}(0)$. The average visibility of the various sources is $83.4 \pm 4.3\%$. Their mean wavepacket overlap is quite homogeneous, with an average value of $88.0 \pm 3.1\%$ corresponding to an average single-photon indistinguishability of $92.2 \pm 2.6\%$. Note that this indistinguishability is obtained without spectral filtering and thus it includes the contribution from the phonon sideband, which is partially suppressed by the cavity funneling effect [142, 155]. The excitons present an average visibility of $87.8 \pm 1.4\%$, a total mean wavepacket overlap of $90.7 \pm 1.1\%$ and a single-photon indistinguishability of $93.4 \pm 1.1\%$. The trions present an average visibility $81.2 \pm 3.4\%$, a total mean wavepacket overlap of $86.6 \pm 2.9\%$ and a single-photon indistinguishability of $91.6 \pm 2.9\%$. The slightly lower indistinguishability values of the sources from sample E are likely due to a higher temperature on that chip (around 10–11 K instead of 7 K). The higher temperature increases the rate of phonon-induced decoherence processes. When neglecting sources from sample E, we find that there is no significant difference between the single-photon indistinguishability of exciton and trion sources at 7 K. These observations also show that, despite a very different temporal structure of the single-photon wavepacket in the case of excitons, the coherence is highly preserved in the frequency domain over the emission process.

**First lens brightness**

| QD | 1 | 2 | 3 | 4 | 5 | 6 | 7 | 8 | 9 | 10 | 11 | 12 | 13 | 14 | 15 |
|---|---|---|---|---|---|---|---|---|---|---|---|---|---|---|---|
| **Fibered single photon rate (MHz)** | 5.7 | 2.3 | 8.9 | 6.6 | 5.0 | 4.3 | 3.3 | 5.0 | 2.8 | 2.8 | 2.8 | 6.0 | 6.7 | 2.3 | 5.5 |

Figure 2.23: Extracted single-photon rates at the output of a single-mode fiber, deduced using a $\sim 30\%$ efficient single-photon detector.

The measurement is performed by plugging the output single-mode fiber into a single-photon detector, as described in 1.5.4. The table in figure 2.23 presents the fibered single-photon rates obtained by dividing the detected count rates by the efficiency of our silicon based avalanche photodiode (30% detection efficiency at ~925 nm).

| Element | Transm. | Uncert. |
|---|---|---|
| Cryostation glasses | 0.954 | 0.010 |
| Objective | 0.865 | 0.022 |
| Waveplates | 0.992 | 0.001 |
| PBS | 0.881 | 0.013 |
| 5 mirrors | 0.981 | 0,010 |
| Telescope | 0.941 | 0.006 |
| Collimator + collection fiber | 0.65 | 0.05 |
| Total | 0.43 | 0.04 |

Table 2.1: Transmission coefficients and uncertainties for elements of the collection line.

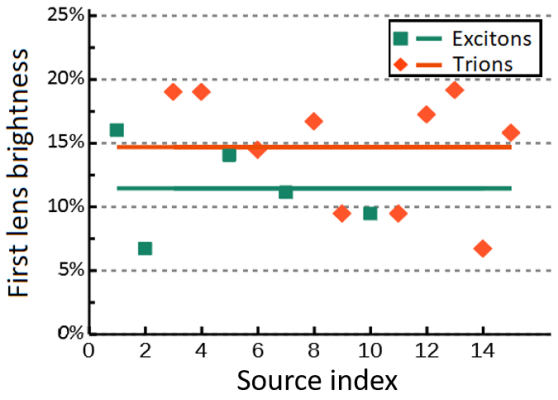


Figure 2.24: First lens brightness, measured when the sources were tuned for maximum brightness. The green squares represent sources based on excitons; the orange diamonds sources based on trions. The horizontal solid lines show the mean value for each type of source. The excitons present an average first lens brightness of $11.5 \pm 3.7\%$ and the trions present an average first lens brightness of $14.7 \pm 4.6\%$.

The first lens brightness is obtained by correcting the values from table 2.23 by the transmission losses of the setup, presented in table 2.1, and dividing by the repetition rate of the excitation laser. The results are presented in figure 2.24. The average first lens brightness is $13.6 \pm 4.4\%$. There is a big variation in brightness from pillar to pillar. For exciton-based sources, the difference is mainly due to the variation in $\theta$ and FSS, which significantly affect the source brightness in cross-polarization as described in section 2.3.3, and are not controlled during the growth process. For trion-based sources the variation is most likely due to the occupation probability, or the proportion of time that the QD spends in the desired charge state, which can vary from device to device. The average first lens brightness of exciton-based sources is lower than the one of trion-based sources, which can be explained by the emission dynamics described earlier. The typical values of FSS we measure for the excitons limit the $\eta_{\text{pol}}$ factor in the definition of the brightness, whereas $\eta_{\text{pol}}$ is just equal to 1/2 for the trion-based sources. Note that when using equation (2.28) with the set of parameters $\{\eta_{\text{top}} = 85\%, \gamma = 0.6\,\mu\text{eV}, g = 17\,\mu\text{eV}, \kappa = 500\,\mu\text{eV}, \omega_{xy} = 8\,\mu\text{eV}, \theta = 22.5°\}$, we obtain a first lens brightness of 14.9%, which is within the uncertainty of the average first lens brightness restricted to exciton-based sources given in figure 2.24, namely $11.5 \pm 3.7\%$. I chose $\theta = 22.5°$ because it is the average value between 0° that would correspond to a 0-brightness and 45° that would correspond to a maximum brightness. These two extreme values $\theta = 0°$ and $\theta = 45°$ give a first lens brightness of 0% and 29.8% respectively. Then we expect exciton-based sources brightness to go from 0% to 29.8% in this configuration, depending on the value of $\theta$. For our devices based on trions, we expect a maximum brightness of $\beta\eta_{\text{top}}/2 = 34\%$ in a cross-polarized setup with nearly degenerate cavity modes. This is a lot higher than the average first lens brightness of $14.7 \pm 4.6\%$ for trions given in figure 2.24, which can be explained by several reasons that are developed in the next section.
The obtained brightness values were on par with state-of-the-art values using a 0.45 NA collection objective, at the beginning of my PhD, in 2018. When the lab was moved from Marcoussis to Palaiseau in 2018, the cleanroom stopped working and with the pandemic only restarted end of 2020. We did not make any new sample for almost 3 years.

**Temporal wavepacket profiles**

To obtain identical remote single-photon sources, the temporal profile of the single-photon wavepackets is another important feature to consider. The physics explained above about the different time dynamics of the emission for excitons and trions in a cross-polarized setup shows that the challenges are different for the two types of sources.
All the different excitons studied in this work show a FSS value ranging roughly from 5 to 10 µeV. I have shown in section 2.3 that their emission temporal profile is governed by this FSS value as well as the asymmetry in the couplings of the QD to the cavity modes. This adds extra challenges to the fabrication of identical sources, although many tools have been developed in the last few years to get control over both the FSS [156] and the cavity birefringence [146]. We propose a new way of controlling the FSS in Chapter 4.

These complex features are circumvented when one considers sources based on a trion. As we can see in figure 2.25, the temporal profiles of trion-based sources are more likely to overlap, with an average decay time of 171 ps and a standard deviation of 27 ps (see

figure 2.25). The variations in the decay time from device to device arises from variation of the Purcell effect, considering that the QD-cavity detuning is set to maximize the brightness and not the acceleration of spontaneous emission. We estimate that the mismatch between the two trions in figure 2.25 with the most different temporal profiles (130 ps and 210 ps) would reduce the maximum accessible mean wavepacket overlap between them to 94.4%. This latter value has been obtained by applying the following formula: $M_\gamma = 4\gamma_1\gamma_2/(\gamma_1+\gamma_2)^2$ [157] with $\gamma_1 = 1/130$ ps$^{-1}$ and $\gamma_2 = 1/210$ ps$^{-1}$. Thus, the variation in trion temporal profiles will likely not be the primary limitation on the indistinguishability of remote sources in the near future.

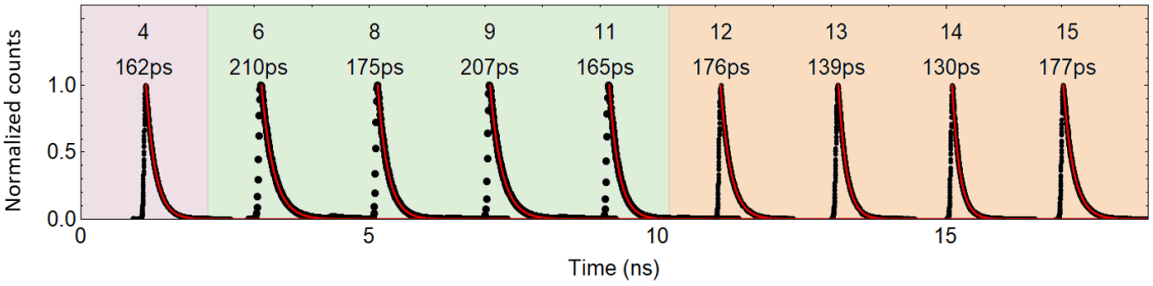


Figure 2.25: Temporal profiles of trion-based sources corresponding to the wavelengths in 2.20 that are optimized for brightness. The profiles show an average exponential decay of 171 ps with a standard deviation of 27 ps. The uncertainty in each fit is about 1 ps.

## 2.6 Discussion and perspectives

We now discuss the limitations to the source brightness, which appear as the next main challenges for our technology. As described in section 1.5.4, the single-photon brightness depends on several parameters as $\mathcal{B}_s = \beta\eta_{\text{top}}p_{\text{QD}}\eta_{\text{pol}}$ which should all be maximized. In the devices studied during this thesis, a strong limitation comes from an imperfect extraction coupling of $\beta\eta_{\text{top}} \simeq 65\%$. Moreover, the use of a cross-polarization configuration of the setup intrinsically limits $\eta_{\text{pol}}$. Finally many sources were not bright enough to be included in this benchmarking because of a non-optimal occupation probability of the QD state and the limited tuning range provided by the Stark effect. We discuss in details these various parameters.

### Degree of linear polarization $\eta_{\text{pol}}$

In the present work, we studied cavities with a small birefringence in a cross-polarization setup. We have shown that both the first lens and fibered brightness are then limited to at most 50% for trions, 9/16 for excitons, due to the rejection of photons orthogonally polarized to the collection mode. This limitation accounts for the $\eta_{\text{pol}}$ factor in the definition of the brightness, introduced in 1.5.4.

For a cavity extraction efficiency of 85% and a large enough NA, we expect a maximum first lens brightness of 34% for our devices based on trions and 30% (based on the brightness $\mathcal{B}$ calculated in section 2.3.3) for those based on excitons, in a cross-polarized setup with nearly

degenerate cavity modes. Trion-based sources with a perfect control of the occupation probability should be able to approach this 34% limit. On the other hand, bright exciton-based sources require $\theta$ close to $\pm 45°$ and a large fine-structure splitting $\omega_{xy}$ to reach the brightness limit of 30%. We present a method to control the FSS in Chapter 4, which might be used in the future to reach a higher brightness in that context.

In 2019, the limit of 1/2 (resp. 9/16) for the brightness of a single-photon source based on a trion (resp. exciton) in a cross-polarization configuration has been overcome using polarized cavities [146]. In that paper, the authors use a strongly elliptical cavity, with a 2.1 µm-long (resp. 1.4 µm-long) major (resp. minor) axis. The detuning between these two modes allow them to have two different Purcell factors, say a small one for the $V$-polarized mode and a large one for the $H$-polarized mode. The QD is excited with a $V$-polarized laser at a $\pi$-pulse power (that corresponds to a stronger pulse than in the case of an isotropic cavity) and its emission is far more enhanced in the $H$-polarized mode of the cavity, which is collected, than in the $V$-polarized one. This strategy allows to go from a 50% loss due to polarization in the case of nearly circular micropillars to a 3.8% loss only.

Another method to excite the QDs has been developed and is now routinely used by our team. A diagram of its principle is shown in figure 2.26. It consists in using longitudinal acoustic phonon-assisted excitation [158–161]. The excitation laser is set at an energy which is the sum of the QD energy and the energy of one longitudinal acoustic phonon. This method allows us to filter the reflected excitation laser in wavelength instead of in polarization. To reach a high polarized brightness, the excitation is now polarized along one of a neutral exciton's axes, leading to a near-unity polarization for the emission. Using this approach, we can overcome the $\eta_{\text{pol}}$ brightness limitation due to polarization filtering, in addition to no longer requiring a FSS larger than the decay rate for exciton-based sources. We obtained 51% first lens brightness [162] with source 5 from the benchmarking study outlined in this chapter, compared to the 15% presented here using resonant excitation.

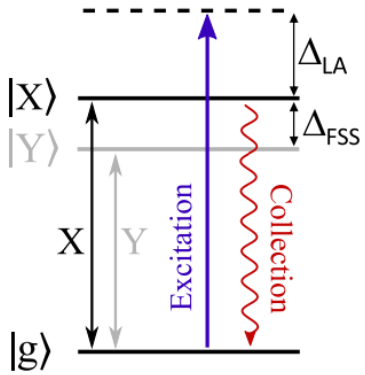


Figure 2.26: schematic showing the principle of longitudinal acoustic phonon-assisted excitation. Figure taken from [162].

### Extraction efficiency $\eta_{\text{top}}$

The extraction efficiency, corresponding to the $\eta_{\text{top}}$ factor in the brightness definition, is intrinsic to the cavity and is very similar for all pillars ($\sim 80-90\%$). This value is due to leakage of photons through the arms of the wheel-shaped device (see figure 1.17(a)) or through the vertical edge of the pillars. It can also be due to absorption losses in the doped layer designed to apply the voltage. A detailed study of these various effects is under way within the postdoc of Thi Huong Au and PhD of Mathias Pont.

### Occupation probability and QD-cavity detuning

The average first lens brightness is further affected by the trion and exciton occupation probabilities $p_{\text{QD}}$. In our case, the occupation probability of the various QD states (empty QD or charged QD) depends on two parameters.

- One of them is the applied voltage. However, this parameter is also used to control the detuning between the QD and the cavity. Hence, the voltage that is chosen to tune the QD in resonance with the cavity mode is unlikely to also be the optimal one for the chosen charge state. This results in a large majority of devices with a reduced brightness. This issue could be solved if the wavelength of the charge state corresponding to the voltage maximizing its occupancy was known while implementing the *in situ* lithography process, described in section 1.4.2. This is an ongoing project of the team.

- The other tool is the use of a second laser, detuned from the resonance. This second approach is used in [91] where the authors use a CW laser at 901 nm wavelength to control the occupation probability of source numbered 3 in this Chapter, reaching a $33 \pm 5\%$ first lens brightness, which is higher than the one displayed in figure 2.24 for the same pillar (around 19%). However, the brightness of source 3 given in [91] was measured in a setup where the excitation laser was not as well filtered as in the setup used to measure the data presented in 2.24. Consequently, the corresponding single-photon purity and indistinguishability were worse. For this study, we chose a set of data where the brightness was lower but where the single-photon purity and the indistinguishability were better.

Even if we knew the exact wavelength of the QD charge state before etching, the diffraction of the green spot on the photo-resist leads to a typical error of 200 nm in the pillar diameter control. Also, a residual strain relaxation during the etching can deviate the cavity mode energy from the expected one by typically 0.5 nm. Compensating the subsequent cavity-QD detuning by applying a voltage can then move the state away from its optimal wavelength and lead to a reduction of the occupation probability. New methods for mask lithography fabrication were developed based on direct laser writing and allowing to reach nanoscale precision on the designed microstructures [163, 164].

### Truncation of the single-photon beam by the objective

For the measurements shown in the benchmarking section, we used a long-distance microscope objective with a numerical aperture of 0.45 placed outside the cryostat. The spatial truncation of the beam caused by this objective leads to a deformation of the wavefront which reduces the coupling into the single-mode fiber by 50 to 60%. Marie Billard, PhD student in Quandela, showed that installing a high NA lens into the cryostat itself allows to strongly increase the fibered brightness [165].

**To sum up**

We have studied how the micropillar cavities birefringence impacts the single-photon sources operation under resonant excitation, investigated two different transitions in QDs (trions and excitons) and their emission's characteristics in a cross-polarization setup. We have benchmarked 15 single-photon sources based on semiconductor QDs for which we determined their optimal operation wavelength, single-photon purity, indistinguishability, fibered brightness (for all the sources), and temporal profiles (for the trion-based sources). By deterministically etching tailored cavities around the QDs, we are able to obtain a large number of sources with highly homogeneous properties, an important step towards scalability. We have finally discussed various paths for further optimization.

# Chapter 3

# Hong-Ou-Mandel interference with imperfect single photon sources

For many quantum technologies, single photons with a high degree of indistinguishability are needed. This is the case for quantum repeaters [166, 167] for example, that are necessary to counter the optical losses when the photons go through fibers for secure long-distance communications. Many quantum repeater protocols require Bell state measurements based on the quantum interference of identical photons. Logical photon-photon gates in the framework of linear optical computing [168, 169] also exploit their quantum interference. It is thus of crucial importance to be able to precisely measure the indistinguishability of the light wavepackets generated by our devices, as we did in the benchmarking presented in section 2.5.3. To quantify the indistinguishability of single-photon wavepackets, we usually perform a Hong-Ou-Mandel (HOM) interference [132], as described in section 1.5.6. Two indistinguishable single photons incident at each input of a 50:50 beam splitter will exit the beam splitter together, resulting in no two-photon coincidental detection events at both outputs. When the single photons only exhibit partial indistinguishability described by a non-unity mean wave-packet overlap $M$ (that is also defined as the single-photon trace purity [170, 171]), coincidental detection events are detected at the outputs and reduce the HOM interference visibility. In such case, the interference visibility $V_{\mathrm{HOM}}$ gives direct access to the single-photon indistinguishability, $M = V_{\mathrm{HOM}}$ [171].

For realistic sources, the wavepackets arriving at the beam splitter generally contain multi-photon components that are quantified by the second order intensity autocorrelation at zero time delay $g^{(2)}$, defined in section 1.5.5. These multi-photon components reduce the measured visibility of HOM interference, since the cases where two photons arrive on the same input of the beam splitter have a 1/2 probability of ending up on different detectors, increasing the probability of coincidental detection. Even for an ideal single-photon indistinguishability (corresponding to $M = 1$), the HOM interference does not show a 100% visibility if $g^{(2)}$ is non-zero. In most cases and in particular for QD based sources, the multi-photon component of the photonic wavepacket depends on the system parameters in a manner that is completely independent of the single photon indistinguishability. To understand the physics at play in our single-photon sources and improve their performance, it is critical to be able to access the single-photon indistinguishability from the measured HOM interference visibility, knowing the

single-photon purity.

It has been shown that the mean wavepacket overlap of the total input state $M_{\mathrm{tot}}$ (including multi-photon components) is linked to the visibility of the HOM interference by $V_{\mathrm{HOM}} = M_{\mathrm{tot}} - g^{(2)}$ [133, 171, 172]. This formula, that we derived in section 1.5.6, can only be used to estimate the indistinguishability of the single-photon part of the wavepacket in the limited case where the additional photons are in the same spectral and temporal mode as the predominant ones [173–175]. In section 3.2, we discuss how to access the single-photon indistinguishability from the HOM interference visibility, knowing the single-photon purity. We limit the present study to the case where the additional photons are separable from the main single-photon wavepacket. We distinguish two limit cases, namely where the extra-photons that reduce the single-photon purity are distinguishable from or identical to the main stream of single-photons. In section 3.3, I show how we emulated the different cases. Then we identify the origin of the imperfections for a source based on a trion and on an exciton, and apply the relevant formula to correctly extract their intrisic single-photon indistinguishability $M_s$, in sections 3.4.1 and 3.4.2 respectively.

## 3.1 Position of the problem

When a source shows a non-zero $g^{(2)}$, the visibility of its HOM interference is reduced since the two detectors can detect coincidences even if the photons are indistinguishable. This phenomenon is taken into account by the community, but no consensus had been found so far about how to proceed. Indeed, in the literature for QD based single-photon sources, different correction factors have been used to account for an imperfect $g^{(2)}$. Some use $M = V_{\text{HOM}} + g^{(2)}$ [135, 155], others use $M = V_{\text{HOM}} + 2g^{(2)}$ [70, 146], and some use $M = V_{\text{HOM}} \times (1 + 2g^{(2)})$ [176].

Knowing the visibility of the HOM interference $V_{\text{HOM}}$ and the normalized second-order intensity correlation function $g^{(2)}$ for a given source single-photon stream allows us to access the mean wavepacket overlap of the state exiting the collection setup, using equation (1.96). In this chapter, we differentiate the total state mean wavepacket overlap, that is the one of the whole collected state (after losses) and that we write $M_{\text{tot}}$, from the mean wavepacket overlap of the single-photon component at the source that we write $M_s$. This is relevant because it is $M_s$, not $M_{\text{tot}}$, that tells us about the severity of various dephasing mechanisms impacting the single-photon source. In addition, the multi-photon components that increase $g^{(2)}$ do not come exclusively from the source, but may also arise from imperfect excitation laser rejection. If any of these unwanted photons, or noise photons, do not have a good mean wavepacket overlap with the single-photon component, which we define as $M_{sn}$, then they inevitably contribute to a reduced measurement of $M_{\text{tot}}$.

This project was conducted in close collaboration with Dr. Stephen Wein under the supervision of Pr. Christoph Simon, from the University of Calgary. In particular, the model on which this work was based and that is presented in section 3.2 was developed by Dr. Stephen Wein. It is possible to derive the final formula from the Schödinger picture as we did in reference [77]. Here we present the derivation using the Heisenberg formalism as in section 1.5.

## 3.2 Relation between visibility and source mean wavepacket overlap

The aim of this section is to derive a theoretical expression of the single-photon indistinguishability as a function of the measured quantities, namely the HOM interference visibility and the single-photon purity.

The first step of the model is to build the imperfect "single-photon" state ($g^{(2)} > 0$) by mixing a true single photon ($g^{(2)} = 0$) with a small amount of separable noise using a beam splitter, as shown on the left part of figure 3.1. This assumption is valid when the noise is not correlated with the main single-photon stream. The annihilation operators in the various modes of the beam splitter are defined as $\hat{a}_s$, $\hat{a}_r$, $\hat{a}_n$ and $\hat{a}_t$ for "*single photons*", "*reflected*", "*noise*" and "*transmitted*" respectively. This approach allows us to consider that the additional photons leading to $g^{(2)} \neq 0$ may not be in the same temporal mode as the

main single photon. We limit our analysis to small $g^{(2)}$ values so that the noise field itself is well-approximated by an optical field with at most one additional photon and a large vacuum contribution. This restriction to a weak, separable noise field is relevant in practice for many single-photon sources, as discussed later.

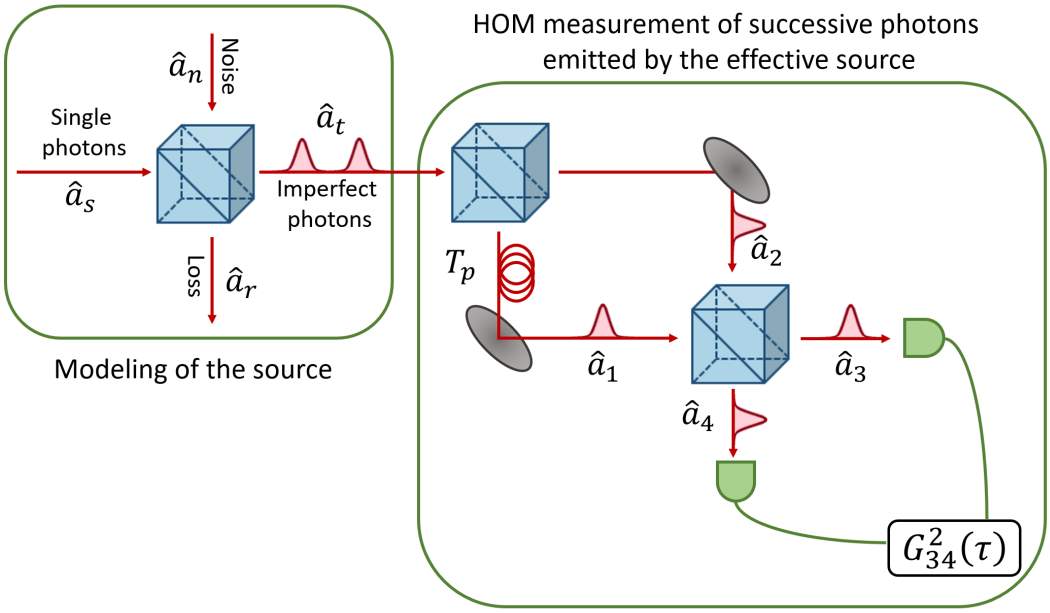


Figure 3.1: Diagram depicting the HOM measurement of an imperfect single photon modeled by separable noise added to a perfect single photon.

We now calculate the total mean wavepacket overlap $M_{\text{tot}}$ and $g^{(2)}$ of these imperfect single photons, and use equation (1.96) to deduce the visibility.

In section 1.5.6, we derived the following general relation between the mean wavepacket overlap of a state, that we write here $M_{\text{tot}}$ and its $g^{(2)}$:

$$V_{\text{HOM}} = M_{\text{tot}} - g^{(2)} \tag{3.1}$$

**Expression of the first order correlation of the imperfect photon**

$M_{\text{tot}}$ is given by:

$$M_{\text{tot}} = \frac{1}{\mu^2} \iint |G^{(1)}_{\text{tot}}(t,\tau)|^2 dt d\tau \quad \text{where} \quad G^{(1)}_{\text{tot}}(t,\tau) = \langle \hat{a}^\dagger_t(t+\tau)\hat{a}_t(t)\rangle \tag{3.2}$$

where $\mu$ is the average number of photons from the source, defined in section 1.5.4. The beam splitter that mixes the stream of single photons with the noise photons is characterized by the following matrix relation:

$$\begin{pmatrix} \hat{a}_t(t) \\ \hat{a}_r(t) \end{pmatrix} = \begin{pmatrix} \cos\theta & -\sin\theta \\ \sin\theta & \cos\theta \end{pmatrix} \begin{pmatrix} \hat{a}_s(t) \\ \hat{a}_n(t) \end{pmatrix} \tag{3.3}$$

where $\theta$ is the parameter that determines the amount of additional noise photons added to the single photons. Then we can expand:

$$\begin{aligned}G^{(1)}_{\text{tot}}(t,\tau) &= \langle \hat{a}^\dagger_t(t+\tau)\hat{a}_t(t)\rangle \\ &= \cos^2\theta\langle \hat{a}^\dagger_s(t+\tau)\hat{a}_s(t)\rangle - \cos\theta\sin\theta\left(\langle \hat{a}^\dagger_s(t+\tau)\hat{a}_n(t)\rangle + \langle \hat{a}^\dagger_n(t+\tau)\hat{a}_s(t)\rangle\right) + \sin^2\theta\langle \hat{a}^\dagger_n(t+\tau)\hat{a}_n(t)\rangle\end{aligned} \tag{3.4}$$

We make the separable noise approximation so that cross-correlations between signal and noise can be separated into coherence terms. For example $\langle \hat{a}^\dagger_s(t+\tau)\hat{a}_n(t)\rangle \simeq \langle \hat{a}^\dagger_s(t+\tau)\rangle\langle \hat{a}_n(t)\rangle$. We assume that there is no single-photon coherence so that these terms vanish: $\langle \hat{a}^\dagger_s(t+\tau)\rangle \simeq \langle \hat{a}_n(t)\rangle \simeq 0$. This assumption was also used to derive equation (3.1). Thus:

$$G^{(1)}_{\text{tot}}(t,\tau) = \cos^2\theta G^{(1)}_s(t,\tau) + \sin^2\theta G^{(1)}_n(t,\tau) \tag{3.5}$$

Taking the square of the absolute value, we get:

$$|G^{(1)}_{\text{tot}}(t,\tau)|^2 = \cos^4\theta|G^{(1)}_s(t,\tau)| + 2\cos^2\theta\sin^2\theta\ \text{Re}\left(G^{(1)}_s(t,\tau)G^{(1)}_n(t,\tau)\right) + \sin^4\theta|G^{(1)}_n(t,\tau)| \tag{3.6}$$

**Expression of the second order correlation function of the imperfect photon**

We now determine the expression of the second-order correlation of the total built wavepackets. We showed in section 1.5.5 that:

$$G^{(2)}_{\text{measure}}(t,\tau) = \frac{1}{4}G^{(2)}_{\text{tot}}(t,\tau) = \frac{1}{4}\langle \hat{a}^\dagger_t(t)\hat{a}^\dagger_t(t+\tau)\hat{a}_t(t+\tau)\hat{a}_t(t)\rangle \tag{3.7}$$

We make the same separability approximation as for $M_{\text{tot}}$. Here, we assume the signal and noise are uncorrelated and have no single-photon coherence in the number basis. We also assume there is no two-photon coherence, so that the terms $\langle \hat{a}^\dagger_s(t)\hat{a}^\dagger_s(t+\tau)\rangle\langle \hat{a}_n(t+\tau)\hat{a}_n(t)\rangle$ and $\langle \hat{a}^\dagger_n(t)\hat{a}^\dagger_n(t+\tau)\rangle\langle \hat{a}_s(t+\tau)\hat{a}_s(t)\rangle$ vanish. We are left with the following cross terms:

$$\begin{aligned}G^{(2)}_{\text{tot}}(t,\tau) = {}& \cos^4\theta\langle \hat{a}^\dagger_s(t)\hat{a}^\dagger_s(t+\tau)\hat{a}_s(t+\tau)\hat{a}_s(t)\rangle + \cos^2\theta\sin^2\theta\langle \hat{a}^\dagger_s(t)\hat{a}_s(t+\tau)\rangle\langle \hat{a}^\dagger_n(t+\tau)\hat{a}_n(t)\rangle \\ &+ \cos^2\theta\sin^2\theta\langle \hat{a}^\dagger_s(t)\hat{a}_s(t)\rangle\langle \hat{a}^\dagger_n(t+\tau)\hat{a}_n(t+\tau)\rangle + \sin^2\theta\cos^2\theta\langle \hat{a}^\dagger_n(t)\hat{a}_n(t)\rangle\langle \hat{a}^\dagger_s(t+\tau)\hat{a}_s(t+\tau)\rangle \\ &+ \sin^2\theta\cos^2\theta\langle \hat{a}^\dagger_n(t)\hat{a}_n(t+\tau)\rangle\langle \hat{a}^\dagger_s(t+\tau)\hat{a}_s(t)\rangle + \sin^4\theta\langle \hat{a}^\dagger_n(t)\hat{a}^\dagger_n(t+\tau)\hat{a}_n(t+\tau)\hat{a}_n(t)\rangle\end{aligned} \tag{3.8}$$

We can now apply our assumption that both the signal and the noise are single photons so that $G^{(2)}_s = G^{(2)}_n = 0$, making the first and last terms vanish. The second and fifth terms are conjugate. By recognizing the average photon number detected per unit of time $N_i(t) = \langle \hat{N}_i(t)\rangle = \langle \hat{a}^\dagger_i(t)\hat{a}_i(t)\rangle$ as well as the first order correlation functions $G^{(1)}_i(t,\tau) = \langle \hat{a}^\dagger_i(t+\tau)\hat{a}_i(t)\rangle$ where $i \in \{s,n\}$, we obtain finally:

$$G^{(2)}_{\text{tot}}(t,\tau) = \cos^2\theta\sin^2\theta\left(N_s(t)N_n(t+\tau) + N_n(t)N_s(t+\tau) + 2\ \text{Re}\left(G^{(1)}_s(t,\tau)G^{(1)*}_n(t,\tau)\right)\right) \tag{3.9}$$

**Average photon number $\mu$**

The average photon number detected per unit of time is given by:

$$N_{\text{tot}}(t) = \langle \hat{a}_t^\dagger(t)\hat{a}_t(t)\rangle = \cos^2 N_s(t) + \sin^2\theta N_n(t) \tag{3.10}$$

The average photon number $\mu$ of the input into the Mach-Zehnder interfometer is then:

$$\mu = \int N(t)dt = p_{1,s}\cos^2\theta + p_{1,n}\sin^2\theta \tag{3.11}$$

since we assume the signal and noise are single photons, and where $p_{1,i} = \int N_i(t)dt$ for $i \in \{s, n\}$.

**Linking $g^{(2)}$ and $M_{\text{tot}}$**

Integrating equations (3.9) and (3.6) over $t$ and $\tau$ and normalizing by $\mu$, we have that:

$$\mu^2 g^{(2)} = 2p_{1,s}p_{1,n}\cos^2\theta\sin^2\theta(1 + M_{sn}) \tag{3.12}$$

and

$$\mu^2 M_{\text{tot}} = p_{1,s}^2\cos^4\theta M_s + 2p_{1,s}p_{1,n}\cos^2\theta\sin^2\theta M_{sn} + p_{1,n}^2\sin^4\theta M_n \tag{3.13}$$

where

$$M_{sn} = \frac{1}{p_{1,s}p_{1,n}}\iint \text{Re}\left(G_s^{(1)}(t,\tau)G_n^{(1)*}(t,\tau)\right)dtd\tau \tag{3.14}$$

and

$$M_i = \frac{1}{p_{1,i}^2}\iint |G_i^{(1)}(t,\tau)|^2 dtd\tau \quad \text{where} \quad i \in \{s, n\} \tag{3.15}$$

$M_{sn}$ quantifies the mean wavepacket overlap between the noise photons and the single photons, and $M_s$ (resp. $M_n$) is the mean wavepacket overlap of the single (resp. noise) photons with themselves.

We can reparametrize by defining $\eta$ so that:

$$\begin{aligned}\cos^2\eta &= \frac{p_{s,1}\cos^2\theta}{p_{s,1}\cos^2\theta + p_{n,1}\sin^2\theta} \\ \sin^2\eta &= \frac{p_{n,1}\sin^2\theta}{p_{s,1}\cos^2\theta + p_{n,1}\sin^2\theta}\end{aligned} \tag{3.16}$$

Using equations (3.1), (3.12) and (3.13), the new expressions of the visibility and $g^{(2)}$ can be derived:

$$\begin{aligned}V(\eta) &= M_s\cos^4\eta\ + M_n\sin^4\eta\ - 2\cos^2\eta\ \sin^2\eta \\ g^{(2)}(\eta) &= 2(1 + M_{sn})\cos^2\eta\ \sin^2\eta\end{aligned} \tag{3.17}$$

We are interested in solving for the visibility $V$ to first order in $g^{(2)}$. Since they are implicitly dependent through the parameter $\eta$, we can look at how the parametric curve

$\{g^{(2)}(\eta), V(\eta)\}$ approaches $g^{(2)}(0) = 0$. First, it is clear that for $\eta = 0$, we have $V(0) = M_s$, as expected. Second, the slope of this parametric curve in the limit of small $\eta$ is given by:

$$\lim_{\eta \to 0} \frac{dV(\eta)}{dg^{(2)}(\eta)} = -\frac{1 + M_s}{1 + M_{sn}} \tag{3.18}$$

Finally:

$$\boxed{V_{\mathrm{HOM}} = M_s - \left(\frac{1 + M_s}{1 + M_{sn}}\right) g^{(2)}} \tag{3.19}$$

This formula shows that the relation between the visibility and the single-photon indistinguishability depends on the overlap between the additional noise and the single photon.

**Case of an unbalanced beam splitter**

When the beam splitter used to implement the HOM interference measurement is not perfectly balanced, we need to use expression (1.98) instead of expression (1.96), with $M = M_{\mathrm{tot}}$. In that case equation (3.19) becomes:

$$V_{\mathrm{HOM}} = 4RT \left(1 + M_s - \left(\frac{1 + M_s}{1 + M_{sn}}\right) g^{(2)}\right) - 1 \tag{3.20}$$

where $R$ and $T$ are the reflection and transmission coefficients of the beam splitter respectively.

**Limiting cases**

In particular, it is instructive to look at the two following extreme cases:

- If the additional photons are identical to the single photons, i.e. $M_{sn} = M_s$, then equation (3.19) reduces to the simple case that $V_{\mathrm{HOM}} = M_s - g^{(2)}$, showing that the total and single photon mean wavepacket overlaps coincide, $M_s = M_{\mathrm{tot}}$.

- On the contrary, if the noise has no overlap with the single photons and $M_{sn} = 0$ , then the visibility is further reduced and given by $V_{\mathrm{HOM}} = M_s - (1 + M_s)\, g^{(2)}$.

How the HOM interference is affected by a non-zero $g^{(2)}$ therefore depends on the origin of the additional photons. In the next section, we will test experimentally the two limiting cases of equation (3.19) described above.

## 3.3 Experimental study of the limiting cases

We now test this theory by building artificial sources. We prepare a train of near-optimal single photons from one of our single-photon sources and add noise photons via a beam splitter, just like in the model. We can tune the $g^{(2)}$ of the artificial source by controlling the amount of additional photons. We can then measure the visibility $V_{\mathrm{HOM}}$ while varying $g^{(2)}$, and

see if it follows the trend predicted by the model. We experimentally create two situations corresponding to the limiting cases described above, namely $M_{sn} = 0$ and $M_{sn} = M_s$. To measure the $g^{(2)}$ and HOM interference visibility of the resultant wavepacket, we use the experimental methods presented in sections 1.5.5 and 1.5.6.

### 3.3.1 Preparation of the near-optimal sources

We start by choosing one of our single-photon sources and optimize the experimental conditions (setup alignment and voltage applied) so that the photons show high single-photon purity and indistinguishability. The source we chose is a trion corresponding to device 8 from the benchmarking of Chapter 2. After optimization we obtained for example a $g^{(2)}$ of $2.8 \pm 0.3\%$ and a HOM visibility of $86.3 \pm 0.8\%$. These values correspond to a total mean wavepacket overlap $M_{\text{tot}}$ equal to $89.1 \pm 0.9\%$. The corresponding histograms are shown in figure 3.2. The experimental setup used to prepare this main stream of nearly ideal single photons is the one described in figure 1.19. A half waveplate and quarter waveplate are used to align the polarization of the excitation pulse along one of the microcavity axes, and the single photon emission is separated from the excitation laser via cross polarization, as it was the case for the results of Chapter 2. The QD is resonantly excited, with a pulse that is derived from a 3 ps Ti-Sapph pulsed laser with a repetition rate of 81 MHz and a central wavelength at 924.9 nm.

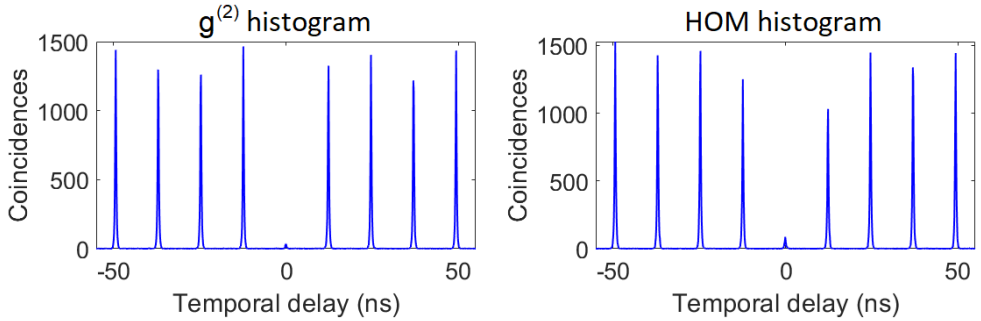


Figure 3.2: Correlation interferograms measured on the QD source used for generating the main stream of single photons. The value of $g^{(2)}$ was calculated from the left panel and $V_{\text{HOM}}$ from the right panel.

Note that in this chapter we show $g^{(2)}$ values for source 8 that are lower than the one presented in Chapter 2. In the benchmarking its $g^{(2)}$ was measured to be about 6.9 % and its HOM visibility was 81.0 %. This is because these latter values were obtained when trying to optimize the collected photon rate $\mathcal{B}$, which is not our aim here. Going slightly beyond $\pi$-pulse decreases the single-photon brightness $\mathcal{B}_s$ but increases $\mathcal{B}$ up to a certain point because multi-photon components increase $\mathcal{B}$ at the detriment of $g^{(2)}$ (see equation (1.81)).

The additional noise is prepared differently according to the limiting case under study.

### 3.3.2 Adding distinguishable photons

We first optimized the alignment on QD 8 to have the lowest $g^{(2)}$ and highest $V_{\mathrm{HOM}}$ reachable. Here we obtained a $g^{(2)}$ equal to $4.8 \pm 0.5\%$ and a HOM visibility of $V_{\mathrm{HOM}} = 84.0 \pm 1.3\%$, corresponding to $M_{\mathrm{tot}} = 88.8 \pm 1.4\%$. We then add fully distinguishable photons. To accomplish this, the broad spectrum of the 3 ps laser pulse is spread using a diffraction grating, as shown in figure 3.3(b). A narrow portion is spatially selected to use as a 15 ps resonant excitation pulse for the QD. We then select a spectrally distinct part of the laser spectrum to play the role of noise. We can see both these components on the spectrum shown in figure 3.3(a).

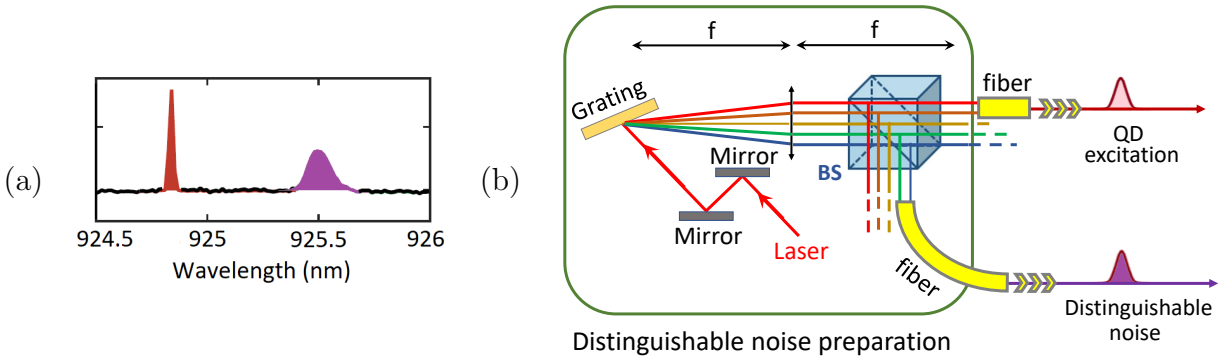


Figure 3.3: (a) Spectrum showing the QD emission (in red) and the portion of laser (in purple) added to the main stream of photons to play the role of distinguishable noise. (b) Experimental setup used to prepare the two parts of the laser: the one dedicated to the QD excitation and the one used as a distinguishable noise.

The experimental preparation of the artificial source is presented in figure 3.4. We make sure that the noise photons have the same polarization as the single-photons by using a polarizer before the beam splitter used to mix them together. A HWP upstream of this polarizer allows to control the amount of distinguishable noise we add to the single-photons, and so the artificial source's $g^{(2)}$. Finally, by appropriately tuning the time delay between the two beams, we ensure that the QD single photons and the spectrally distinguishable photons arrive at the beam splitter at the same time.

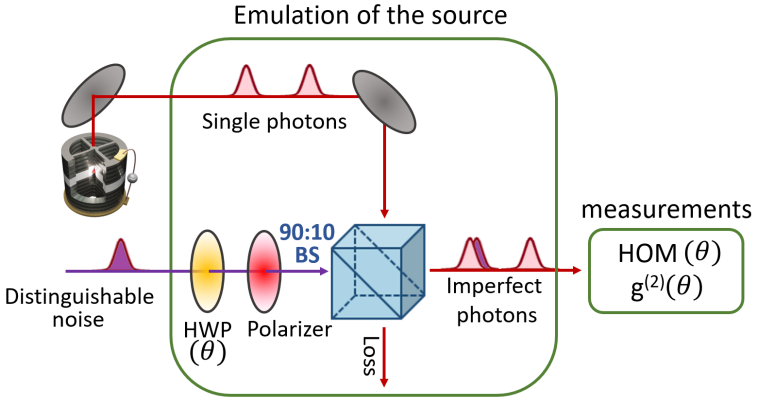


Figure 3.4: Experimental setup used to emulate an imperfect single photon source with distinguishable noise.

For different values of the HWP angle, we measure the second order intensity autocorrelation at zero time delay $g^{(2)}$ and the HOM visibility of the effective source. Since the photons emitted by the QD and the additional laser photons are spectrally distinguishable, we expect $M_{sn} = 0$, so our model predicts that $V_{\mathrm{HOM}} = M_s - (1 + M_s)g^{(2)}$.

All the correlation histograms to measure $g^{(2)}$ and $V_{\mathrm{HOM}}$ are shown in figure 3.5. As expected, the central peak rises with $g^{(2)}$, and so the visibility of the HOM interference decreases when the $g^{(2)}$ increases. We plot this evolution in figure 3.6.

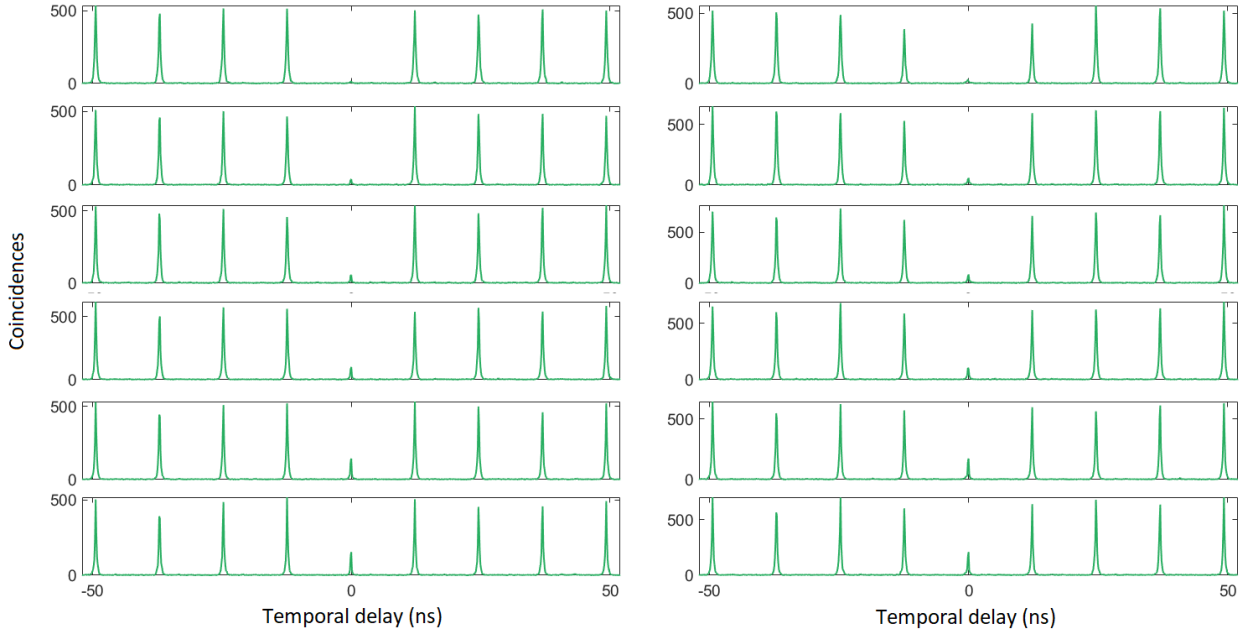


Figure 3.5: Second-order correlation histogram as a function of the delay between two detectors on the left column, and corresponding HOM interferograms on the right column. This plot corresponds to the case where distinguishable noise is added to the photons from the source.

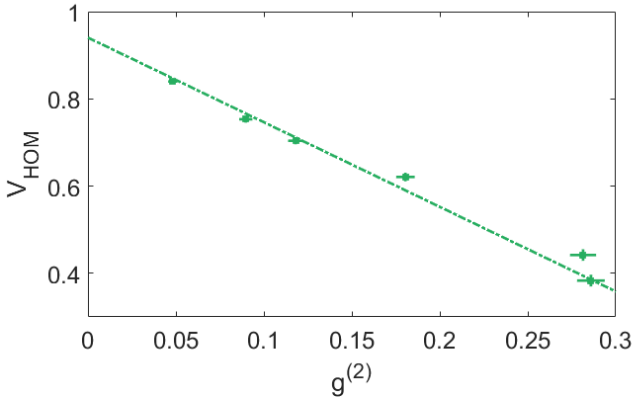


Figure 3.6: Visibility of HOM interference $V_{\mathrm{HOM}}$ measured as a function of $g^{(2)}$ in the case where distinguishable noise is added to the photons from the source. The line is the prediction from the theoretical model ($V_{\mathrm{HOM}} = M_s - (1 + M_s)g^{(2)}$, with $M_s = 0.94 \pm 0.02$).

The line in figure 3.6(b) shows that this model fits the data very well with $M_s = 0.94 \pm 0.02$. This is remarkable since $M_s$ is the only parameter that governs both the slope and the intersect of the line. This value $M_s$ is higher than the value of $M_{\text{tot}} = V_{\text{HOM}} + g^{(2)} = 88.8 \pm 1.4\%$ calculated earlier from the initial near-optimal source $g^{(2)}$ and $V_{\text{HOM}}$ values. This is because $M_{\text{tot}}$ does not take into account that the noise could be distinguishable from the "useful" single photons and thus further decreases the visibility of the HOM interference.

### 3.3.3 Adding indistinguishable photons

Here again, we add noise to a stream of single photons coming from the same QD based single photon source as in the previous subsection.

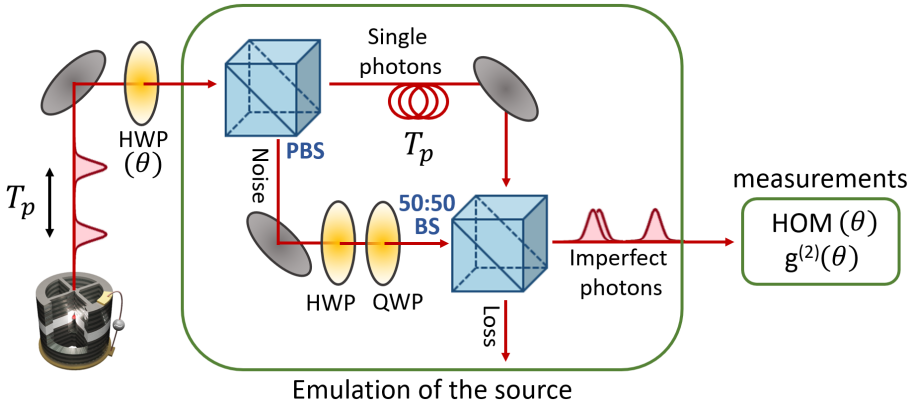


Figure 3.7: Experimental setup used to emulate an imperfect single photon source with identical noise.

To emulate the other limiting case, we build another effective source where the added photons are identical to the predominant single photon component. For that purpose, we use photons from the source itself but emitted at a different time to play the role of noise. The setup is represented in figure 3.7. More specifically, we split the stream of photons coming from the source into two beams using a polarizing beam splitter. One of these two beams is used to simulate the indistinguishable noise. We use a HWP to tune the amount of noise we want relatively to the main single-photon stream. The noise photons are delayed by the time $T_p$ between two successive excitation pulses, and their polarization is modified using a HWP and a QWP, to match the polarization of photons in the other arm. That way, when they are recombined with the main stream of photons thanks to a 50:50 beam splitter, some of them are added to pulses that already contain a single photon. Actually, since the photons from the two streams come from the same source and furthermore were emitted subsequently, they are nearly indistinguishable. They arrive at the same time at the 50:50 beam splitter where the HOM effect occurs and the two photons exit through the same output. Then there is a half probability that they exit together towards the output we measure. The artificial source's $g^{(2)}$ is increased because some of the output pulses now contain two identical photons.

Turning the first HWP allows us to tune the relative intensity of the predominant single photon pulse and the additional photons, and thus governs the $g^{(2)}$ of the output states. The

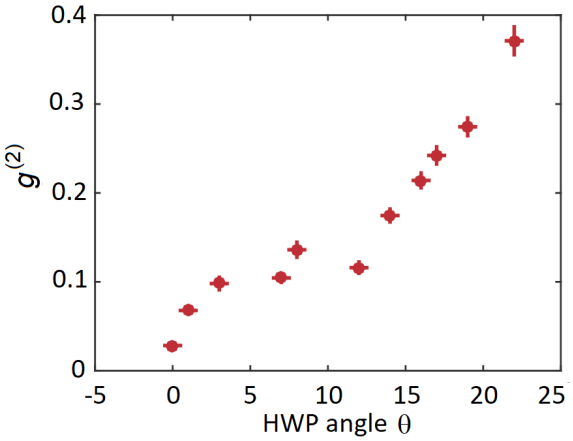


Figure 3.8: Second-order intensity correlation function $g^{(2)}$ as a function of $\theta$, the first HWP angle that governs how much noise photons we let through the PBS in figure 3.6.

evolution of $g^{(2)}$ as a function of the HWP angle is shown in figure 3.8.

By rotating the HWP over a range of about 25°, we tune the $g^{(2)}$ up to about 0.4. For each of measured value of $g^{(2)}$, we implement a HOM measurement. All the histograms are shown in figure 3.9 on the following page, ordered from the lowest value of $g^{(2)}$ to the highest. As expected, the visibility of the HOM interference decreases when $g^{(2)}$ increases.

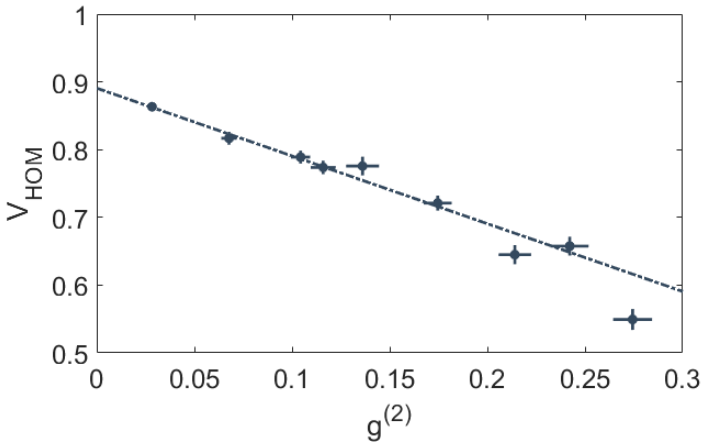


Figure 3.10: Visibility of HOM interference $V_{\mathrm{HOM}}$ measured as a function of $g^{(2)}$ in the case where identical noise is added to the photons from the source. The line is the prediction from the theoretical model ($V_{\mathrm{HOM}} = M_s - g^{(2)}$, with $M_s = 0.89 \pm 0.01$).

Figure 3.10 presents the HOM visibility as a function of $g^{(2)}$ that we tune by adding identical photons. When injecting $M_{sn} = M_s$ into equation (3.19), we get $V_{\mathrm{HOM}} = M_s - g^{(2)}$: the model predicts a linear dependence with slope of $-1$. The line in Figure 3.10 again demonstrates that the model gives a very good fit to the data, with an extracted $M_{\mathrm{s}} = 0.89 \pm 0.01$. Here we made the assumption that the noise photons are indistinguishable from the "useful" single photons, so that they do not dampen the visibility of the HOM interference as much as

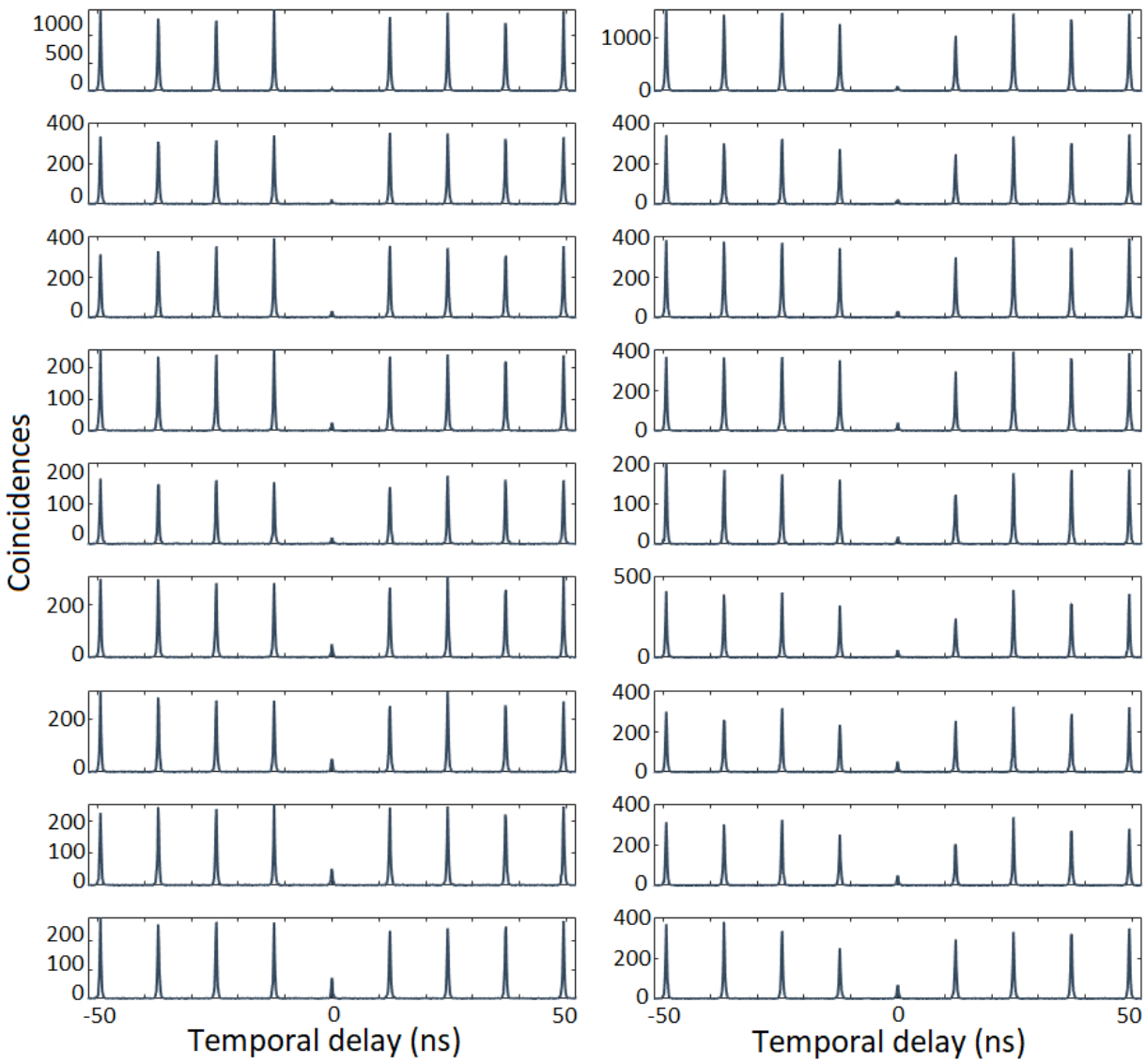


Figure 3.9: Second-order correlation histogram as a function of the delay between two detectors on the left column, and corresponding HOM interferograms on the right column. This plot corresponds to the case where indistinguishable noise is added to the photons from the source.

distinguishable noise photons would have. In that case, we have $M_s = M_{\text{tot}}$, which is coherent with the value of $M_{\text{tot}}$ equal to 87.9 % calculated in section 3.3.1 from the values of $g^{(2)}$ and $V_{\text{HOM}}$ given in the benchmarking of Chapter 2 from this source.

This value of $M_s$ is different from the one obtained in the previous subsection, since we made a different assumption for the origin of the noise. Which one we should retain depends on the nature of the actual noise causing the $g^{(2)}$ of emission from the QD. More specifically, if the noise that causes the lowest $g^{(2)}$ value we obtain is distinguishable (resp. indistinguishable) from the "useful" single photons, then we retain that $M_s = 0.94 \pm 0.02$ (resp. $M_s = 0.89 \pm 0.01$).

### 3.3.4 Discussion

We gathered the two curves obtained adding either distinguishable or indistinguishable noise on the same graph in figure 3.11.

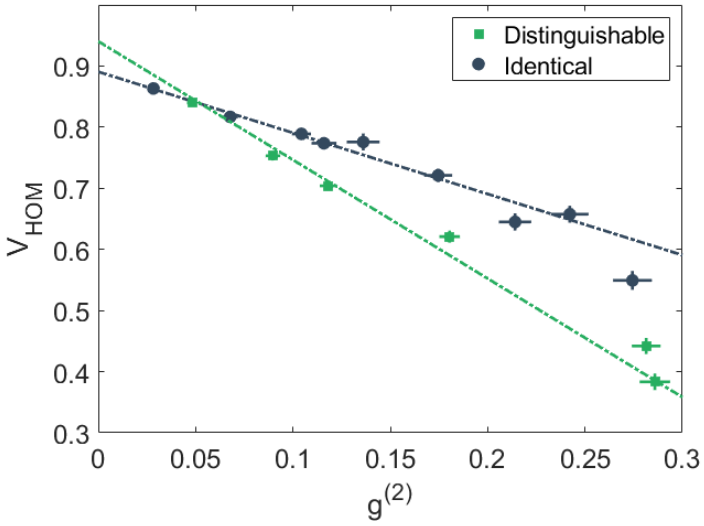


Figure 3.11: Visibility of HOM interference, $V_{\text{HOM}}$ measured as a function of $g^{(2)}$ for distinguishable (green squares) and identical (black circles) noise sources. The lines are the predictions from the theoretical model.

The extracted values of $M_s$ given by the intercepts of the curves with the vertical axis ($g^{(2)} = 0$) in the two cases represent the upper and lower bound of the intrinsic single photon indistinguishability of the QD single-photon source used in these measurements. Indeed, we know that if the unwanted emission increasing the $g^{(2)}$ is distinguishable (resp. indistinguishable) from the single-photons, then $M_s = 0.94 \pm 0.02$ (resp. $M_s = 0.89 \pm 0.01$). It is then crucial to know the origin of the unwanted photon emission in order to be able to extrapolate the data back to $g^{(2)} = 0$. In the following, we discuss how to properly estimate the single photon indistinguishability for exciton and trion-based single-photon sources.

## 3.4 Application to our single-photon sources

As shown in chapter 2, the optical selection rules and photon emission processes differ significantly between the excitons and trions, which lead to a different origin of the multi-photon component. Then, it could be necessary to adapt the formula we apply to each case to retrieve the single-photon mean wavepacket overlap $M_s$ from the measured quantities $g^{(2)}$ and $V_{\mathrm{HOM}}$.

### 3.4.1 Trion-based sources

#### Origin of the multi-photon components

The description of a trion is shown in 2.2. We recall that it is a four-level system, made of two ground states and two excited states. The two ground states contain one charge each, with opposite spins. The two excited states contain an electron-hole pair with an extra charge each, with opposite spins as well. The optical selection rules entail that the two excited states decay to (resp. are reached from) the two ground states by emitting (resp. receiving) circularly polarized photons, with opposite directions according to the spins involved. Thus, linearly polarized light like we use in our experimental setup excites the ground state whatever its spin is, and the emission in the crossed polarization is instantaneous. This is why in a cross-polarized setup, the single photon emission shows a rapid rise time and mono-exponential decay as we saw in figure 2.8. Since the single photon emission process is fast, there is a chance that the photon gets emitted during the laser pulse. In that case, the system is back in its ground state while the pulse has not finished, so it can be excited a second time and emit another photon. In paper [177] from Fischer *et al*, the authors give a plot (see figure 3.12) showing the probability of two-photon emission when the excitation is realized by a $\pi$-pulse excitation for a two-level system. The red area shows that a first photon can be emitted soon enough within the excitation pulse to leave time for another excitation and thus give rise to another photon emission. Therefore, re-excitation is the primary origin of a non-zero $g^{(2)}$ for a trion-based source.

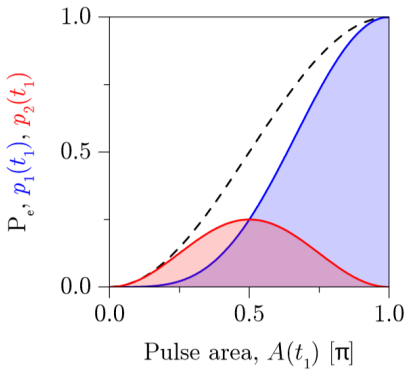


Figure 3.12: Re-excitation dynamics for a two-level system under interaction with an extremely short $\pi$-pulse. This plot was extracted from reference [177]. The abscissa variable $A(t_1)$ is the integrated pulse area, that increases when $t_1$ increases and reaches $\pi$ when the pulse ends. $P_e$ is the probability that the system is in the excited state if no emissions occur, $p_1(t_1)$ is the probability density to have a single photon emission at time $t_1$ and $p_2(t_1)$ is the probability density to have a pair of photon emission beginning at time $t_1$.

To experimentally confirm this, we study the evolution of $g^{(2)}$ at maximum emitted photon rate for a QD source based on a trion, whilst varying the duration of the excitation pulse from 3 ps up to 25 ps, using the 4-f setup shown in figure 1.18 in Chapter 1. To achieve even longer pulses, an etalon is used to spectrally filter the laser spectrum even further so that pulse durations up to 80 ps can be achieved. This experiment was carried out with the same source as the one we used in the previous section, namely source 8 from the benchmarking of Chapter 2. The results are presented in figure 3.13.

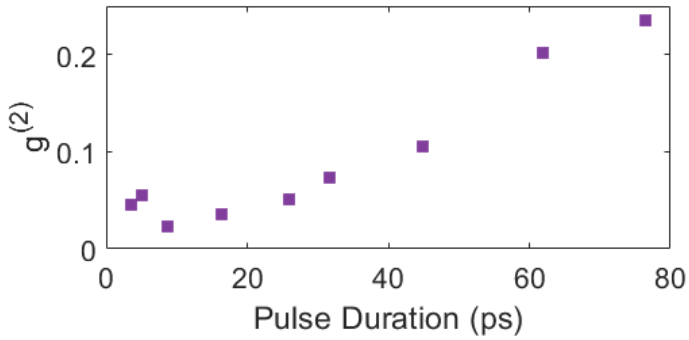


Figure 3.13: Measured $g^{(2)}$ for a source based on a trion as a function of the excitation pulse duration at $\pi-$pulse. The error bars are within the size of the plotted points.

As expected, we see that when the pulse duration increases, the reexcitation becomes more and more probable, increasing its $g^{(2)}$.

We notice that the single-photon purity degrades for very short pulses. The extra photons that increase the $g^{(2)}$ in this case actually come from the portion of laser that is not properly rejected in polarization by the polarizing beam splitter in the collection setup. The intensity of that portion of laser is proportional to the number of photons sent to excite the QD, and the shorter the excitation pulse is, the more photons we need to send to reach $\pi$-pulse. To simplify the explanation, we consider a square pulse of duration $\tau_P$ and the laser power is chosen so that $\Omega_R \tau_P = \pi$ to maximize the excitation probability. We have seen in the section about Rabi oscillations with power, in section 1.3.3, that the Rabi frequency $\Omega_R$ is proportional to the square root of the excitation pulse power $P$. We have then that the excitation pulse power is proportional to $1/\tau_P^2$. The total energy per pulse, that is given by $\tau_P \times P$, is then proportional to $1/\tau_P$. Hence for very short pulses ($< 10$ ps), more photons are needed to reach $\pi$-pulse and the $g^{(2)}$ is limited by imperfect suppression of the excitation laser. Sources based on trions are limited by re-excitation for pulses longer than 15 ps.

### Example of determination of indistinguishability

In this section, we increase the $g^{(2)}$ of the same trion-based single-photon source by tuning the main parameter that is responsible for the multi-photon component, namely the probability of re-excitation. For each measured value of $g^{(2)}$, we measure the visibility of the HOM interference as well. By deliberately introducing noise with the same origin as that which

limits the $g^{(2)}$, we ensure that we can extrapolate the relationship between $g^{(2)}$ and $V_{\mathrm{HOM}}$ to values below the lowest $g^{(2)}$ that we can measure.

Here we identified the main source of multi-photon components to be the re-excitation of the QD during the laser pulse. We then measured the $g^{(2)}$ and the HOM visibility for a set of different pulse durations, from 15 ps to 50 ps, at $\pi$-pulse. The results are shown in figure 3.14.

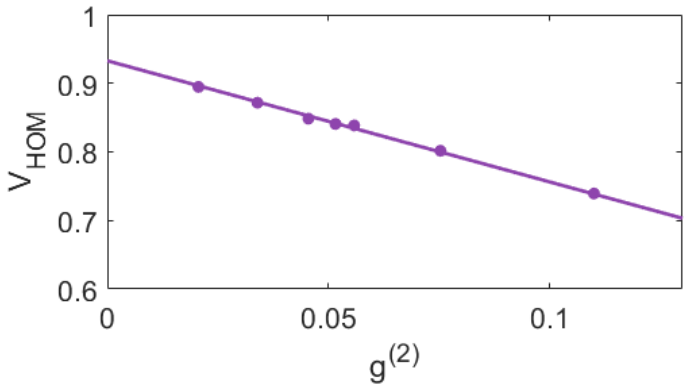


Figure 3.14: Measured HOM visibility as a function of the $g^{(2)}$ for a trion source as the pulse duration is increased. The solid line gives the theoretical prediction for these data. The error bars are within the size of the plotted points.

Since the extra photon is necessarily emitted during the laser pulse for re-excitation to occur [177], we can assume that it is temporally distinguishable from the main single photon emission that typically takes place after the laser pulse with the trion radiative decay time of approximately 170 ps. This noise is thus expected separable and distinguishable. We apply equation (3.19) to fit our observations and we find $M_s = 0.93 \pm 0.01$ and $M_{sn} = 0.09 \pm 0.02$, indicating that the overlap between the noise photons and the single photons from the QD is indeed very low. If we fit the data using the distinguishable noise model ($M_{sn} = 0$) we extract a single parameter $M_s = 0.94 \pm 0.01$, which is very close to the value extracted using equation (3.19).

### 3.4.2 Exciton-based sources

#### Origin of the multi-photon components

An exciton is described by a three level system (see figure 2.11), where the excitation pulse creates a superposition of the two excitonic linear dipoles with an energy difference given by the fine-structure splitting [178]. The temporal wavepacket profile is shown in figure 2.13: we see a beating due to the time-dependent phase between the two exciton eigenstates, with a period related to the fine structure splitting [76, 179]. The optical selection rules imply that the single photon emission in cross polarization happens mostly after the excitation pulse is over, leading to a very small probability of collecting two photons via re-excitation. This implies that the $g^{(2)}$ for the exciton-based source is likely dominated by imperfect laser rejection, rather than re-excitation.

Here again, just like we did for the trion, we vary the pulse duration and measure the obtained $g^{(2)}$ from a source based on an exciton. More precisely, we used source 10 from the benchmarking of Chapter 2. The results are shown in figure 3.15.

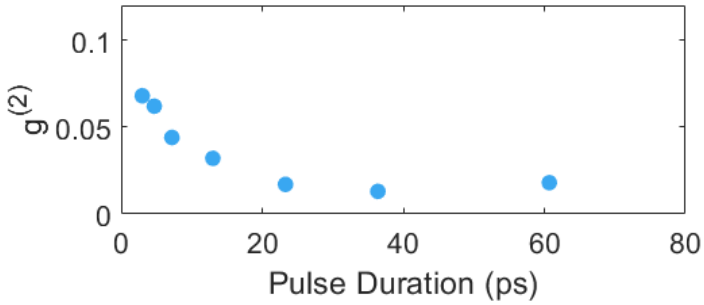


Figure 3.15: Measured $g^{(2)}$ for a source based on an exciton (source 10 from the benchmarking of Chapter 2) as a function of the excitation pulse duration at $\pi-$pulse. The error bars are within the size of the plotted points.

As expected, we see that when the pulse duration increases, the exciton-based source keeps showing a low $g^{(2)}$ for pulse durations higher than 20 ps. Any extra photon that would increase $g^{(2)}$ is emitted during the laser pulse and is rejected by the laser filtering of the setup because of its polarization. For the same reasons as in the case of the trion, the single-photon purity degrades for very short pulses. This remains the dominant source of an imperfect $g^{(2)}$ for exciton sources up to a pulse duration of 80 ps.

**Example of determination of indistinguishability**

For the exciton-based source, we found that laser photons that are not rejected by the collection setup are responsible for the non-zero value of $g^{(2)}$. It is thus by purposely adding laser photons to the single photon emission from the QD that we are able to tune the $g^{(2)}$ in this case. There are two available ways to do so. First, we can decrease the pulse duration which means that we require more power to reach $\pi$-pulse, and therefore there is a higher probability of detecting a laser photon. Second, we can slightly rotate the quarter waveplate (QWP) of the excitation pulse (see Figure 1.19), so that the excitation polarization is no longer perfectly aligned along one of the polarization axes of the cavity. The light then experiences a polarization rotation due to the birefringence of the cavity, described in section 2.1.4. Some fraction of the excitation pulse will now be collected in the orthogonal polarization with the single photons. By adjusting the QWP we can tune the amount of laser photons we collect. We use these two methods to vary the $g^{(2)}$ of two different exciton-based sources: the decrease of the pulse duration on source 10 and the QWP rotation on source 7 from the benchmarking of Chapter 2. In each case we acquire a set of couples $\{g^{(2)}, V_{\mathrm{HOM}}\}$ to see how the multiphoton-component affects the HOM interference. The data is shown in figure 3.16.

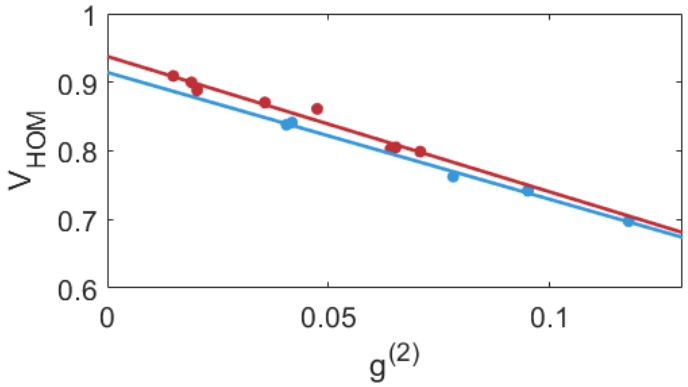


Figure 3.16: Measured HOM visibility as a function of the $g^{(2)}$ for exciton sources. The $g^{(2)}$ is increased by two different methods consisting of either decreasing the pulse duration of the excitation pulse (red), or decreasing the suppression of the excitation laser (blue). The two methods are performed on different exciton sources (sources 10 and 7 respectively). The solid line gives the theoretical prediction for these data. The error bars are within the size of the plotted points.

We use equation (3.19) to fit the data. We extract $M_s = 0.94 \pm 0.01$ (resp. $M_s = 0.91 \pm 0.01$) and $M_{sn} = -0.02 \pm 0.09$ (resp. $M_{sn} = 0.03 \pm 0.06$) for the case where we change the pulse duration (resp. degree of polarization extinction). In both cases, the extracted value of $M_{sn}$ is equal to zero within error. This was expected since there is very little temporal overlap between the noise from the laser and the single photons, as we can see in figure 2.13. We note that the two data sets were performed on different excitons (sources 7 and 10 from the benchmarking of Chapter 2) which explains the slight difference in $M_s$ of the two devices.

## 3.5 Conclusion

In this chapter, we revisited the use of the visibility of the Hong-Ou-Mandel interference to determine the single-photon indistinguishability for imperfect sources. We proposed a reliable method to take into account for the first time the nature of the noise that increases the multi-photon component. Then, we studied the origin of that noise in our sources. Despite their different physical origins, we find that the multi-photon component of both exciton and trion-based sources can be treated as separable distinguishable noise. In the limit of low $g^{(2)}$, the single photon indistinguishability can thus be obtained using:

$$M_{\mathrm{s}} = \frac{V_{\mathrm{HOM}} + g^{(2)}}{1 - g^{(2)}}. \tag{3.21}$$

In the case where the beam splitter where the HOM interference occurs is unbalanced, we use equation (3.20) and obtain that the equation should be adapted as follows:

$$M_s = \frac{V_{\mathrm{HOM}} + 4RT(1 + g^{(2)}) - 1}{4RT(1 - g^{(2)})} \tag{3.22}$$

where $R$ and $T$ are the reflection and transmission coefficients of the beam splitter respectively. This formula allows us to extract the single-photon indistinguishability $M_s$ of a single-photon source from the measurement of its visibility of HOM interference and knowing its single-photon purity. $M_s$ gives the upper bound to the indistinguishability that could be achieved with an ideal experimental setup and fundamentally quantifies how temporally coherent the source itself is. We now use this correction for our sources, as we did for the benchmarking in Chapter 2. Although the overall mean wavepacket overlap is what matters for setting up efficient quantum technologies, this understanding is necessary to quantify the intrisic indistinguishability of the single photons from the source and identify the next challenges towards an ideal one. For both the exciton and trion-based sources we experimented on in this chapter, the extracted single-photon indistinguishability $M_s$ is approximately equal to 0.93. The residual distinguishability, which is not due to a non-zero $g^{(2)}$, is due to phonon-induced decoherence such as phonon-assisted emission into the phonon sideband, or pure dephasing of the zero phonon line. We underline here that, as compared to reference [70], the cavities under study show a lower Q and hence a lower filtering of the phonon sideband. Values closer to 1 can be obtained using an additional etalon.

Recently, our team explored a new technique to increase the source efficiency, consisting of using longitudinal acoustic phonon-assisted excitation [162]. In that configuration, we collect the emitted light without rejecting any polarization so the source brightness is increased by a factor of 2 when exciting an exciton along one of its intrisic polarizations. There is no longer a delay between the excitation and the emission in the case of sources based on excitons. Then we expect that the noise will be temporally distinguishable from the main single photons stream, similarly to the case of resonantly excited trion-based sources. The formula 3.21 will still apply.

Finally, we note that the model developed in section 3.2 of this chapter should be applied to QD-based single-photon sources in general. This implies that some research group mentioned in section 3.1 underestimated the "corrected" indistinguishability of their sources [135, 155]. Our approach is also applicable beyond the scope of QDs and applies to many other types of single quantum emitters, whether the residual $g^{(2)}$ arises from imperfect laser filtering or re-excitation. In some cases, it is also applicable to single-photon sources based on non-linear optical frequency conversion. The non-zero $g^{(2)}$ in sources based on SPDC is either due to imperfect suppression of the pump laser or to multi-photon pair generation. In the first case, our model can be applied because the laser is separable and distinguishable from the single photons. However, for multi-photon pair generation, we need to distinguish two configurations characterized by their joint spectral intensity. This latter can be defined as the two-dimensional probability distribution associated with signal and idler emission frequencies [180] and carries information about their correlations. If the source is single-mode, i.e. its joint spectral intensity between the signal and the idler photons is separable, then the generation of two {signal+idler} pairs in the same excitation pulse gives a two-photon Fock state where the two photons are identical and separable. This can be repoduced by the beam splitter model presented here via photon-bunching, and hence the separable noise model with indistinguishable noise photons applies. In the second scenario, the source is multi-mode and its joint spectral intensity is correlated. In that case, the signal and idler photons are entan-

gled in a given degree of freedom. The detection of the idler photon projects the signal photon into a mixed state of all possible modes, leading to a low visibility of the HOM interference even if the $g^{(2)}$ is low. Similarly, if two pairs are generated in the same pulse, the two signal photons will not necessarily be in the same mode and our model does not apply in principle. Such a situation requires further theoretical investigation.

**To sum up**
We have revisited the HOM experiment for imperfect single-photon sources. We have both theoretically and experimentally shown that the nature of the noise (indistinguishable or distinguishable) strongly modifies the impact on the HOM visibility. We have then applied this general study to the specific cases of an exciton and trion-based single-photon sources showing that the distinguishable noise model should be adopted. This study refines the diagnostic tools that we use to improve the performances of our single-photon sources.

# Chapter 4

# Controlling the symmetry of a quantum dot via remote electric potentials

Quantum dots have been shown to be reliable for the generation of single-photons, which are basic elements for the implementation of optical quantum networks as well as quantum processors. We have seen in Chapter 1 that QDs usually show an in-plane asymmetry that leads to a fine structure splitting when it contains an exciton. The brightness of single-photon sources based on excitons depends on this parameter, thus tuning the FSS would allow one to reach a higher brightness from excitons in a cross-polarization setup. Moreover, our team recently demonstrated that an excitation scheme based on LA phonon assisted excitation allows for reaching high brightness and indistinguishability. This scheme allows for collecting the single photons in all polarization directions and make use of the exciton FSS for the generation of frequency-encoded qubits. Another characteristic that makes QDs very attractive is their ability to produce on-demand polarization entangled photon pairs via the biexciton-exciton radiative cascade [52]. The photons are entangled when the excitonic fine structure splitting is reduced to less than the photons linewidth. Entangled photon pairs are highly sought after to realize quantum repeaters [181] and quantum relays [54] as well as quantum teleportation. Again, bright sources of entangled photon pairs can be obtained using individual epitaxial semiconductor QDs in microcavity structures [63]. Developing tools to control the FSS of an exciton thus appears essential for multiple applications.

Over the past years, several techniques have been proposed to tune the excitonic fine structure splitting [182], including rapid thermal annealing [183], mechanical strain [184], magnetic or electric fields [185, 186] or strain manipulation [187, 188] among others. The aim is to restore the $D_{2d}$ symmetry of the quantum dot. Later on, it was shown that it is possible to eliminate the fine structure splitting by combining the use of large strains and/or electric fields along the three directions of space [189]. This led to generation of entangled photon pairs with a record fidelity [190]. To the best of our knowledge, such a control has not been implemented for QDs that are coupled to a cavity so far. In this chapter, we present a new technique that we developed to control the exciton fine structure splitting based on the use of three electrical knobs that allow us to manipulate the electric field at the position of the

dot in the three dimensions of space. In this case, the voltages needed are much lower than the ones required for piezoelectric strain (about $10^2$ less). Moreover, this control is applied to QDs in microcavities, which would simultaneously allow for a high brightness by taking advantage of the Purcell enhancement of the radiative transitions.

The chapter is organized as follows. We first detail the motivations of this work by describing the potential applications of fine structure splitting tuning. Then we give an overview of the state of the art in FSS control. In a third section, we present the principle of the technique we propose. We then present simplified simulations with COMSOL that allow exploring the physics behind our approach, in section 4. We then present our experimental study and demonstrate an electrical control of the exciton FSS for QDs in pillar cavities. We finally discuss the quality of the generated photons and remaining challenges.

## 4.1 Motivation

As briefly introduced, controlling the FSS of an exciton offers many possibilities. Under resonant excitation, it allows to maximize the single-photon source brightness as shown in 2.3.3. For many years now, QDs with zero FSS have been explored to generate entangled photon pairs. Most recently, using a slightly detuned excitation, our group showed that the FSS can be exploited to generate frequency-polarization hyper-encoded qubits. Since the first application has been discussed in Chapter 2, I briefly present the last two motivations below.

### 4.1.1 Entangled photon pairs via a biexcitonic cascade

A QD can confine a biexciton made of two electron-hole pairs coupled by the Coulomb interaction and sharing the same ground state. As the biexciton decays, it cascades first to the exciton state before reaching the ground state, emitting two photons of different energy. There are two possible cascades that take the system to the ground state, as we can see in figure 4.1.

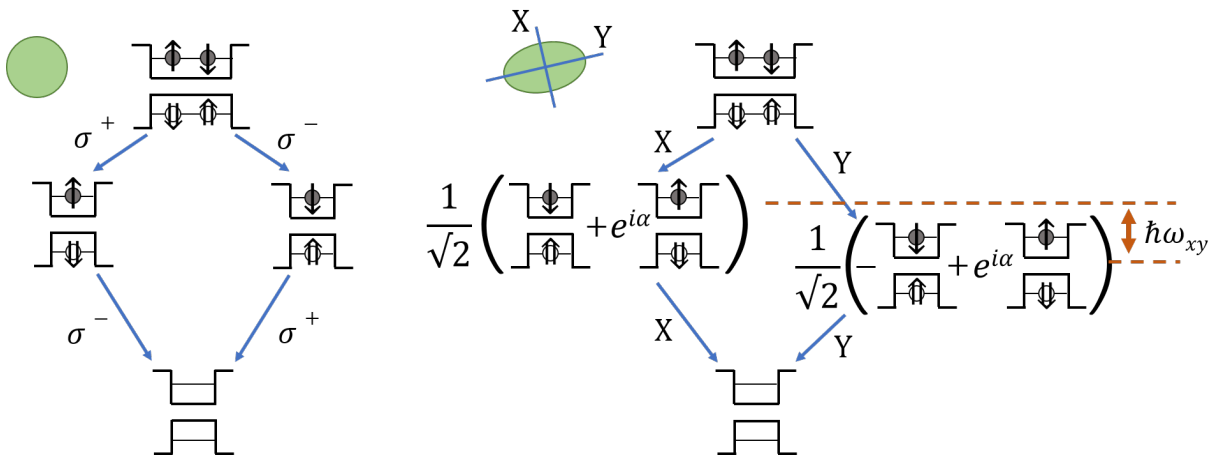


Figure 4.1: Diagram showing the optical selection rules for a biexciton in two cases: a zero FSS on the left panel, and a non zero FSS on the right panel. $\alpha$ and $\alpha'$ depend on the shape anisotropy and strain of the QD. In the absence of strain, $\alpha = 2\theta_d$ (see section 1.2 from Chapter 1).

We can distinguish two configurations for the biexciton cascades depending on the exciton symmetry. These two configurations give rise to different polarizations for the emitted photons when the recombinations take place. We detail these two cases that allow understanding of what gives rise to entanglement for one of them. We restrict ourselves to the cases where there is no heavy-/light-hole mixing.

#### Case of a symmetric exciton wavefunction

If the exciton wavefunction has a $D_{2d}$ or higher symmetry (see Appendix A), the intermediate excitonic states are degenerate. These states either correspond to:

- the eigenstate we referred to as $|\psi_{\mathrm{HH}}^{+1}\rangle$ in Chapter 1, namely a pair composed of a $J_z = +3/2$ heavy-hole and a $J_z = -1/2$ electron (case where the other pair, $J_z = -3/2$ heavy-hole and the $J_z = +1/2$ electron recombined first),
- the eigenstate we referred to as $|\psi_{\mathrm{HH}}^{-1}\rangle$ in Chapter 1, namely a pair composed of a $J_z = -3/2$ heavy-hole and a $J_z = +1/2$ electron (reverse order of recombinations).

We can describe these two cases in terms of annihilation operators as introduced in reference [185]. They correspond respectively to $\hat{a}_{+1}\hat{a}_{-1}$ and to $\hat{a}_{-1}\hat{a}_{+1}$ where $\hat{a}_{\pm 1}$ is the annihilation of the $|\psi_{\mathrm{HH}}^{\pm 1}\rangle$ bright exciton, appearing in the recombination of the electron-hole pair and allowing for the emission of a photon. In QDs, excitons behave like fermions and respect Pauli exclusion principle: two excitons cannot occupy the same quantum state (the biexciton does not have twice the energy of the exciton). Then we have that $\hat{a}_{+1}\hat{a}_{+1} = 0$ and $\hat{a}_{-1}\hat{a}_{-1} = 0$, but $\hat{a}_{+1}\hat{a}_{-1} \neq 0$ and $\hat{a}_{-1}\hat{a}_{+1} \neq 0$. The total angular momenta of these states are respectively $M = +1$ and $M = -1$. Then, a first recombination giving rise to a $\sigma^+$-polarized (resp. $\sigma^-$-polarized) photon has to be followed by a $\sigma^-$-polarized (resp. $\sigma^+$-polarized) photon. The emitted light state is then:

$$|\psi\rangle = \frac{1}{\sqrt{2}}(|\sigma^+\sigma^-\rangle + |\sigma^-\sigma^+\rangle) \tag{4.1}$$

$|\psi\rangle$ is a Bell state that shows perfect correlation for the polarization of the two photons. The circular polarization is usually chosen as a convention to describe the generated state, like in figure 4.1. But actually for degenerate exciton states, it can be re-written in any basis. For example in the $\{|H\rangle, |V\rangle\}$ basis where $|\sigma^+\rangle = \frac{1}{\sqrt{2}}(|H\rangle + i\,|V\rangle)$ and $|\sigma^-\rangle = \frac{1}{\sqrt{2}}(|H\rangle - i\,|V\rangle)$, we have:

$$|\psi\rangle = \frac{1}{\sqrt{2}}(|HH\rangle + |VV\rangle) \tag{4.2}$$

a state that also shows perfect correlation in linear polarization. However, the quantum correlation in circular polarization is not maintained when an FSS is introduced, whereas a classical correlation between $|H\rangle$ and $|V\rangle$ is maintained with a large FSS. The correlations in the circular basis are then usually used to demonstrate entanglement.

**Case of an exciton wavefunction with low degree of symmetry**

If the exciton wavefunction has a symmetry lower than $D_{2d}$, the electron-hole exchange interaction mixes the bright exciton states into a non-degenerate doublet, as shown in section 1.2. Recall that the two states of this doublet can be written:

$$\begin{aligned} &\frac{1}{\sqrt{2}}(|\psi_{\mathrm{HH}}^{+1}\rangle + e^{i\alpha}\,|\psi_{\mathrm{HH}}^{-1}\rangle) \\ &\frac{1}{\sqrt{2}}(-\,|\psi_{\mathrm{HH}}^{+1}\rangle + e^{i\alpha'}\,|\psi_{\mathrm{HH}}^{-1}\rangle) \end{aligned} \tag{4.3}$$

where $\alpha$ (resp. $\alpha'$) is the polarization angle of the photon emitted first in the cascade through the top (resp. bottom) eigenstate, with respect to an arbitrary direction. Let us write $\beta$ the polarization angle of the second emitted photon, with respect to the same arbitrary direction.

The annihilation operators corresponding to the cascade through the $\frac{1}{\sqrt{2}}(|\psi_{\mathrm{HH}}^{+1}\rangle + e^{i\alpha}|\psi_{\mathrm{HH}}^{-1}\rangle)$ path are then:

$$\begin{aligned}\hat{a}_{\alpha} &= \frac{1}{\sqrt{2}}(\hat{a}_{+1} + e^{i\alpha}\hat{a}_{-1}) \\ \hat{a}_{\alpha+\beta} &= \frac{1}{\sqrt{2}}(\hat{a}_{+1} + e^{i\alpha+\beta}\hat{a}_{-1})\end{aligned} \tag{4.4}$$

Here Pauli exclusion principle imposes $\hat{a}_{\alpha}\hat{a}_{\alpha+\beta} = 0$. One can develop the calculation:

$$\hat{a}_{\alpha}\hat{a}_{\alpha+\beta} = \frac{1}{2}\left(\hat{a}_{+1}\hat{a}_{+1} + e^{i(\alpha+\beta)}\hat{a}_{+1}\hat{a}_{-1} + e^{i\alpha}\hat{a}_{-1}\hat{a}_{+1} + e^{i(2\alpha+\beta)}\hat{a}_{-1}\hat{a}_{-1}\right) \tag{4.5}$$

As previously, we have $\hat{a}_{+1}\hat{a}_{+1} = \hat{a}_{-1}\hat{a}_{-1} = 0$ but $\hat{a}_{+1}\hat{a}_{-1} \neq 0$ and $\hat{a}_{-1}\hat{a}_{+1} \neq 0$. Knowing that $\hat{a}_{+1}$ and $\hat{a}_{-1}$ anticommute, the only way $\hat{a}_{\alpha}\hat{a}_{\alpha+\beta}$ is allowed is if $\beta = 0[2\pi]$, which means that a first photon linearly polarized along a given direction must be followed by a second photon that is also linearly polarized along the same direction. A similar calculation holds for the path passing through the other eigenstate $\frac{1}{\sqrt{2}}(-|\psi_{\mathrm{HH}}^{+1}\rangle + e^{i\alpha'}|\psi_{\mathrm{HH}}^{-1}\rangle)$.

These selection rules are sketched in figure 4.1.

**FSS, radiative lifetime and entanglement**

In the case of a $D_{2d}$ (or higher) symmetry of the excitonic wavefunction, the two paths are indistinguishable, as shown on the left panel of figure 4.1. Then the so-called which-path information is erased: one cannot tell which transition gave rise to the emitted photons. The two photons are then maximally polarization-entangled. On the contrary, when the degree of symmetry is lower, the energy diagram corresponds to the right panel of figure 4.1. In that case, one could tell which path was followed by the system, for example by precisely measuring the photon(s) wavelength. There is no entanglement in polarization in principle. However, distinguishability in wavelength can be overcome by resolving the entangled state in time, which reveals that the FSS causes a time-dependent phase evolution of the entangled state [191].

Physically, the two paths are indistinguishable if the FSS $\hbar\omega_{xy}$ is smaller than the emitted photon emission linewidth. Indeed, it is in that case that measuring the wavelength of an emitted photon does not allow to know which path has been experienced by the system. Note that the Purcell effect widens the radiative linewidth, so the entanglement can be restored by accelerating spontaneous emission [48].

If there is a heavy-light hole mixing, as described in 1.2, the selection rules lead to slightly differently polarized light in the different scenarios. If the eigenstates are not degenerate (case of an asymmetric excitonic wavefunction), the emitted photons are not H and V polarized any more, and are not perfectly orthogonal. When the eigenstates are degenerate (zero FSS, in the case of a symmetric excitonic wavefunction), then the photons emitted via the biexcitonic cascade are no longer perfectly $\sigma^+$ and $\sigma^-$ polarized, but contain some $\sigma^-$ and $\sigma^+$ components respectively.

### History and state of the art

Since the original proposal was published over two decades ago [52], the possibility to generate entangled photon pairs from QDs has been a primary motivating factor in QD device development. Unlike spontaneous parametric down conversion, which suffers from a fundamental efficiency-quality trade-off [70], QD devices promise near deterministic generation of high-quality polarization-entangled photon pairs.

The first demonstrations of polarization correlations from a biexciton cascade were published soon after the initial proposal [192–194]. However, the presence of large excitonic FSS prohibited the observation of quantum entanglement. In 2006, the first observations of polarization entanglement were achieved by spectrally filtering classically correlated emission to recover entanglement, at the cost of a significant reduction in efficiency [53]. It was also demonstrated in the same year that some QDs with naturally small FSS can be tuned using an external magnetic field to provide entangled emission [195]. In the following years, the limitations on the quality of entanglement due to the finite FSS were studied in depth [196–198], emphasizing the need for a fine control over the FSS. However, all these demonstrations so far had only been implemented using QDs in bulk or planar cavities, which significantly limited the pair collection efficiency.

Collection efficiency can be improved by embedding the QD inside an optical cavity. For the biexciton cascade, this is challenging because it requires a cavity geometry tailored for two different QD transitions with different frequencies of emission. This challenge was overcome in 2010 by our group using the *in situ* lithography technique to fabricate a molecular cavity mode that couples to both transitions of the cascade [48], leading to a significant enhancement in entangled pair collection rate. However, the fabricated device still relied on the chance to obtain a QD with a naturally small FSS, and could not tune the cascade emission wavelengths post-fabrication. In addition, for many applications in quantum technology, pair generation efficiency and degree of polarization entanglement are not the only requirements; each individual photon must also be sequentially indistinguishable.

Evidence of spectrally coherent emission under continuous wave excitation was observed in 2012 [199]. However, indistinguishability in time requires deterministic excitation. Interestingly, because of the Coulomb interaction, the biexciton is not exactly twice the energy of one exciton. The biexciton state can thus be prepared using two-photon excitation with a laser energy set at the mean energy between the X and XX transitions [200, 201], which allows for efficient filtering of the excitation pulse. Using this technique, the generation of entangled photon pairs with high indistinguishability was demonstrated in 2014 [202]. In combination with advances in growing naturally symmetric droplet-etched GaAs QDs, two-photon excitation also led to the current state-of-the-art in photon pair quality, showing an indistinguishability up to $0.93 \pm 0.07$ [138] and entanglement fidelity as high has $0.978 \pm 0.005$ [203]. The entanglement fidelity is computed by performing polarization tomography to obtain the density matrix of the entangled polarization state of light. Then, the fidelity is given by the expectation value of the measured density matrix with respect to an ideal maximally entangled state. Hence, a value of 0.5 represents a classically-correlated state and a value of

1 represents a maximally entangled state.

In 2019 it was demonstrated that limits on extraction efficiency and entanglement fidelity due to finite FSS could be simultaneously overcome by coupling a QD to a broadband circular Bragg grating [63, 204]. Although this approach showed an impressive pair generation probability of $0.59 \pm 0.01$ and extraction efficiency of $0.62 \pm 0.06$, the measured entanglement fidelity ($0.90 \pm 0.01$) and indistinguishability ($0.90 \pm 0.01$) did not improve upon the state-of-the-art. In particular, the plateau in achievable indistinguishability opened questions about the fundamental limits due to the biexciton and exciton lifetimes [51].

### 4.1.2 Frequency-encoded qubits

In this section, we discuss how the exciton FSS can be used to generate frequency-encoded qubits. We have seen in section 2.3 that the temporal wavepacket of the photons emitted by a QD based on an exciton shows an oscillation with a frequency that is proportional to the fine structure splitting. Very recently, it has been experimentally shown in the group that we are able to excite the QDs using longitudinal acoustic phonon-assisted excitation, a configuration where the excitation laser can be rejected simply by frequency filtering [162]. In this assisted excitation process, the polarization of the excitation laser still dictates the QD excited state. Now, since polarization filtering is no longer necessary, we can either collect all the polarizations or to choose in which polarization basis we collect. For example, if we excite the QD with a linear superposition of the two excitonic dipoles, $|x\rangle$ and $|y\rangle$, oriented along an angle $\theta$ from the $X$ axis, the initial state of the QD is written $|\psi_\theta(t=0)\rangle = \cos\theta\,|x\rangle + \sin\theta\,|y\rangle$. Then, the temporal evolution of the QD state is given by:

$$|\psi_\theta(t)\rangle = \cos\theta e^{-i\omega_x t} e^{-t/2\tau}\,|x\rangle + \sin\theta e^{-i\omega_y t} e^{-t/2\tau}\,|y\rangle \tag{4.6}$$

In the bad-cavity regime, the state of light collected by the cavity is proportional to the state of the QD. Hence, the state of the emitted light can be approximately represented by

$$|\Psi_\theta(t)\rangle = \cos\theta e^{-i\omega_x t} e^{-t/2\tau}\,|\omega_x, X\rangle + \sin\theta e^{-i\omega_y t} e^{-t/2\tau}\,|\omega_y, Y\rangle \tag{4.7}$$

where $\omega_x$ (res. $\omega_y$) and $X$ (res. $Y$) is the frequency and polarization of state $|x\rangle$ (resp. $|y\rangle$). This expression corresponds to a hyper-encoded state since it is encoded in both frequency and polarization, these two quantities being entangled. By filtering the emission in polarization using a filter with an angle $\phi$ from the $|x\rangle$ dipole orientation $|\phi_{\text{coll}}\rangle = \cos\phi\,|X\rangle + \sin\phi\,|Y\rangle$, we obtain a frequency-encoded qubit:

$$\langle\phi_{\text{coll}}|\Psi_\theta(t)\rangle = e^{-t/2\tau}\left(\cos\theta\cos\phi e^{-i\omega_x t}\,|\omega_x\rangle + \sin\theta\sin\phi e^{-i\omega_y t}\,|\omega_y\rangle\right) \tag{4.8}$$

This expression shows that by choosing the relative angle between $\theta$ and $\phi$, we can generate any qubit encoded with two frequencies $|\omega_x\rangle$ and $|\omega_y\rangle$.

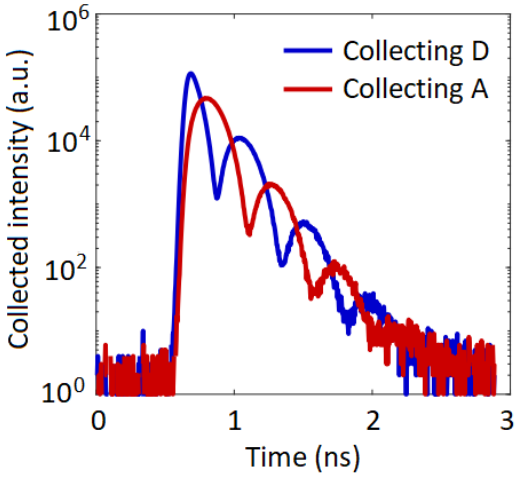


Figure 4.2: Temporal profiles of the emitted photons when exciting with diagonal polarization D (corresponding to $\theta = \pi/4$). The blue (resp. red) curve corresponds to the measured intensity in the D polarization, corresponding to $\phi = \pi/4$ (resp. A polarization, corresponding to $\phi = 3\pi/4$).

Figure 4.2 shows the temporal wavepacket profile of the emitted photons for an excitation polarized at $\pi/4$ from the exciton axes. The temporal profiles of the emitted photons in the diagonal D ($\phi = \pi/4$) and antidiagonal A ($\phi = 3\pi/4$) polarizations evidence the different quantum superpositions of the frequency qubits.

The state $|\omega_x\rangle$ ($|\omega_y\rangle$) represents a single photon occupying the mode with a resonance centered at $\omega_x$ ($\omega_y$). These states form the basis of the frequency qubit. By tuning the FSS ($\omega_x - \omega_y$), we can control the spectral separation of these two frequency modes in which we can encode information.

## 4.2 State of the art for FSS tuning

For the two applications presented in the last section, control over the QD FSS would be useful. For the generation of frequency-encoded qubits, controlling the QD symmetry would allow for controlling the FSS $\omega_x - \omega_y$ but also the mean frequency of the source $(\omega_x + \omega_y)/2$. In the case of entangled photon pair generation, relying on the probabilistic growth of dots with naturally small FSS poses a problem for scalability, as it greatly reduces the fabrication yield. The aim of tuning the FSS to zero has generated a lot of interest for applications in photon pair generation. Furthermore, this new proposed application of using the exciton as a frequency-encoded qubit has introduced a new application for FSS splitting, and it is advantageous to be able to precisely control and even increase the FSS. In this section, I describe some of the state of the art in terms of FSS tuning.

### 4.2.1 Irreversible FSS control

#### Growth methods

In general, self-assembled semiconductor QDs show an in-plane asymmetry, which leads to a $C_{2v}$ symmetry, while we need a $D_{2d}$ symmetry to have a zero FSS. However, it has been shown that some growth methods can lead to low values of FSS.

- It has been shown that the FSS is lower for smaller QDs. In reference [205], the authors characterized a large number (200) of InAs/GaAs QDs grown under various conditions and concluded that the small dots with the most symmetric electron and hole wavefunctions and emitting at an energy of around 1.4eV ($\lambda \simeq 880$nm) were the ones showing the lowest FSS (no more than 10 µeV and as low as about 1 µeV which is lower than 1pm between the two dipoles at this wavelength). One of them has been used to demonstrate the generation of entangled photon pairs with high-fidelity [197].
- The fabrication by droplet epitaxy of GaAs/AlGaAs QDs leads to high symmetry and very low FSS values were reported in [206]. Holes with controllable symmetry were etched into GaAs and were then filled with AlGaAs or vice versa. The weak intermixing between GaAs and AlGaAs allows them to assume that the QDs take the shape of the etched hole. Three samples were fabricated, corresponding to a given QD aspect ratio each, and the FSS was measured on a large number of QDs for each sample. The sample with the most symmetric QDs (aspect ratio equal to 1.02) gives an average FSS value of $3.9 \pm 1.8\mu$eV ($\simeq$ 2pm), compared to $49 \pm 6\mu$eV ($\simeq$ 25pm) for an aspect ratio equal to 1.13. However, the success of this method highly depends on which materials are used as substrates [207]: using materials that show more intermixing and diffusion in preferential directions is likely to make the QD geometry less controllable [208].

#### Thermal annealing

It has been shown that it is possible to modify excitons spectra by using rapid thermal annealing. A transmission electronic microscope image of one of our QDs before and after annealing is shown in figure 4.3. In reference [209], the authors work with individual self-assembled


Figure 4.3: Transmission microscope image of one of our QD (a) before and (b) after annealing.

InAs QDs on which they perform short steps of annealing at relatively low temperature. They show that this reproducibly blueshifts the excitonic transition lines, as well as varies the FSS through zero (see figure 4.4(a)) and controls the energy difference between the biexcitonic and the excitonic transitions (see figure 4.4(b)). However, these three parameters (wavelength, FSS and biexciton binding energy) are not controllable separately. This technique is useful to cancel a given QD FSS definitively which is an advantage for the generation of entangled

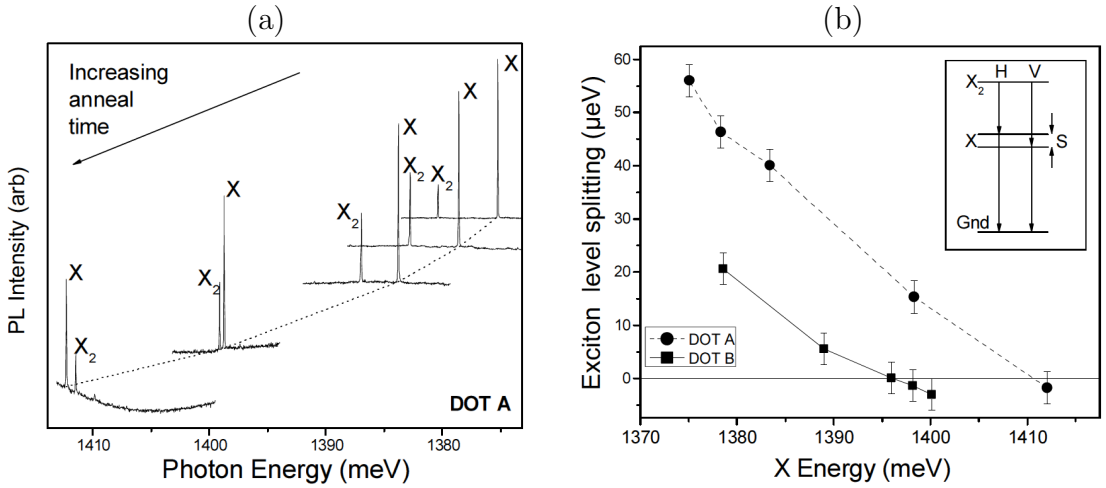


Figure 4.4: (a) Photoluminescence spectra from an individual InAs QD, taken in between successive 5 minutes long annealing steps. The line labelled $X$ (resp. $X_2$) corresponds to the exciton (resp. biexciton) transition. (b) Fine structure splitting as a function of the exciton energy, for two different InAs QDs. Each point is measured after an annealing step of the sample. These figures are taken from [209].

photon pairs, but the modification is irreversible so it can not be used to tune the FSS *in situ*.

The inversion of the FSS can be explained by the competition between the shape of the QD and the strain of its environment. Annealing modifies the shape so if the strain has a different direction than the initial shape and becomes dominant as the annealing is implemented, the FSS can change sign.

For the generation of frequency-encoded qubits described in section 4.1.2, it is useful to be able to tune the FSS *in situ*. This is not allowed by the two methods described previously that are irreversible, and requires other FSS tuning techniques.

### 4.2.2 FSS tuning with one knob

#### Off-plane electric fields

An off-plane electric field allows one to tune the wavelength of the transitions, as we saw in Chapter 1. It is possible to use it to tune the FSS since the two excitonic transitions do not shift with the same dependence on the electric field.
Vertical electric fields are easy to implement on samples made by molecular beam epitaxy for example, can be varied *in situ* and do not require very high voltages. The main drawback of this technique is that the accessible range over which one can tune the QD wavelength and FSS is quite limited, since there is a point where the carriers tunnel out of the dot. In reference [210], the authors overcome this issue by using a specific doping configuration shown in figure 4.5(a). They report a linear dependence of the FSS over the vertical electric field over 100 µeV. However, this linear dependence does not hold when the FSS is close to zero: the authors observe for the first time an anticrossing of the exciton states (see figure 4.5(b)). The

FSS reaches a non-zero minimum. For some QDs, this minimum is lower than the emission linewidth so they can generate entangled photon pairs.

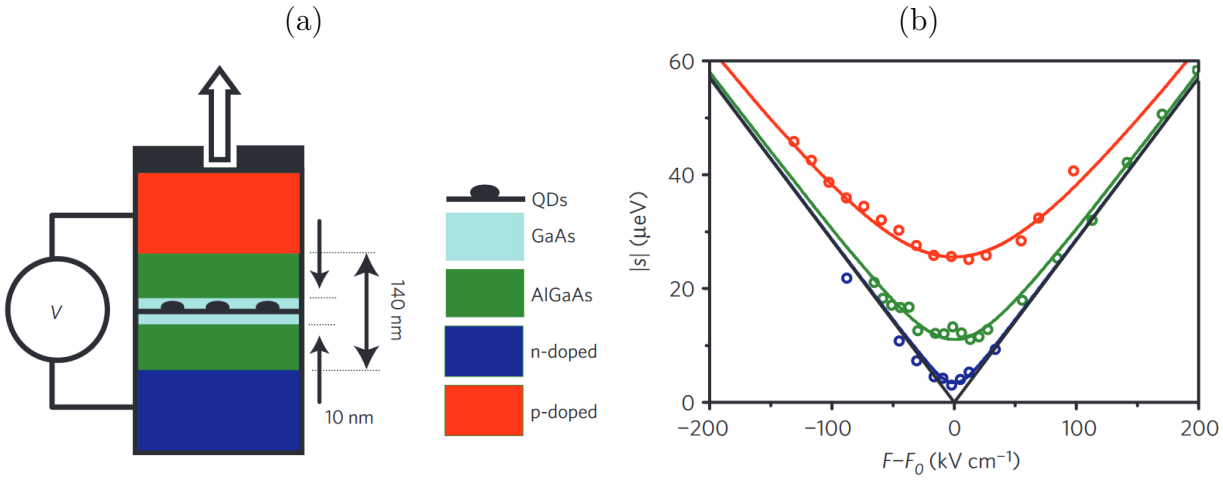


Figure 4.5: (a) Design of the device used to apply an off-plane electric field to InAs/GaAs QDs. (b) Evolution of the FSS with the electric field. $F_0$ is the electric field corresponding to the minimum reachable FSS. These figures are extracted from [210].

### In-plane electric field

Self-assembled QDs that are elongated along a given direction usually show a non-zero FSS because their electron and hole wavefunctions are asymmetric. A possible approach to tune the FSS is then to use in-plane electric fields, by taking advantage of the quantum confined Stark effect. It is the case for example in reference [211] where the effect of an in-plane electric field is investigated using the device design shown in figure 4.6.

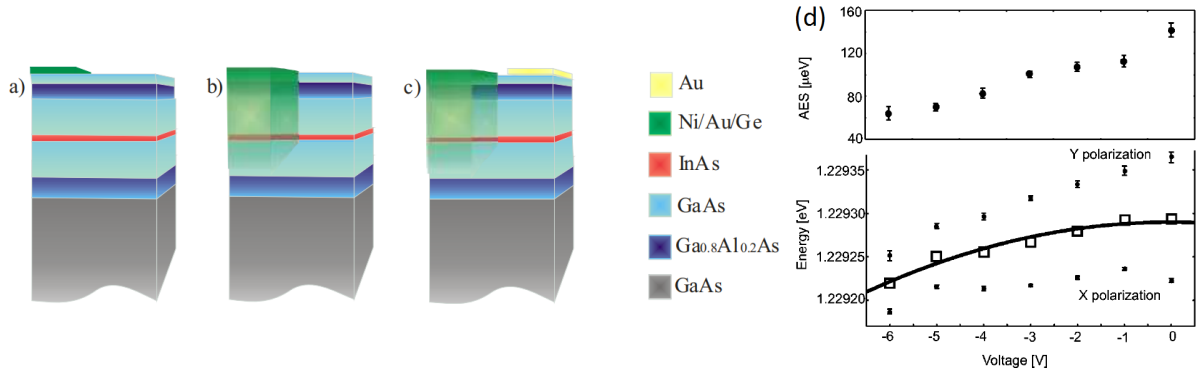


Figure 4.6: Steps of fabrication of the device used in reference [211] to apply an in-plane electric field on InAs/GaAs QDs (figure extracted from [185]). (a) metal deposition of Ohmic contact, (b) diffusion by annealing, (c) Schottky barrier deposition. Panel (d) was extracted from [211] and shows the experimental results: the upper plot is the FSS (anisotropic exchange splitting) and the lower one is the average exciton energy, both as the applied voltage is varied. This figure was extracted from [211].

The semiconductor device has a Ohmic contact on one side that diffused downwards by annealing of the sample, and a Schottky contact deposited on the sample surface on the other side. The field was applied in the dot elongation direction, which turns out to be roughly the same for all the QDs in the sample (their eigenaxes were aligned along the crystallographic axes of the sample). A variation of the FSS from 140 to 60 µeV and a shift of the average wavelength by about 70 µeV were observed. Many QDs from the sample showed similar behaviours.

A larger tuning range (about 100 µeV) was achieved in reference [186], again using an in-plane electric field. This time the electric field is applied using two Schottky gates deposited on the surface of the sample. The evolution of the FSS with applied bias for three different QDs is shown in figure 4.7(a). We see in figure 4.7(b) that the intensity of the photoluminescence signal decreases while the emission linewidth increases as the Stark shift is increased. This makes this technique applicable only for QDs that originally have a relatively low FSS.

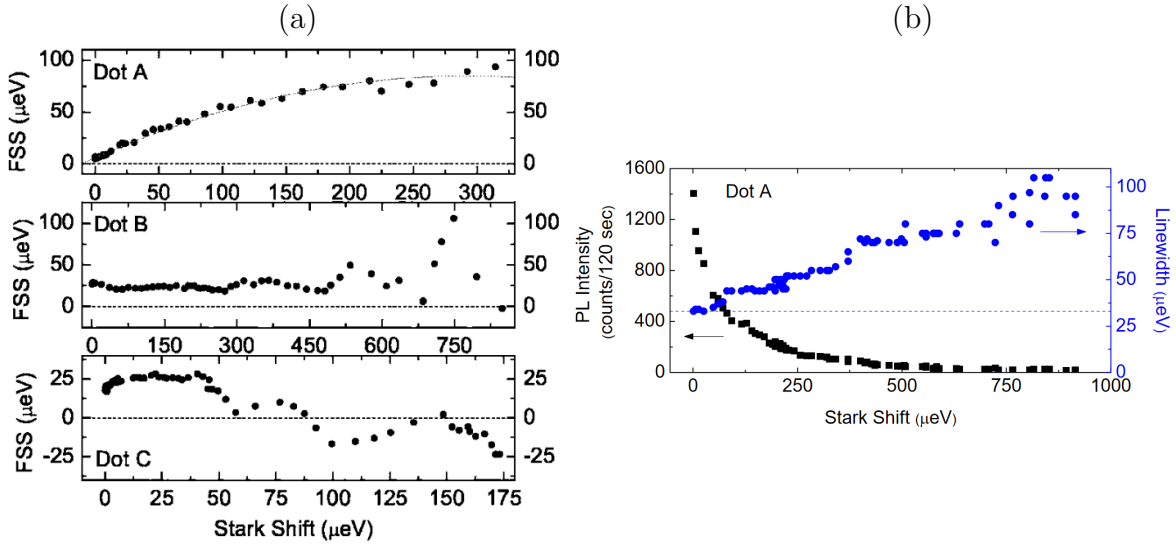


Figure 4.7: (a) FSS of three QDs as a function of Stark shift. In dot A, the splitting shows a square root dependence on the Stark shift. Dots B and C exhibit a splitting with an oscillatory response to the Stark shift. (b) Evolution of the photoluminescence intensity (in black) and the emission linewidth (in blue) as the Stark shift is increased. These figures are extracted from [186].

For both of these last mentioned experiments, this technique allows to tune the FSS. However, here again the average wavelength and the FSS can not be tuned independently, and the field has to be applied along the QD elongation axis. Finally, a too high horizontal field can lead to the reduction of exciton oscillator strength and can make the charges tunnel out of the QD, reducing the radiative efficiency. This limits the range of voltage one can use to tune the FSS.

In 2019, a new scheme was proposed [212] to apply a quadrupole electric field to a QD embedded in a nanowire, in order to cancel its FSS while maintaining a strong electron-hole overlap and a high extraction efficiency. The authors describe a device made of four electric

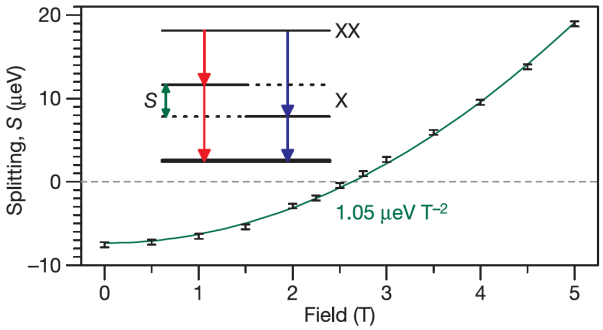


Figure 4.8: Evolution of the FSS with the in-plane magnetic field applied to InAs/GaAs QDs. The green line shows a quadratic fit, with a coefficient of $1.05\mu\text{eV}/T^2$. This figure was extracted from [205].

gates around a nanowire structure embedding a QD. They show theoretically that this device should allow for reaching a near-zero FSS (0.05 µeV) with a 90% electron-hole overlap. This scheme has not been experimentally implemented yet.

#### In-plane magnetic field

It is also possible to apply in-plane magnetic fields to change the fine structure splitting, as it was demonstrated in [205] where the authors apply up to 4T and observe an increase of the FSS. Their results are shown in figure 4.8. The evolution of the FSS shows a quadratic dependence on the magnetic field.

Here again the FSS and the wavelength can not be tuned independently, and the magnetic field has to be aligned along the dot elongation axis.

### 4.2.3 FSS tuning with two knobs to overcome anticrossing

These last mentioned techniques give only one degree of freedom because they are applied only in one direction. It was shown theoretically [213] and demonstrated experimentally [184] that in such case, the FSS can not reach zero unless the applied field is aligned along the direction of the dot elongation. Hence, as mentioned earlier tuning the external knob leads to an anti-crossing of the excitonic states, due to the coherent coupling between them.

In reference [189], the authors show that a zero FSS can be recovered for any QD using one knob controlling a biaxial in-plane mechanical strain and another one controlling a vertical electric field. The QD orientation is first modified using the mechanical strain so that it is aligned along the orientation of the other perturbation. After that, the vertical electric field is varied to reduce the FSS to zero. The results are shown in figure 4.9: we see that choosing the proper value of $V_p$ brings the minimum of the FSS as a function of $V_d$ to zero. Without applying the in-plane strains beforehand, there would be an anticrossing as described earlier.

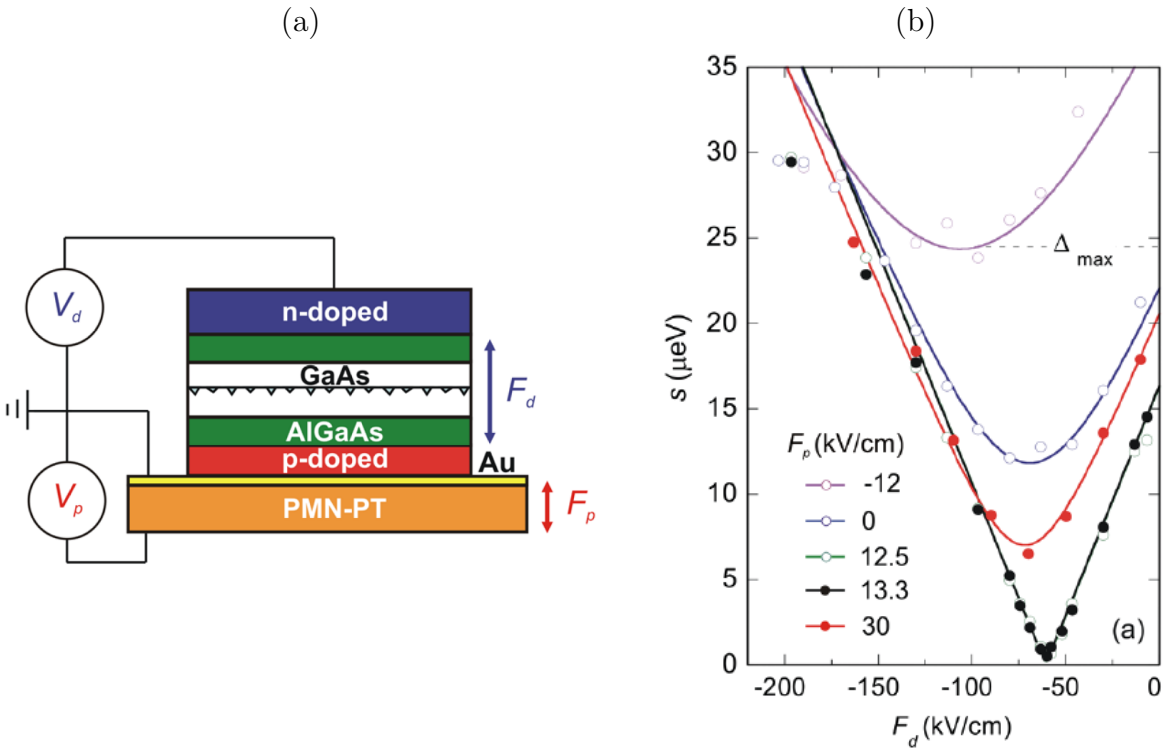


Figure 4.9: (a) Design of the device: *n-i-p* structure on top of a piezoactuator: $V_p$ controls an anisotropic biaxial strain and $V_d$ a vertical electric field. (b) Evolution of the FSS with the two applied voltages. These figures are extracted from [189].

This technique led to generation of entangled photon pairs with a high degree of entanglement [190].

More generally, reaching a zero FSS is possible using any pair of independent and non-parallel external knobs.

### 4.2.4 Tuning the FSS and the average wavelength: need for three knobs

For quantum protocols such as the implementation of quantum relays, it is necessary to generate entangled photons from two sources that present the same wavelength. However, the FSS is lower than the emission linewidth over a very small range of average wavelength, which leaves very little freedom to tune the average excitonic energy while keeping a high degree of entanglement for the generated photon pairs. In reference [156], the authors show that three knobs are necessary to simultaneously tune the FSS and the wavelength in an independent way. The authors propose a design of piezoelectric actuator with six legs, represented in figure 4.10(a) that allows them to apply in-plane stress fields which naturally represent three knobs (three components of the stress tensor $\sigma_{xx}$, $\sigma_{yy}$ and $\sigma_{xy}$). The results from the experimental implementation of this technique was reported in reference [214]. As we can see in figure 4.10, a zero FSS was obtained for different values of average exciton energy over a large energy range.

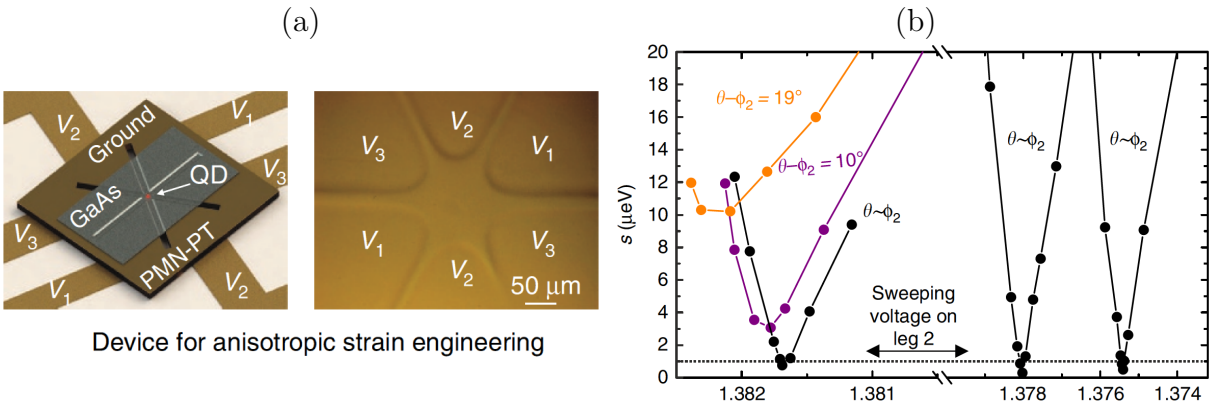


Figure 4.10: (a) Design of the six-legs device. Three independent voltages control the in-plane biaxial stress. (b) Behaviour of the FSS as a function of the average exciton energy. The orange and purple curves show the anticrossing due to a non-alignment of the dot elongation with the last knob direction (it is the same phenomenon as the one described in figure 4.9). Tuning one of the three voltages and then using the two others to recover a zero-FSS allows to obtain zero-FSS for several exciton wavelengths. These figures are extracted from [214].

This technique is applicable to any QD to simultaneously tune the FSS and the wavelength.

### 4.2.5 Challenge to overcome: FSS tuning in cavities

In order to obtain a high brightness for the generation of entangled photon pairs or for the other application exploiting a control of the FSS, it is critical to combine FSS tuning with a cavity providing a large Purcell factor. To the best of our knowledge, such approach remains quite challenging and very few works have reported such effort so far. In reference [215], the authors developed a QD micropillar cavity on a piezoelectric actuator in order to use strain to tune the QD in resonance with the cavity. A compressive (resp. tensile) biaxial strain leads to a linear increase (resp. decrease) of the QD energy. The dependence is linear. On one hand, etching the micropillar down to the bottom strongly reduces the transfer of the strain from the substrate to the QD, restricting the tuning range of the QD energy. On the other hand, leaving DBR mirrors not etched at the bottom of the micropillar reduces the Q-factor, increases the mode volume and thus reduces the Purcell factor. Furthermore, it reduces the photon extraction efficiency. There is thus a trade-off between the Q factor of the cavity and the obtainable tuning range. In the paper, the authors chose to etch the micropillar down to 2 to 4 pairs of bottom DBR layers, losing a factor of 2 for the Q factor in comparison with a pillar that would be etched down to the bottom. The extraction efficiency is decreased by 10 to 40%. At this cost, applying 27 kV/cm to the piezoactuator allows the authors to sweep the QD energy over a 0.75 meV range (about 0.5 nm). No report of the QD FSS was presented in this work.

## 4.3 Principle of our approach

We propose a device configuration where the user can control the electric field in the three directions of space at the position of the QD which is embedded in a pillar cavity. This is done by applying three voltages and allows for controlling both the FSS and the average wavelength of the exciton.

In the framework of developing single-photon sources, we showed that we apply an electric field to tune the QD wavelength and suppress charge noise. The way we apply this voltage is recalled in figure 4.11(a): we use pillar cavities connected to a frame, which itself is connected to a large mesa where the electrical contact is defined. An observation one can make from this figure is that the contact is not on top of the micropillar but on the side at a given distance, which probably creates a horizontal component of the electric field. Indeed when varying this electric field, we noticed that the splitting between the wavelengths of the fundamental modes $h$ and $v$ of the cavity can change. Such observation is presented in figure 4.11(b).

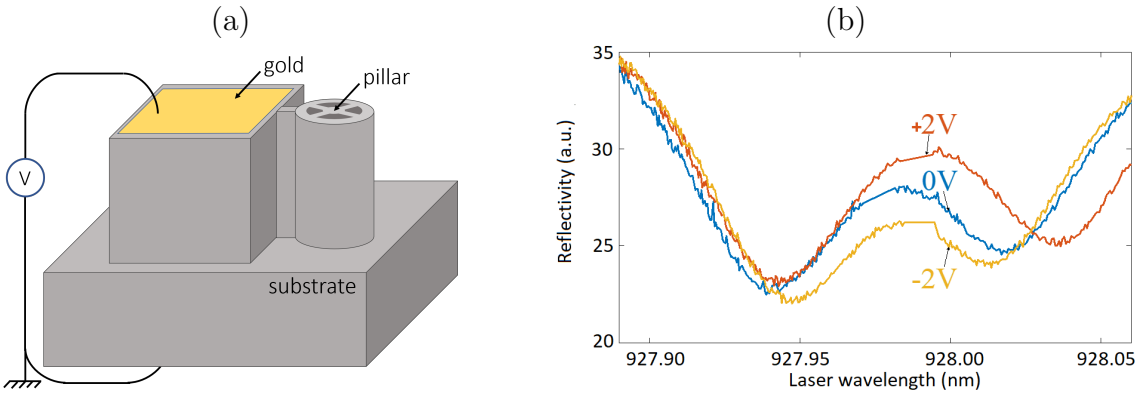


Figure 4.11: (a) Drawing showing the position of the electrical contact with respect to the micropillar for single-photon sources studied in the previous chapters. (b) Reflectivity measurement showing the cavity splitting, that changes with the applied voltage.

Such a modification in the cavity splitting is explained by a change of symmetry of the pillar in the horizontal plane. This is probably due to the piezoelectric properties of GaAs [216] that lead to a change in refractive index, and so to a modification of the cavity modes properties when an electric field is applied.

This phenomenon has been used in 2018 in reference [217] to cancel the cavity splitting of a micropillar containing QDs. This would for instance allow excitation of the QD in a cross-polarization configuration with any polarization angle without collecting any rotated light from the cavity. Since the cavity rotated light is the main origin for multi-photon components in the case of exciton-based sources (see section 3.4.2), having degenerate cavity modes would lead to higher values of single-photon purity. In practice, the authors of [217] deposited three electrical contacts on a structure that is shown in figure 4.12(a). The contact deposited on the top mirror allows to fine tune the cavity polarization splitting that arises from asymmetries of the cavity, using the electro-optic effect. The two cavity mode frequencies are plotted as a function of the applied top voltage in figure 4.12(b). A clear crossing between the two curves is

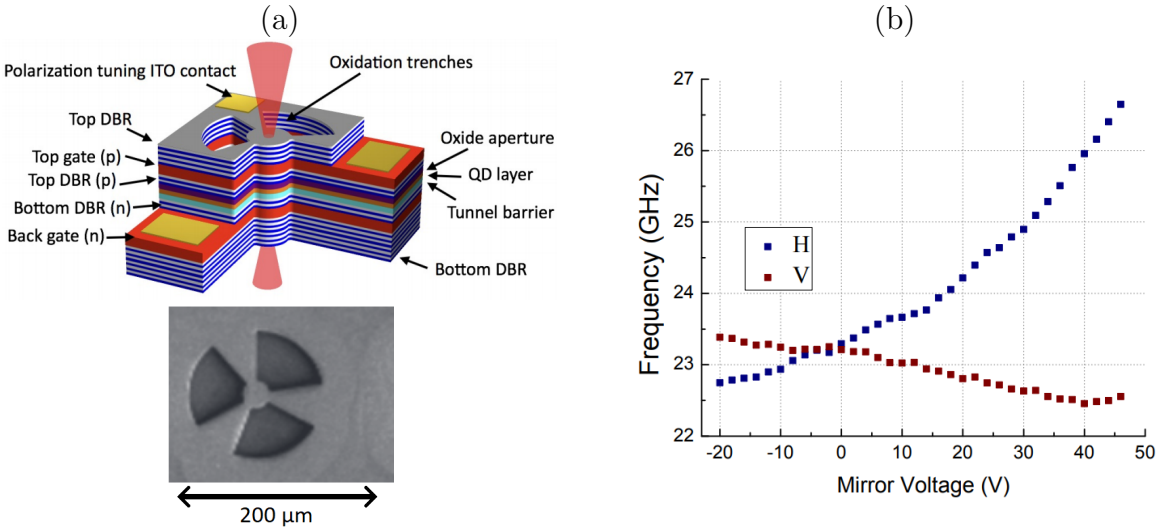


Figure 4.12: (a) Drawing of the structure allowing for tuning of the cavity modes splitting. (b) Cavity mode frequencies varying with the applied top voltage. These figures are extracted from [217] and [218].

observed, corresponding to a perfectly degenerate configuration. The other contacts allow the authors to still be able to tune the QD wavelength. Note that despite their visual similarities, the cavity structure of reference [217] strongly differs from ours in size (>100 µm) and optical field confinement mechanism.

In our experimental configuration, the observation of a change in the cavity birefringence when applying a remote bias indicates the appearance of an in-plane electric field that we could exploit to control the FSS. We use the semiconductor module of the software COMSOL to explore theoretically the electric field profile in our structure when such remote voltages are applied. We consider the geometry shown in figure 4.13. A 4 µm diameter pillar (on the left of the figure) is connected to a 12 µm wide and 4 µm long mesa (on the right) through a 1.5 µm wide and 10 µm long arm. The dimension along $z$ of these three elements is the real sample one, namely 7.5 µm. They are positioned on a wafer to which we attributed a 45 µm diameter and a 5 µm thickness, which is much smaller than in the real sample for the sake of computation time. The voltage is applied on the metallic surface defined on the top of the mesa. We defined the whole structure material to be only GaAs. We do not use the real structure where GaAs and AlGaAs are alternated, as these Bragg mirror pairs are too thin for COMSOL to take into account in reasonable computation durations. Moreover, this study is not about the light confinement but only about the electric behaviour of the device. The horizontal layers that we can see in figure 4.13(a) are the boxes where the different doping values are defined. The corresponding doping profile is close to the actual doping structure of our samples and is shown in figure 4.13(b). The intrisic region shows a $10^{14}\text{cm}^{-3}$ residual doping (both $n$ and $p$) because of interdiffusion between the layers. We consider a QD located at the bottom of the intrisic region in $z$ (20 nm above the $n$-doping layer), as shown on the right panel of figure 4.13, and we suppose that it is located in the middle of the pillar in $x$ and $y$. The temperature in the simulation was set equal to 10 K.

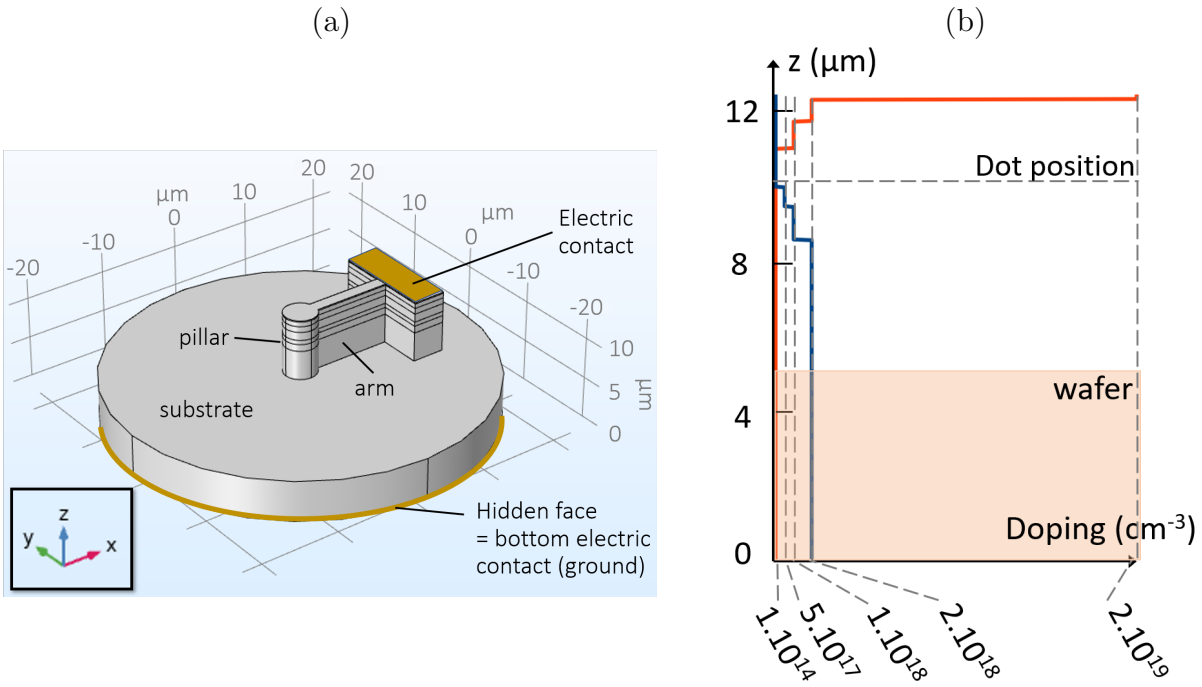


Figure 4.13: (a) Geometry of a semiconductor design with one pad, built in COMSOL to simulate the behaviour of electric fields, current densities, etc. (b) Doping profile of the structure, invariant by translation in the $x$ and $y$ directions. The orange (resp. blue) line corresponds to the concentration of $p$-type (resp. $n$-type) dopants. The shaded orange area corresponds to the wafer which has a thickness set to 5 micrometers. The vertical dashed lines are guides for the eyes corresponding to the different concentrations of dopants in the device. In the intrisic region, the doping is on the order of $10^{14}$ cm$^{-3}$ in both $p$ and $n$.

We swept the voltage from $-2$ to $+2$ V and calculated the electric field and current density components at the position of the dot. We then obtain the curves presented in figure 4.14, for both the electric field and current density at the QD position.

Figure 4.14(a) shows the $E_z$ component of the electric field at the QD position. It is non-zero and varies with the voltage between $-2$V (and probably lower) to about $+1.5$V. This is the main regime that we use when we apply the bias voltage to tune the QD in resonance with the cavity fundamental mode wavelength, via the confined Stark effect, as mentioned earlier. We check (see figure 4.14(b)) that the component of the electric field $E_y$ is zero, which is consistent with the symmetry of the device with respect to the $(xz)$ plane. However we observe a non-zero horizontal component along $x$ rising when the voltage is positive and beyond 1.3 V. The $E_x$ component of the electric field for a top voltage set to 1.6V is presented in figure 4.15. Its amplitude is non-zero at the QD position.

Figure 4.14(c) shows the intensity of currents flowing through the top electric contact and through the bottom of the wafer (set as the ground). We see that the voltage for which the non-zero horizontal electric field component rises corresponds to the diode threshold since a current flows through it (a current arrives in the structure from the top contact and is evacuated through the bottom contact).

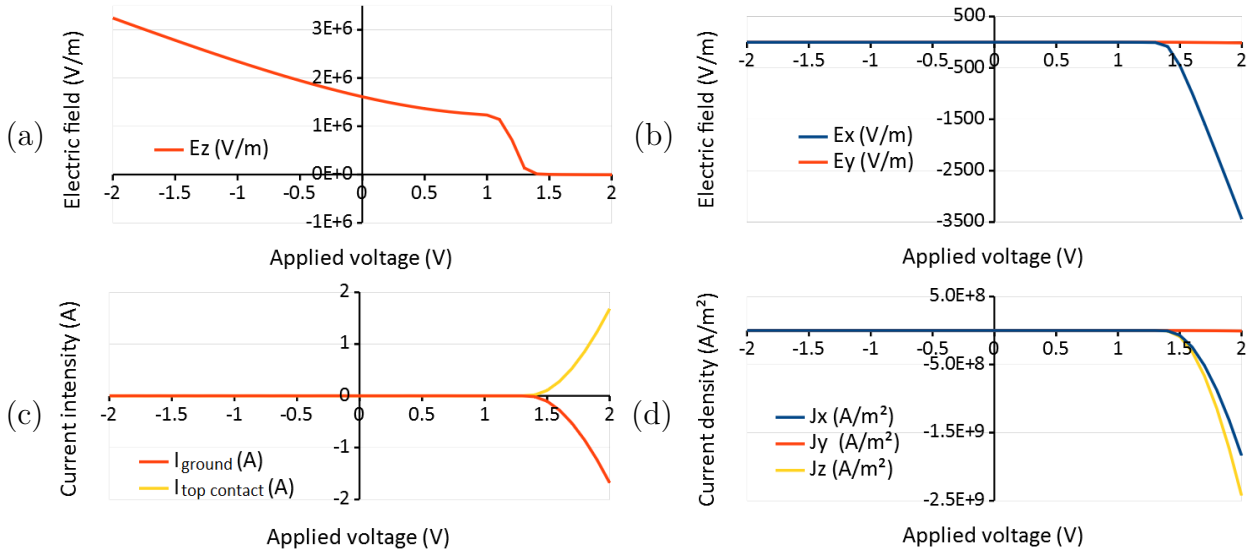


Figure 4.14: Panels (a), (b) and (d) correspond to quantities evaluated at the QD position. They correspond to: (a) Vertical component of the electric field (along $z$). (b) Horizontal components of the electric fields (along $x$ in blue and along $y$ in orange). (d) Components of the current density (along $x$ in blue, along $y$ in orange and along $z$ in yellow). Panel (c) shows the current intensities flowing through the electrical contacts (top of the diode and bottom of the wafer, namely the ground).

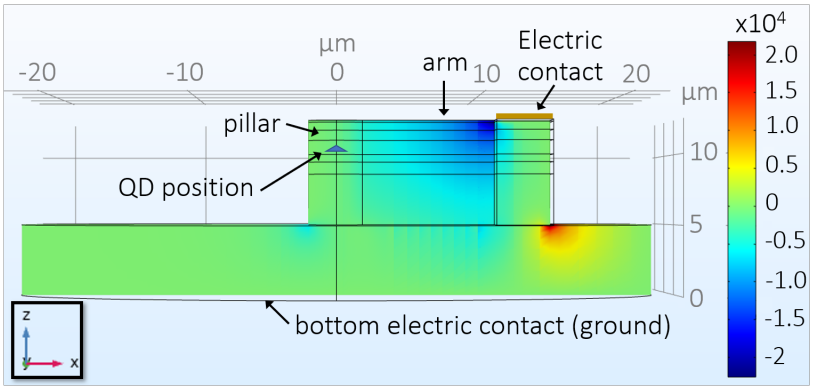


Figure 4.15: $E_x$ component of the electric field (in V/m), for a top voltage set to 1.6V.

Figure 4.16 shows the distribution of current density in the simulated device for an applied voltage equal to 1.6V. We can see that most of the current is flowing vertically through the diode, but a small component is also flowing towards and through the micropillar. The current density thus existing at the position of the QD is plotted in figure 4.14(d). The amplitude of this current, which could be detrimental to the QD optical properties, actually strongly depends on the whole structure geometry as discussed later.

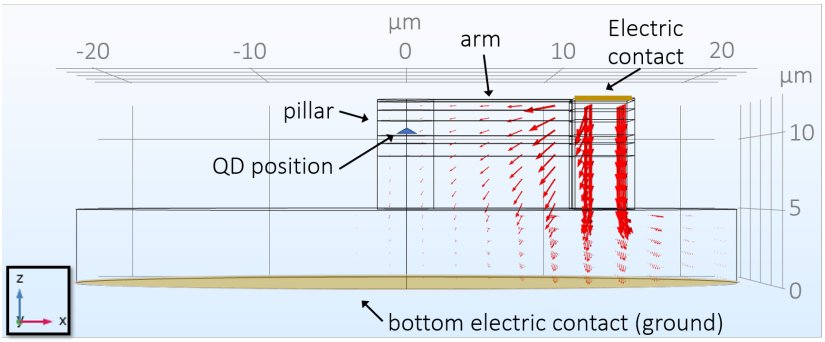


Figure 4.16: Current density in the device, seen in the $(xz)$ plane.

From figures 4.14(a) and (b) we see that around 1.3V, the vertical component of the electric field drops whereas the horizontal one increases in absolute value. Figure 4.17 shows the ratio $E_x/E_z$ between 1.4 and 1.7V. The left panel is in linear scale and the right one represents the absolute value of that ratio in log scale.

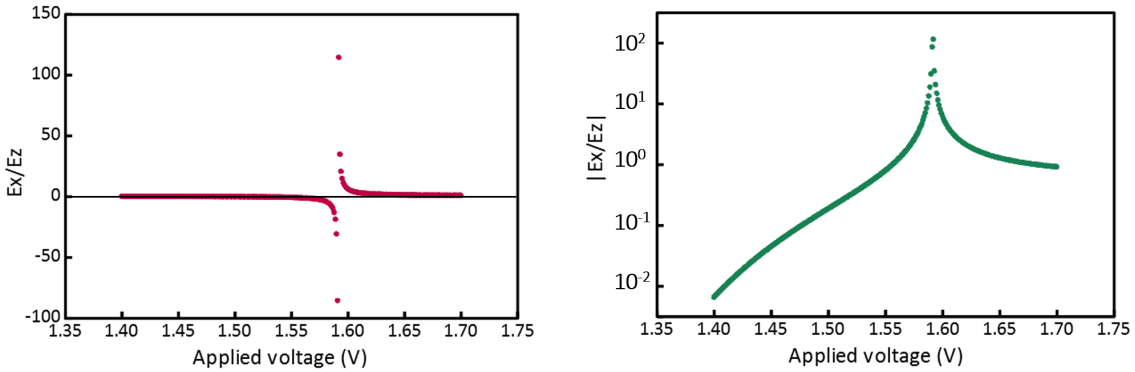


Figure 4.17: Left panel: ratio $E_x/E_z$ as a function of the applied voltage, in linear scale. Right panel: absolute value of the ratio $E_x/E_z$ in logarithmic scale.

Figure 4.17 shows that we can set the ratio $E_x/E_z$ to any value between $10^{-2}$ and infinity as $E_z$ crosses zero. We conclude that when applying a voltage on the top of the device but not directly above the pillar, and around a value for which the diode defined by the big mesa becomes conductive, it is possible to achieve, at the QD position, any direction of $\mathbf{E} = E_x\mathbf{e}_x + E_z\mathbf{e}_z$ with $E_z > 0$.

### 4.3.1 Proposed design to tune FSS and wavelength

Based on the previous study we propose a new technique to apply a three-dimensional electric field to be able to simultaneously tune the FSS and the average energy of the exciton as it was done with strain. This technique is fully compatible with all the light extraction methods that we have already implemented to obtain bright single-photon and entangled photon sources [48, 67]. The use of three knobs should allow us to make sure that the QD transition energy matches the modes of the cavity while controlling the FSS. The idea is to use the same kind of wafers as the ones presented so far, and implement the *in situ* lithography process as well.

However, instead of etching a wheel-shape device as shown in figure 1.17, we would etch a micropillar connected to three metal pads via long ridges. Each metal pad is then connected to an independent voltage source. A picture of the typical structure is shown in figure 4.18(a), where we added fake color for the deposited gold defining the top contact. The bottom contact is applied to the back of the sample over the whole surface. Figure 4.18(b) presents an optical microscope image of the sample with wire bonding.

(a)

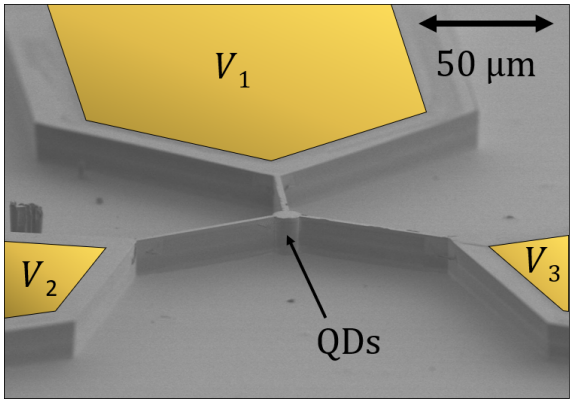


(b)

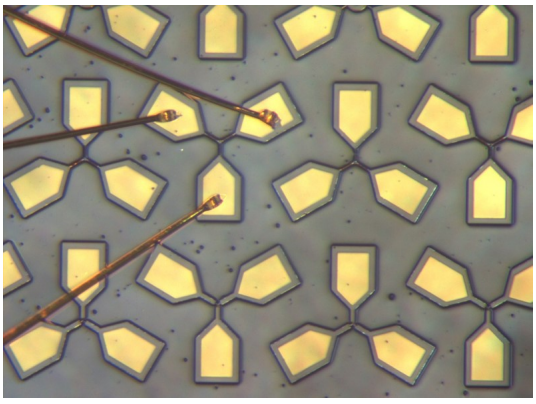

Figure 4.18: (a)Scanning electron microscope image of a micropillar optical microcavity hosting epitaxial quantum dots (QDs). We apply up to three voltages (V1-V3) to metal pads (false color yellow) connected to the cavity via narrow ridges and remotely control the vectorial electric field around the QDs. The micropillars have a 10 µm diameter and the ridges are 2 µm thick. (b) Optical microscope image of the sample with wire bonding.

This structure would allow to tune the FSS and the average excitonic energy, after the processing, by allowing us to tune all the components of the electric field at the QD position.

## 4.4 Simulation of the electric field profile

In this section, we show that we can control both the horizontal component for the electric field at the QD location, and the vertical one. More generally, we study the behaviour of the electrical quantities in the devices. In particular, we investigate the currents flowing through the device to see if there is a regime of voltage operation where we can obtain tunable horizontal field components without a large current flowing through the QD. For that purpose, we implemented simulations with COMSOL in the Semiconductor module.

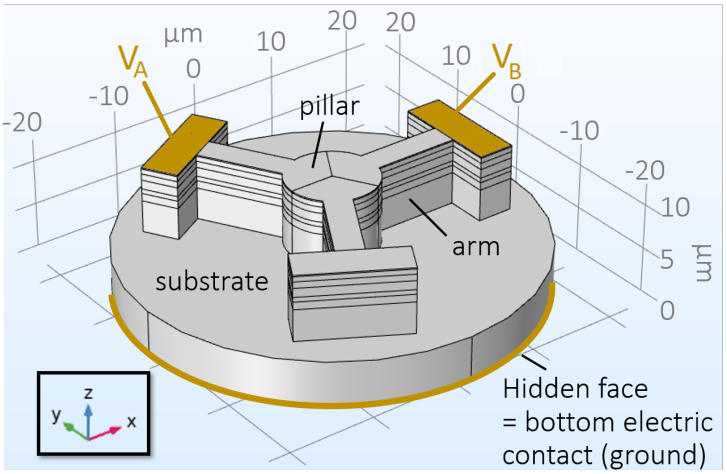


Figure 4.19: The model geometry developed in COMSOL to simulate the electrical properties of devices fabricated to tune the exciton FSS.

The device designed in the software is shown in figure 4.19. The wafer is simulated by the 45 µm diameter and 5 µm thick bottom cylinder. The metallic contacts are the top surfaces of the three rectangular pads that are 12 µm wide and 4 µm long. These pads are linked to the 10 µm-diameter pillar through 10 µm long and 3 µm thick arms. In reality, the wafer is a lot thicker in the $z$ direction and wider in the $(xy)$ plane, the arms are much longer and the pads are much wider in the $(xy)$ plane as well. To limit the calculation time, we had to optimize the geometry. We will study the impact of the reduced arms length in section 4.4.3. The doping profile is the same as shown in figure 4.13(b). The temperature is set equal to 10 K here as well. We swept the two voltages $V_A$ and $V_B$ from $-2$V to $+2$V and the third diode is not connected to any voltage supply (open circuit). We plot maps of the electrical quantities probed at the QD position, which we assume to be at $x = y = 0$ and 25 nm above the bottom of the intrisic region.

### 4.4.1 Electric field

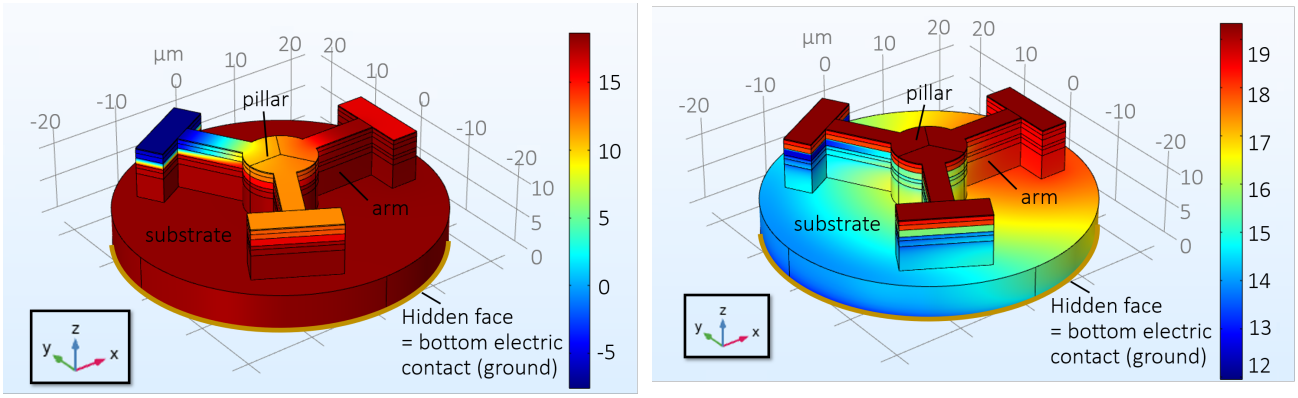


Figure 4.20: On the left (resp. right) panel, logarithm of the electron (resp. holes) concentration in the device, for $V_A = 0$V and $V_B = 1.8$V.

Figure 4.20 shows the concentrations (in logarithmic scale) of electrons and holes in the device for $V_A = 0$V and $V_B = 1.8$V. Since the voltage on diode B is positive and larger than the threshold voltage of the diode, the electrons flow towards the top of diode B because the top part is $p$-doped (and thus lets the electrons travel). Since the top part of diode B is very rich in electrons, the bottom part, on the other side of the intrisic region, gathers a high concentration in holes.
Figure 4.21 shows the three electric field components at the QD position.

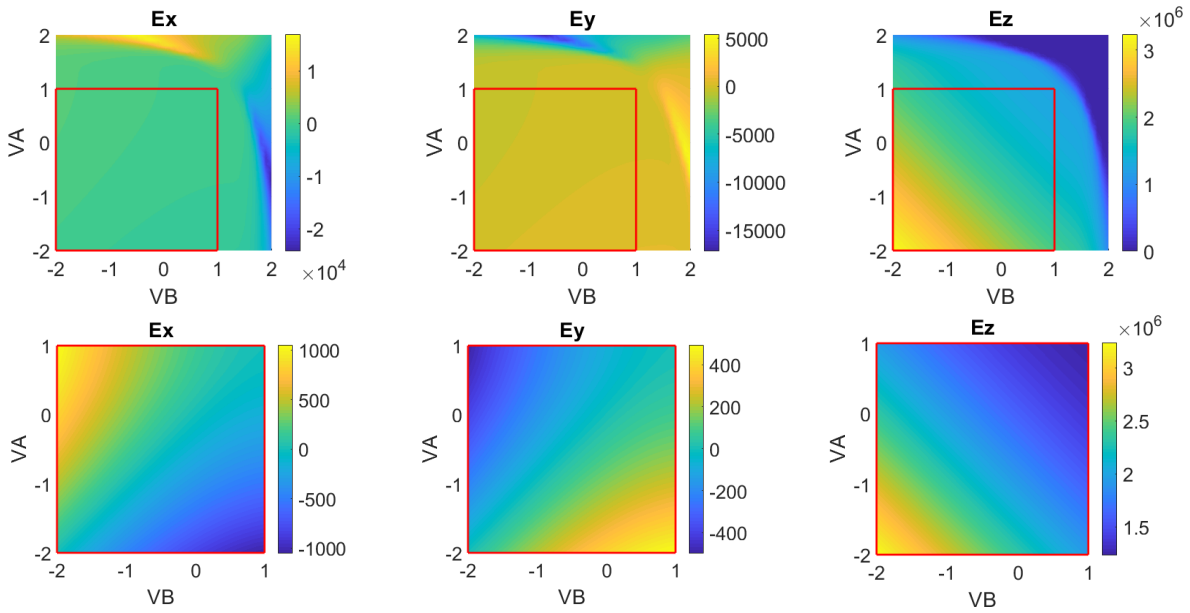


Figure 4.21: From left to right, the panels show the $E_x$, $E_y$ and $E_z$ components of the electric field. Since the scale does not allow us to see any variation of $E_x$ and $E_y$ other than on the top and the right parts of the plots, we plot these three quantities over a smaller range in the bottom line. All voltages are plotted in units of V and all electric field components are in units of V/m.

As we saw from the one-dimensional model in figure 4.17, the dramatic drop of $E_z$ matches with a rise of the absolute values of the in-plane components $E_x$ and $E_y$. Depending on which diode is current-passing (A or B), the in-plane components $E_x$ and $E_y$ can be chosen to be positive or negative. We conclude that we are able to control both the amplitude and the sign of the in-plane electric field components.

Figure 4.22 shows the evolution of the three components of the electric field as a function of $V_B$, for fixed values of $V_A$ set to 0, 1 and 2V. Note that connecting the second electrical contact makes the behaviour of $E_x$ and $E_y$ different from the one of $E_x$ in figure 4.14(b). We observe that for $V_A = 0$V and 1V, the amplitude of $E_z$ is much larger than the in-plane components $E_x$ and $E_y$. However, for $V_A = 2$V, the three components are tunable with a comparable amplitude. The ratios $|E_x/E_z|$ and $|E_y/E_z|$ tend to infinity as $E_z$ crosses zero. Also, the tuning range of $E_x$ is larger than $E_y$ in the present case since the swept voltage is aligned along $x$ with the pillar. Note that $E_x$ also changes sign in figure 4.22(e) (for $V_A = 2$V).

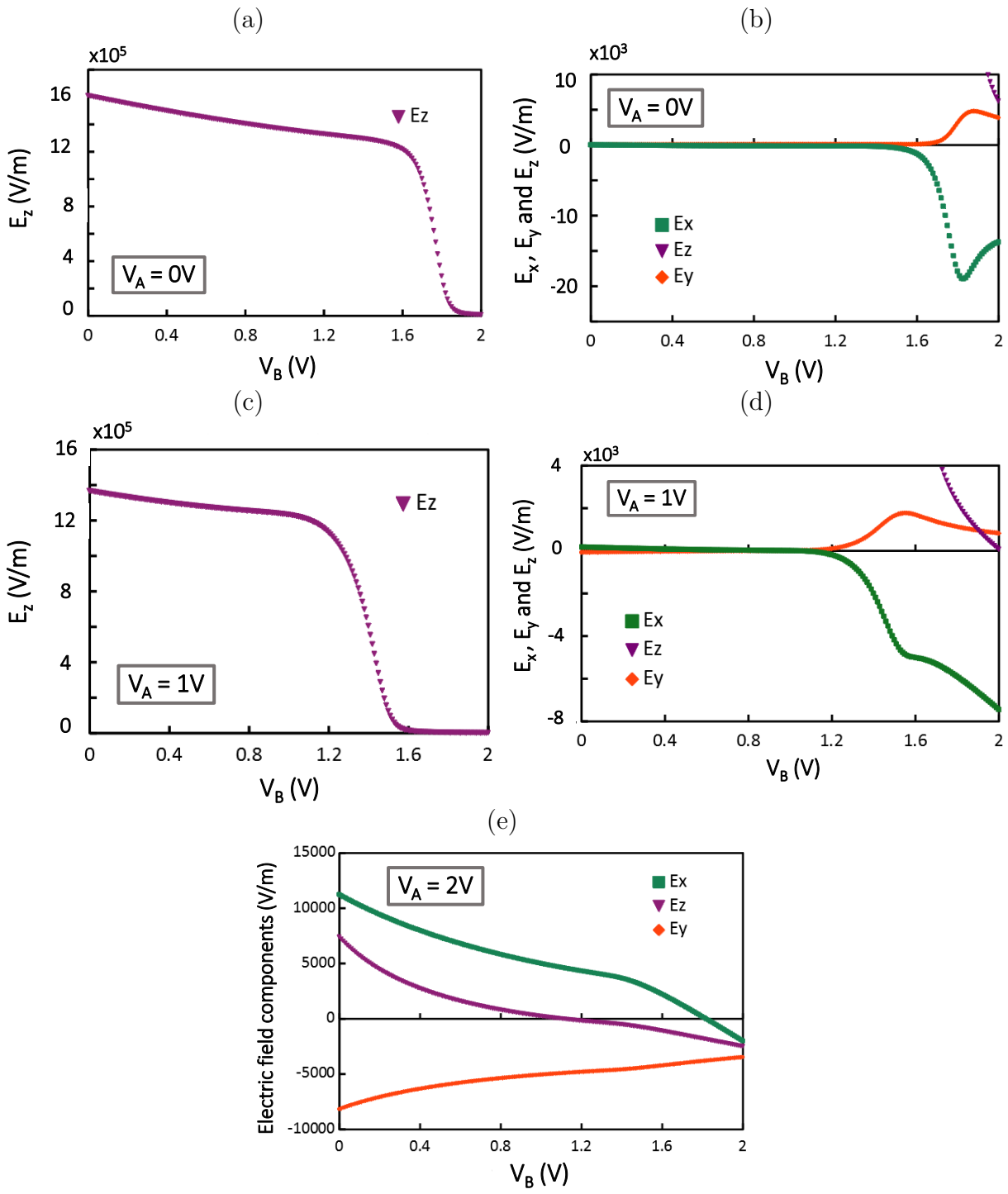


Figure 4.22: (a) Vertical component of the electric field as a function of $V_B$ for $V_A = 0$V. (b) In-plane components of the electric field ($E_x$ and $E_y$) as a function of $V_B$ for $V_A = 0$V. (c) Vertical component of the electric field as a function of $V_B$ for $V_A = 1$V. (b) In-plane components of the electric field ($E_x$ and $E_y$) as a function of $V_B$ for $V_A = 1$V. (e) Three components of the electric field $E_x$, $E_y$ and $E_z$, for $V_A = 2$V. All the displayed electric fields were evaluated at the QD position and are expressed in units of V/m.

### 4.4.2 Current flowing through the terminals (metallic contacts)

We are interested in obtaining a controllable electric field in the three directions of space at the QD position. In this section, we calculate the current intensity crossing the pads A, B and the ground (that we write respectively $I_A$, $I_B$ and $I_{\text{ground}}$) as a function of the voltage values applied to the two diodes. We have seen previously that we can control the ratio of horizontal over vertical electric field when the diode lets current pass through. Calculating the current crossing the terminals (metallic contacts) then enables us to establish the link between the ranges of voltages where we can control $E_x$, $E_y$ and $E_z$ and its experimental signature: a current crossing the diode.

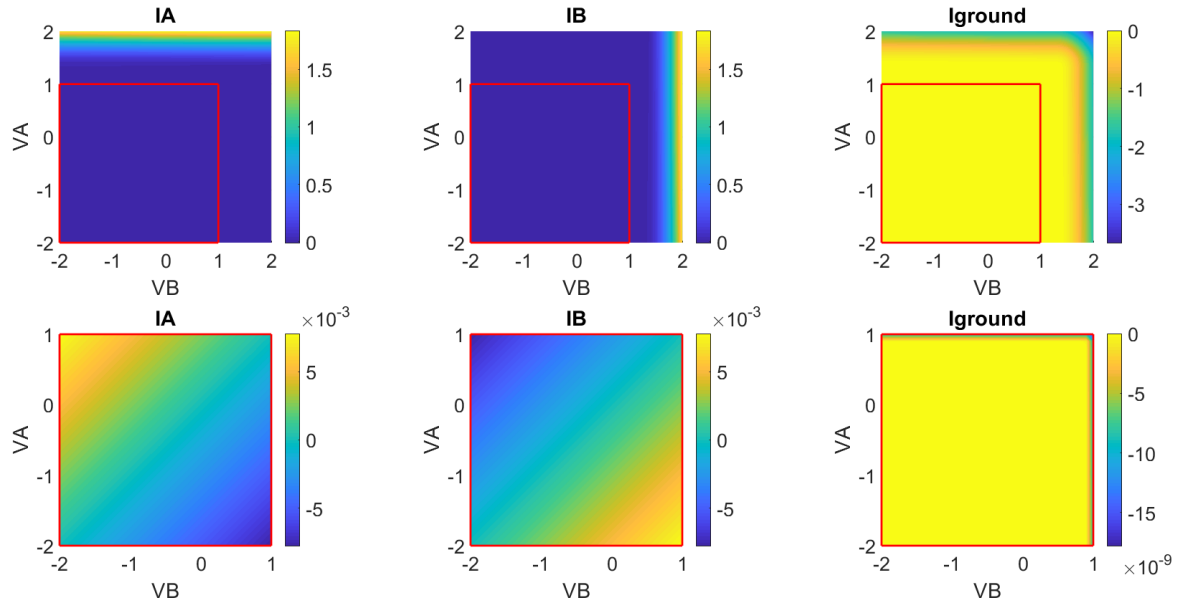


Figure 4.23: On the top line, from left to right: current flowing out of the top of diode A, current flowing out of the top of diode B, current flowing out of the bottom of the wafer (ground). All these quantities are given in amps. Since the scale does not allow us to see any variation other than on the top and the right parts of the plots, we plot these three quantities over a smaller range, namely from -2V to 1V, in the bottom line.

On the top panels of figure 4.23, we see that when one voltage is too high, current flows through the corresponding diode and goes to the ground. It corresponds to an IV curve invariant per translation along the other voltage. On the top right of the $I_{\text{ground}}$ curve, the ground receives current from both diodes, so it receives twice as much as on the right edge and top edge of the map. This is consistent with the conservation of the current intensity in the device, that is $I_{\text{ground}} = -(I_A + I_B)$ Comparing to figure 4.21, we see that we can experimentally identify the regime where we gain the most control on the electric field.

### 4.4.3 Control of the electric field in the passing diode regime

From the simulation plots obtained previously showing the possibility to apply an electric field in the three directions of space, we expect to control the FSS in the areas on the top right

of the maps, namely for $V_A$ and $V_B$ between 0V and 2V. To have a better insight of what happens in these regions, we plot various quantities for $V_A$ =0V and $V_B = 1.8$V.

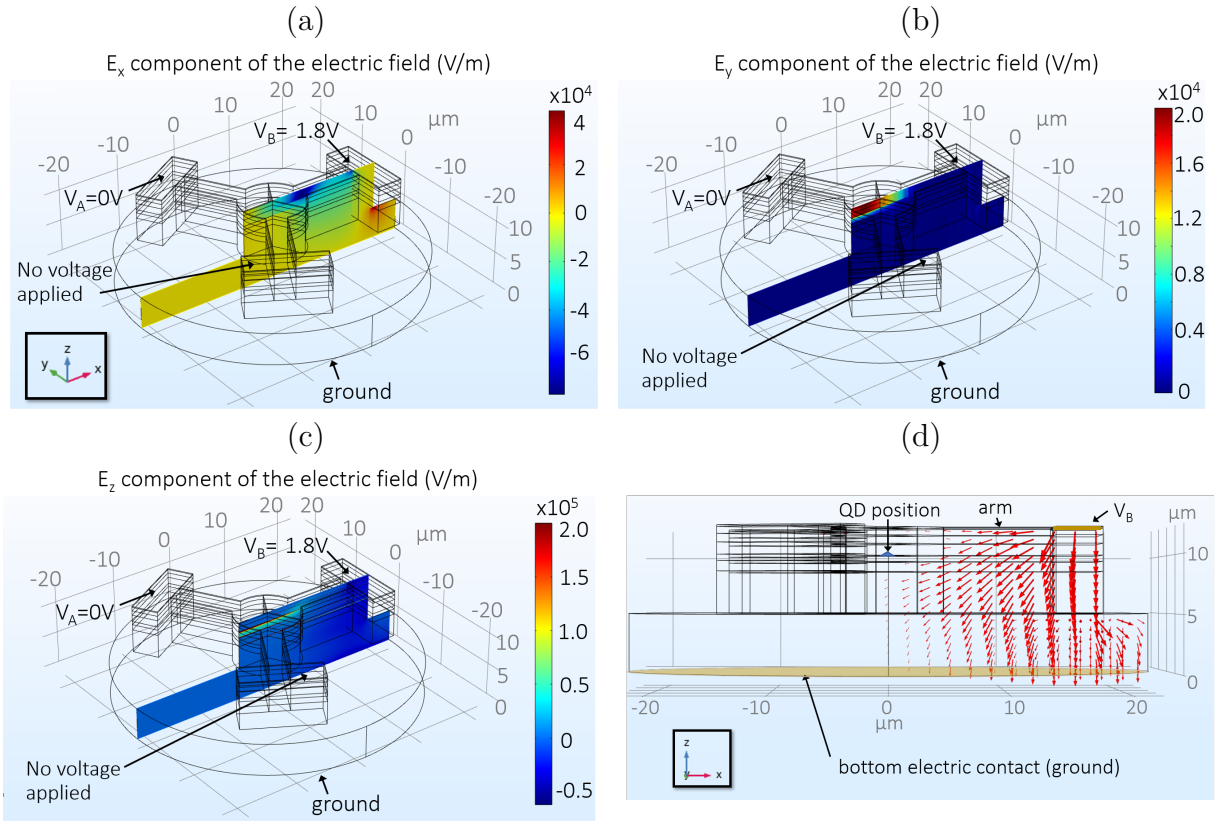


Figure 4.24: Panels (a), (b) and (c) show the $x$, $y$ and $z$ components of the electric field respectively (in V/m) in the $y = 0$ plane for $V_A = 0$V and $V_B = 1.8$V. At the position of the QD, we have $E_x = -1.8 \times 10^4$V/m, $E_y = 3.1 \times 10^3$V/m and $E_z = 2.9 \times 10^5$V/m. (d) Current density at every position in the $y = 0$ plane, for $V_A = 0$V and $V_B = 1.8$V. The length of the arrows represents the current density magnitude, in a logarithmic scale.

Figure 4.24 shows the electric field components and the current density in the $y = 0$ plane of the device, evidencing an electric field component in the plane at the QD location. Figure 4.24(d) shows that the current flows mainly through the large mesa diode or along the surface of the device, and a current flowing through the intrisic region of the pillar lower than elsewhere. An important question of this FSS control method is the current density created at the QD position, since it could impact the properties of its emission. As discussed later on (see section 4.5.4), the absolute value of the currents flowing at the QD position cannot be deduced from these simplified calculations. Here we discuss the qualitative dependence on the device geometry. From figure 4.24(d), we anticipate that if the arms are longer, then the current density at the position of the dot is lower. To verify this, we ran a simulation with the same geometry but longer arms (20 µm, which is the double of what we used in the rest of the chapter). The results are summarized in figure 4.25.

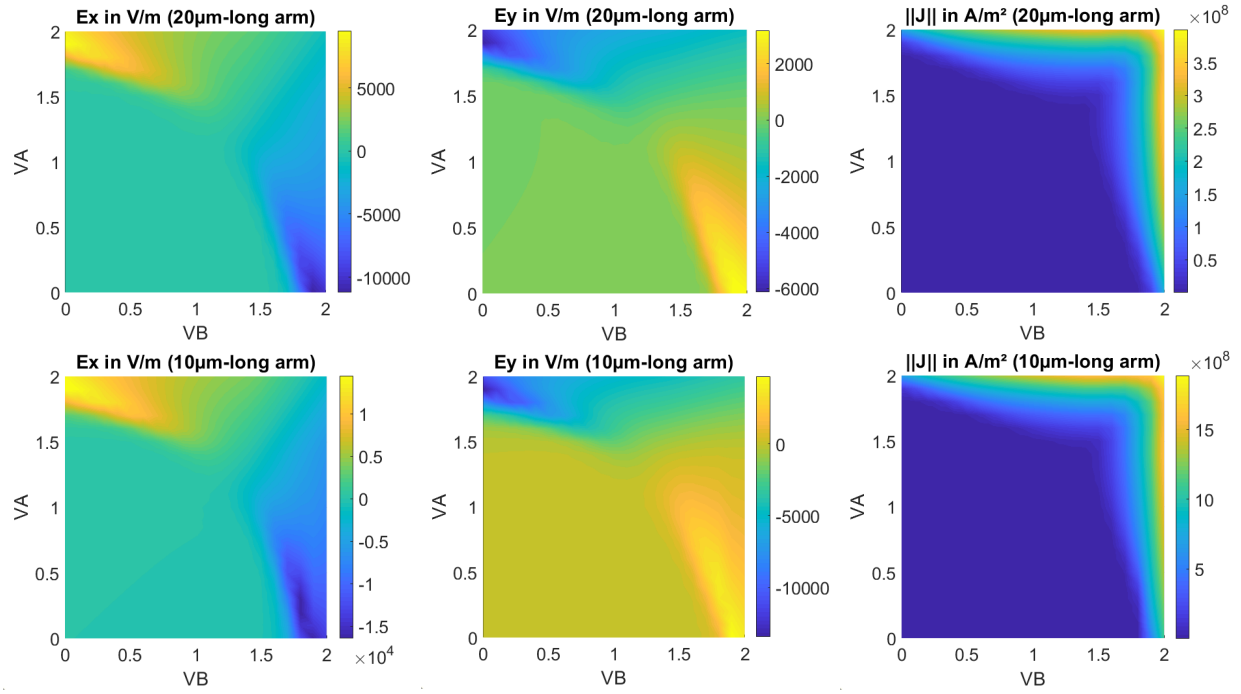


Figure 4.25: Comparison for the horizontal components of the electric field ($E_x$ and $E_y$) and the norm of the current density $||\mathbf{J}||$, between configurations with 20 and 10 micrometers long arms. The top line corresponds to a geometry with 20 micrometers long arms. For comparison, the bottom line corresponds to 10 micrometers long arms, which was the configuration used in the previous section.

In the regime where the diode is not pass-through, increasing the length of the arms from 10 µm to 20 µm leads to a decrease by a factor 2 of the current intensity $I_A$ flowing through the metallic contact on top of diode A, $I_B$ on top of diode B, the in-plane electric field components $E_x$ and $E_y$, and the current density at the QD position $J_{\text{norm}}$, as well as $J_x$, $J_y$ and $J_z$ (meaning that it has no impact on the current density direction). However, $E_z$ does not change.
In the other regime, namely when the diode becomes pass-through and shows a dependence on the resistance, increasing the length of the arms by a factor of 2 does not impact the values of $I_A$ nor $I_B$. Figure 4.25 shows the horizontal components of the electric field $E_x$ and $E_y$, and the norm of the current density, for devices with 20 µm and 10 µm long arms. The electric field components are about twice as low while the current density at the QD position is about 5 times lower than when the device has 10 µm long arms. We conclude that in the area where the ratio $E_x/E_z$ is tunable, an increase in the length of the arms results in a much quicker decrease of the current density than for the electric field seen by the QD. This study shows that controlling the arms length should allow controling the electric field at the QD position without having a significant current flowing through.

### 4.4.4 Regime of non-passing diode

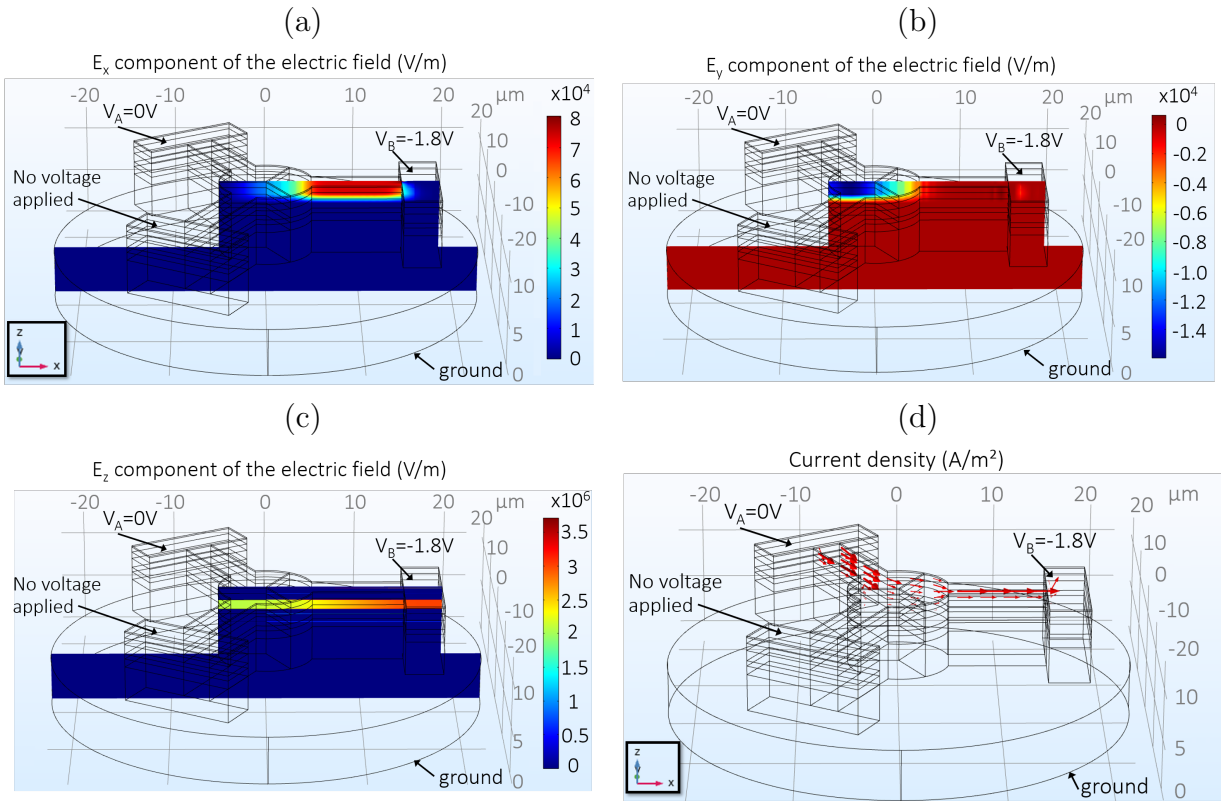


Figure 4.26: (a), (b) and (c) correspond respectively to the $x$, $y$ and $z$ components of the electric field (in V/m) in the $(xz)$ slice of the device at $x = 0$. At the position of the QD, we have $E_x = 7.3 \times 10^2$V/m, $E_y = -3.4.10^2 \times 10^3$V/m and $E_z = 2.3 \times 10^6$V/m. (d) Current density in the device. These four images were acquired for $V_A = 0$V and $V_B = -1.8$V.

We discuss here the other limit, where none of the diodes are passing. We set the voltages to $V_A = 0$V and $V_B = -1.8$V. In figure 4.26, we see that the current flows through the top of the device and that the electric field still shows horizontal components in the QD plane, but this time its value is positive so it is oriented in the other direction compared to figure 4.24 where $V_A$ and $V_B$ were set equal to 0V and +1.8V respectively. The $E_z$ component is about $2 \times 10^5$ in the intrisic region

However, the in-plane components of the electric fields are orders of magnitude lower than the vertical one when none of the diodes is passing. The regime where at least one diode is passing, is thus more likely to allow for control of the exciton FSS and wavelength.

## 4.5 Experimental study

We now turn to the experimental study of the proposed scheme. Since this project started not long before the move of the lab, we did not have enough time to implement the *in situ* lithography process on the sample before taking measurements. In order to have QDs in resonance

with the cavity, we then chose to work with a sample with a large number of QDs per unit of energy. When working in the context of single-photon generation, we avoid having such a high QD density to not have more than one transition line at the wavelength we are interested within the diameter of a micropillar. A way to reduce this density is to anneal the samples. As mentioned before, the annealing also leads to a reduction of the FSS [219, 220]. Here we use a sample which had not been annealed, so where several QD transitions are measured in the cavity modes spectral range. Since the position of the QD is not controlled within the pillar, we do not study the effect of the cavity. However, the method described in this section is fully compatible with the *in situ* technique developed to make bright photon sources in our group.

We fabricated a sample with two different structures, which picture is shown in figure 4.27(b). The shape shown on the left of figure 4.27(a) was the initial idea, with 50 µm-long 2 µm thick arms. We also fabricated the one shown on the right, with a shorter portion of the arms with a 2 µm width and a wider 15 µm thick second part, in case the long thin ridges would not be wide enough to be etched properly. The pillars have a 10 µm diameter to observe several QD lines per pillar.

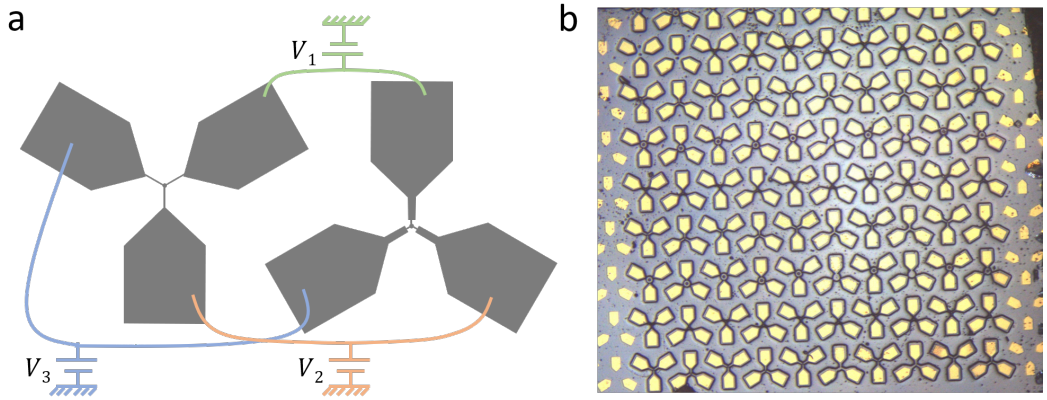


Figure 4.27: (a) Drawings of the two explored geometries with the wires set up to connect several pillars at once. (b) Picture of the sample using a microscope.

After implementing the wire bonding (that we can see in figure 4.18(b)), the sample was cooled down to 7 K in a cryostation that has only 5 electrical outputs. Connecting one device already requires 4 of these outputs, one per diode and one for the ground. In order to be able to explore the characteristics of several devices without having to warm up, change the connections and cool down the sample again, we connected several devices together at once, as shown in figure 4.27(a).

### 4.5.1 Determination of the FSS

For the generation of entangled photon pairs, one needs to find a biexciton with the corresponding exciton. A way of identifying such a set of states is to vary the excitation power and observe the dependence of the transition emission intensity of the line. If the intensity

increases linearly (resp. quadratically), it is a good indication that the line corresponds to an exciton (resp. biexciton) [221]. This is due to the fact that the intensity of the exciton (resp. biexciton) line is proportional to the probability to create one (resp. two) electron-hole pair(s) with one excitation pulse. Once we know which transitions are excitons and which are biexcitons, we can vary the excitation polarization angle and see which couple has complementary behaviours ($E_X + E_{XX} = \text{constant}$). With our sample presenting many QD lines, we had a hard time adopting such approach. Instead, we focus on transitions that show an FSS, and we work at low power so the studied transitions are mainly excitons.

The experiments of this chapter were implemented using the same cross-polarization setup as used in the rest of the thesis, but using non-resonant excitation. An example of a spectrum we obtained is shown in figure 4.28. Using a least-squares curve fit in MATLAB to fit individual lines by Lorentzian functions, we could determine their central wavelength and intensity.

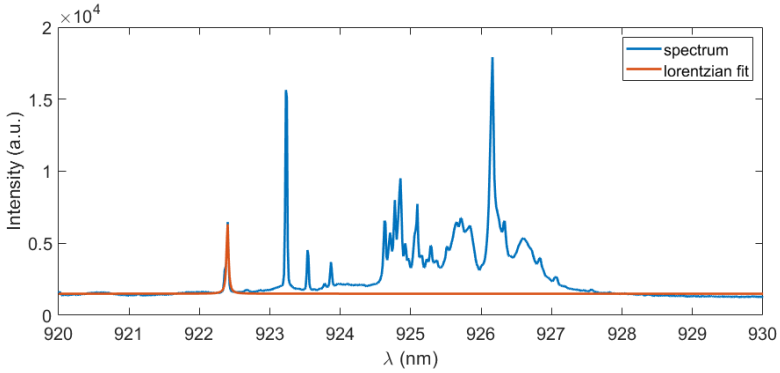


Figure 4.28: Example of a spectrum, taken at $V_1 = 0$ and $V_2 = 0$, with a 10 seconds integration time. The excitation laser power was 86 µW and its wavelength was 830nm. The orange line is the fit for one of the transition lines, using a Lorentzian function.

By rotating the HWP between the PBS and the sample, the polarization of the excitation light was varied, as well as the polarization of the collected light. However, non-resonant excitation is known to lead to a mostly non-polarized emission thanks to the rapid decoherence of the hole spin during the relaxation towards the ground state [222]. Then whatever HWP angle we use, both the QD exciton states are incoherently populated and we eventually only control the collected light polarization. When exciting an exciton, we collect one of the two excitonic states' polarization (say $X$) for a given angle, and switch progressively to the other one ($Y$) by rotating the HWP, reaching it completely for a rotation of $\pi/4$.

We acquire spectra for a wide set of HWP angles and select several lines that look promising (isolated and bright) and fit them with a Lorentzian function. Plotting the obtained wavelength of the peak as a function of the HWP angle allowed us to identify the interesting transitions, namely those that showed an oscillation in wavelength when the HWP is rotated. An example of such an oscillation is presented in figure 4.29. The FSS is equal to the peak-to-peak amplitude of the sinusoid, here $9.2 \pm 0.4$ pm. This measurement allows us to determine the two HWP angles corresponding to the lowest and highest wavelengths that are the wavelengths of the two dipoles.

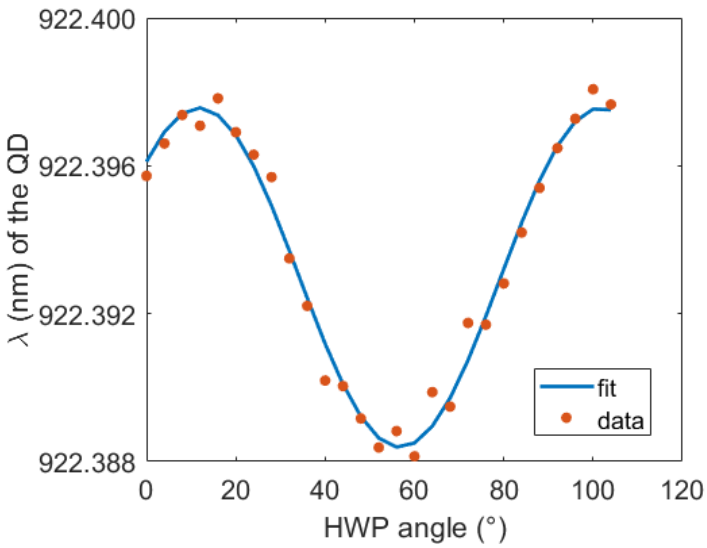


Figure 4.29: Wavelength of the QD line which is fitted in figure 4.28 as a function of the HWP angle. This measurement allows us to determine two angles of the HWP corresponding to an excitation along the different dipoles. The expression used to fit is $\lambda(\phi) = c_1 \cos((2\pi/90)(\phi - c_2)) + c_3$ where $c_i$ are the fit parameters. The returned result was $\{c_1 = 0.0046 \pm 0.0003$ nm, $c_2 = 11.7 \pm 0.9°$, $c_3 = 922.3930 \pm 0.0002$ nm$\}$, corresponding to an FSS of $9.2 \pm 0.4$ pm, HWP angles for the maximum and minimum of wavelength of $11.7 \pm 0.9°$ and $56.7 \pm 0.9°$, and $c_3$ is the central wavelength.

We present results coming from two sets of measurements on two samples. For the first one, we used non-resonant excitation, and the voltage control was manual. For the second one, the QD density was too high and we used p-shell excitation to reduce the number of emission lines, and the voltage variation was automated.

### 4.5.2 FSS control

In this section, the considered device has the geometry displayed on the left in figure 4.27(a). We first determined the two angles for each QD as explained previously. For each of these two angles, we acquired spectra for each set of voltages, exciting the dots with a 38 µW continuous wave non-resonant laser (830 nm). Exciting that far off-resonance allows us to obtain spectra with lots of visible lines. Only two voltages out of three were varied, to start simply, and also because it was a very long process: the experiment was not automated yet. The third diode was not connected. We fit each spectrum to get the wavelengths of both dipoles, calculated the difference (equal to the FSS) and plotted it as a function of the two varied voltages.

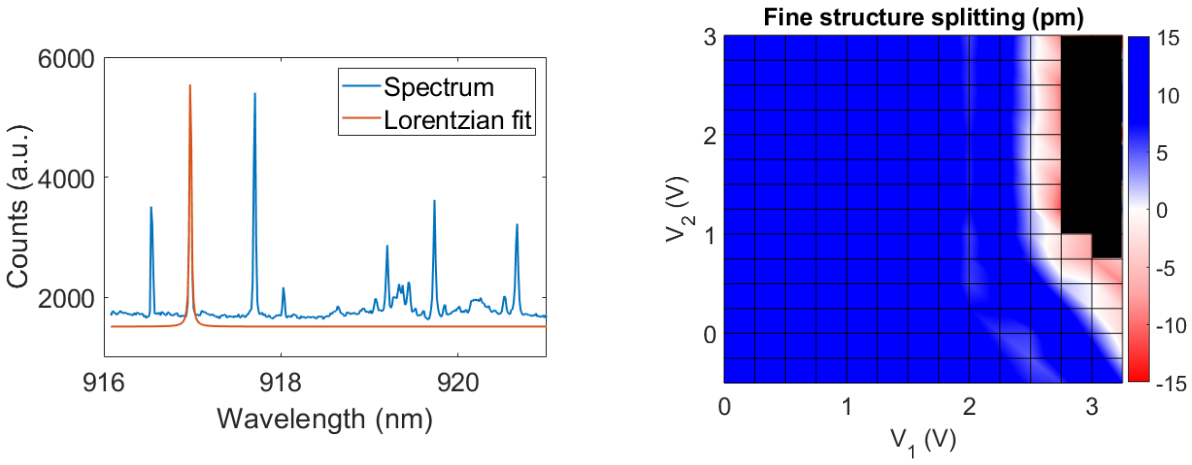


Figure 4.30: Left panel: spectrum, taken at $V_1 = 0$ and $V_2 = 0$, with a 10 seconds integration time. The excitation laser power was 38 µW and its wavelength was 830 nm (non-resonant). The orange line is the fit using a Lorentzian function, for one of the transition lines showing an FSS. Right panel: fine structure splitting for the line fitted on the left panel, as a function of two voltages $V_1$ and $V_2$, applied on two of the three diodes. The black points correspond to inconclusive measurements due to the weak signal.

The white areas of the 2D map in figure 4.30 correspond to a zero FSS, which is reachable for a continuous set of voltages. For this given QD, the FSS can be varied from around −5pm to around +15pm and it is possible to tune it to zero with the two electrical knobs. The FSS variation happens mostly for high values of $V_1$, which most probably corresponds to the regime where the diode is pass-through, as we saw in section 4.4.1. Furthermore, we notice that the result is not symmetric with respect to the $V_1 = V_2$ line of the plot. This means the influences of the two voltage sources are different: that may be explained by the fact that the two different electrical paths have different resistances, and/or the fact that the dot might not be positioned equidistantly from the diodes. The black area on the top right of the 2D map in figure 4.30 are outliers (they correspond to failed fits). This is due to a drastic decrease of the dipoles' emission intensity for these sets of voltages, as shown in figure 4.31. This decrease can be explained by the fact that the Stark effect has an impact not only on the wavelength of a given dipole, but also on its strength.

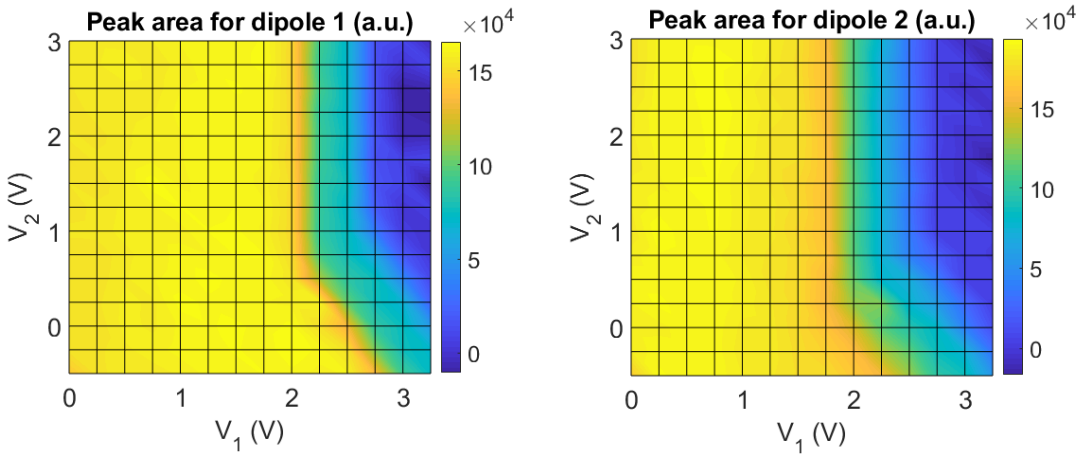


Figure 4.31: Intensity of the peak at wavelength 916.9 nm, for the two predetermined HWP angles.

### 4.5.3 Simultaneous FSS and wavelength control

Another QD transition was analyzed from the same set of measurements, that demonstrates both a control of the FSS and the wavelength. We found the HWP angles corresponding to the exciton dipoles are the same as for the previous transition. This observation shows that the various QD lines are likely to be determined by the crystal environment and strains that do not change drastically within the excitation laser spot diameter. For the transition showing a wavelength equal to 919.7 nm, the obtained map is shown in figure 4.32.

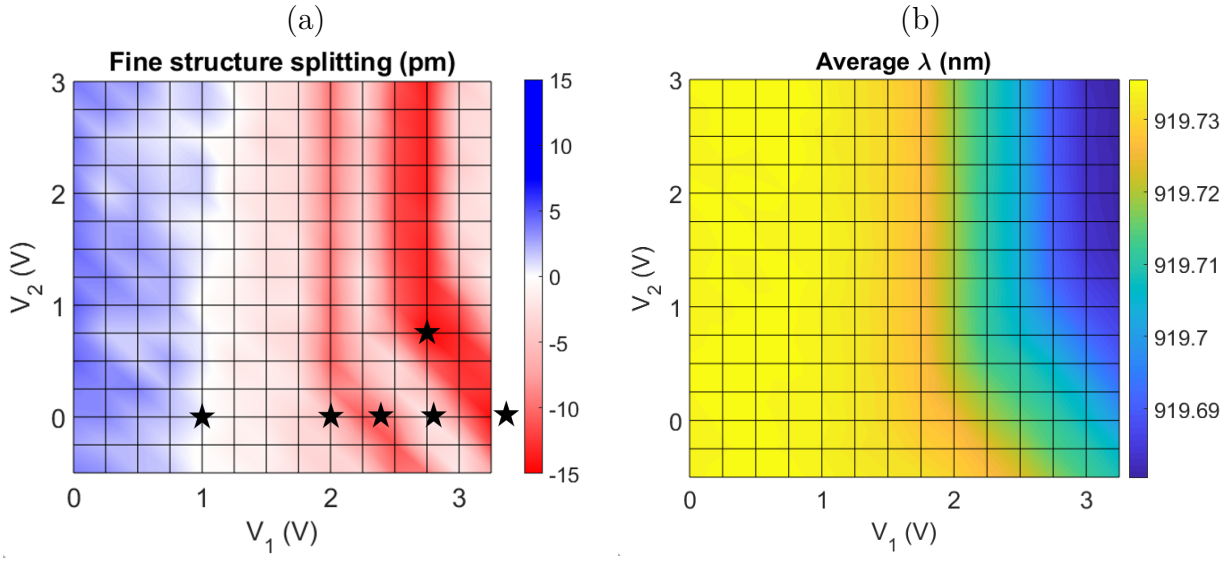


Figure 4.32: (a) FSS as a function of two of the voltages, for an emission line of wavelength around 919.7 nm. The black stars show the sets of voltages that I chose to investigate to see if the dipoles rotate while we vary the voltages. (b) Corresponding average wavelength of the two dipoles $(\lambda_1 + \lambda_2)/2$, in nm.

The intensity of this QD transition is shown in figure 4.33 for the two dipoles.

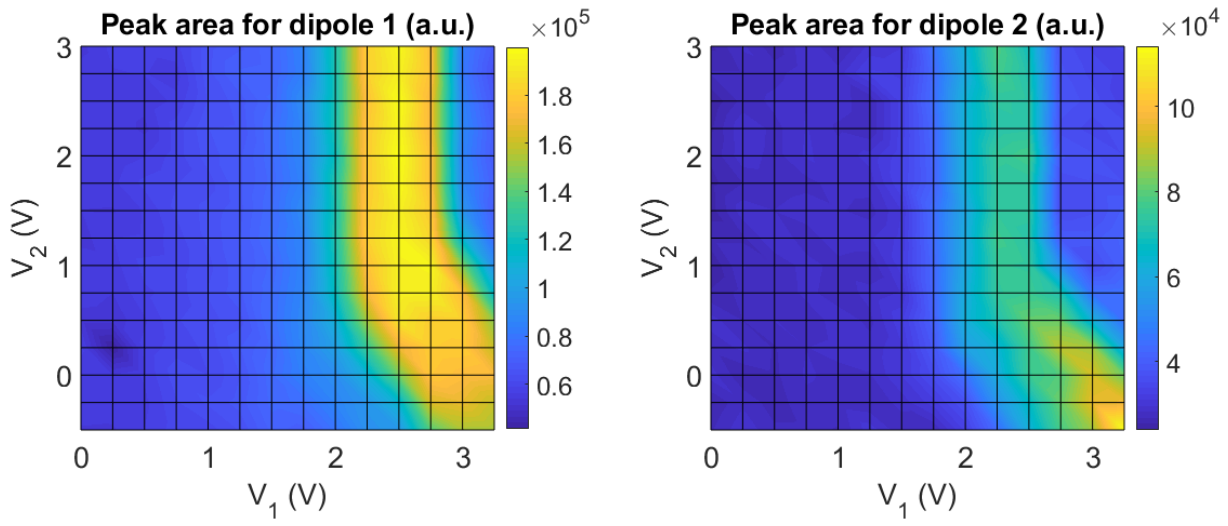


Figure 4.33: Intensity of the peak at wavelength 919.7 nm, for the two predetermined HWP angles.

The first observation we make is that it is possible to reach a zero FSS without having a drop in intensity of the QD transition, for a continuous set of voltage values, corresponding to the white area in figure 4.32(a).
We also see, when looking at figures 4.32(a) and (b), that a zero FSS is reached for a given average wavelength, and almost reached for two other average wavelengths. The use of the third diode should allow for a perfectly zero FSS for several wavelengths. Overall, the wavelength varies by around 50 pm, a small value compared to values reached with strain tuning in bulk samples. However, this tuning range is close to the cavity linewidth used in our micropillar cavity devices operating in the strong Purcell effect [70].

Finally, we checked that for this set of measurements the QD dipoles do not rotate with the voltages, validating the results of figure 4.32. Indeed in case of dipole rotation, the HWP angles we use would no longer correspond to the minimum and maximum of the abscissa of the peak. For that purpose, we went back to some couples of voltages values (marked by black stars in figure 4.32). For each of these points we acquired spectra for different HWP angles, from 140 to 232 degrees, by steps of 4 degrees. The spectra are presented in figure 4.34.

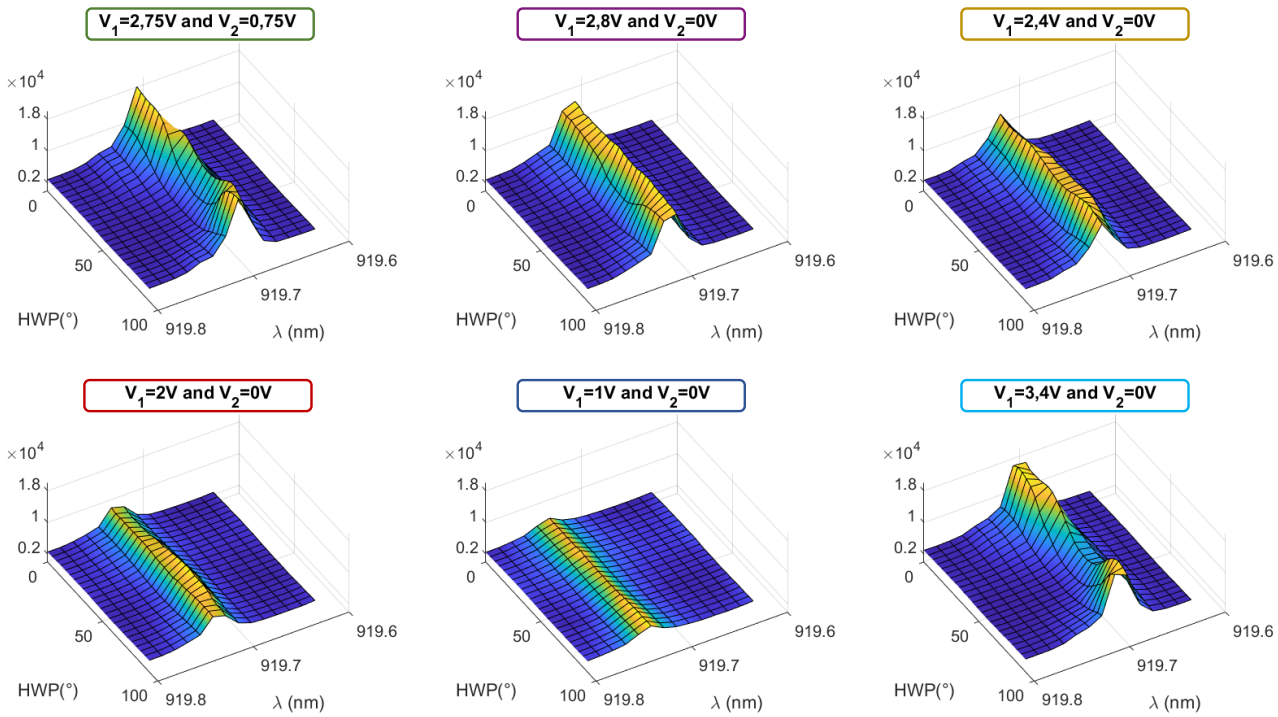


Figure 4.34: Spectra as a function of the HWP angle, for the couples $\{V_1, V_2\}$ marked by black stars in figure 4.32.

We fit all the spectra by Lorentzian functions and extracted the central wavelength, that we plot as a function of the HWP angle in figure 4.35. We fit the obtained data with sinusoids and extract the amplitude (equal to the FSS), the average (equal to the central wavelength) and the phase (that indicates the dipoles orientation).

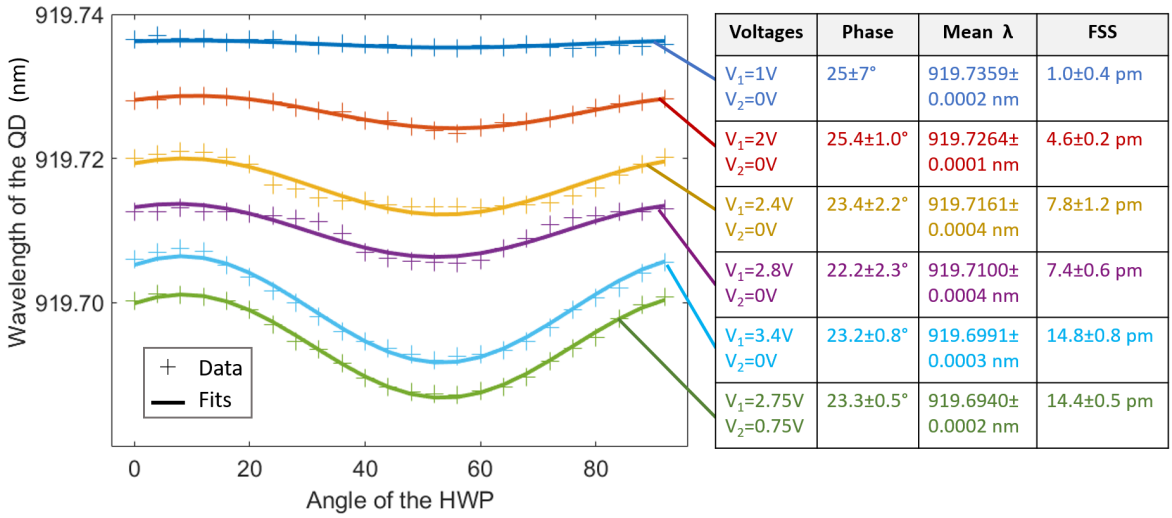


| Voltages | Phase | Mean λ | FSS |
|---|---|---|---|
| $V_1$=1V $V_2$=0V | 25±7° | 919.7359± 0.0002 nm | 1.0±0.4 pm |
| $V_1$=2V $V_2$=0V | 25.4±1.0° | 919.7264± 0.0001 nm | 4.6±0.2 pm |
| $V_1$=2.4V $V_2$=0V | 23.4±2.2° | 919.7161± 0.0004 nm | 7.8±1.2 pm |
| $V_1$=2.8V $V_2$=0V | 22.2±2.3° | 919.7100± 0.0004 nm | 7.4±0.6 pm |
| $V_1$=3.4V $V_2$=0V | 23.2±0.8° | 919.6991± 0.0003 nm | 14.8±0.8 pm |
| $V_1$=2.75V $V_2$=0.75V | 23.3±0.5° | 919.6940± 0.0002 nm | 14.4±0.5 pm |

Figure 4.35: Wavelength of the peak as a function of the HWP angle for different sets of voltages, corresponding the the black stars shown in figure 4.32. The crosses (+) correspond to the experimental data and the solid lines correspond to fits by sinusoids, of expression $\lambda(\phi) = c_1 \cos((2\pi/90)(\phi - c_2)) + c_3$ where $c_i$ are the fit parameters. The parameter $c_1$ is equal to half the FSS, $c_2$ is the phase in degrees and $c_3$ is the central wavelength. The returned results are displayed in the table on the right.

Figures 4.34 and 4.35 confirm that the set of parameters $V_1 = 1V$ and $V_2 = 0V$ allows for a zero FSS. The phase varies by 2.2° at most. We see that, for the present QD, the dipoles do not rotate when the voltages are varied.

### 4.5.4 Link with current flows

In this section, we evidence the connection between the observed FSS and the currents flowing in the device.

Here a higher density sample is explored. In order to obtain spectra where the lines are more isolated, we excited the QD transitions more selectively by using p-shell excitation. This consists in using a lower excitation energy to excite only transitions corresponding to both electron and hole states confined in the QD. Also at that point, we automated the data acquisition: the two voltages were swept automatically, as well as the rotation of the HWP over a range of 90° so that we can detect a variation of the sinusoid phase from one voltage to another. This automatization allowed us to use much smaller steps and obtain more detailed maps. For each set of parameters, the spectra were acquired, as well as the current flowing into each terminal. We used a continuous wave laser with a power of 300 µW. The integration time of each spectrum was set to 1 second and we swept the voltages from −3V to +5V. The excitation wavelength is equal to 900.35 nm, thus closer to resonance than in the previous study. To choose this wavelength, we scanned the continuous wave laser until we observed isolated emission lines with a high intensity.

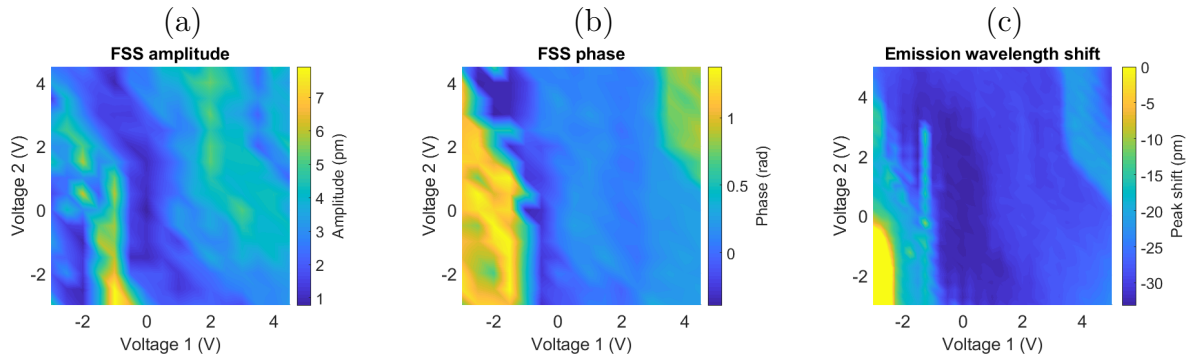


Figure 4.36: (a) FSS given by the peak-to-peak amplitude of the sinusoid obtained by plotting the central wavelength of the fit of the spectra. (b) Phase of the sinusoid mentioned before. (c) Shift of the average wavelength of the two excitonic peaks, in pm. The central wavelength corresponding to a 0 pm shift is $931.86 \pm 0.03$nm. The yellow region in the bottom left of the map actually corresponds to a shift of up to +30 pm but was dominating the colormap so we set it to zero.

Like in the previous study, a variation of the FSS is observed as a function of the two applied biases (see figure 4.36(a)). This time, we had continuously access to the phase since we rotated the HWP for each couple of voltages. We observe on figure 4.36(b) that the phase changes by $\pi$ when the voltages cross the FSS dip in the region corresponding to high voltages, meaning that the FSS actually goes from positive to negative when crossing that dip. It thus shows that a zero FSS is achievable for this QD with the two knobs used in this study. Here we observe a significant variation in phase for the lowest values of $V_1$, which shows that the QD dipoles rotate when changing the voltages. The shift of the average peak position around an average wavelength equal to $931.86 \pm 0.03$ nm is represented in figure 4.36(c). It varies as well with the voltage, by around 60 pm.

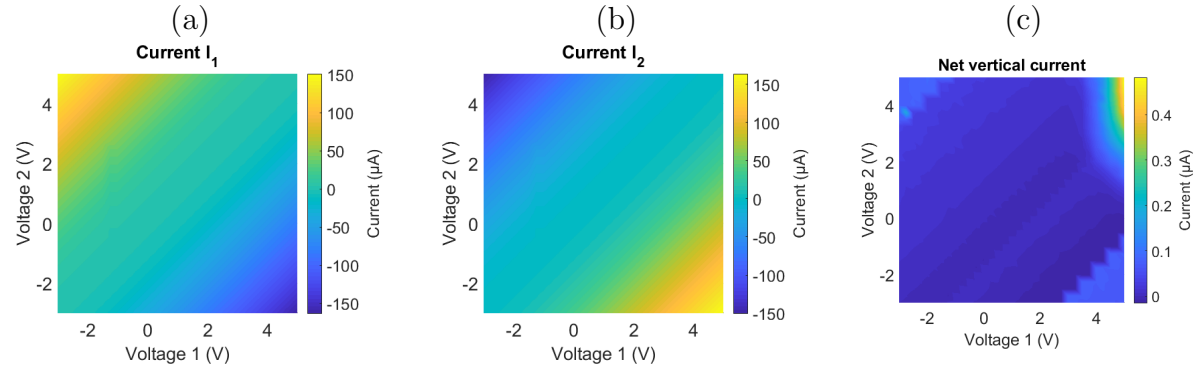


Figure 4.37: Panels (a) and (b) show the currents flowing through the two connected pads. Panel (c) corresponds to their sum. The flat blue areas on the top left and bottom right regions in panel (c) correspond to the minimum detectable current.

For these measurements, we connected only one device at once, so the currents flowing in the sample are determined only by the resistances in the studied device.

Note that in figure 4.37(a) and (b), we retrieve the trend given by the simulation for the currents $I_A$ and $I_B$, when restricting the ranges of $V_A$ and $V_B$ to [-2V,+1V]. The corresponding plot obtained from the COMSOL simulation was shown in the bottom panels of figure 4.23. Figure 4.37(c) shows the sum of currents $I_1 + I_2$. When $V_1$ increases, we approach the regime where the ground receives current, which means that the diode becomes pass-through. The transition towards that regime is where the FSS amplitude varies, which confirms that the current flowing through the diode gives rise to a controllable horizontal component of the electric field at the QD position.

## 4.6 Discussion

In this section, we discuss the differences between the features from the calculated maps of electric field and from the measured FSS. We then discuss the outcome of this study in terms of quality of the emitted photons and discuss the next steps of this study.

### 4.6.1 Difference between the numerical field maps and the FSS experimental features

The experimental observations for the FSS and wavelength (see figures 4.32 and 4.36) do not show the same symmetry as the theoretical calculated maps for the in-plane electric field such as 4.21. Indeed, self-assembled QDs show random size and orientation, and their symmetry is randomly reduced from combined mechanisms (in-plane asymmetry, heavy/light hole mixing). We thus do not expect to observe an exact mapping between the calculated electric field 2D maps and the measured FSS ones. Moreover, depending on the position of the QD and the relative resistance of the ridges, asymmetries in the electric field itself can be retrieved by the simulations, as shown in this section.

(a) (b)

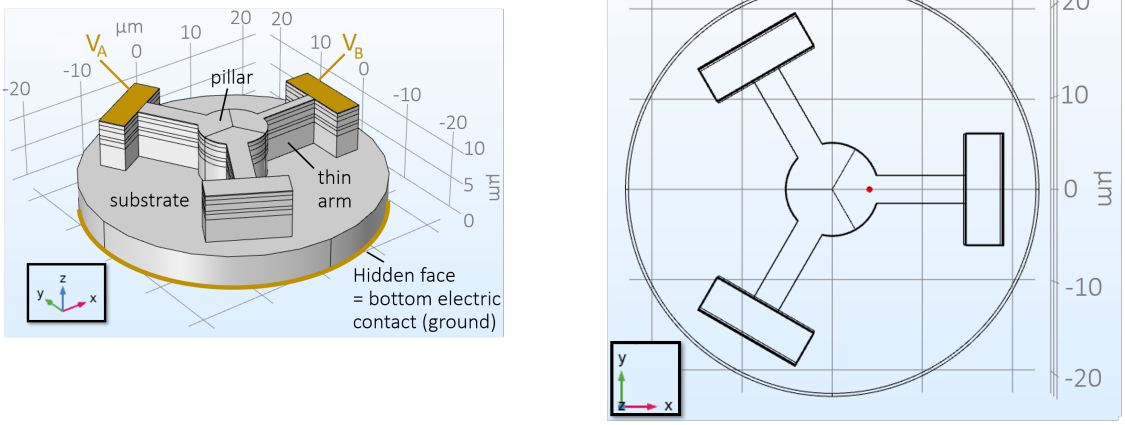


Figure 4.38: (a) Geometry built in COMSOL to simulate a device where the resistance of the different arms is not equal. The arm connecting the micropillar to diode B is one micrometer thick, which is half the thickness of the one connecting the micropillar to diode A. (b) Position of the dot at which the quantities are evaluated to see the effect of a non-centered QD. The coordinates of the dot are $x = 4$ micrometers and $y = 0$ micrometers).

### Asymmetry of the resistance of the arms

In this section, we aim at studying the effect of having a device with arms of difference resistances, which could arise from etching defects on very thin arms. To explore this numerically, we ran a simulation where one of the arms is half as thick as the other, as shown in figure 4.38(a). The sweeping range is from 0V to 2V for both the connected diodes.

Figure 4.39 allows us to compare the behaviour of the $E_z$ component of the electric field between the geometry with one thinner arm and the geometry with equally thin arms. We see that the drop happens for higher values of $V_B$ than $V_A$. This change is visible on every other quantity, as for the norm of the current density for example, which is shown in figure 4.39(b). This could explain the fact that 3V is not a high enough upper bound for $V_2$ to observe an effect on the experimental figures 4.30 to 4.33 of the chapter.

### Asymmetry of the QD position

To illustrate the asymmetry in electrical quantities due to the non-centering of the QD in the micropillar, we evaluated the values of the electrical quantities for a QD located at $x = 4\,\mu$m from the center of the 10 µm-diameter micropillar, as shown in figure 4.38(b).

In that configuration, the $E_z$ component of the electric field and the norm of the current density at the new position of the QD are presented in figure 4.40. At that position for example, it requires less voltage on diode B than on diode A to reach the interesting regime where we can control the ratio of electric field in the plane over the vertical field.

With smaller pillars comprising fewer QDs, the asymmetry related to the QD position should vanish, but the conductivity of the arms is not easily controllable. For example, it

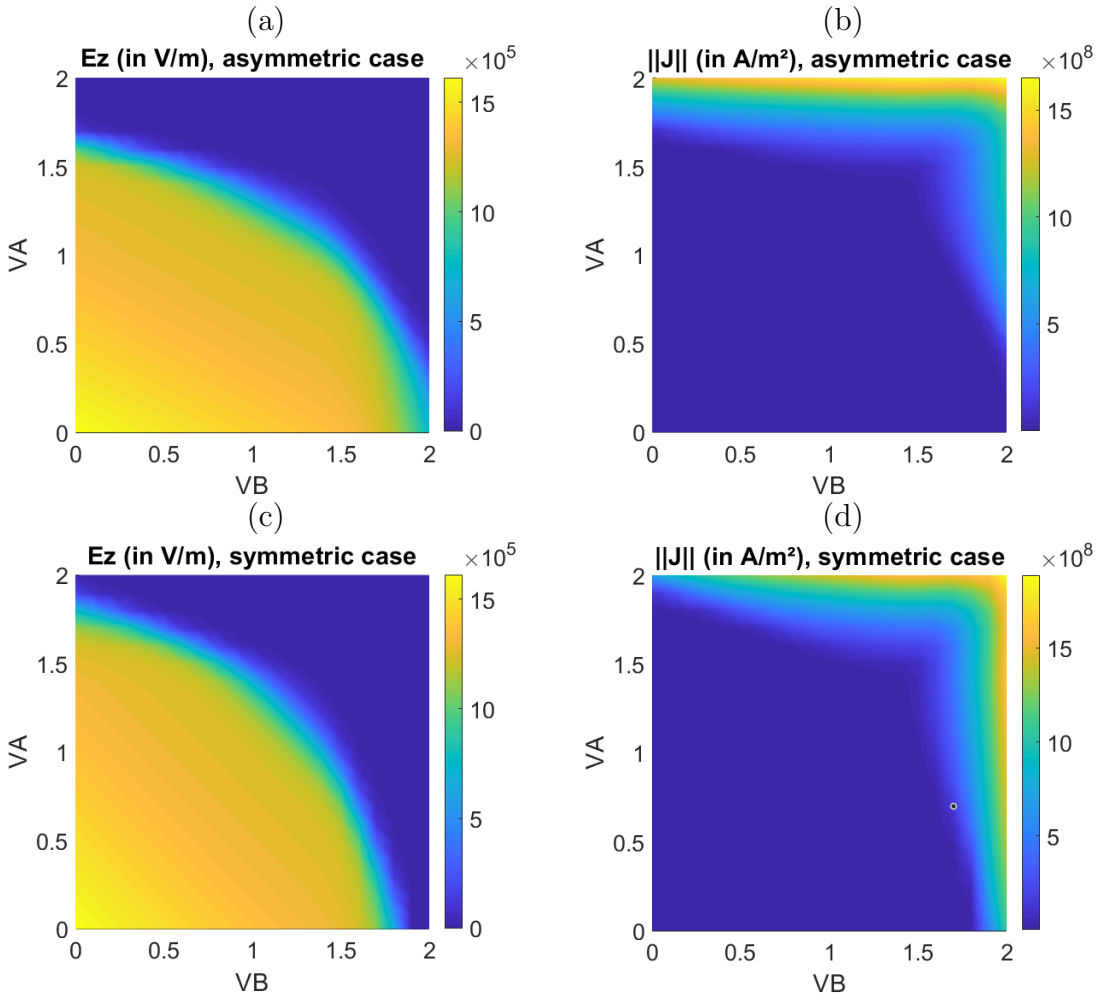


Figure 4.39: Panels (a) and (b) show respectively the $E_z$ component of the electric field (in V/m) and the norm of the current density $||\mathbf{J}||$ (in A/$m^2$), in the case where the device has one arm (the one leading to diode B) that is half as thick as the others. For comparison, panels (c) and (d) show the same quantities but in the case where all the device's arms have the same thickness.

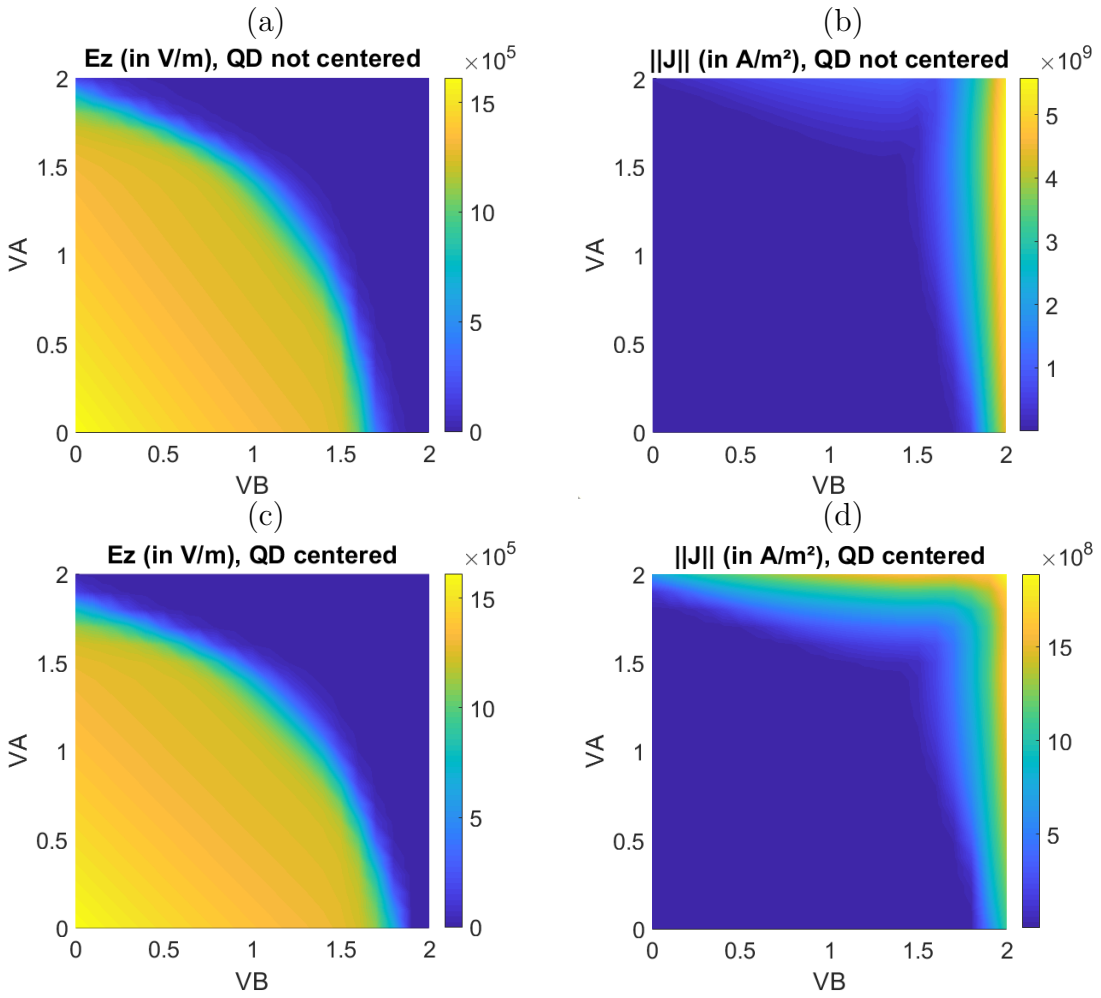


Figure 4.40: Panels (a) and (b) show respectively the $E_z$ component of the electric field (in V/m) and the norm of the current density $||\mathbf{J}||$ (in A/$m^2$), in the case where the QD is not at the center of the micropillar ($x = 4$ micrometers and $y = 0$). For comparison, panels (c) and (d) show the same quantities but in the case where the QD is centered.

happens that some of the devices arms are damaged, especially the long and thin ones (see figure 4.18). This implies that the field at the position of the QD is not foreseeable. One thus needs to first acquire spectra for each set of 3 voltages, see the effect on the wavelength and on the FSS, and decide on which set of parameters it is best to operate.

### 4.6.2 Current flowing through the QD

While our technique is based on generating a current that flows vertically through the diodes, we need to make sure that the current flowing at the vicinity of the QD remains quite low. Indeed, the contrary could lead to charge instability and decrease the indistinguishability.

The experimental currents crossing the metallic contacts shown in figures 4.37(a) and (b) are at least 5 orders of magnitude lower than the currents predicted by the simulation (see the plots of $I_A$ and $I_B$ in figure 4.23). This is probably due to how simplified our COMSOL model is. We assigned the material GaAs to the whole structure without taking into account the alternated layers of GaAs and AlGaAs of the Bragg mirrors. These layers make the path more difficult for charges to propagate through the structure.

On the edge of the $E_z$ drop on the 2D maps from the simulation section, the norm of the current density is on the order of magnitude of $10^8$ A/$m^2$. If we consider that the intensity of current crossing the metallic contacts is proportional to the current density at the QD position, then the actual current density is 5 orders of magnitude lower, meaning $10^3$ A/$m^2$. Furthermore, we have seen in section 4.4.3 that an increase of a factor 2 of the arms length leads to a decrease of the current density by a factor 5. This means that we can reasonably assume that the real length of the arms of 50 µm leads to a reduction by a factor of at least 10. The QD in-plane (resp. vertical) cross-section is about 10nm × 10nm (10nm × 3nm) and the current density at its position is on the order of $10^2$ A/$m^2$. We can calculate the current crossing an area centered on the QD and 10 times larger in the two dimensions: $S = 10^4\text{nm}^2$. In that case $J \times S$ is of the order of $10^{-12}$ A, which corresponds to $6 \times 10^6$ electrons per second. In a photon lifetime that is about 200 ps, there is on average $10^{-3}$ electrons crossing the QD in one photon emission lifetime. Electrons crossing the QD with such a low probability would be likely not to degrade the emitted photons' properties. This calculation of order of magnitude indicates that many parameters control the current actually flowing in the vicinity of the QD and that practical configurations can allow to minimize it. This analysis is further supported by experimental observations on the QD linewidth, as discussed now.

### 4.6.3 Quality of the generated photons

The current flowing through the QD is very low and is unlikely to degrade the photons' properties.

A first indication of whether this FSS control method could preserve the photons' quality is to study the linewidth of the emission line. We thus studied the possible modifications of linewidth and emission intensity as a function of the applied voltages. Note that here, the

diameter of the pillars is so large that we can consider that the QD is embedded into a planar cavity. We thus do not expect a modification of the spontaneous emission rate by cavity quantum electrodynamics.

The linewidth we measure under non resonant continuous wave excitation is in general determined by the charge noise at a long timescale (spectral wandering over a range on the order of 1 ms or more) instead of by the radiative linewidth. This is confirmed by the observation of linewidths larger than the minimal spectral resolution of about 13 pm, much beyond the transitions' radiative linewidths (on the order of 1 pm). Then, the variations in linewidth indicate a variation of the charge noise in the QD vicinity. However, this is true only as far as the emission intensity is not very reduced. Indeed, the peak area in continuous wave excitation is determined by the inverse of the transition radiative lifetime as well as by the probability to find the state in the considered state (quantified by $p_{\mathrm{QD}}$ introduced in section 1.5.4). A reduction of the signal can thus mean an increase of the radiative lifetime (by a decrease of the electron-hole overlap) or a decrease of the quantum efficiency due to charges tunneling out of the QD. The first option translates into a smaller intrisic radiative linewidth, the second one by an increase of the linewidth much beyond the radiative one. Then, a widened linewidth together with a signal reduction is the signature of charges tunneling out of the QD and of a reduction of quantum efficiency. This is what we observe at very high voltages (and high current intensities) on all the data presented here. However, for lower voltages, various behaviours are observed.

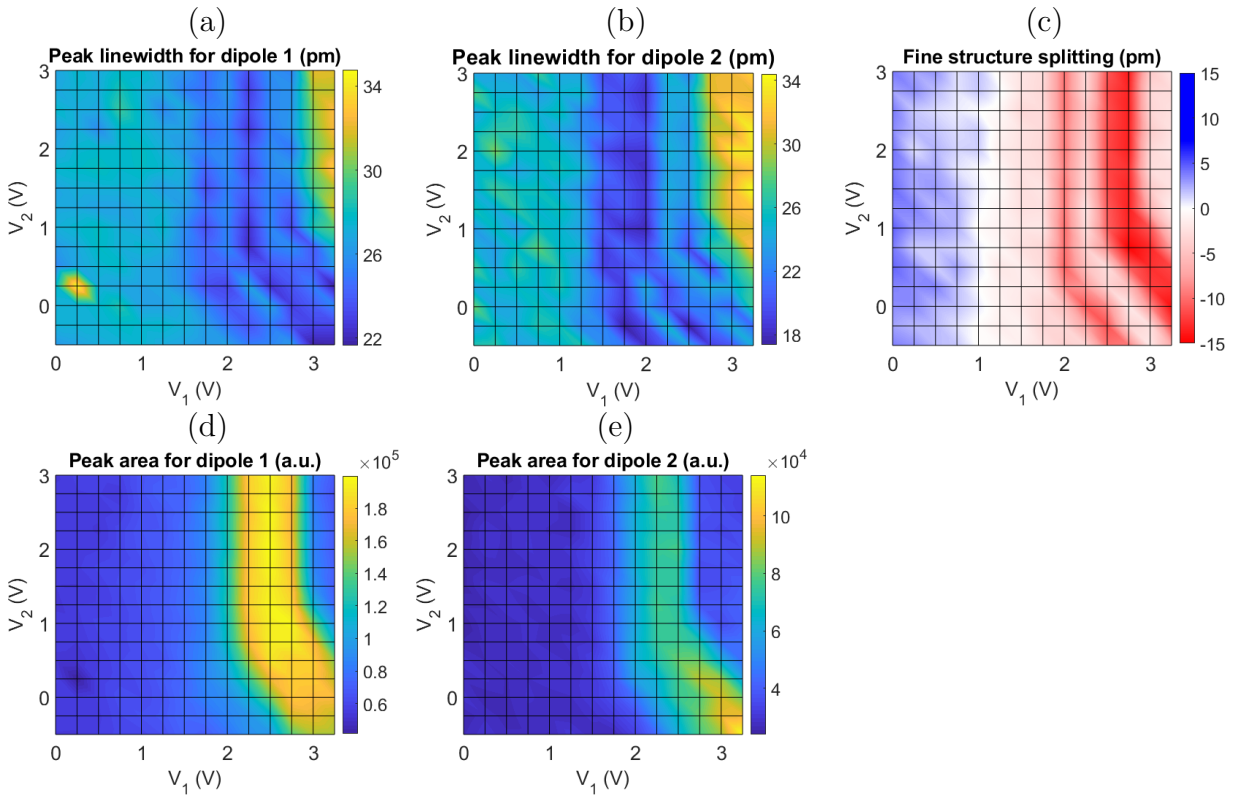


Figure 4.41: (a) and (b) show the linewidth (FWHM) of the emission from the two dipoles of the exciton studied in section 4.5.3. (c) shows the corresponding measured FSS recalled from figure 4.32. (d) and (e) are copied from figure 4.33 to make the comparison easier.

Figures 4.41(a) and (b) show the emission linewidth of the two dipoles for the device presented in section 4.5.3. We can see that while the FSS goes from positive to negative values when $V_1$ increases (between 1 and 2V), the emission linewidth does not increase. A decrease of linewidth is actually observed while the signal intensity increases, indicating a reduction in the charge noise, in the area where $V_1$ is lower than in the passing regime of the diode.

The analysis of this section indicates that it is possible to find conditions where the FSS can be tuned below the voltages for which a too high current flows through the QD's vicinity. These observations are confirmed by measurements made on our single-photon sources that are often operated under positive voltages and for which very high indistinguishabilities are measured. For example, a device from sample D from the benchmarking of Chapter 2 (see figure 2.20) showed a mean wavepacket overlap of 94% while a voltage of 4V was applied.

## 4.7 Conclusion and perspectives

### 4.7.1 Summary of the results

We have developed a new method to control the FSS. In an original way, we exploit the different resistances of the various elements of the device (pillar, arms and pads) to make a current flow through a restricted part of the device in order to create a horizontal component of the

electric field at the QD position.

We performed a numerical study with COMSOL that allows for understanding qualitatively the experimental observations. From our simulations, we have demonstrated a control of the $E_x$, $E_y$ and $E_z$ with two of the three available knobs. Using them all could then allow us to control $E_x$, $E_y$ and $E_z$ independently, and thus to tune simultaneously the FSS and the average emission wavelength. This represents the first demonstration of FSS control in a structure allowing for efficient light extraction, using all the already existing technologies developed in the group.

We managed to tune the FSS over a range of typically 30 pm for various QDs in various samples. For one QD, we also found several working points where the FSS vanishes, for different values of average wavelength. The tuning range in wavelength is much smaller than in the case of strain tuning, but is well adapted to sources coupled to high Q-factor cavities.

### 4.7.2 Perspective

The structure could be optimized by playing on the length and shape of the arms to further reduce the current at the QD position if needed. The vertical doping profile can also be studied to better control the ratios between the different components of the electric field.

In the future, we aim at implementing the *in situ* lithography process presented in Chapter 1, but with the device geometry presented in this chapter. This would allow us to target only one exciton and address it with the three remote voltage knobs. From there, an aim of the group is to experimentally demonstrate the generation of tunable frequency-encoded qubits. Another natural application of this technique is the implementation of bright sources of entangled photon pairs, by inserting the QDs into a cavity molecule. We discuss this perspective in more details in Chapter 5.

**To sum up**
We have demonstrated a new method to tune the exciton fine structure splitting based on the use of three voltages, that allow us to control independently the three components of the electric field at the position of the QD. We showed the results of numerical simulations as well as experimental data. The principle is to generate a current that flows vertically through the diodes, while the current at the vicinity of the QD remains negligible. This technique is fully compatible with the use of cavities to simultaneously tune the FSS, the average wavelength and enhance the spontaneous emission.

# Chapter 5

# Conclusion and perspectives

With the acceleration of the development of quantum technologies in the last few years, the competition has accelerated between the different physical platforms for each building block of quantum computers and communications. In this thesis, we focused on semiconductor quantum dots that are promising candidates for being used as single-photon sources, i.e. photonic qubit generators.

In Chapter 1, we have described the fundamentals of single-photon emission from QDs coupled to microcavities. We have recalled the various energy levels of a QD and defined the exciton fine structure splitting. These levels strongly depend on the QD cristallographic and strain environment, and they govern the polarization of the emitted light through optical selection rules. Finally, we gave the figures of merit used to characterize single-photon sources as well as the techniques we use to measure them.

In Chapter 2, we have studied the characteristics of micropillar cavities as well as two different transitions in QDs: trions and excitons. We have benchmarked 15 single-photon sources, evaluating their optimal functioning point in terms of wavelength, single-photon purity, indistinguishability, fibered brightness, and finally their temporal profiles for the trion-based sources. We work with naturally grown QDs, which currently have a higher single-photon purity than site controlled QDs [223, 224]. By post-processing them, namely using the *in situ* lithography process, we overcome the QD random distribution in both spatial and spectral degrees of freedom by selecting them and building a tailored cavity around them. This allows us to obtain a large number of sources with highly homogeneous properties. This demonstrates the reproducibility of our single-photon source technology, making it promising for large-scale production which is a key element in the industrial development of quantum technologies. We also discussed the physics of the sources' behaviour in a cross-polarized resonant excitation scheme, and identified the parameters controlling the wavepacket temporal profile and the source brightness.

In Chapter 3, we have derived a general formula giving access to a source's indistinguishability from the measured visibility of its HOM interference when the latter is affected by a noise that can be distinguishable or indistinguishable from the main single-photon stream. We have investigated the nature of the extra-photons for the two types of sources and found

that, although the physics behind it differs strongly, both source types display mostly distinguishable noise.

In Chapter 4, we have described a new strategy to tune the FSS of excitonic photon sources. The principle is based on the use of three electrical voltages applied to diodes that are 120° apart around a micropillar embedding the studied exciton. We have numerically shown that these knobs allow for controlling the electric field in three dimensions, which could govern the FSS and the average wavelength independently. We have shown experimental results showing that it indeed allows for tuning the FSS and that the average wavelength can be varied over about 30 pm. We propose two applications for this device. First, the generation of entangled photon pairs from a biexciton cascade requires to erase the fine structure splitting. Second, by doing the opposite and increasing the FSS, tuning would allow one to generate frequency-encoded qubits. With a phonon-assisted excitation technique, we can excite the QD off-resonantly and the filtering in polarization is no longer necessary: we can arbitrarily excite and collect any polarization. If the FSS is large enough so that the two exciton eigenstates can be separated by more than the individual linewidth, then the temporal wavepacket of the emission can be encoded in frequency.

In the following, I sketch some possible perspectives to this PhD work.

## 5.1 Towards identical remote sources

Implementing quantum operations with photons coming from different places requires the fabrication of identical sources to generate photons that can undergo a quantum interfere at a beam splitter. In that context, a visibility of $51 \pm 5\%$ was reported in 2017 in reference [225], from remote strain-tunable GaAs quantum dots emitting on-demand photon pairs. This was done for QDs in bulk structures, without efficient collection.

### 5.1.1 Preliminary results

Within the PhD of Mathias Pont, the team is currently interfering photons coming from two different samples (samples C and D, see figure 2.24). We tried to interfere a few pairs of sources from these samples. As we mentioned in Chapter 2, trion-based sources are expected to be better for remote interference since their temporal profiles should give a higher overlap than exciton-based sources. However, the highest visibility we obtained, equal to 69%, was reached so far by interfering photons from sources 5 and 10, which are both excitons. This preliminary result is shown in figure 5.1. The two remote sources were excited resonantly. This is a state-of-the-art value for interfering remote sources [21] along with a high collection efficiency due to the cavity design. Note that a higher visibility was only observed for remote QD sources for very low excitation where single photons preserve the laser spectrum (coherent scattering) [226]. First analysis shows that the measured visiblity is currently limited by some electrical and mechanical noises in our setup. In order to reach higher visibilities with remote sources, the team is currently identifying and tackling the different potential sources of noise that might explain these fluctuations.

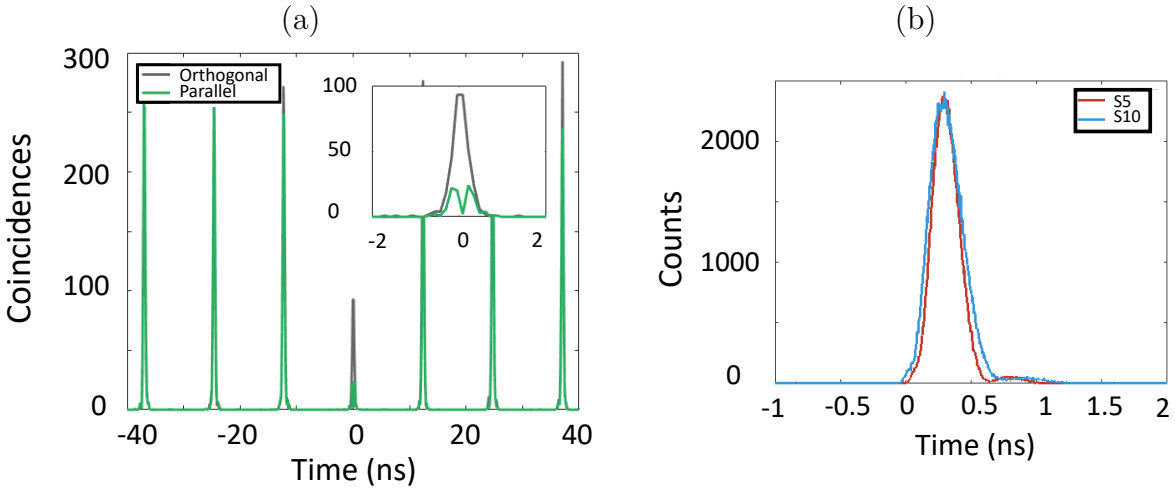


Figure 5.1: (a) Histogram of the Hong-Ou-Mandel interference obtained from remote sources (labeled 5 and 10 in the benchmarking from Chapter 2) under resonant excitation. (b) Temporal wavepacket profiles of the two corresponding sources (5 in red and 10 in blue).

### 5.1.2 Remaining fabrication challenges

All the experimental work reported in this manuscript has been done on devices fabricated in 2018, since the cleanroom had to close mid-2018 and only reopened early 2021 due to the pandemic. I sketch below some challenges that will be addressed in the near future now that technological developments have restarted.

#### More uniform wafers

As shown in section 2.5.3, the average wavelength shows a standard deviation of 0.5 nm when considering the sources from all the samples, whereas this value is reduced by a factor of $\simeq 10$ for sources within a given sample. This is due to the epitaxial growth process implemented in the C2N cleanroom: the different elements deposited in the molecular beam epitaxy chamber come with different angles with respect to the wafer. The wafer is set on a spinning platform during the epitaxy to homogenize the thickness of the layers, but the wafer can still show a variation on the order of $1-2\%$ in thickness by translation, which makes the emission wavelength vary significantly from one piece of the wafer to another and thus increases the sources' wavelength standard deviation. Growing the sources on a more industrial machine would be one way to counter this issue.

#### Better control over the charge state

As explained in section 2.6, the voltage influences both the source QD-cavity detuning and the QD charge state. Having only one knob for these two parameters prevents us from simultaneously minimizing the detuning and controlling the charge state. A way to overcome this issue is to set up a way to apply a voltage during the lithography step. That way, we would be able to explore the different available charge states and their wavelength prior to the QD selection and cavity definition, and then etch the micropillar with a more appropriate diameter. The optimization of the corresponding device brightness would then require a smaller

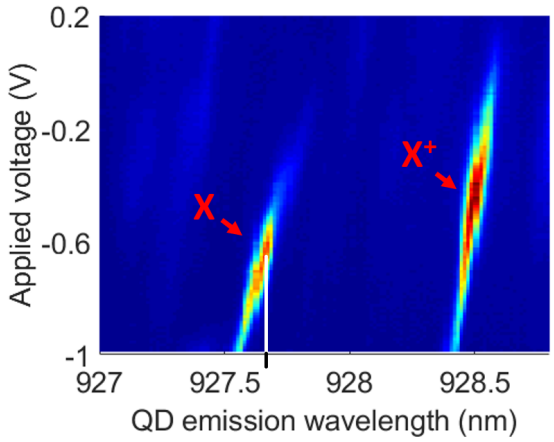


Figure 5.2: Evolution of the QDs emission wavelength as a function of the applied voltage. This was acquired on a sample where the micropillar cavity etching had not been implemented. Each line corresponds to a given transition.

voltage tuning range.

An example of how the QD charge state and emission wavelength evolve with the applied voltage is shown in figure 5.2. This was acquired from a planar cavity (no micropillar had been etched yet), as it would be done during an *in situ* lithography process. If the objective were to fabricate a longitudinal acoustic phonon-assisted single-photon source based on an exciton, the wavelength would be the one corresponding to its highest occupancy, around 927.7 nm, marked with a white line on figure 5.2.

## 5.2 Towards higher quantum purity

The very ambitious goal of using single-photon sources for quantum computing requires the highest possible visibility of HOM interference (ideally $V_{\mathrm{HOM}} = 1$). In practice, the HOM visibility is reduced both by the "true indistinguishability" of the sources $M_s$ and their non-zero $g^{(2)}$. Together with increasing the source efficiency and fabrication reproducibility, pushing its overall quantum purity towards unity is critical.

### 5.2.1 Improving the single-photon mean wavepacket overlap

As explained in [155], when the zero phonon line is resonant with a narrow cavity mode and experiences a strong Purcell effect, the fraction of emission in the phonon sideband can be strongly reduced. This allowed the team to obtain near-unity $M_s$ with high $Q$-factor cavity. In the results presented in this thesis, the samples were different from the ones used back then: the $Q$ factor of the cavity was lower as well as the Purcell factor, and there was more emission from the phonon sideband. This entailed that the values of $M_s$ presented in this thesis are lower than the ones of the previously cited paper. Fabricating cavities with a higher $Q$-factor would allow to enhance more of the the zero phonon line emission via the Purcell factor, which leads to higher values of $M_s$. However, in that case the lifetime becomes shorter

and then there is more re-excitation, which deteriorates the single-photon purity (and thus also the total mean wavepacket overlap as well as the visibility of the HOM interference).

A way to overcome the problem of an increased re-excitation probability is to fabricate cavities with higher $Q$-factor but not showing higher Purcell factors [155]. Figure 5.3(a) shows the indistinguishability as a function of the cavity linewidth for a fixed Purcell factor of 24. We see that the indistinguishability can reach very high values for low values of the cavity linewidths (i.e. large $Q$-factors). In our case, this is achievable by increasing the thickness of the pillar cavity along the growth direction for example. This increases the mode volume $V$ but maintains the same value of the Purcell factor because the $Q$-factor increases as well since the photon travels over a longer distance in the cavity. However, the effective thickness $L_{\text{eff}}$ of the spacer is actually not $\lambda$ (the QD emission wavelength) but closer to $3\lambda$ because of the penetration depth of the photons in the top and bottom mirrors, as shown in figure 5.4. Then, increasing the spacer's thickness by a factor of 10 leads to an effective thickness of $L_{\text{eff}}$ around 12 and thus actually only increases the mode volume by a factor of 4. This approach is promising but will require development on the growth and etching procedures. Moreover, as we can see on figure 5.3(b), the fraction of emission into the cavity mode decreases as the cavity linewidth decreases. Thus, there is a trade-off between high efficiency and high values of $M_s$.

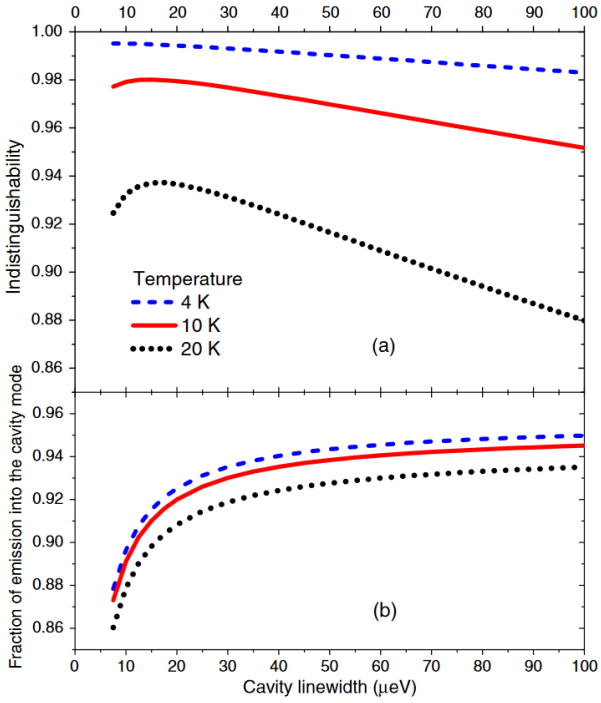


Figure 5.3: (a) Indistinguishability as a function of the cavity linewidth for a Purcell factor equal to 24 and different temperatures. (b) Corresponding fraction of the emission into the cavity mode. The QD and the cavity are assumed to be resonant. This figure was extracted from [155].

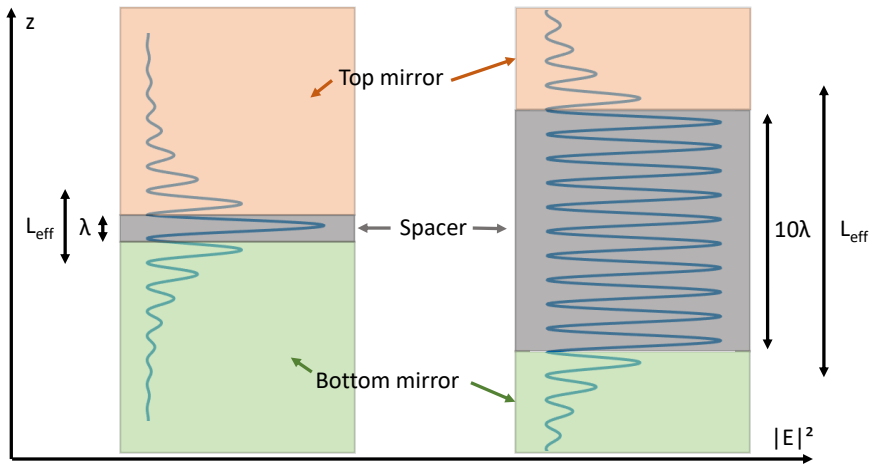


Figure 5.4: Schematic of a spacer of thickness equal to the QD emission wavelength $\lambda$ on the left, and $10\lambda$ on the right.

### 5.2.2 Improving the single-photon purity by pulse shaping

As discussed in Chapters 2 and 3, the HOM visibility is strongly dependent on the $g^{(2)}$. For exciton sources, it is mostly limited by the laser rejection. For trion-based sources, it is limited by recapture phenomena (re-excitation). An interesting perspective could be to study the influence of the excitation laser pulse shaping on the single-photon purity. In our team, we simply shape the laser using the 4-f optical setup shown in section 1.5.1 to match the excitation laser bandwidth with that of our micropillar cavity. This can be further improved by replacing the slit used to select the spectral portion we select to excite the QD by a spatial light modulator (SLM). This solution is investigated by the team of Pr. Andrew White who implemented a feedback loop to control the phase of each pixel of the SLM until the $g^{(2)}$ reaches the lowest possible value [227], opening a new path to improve the overall source performances.

## 5.3 Towards bright sources of entangled photons

In this thesis, we demonstrated a new control of the FSS (that reached values lower than the QD linewidth) for QDs in large pillar cavities. The next step is to show such a control over a QD that is embedded into a cavity with resonances that match its wavelengths. For that purpose, new samples, annealed to have a low density of QDs, will be studied to identify biexciton and exciton states before being processed with the *in situ* lithography. For efficient extraction of both photons, coupled cavity structures will be defined around the QD as discussed now.

### 5.3.1 Efficient collection

In order to collect both photons from the cascade, and since each photon has a different wavelength, we will use the concept of coupled microcavities, introduced by the team in 2010. Such a structure, shown in figure 5.5(a), presents two modes: one for each photon wavelength.

The dependence of the optical mode resonances as a function of the center-to-center distance is presented in figure 5.5(b).

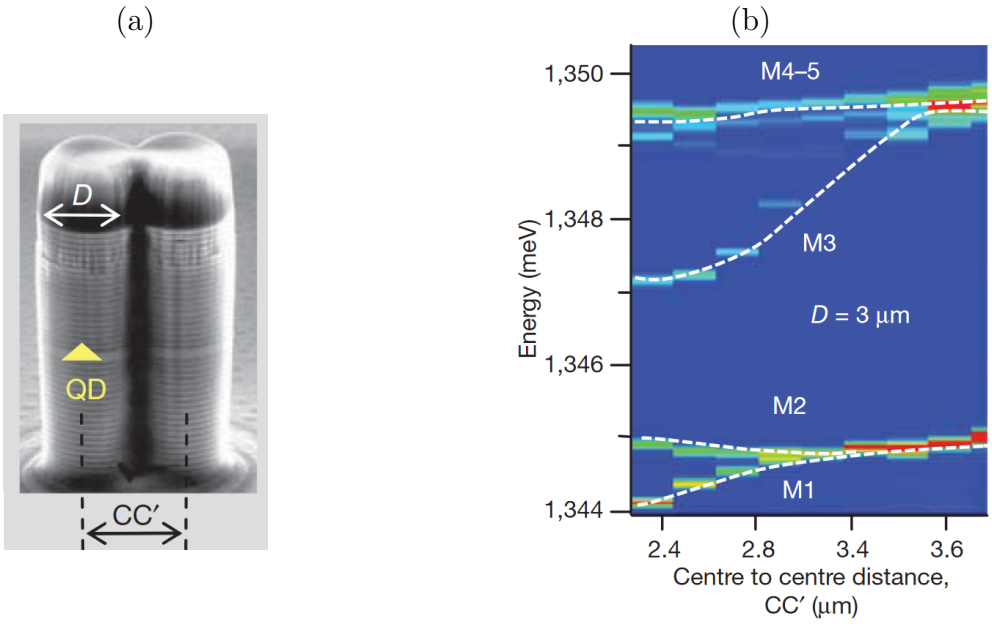


Figure 5.5: (a) Coupled micropillars that allow for collecting both photons from the radiative biexciton cascade efficiently, despite their different wavelengths. (b) Dependence of the optical mode resonances of the coupled micropillars cavity as a function of the distance between their centers. Both of these figures are extracted from reference [48].

It was shown that by choosing the proper diameter and center-to-center distance, one can make each of the two optical transitions resonant with one of the two cavity modes. For the current project, a study is needed to understand how the ridges used to apply the remote bias for the FSS control may affect the cavity mode resonances. The geometry of the 3-ridges connected coupled microcavities should be designed in such a way that the two energy modes match the energies of the two photons emitted in the cascade. The final geometry and $Q$-factor should also be chosen so that each cavity mode presents a polarization splitting negligible with respect to their linewidth. For that purpose, a sample where coupled microcavities coupled to 1D ridges were etched will be investigated (see figure 5.6). It contains a large number of pillars with different diameters and center-to-center distances, and with arms to see how these parameters affect the cavity modes.

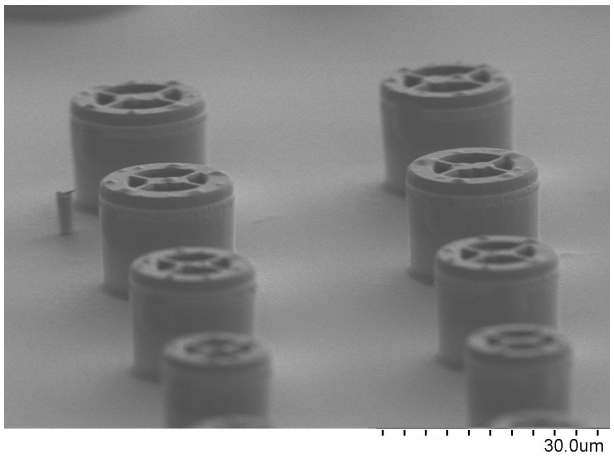


Figure 5.6: Picture of the sample with coupled microcavities. The plan is to investigate the fundamental modes of the different geometries (with different pillar diameters and center-to-center distances).

The use of coupled cavity structures to extract the entangled photon pairs may allow for solving an important challenge regarding the indistinguishability of each individual photon emitted by the cascade as discussed now.

### 5.3.2 Indistinguishability of the entangled photon pairs

It was recently shown [51] that the indistinguishability of entangled photon pairs generated through the biexcitonic cascade cannot exceed a given value. The authors analytically derive that this higher bound to the indistinguishability is equal to the ratio $\gamma_{XX}/(\gamma_X + \gamma_{XX})$, where $\gamma_X$ and $\gamma_{XX}$ are the decay rates of the excitonic and biexcitonic states, respectively. For quantum dots, it is commonly assumed that $\gamma_{XX} = 2\gamma_X$, which corresponds to a higher bound for the indistinguishability of $\simeq 0.66$. However, this ratio has been shown to depend on the QD [228]. The authors give experimental data in agreement with this statement. Indeed, they showed that excitons that give very high visibility when excited resonantly give a visibility lower than 0.66 under two-photon excitation.

Qualitatively, this limit arises from the fact that the excitonic population builds up as the biexciton decays, with a jitter linked to the emission rate of the biexcitonic state, $\gamma_{XX}$. This makes the indistinguishability decrease since the jitter emission from the excitonic state does not depend only on the excitonic emission rate $\gamma_X$ any more, but on both $\gamma_X$ and $\gamma_{XX}$. The limitation in indistinguishability is then related to the entanglement in time of the cascaded emission.

For short-distance or direct satellite-based quantum key distribution, the indistinguishability of entangled photon pairs is not a requirement, showing that there are applications despite this limitation. However, for long-distance quantum communications, high indistinguishability is needed to implement quantum relays and repeaters. A way to overcome this limitation would be to use an asymmetric Purcell enhancement. By decreasing the ratio $\gamma_X/\gamma_{XX}$, one could increase the upper bound to the visibility. This would require to be able to accelerate

the biexciton emission and/or inhibit the exciton emission, which is possible by coupling the QD to confined Tamm plasmon modes for example [229]. It can also be done using coupled microcavities: it was shown in reference [230] that different Purcell factors can be obtained for the different modes of a coupled microcavity. Figure 5.7 (extracted from [230]) shows the Purcell factor for two different modes of a coupled micropillar cavity (with a quality factor of $Q = 3000$) as a function of the QD's normalized position and $G = CC'/D - 1$ where $CC'$ is the center-to-center distance and $D$ is the diameter of the pillars. Such a scheme requires an unprecedented level of control in QD position and cavity design during the *in situ* lithography. Yet, such a technological challenge is foreseeable in the future if one considers the possibilities offered by advanced lithography techniques [163].

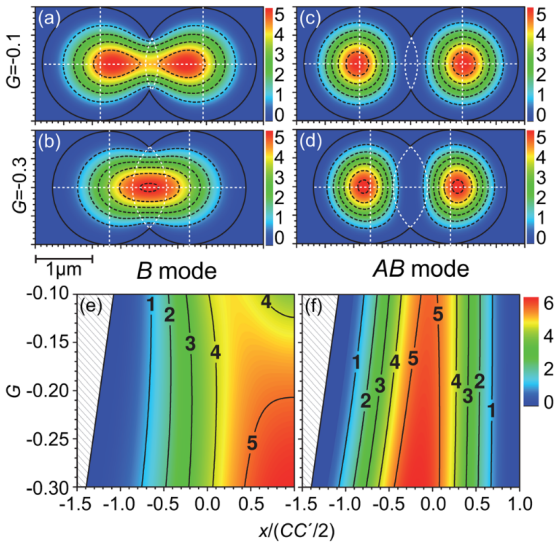


Figure 5.7: Panels (a) to (d) show the intensity distribution of the electric field for the $B$ and $AB$ modes for $G = -0.1$ (top row) and $G = -0.3$ (bottom row), $G$ being defined as $G = CC'/D - 1$, where $CC'$ is the distance between the two pillars' centers and $D$ is the pillars' diameter. Panels (e) and (f) show the Purcell factor calculated for the two modes ($A$ and $AB$) of a cavity of quality factor equal to $Q = 3000$ as a function of the QD's normalized position and $G$. This figure was extracted from [230].

# Bibliography


[1] W. Thomson, "Nineteenth century clouds over the dynamical theory of heat and light", The London, Edinburgh, and Dublin Philosophical Magazine and Journal of Science **Sixth series**.

[2] M. Nauenberg, "Max planck and the birth of the quantum hypothesis", American Journal of Physics **84**, 709–720 (2016).

[3] G. Grynberg, A. Aspect, and C. Fabre, *Introduction to quantum optics: from the semi-classical approach to quantized light* (Cambridge University Press, 2010).

[4] S. Lloyd, "Universal quantum simulators", Science **273**, 1073–1078 (1996).

[5] R. P. Feynman, "Simulating physics with computers", International Journal of Theoretical Physics **21**, 467–488 (1982).

[6] J. S., "Feeding the world with die rolls: potential applications of quantum computing", Dartmouth Undergraduate Journal of Science **20**, 34–36 (2017).

[7] M. Reiher, N. Wiebe, K. M. Svore, D. Wecker, and M. Troyer, "Elucidating reaction mechanisms on quantum computers", Proceedings of the National Academy of Sciences (2017).

[8] R. Orus, S. Mugel, and E. Lizaso, "Quantum computing for finance: overview and prospects", Reviews in Physics **4**, 100028 (2019).

[9] J. Biamonte, P. Wittek, N. Pancotti, P. Rebentrost, N. Wiebe, and S. Lloyd, "Quantum machine learning", Nature **549**, 195–202 (2017).

[10] F. Arute, K. Arya, R. Babbush, D. Bacon, J. C. Bardin, R. Barends, R. Biswas, S. Boixo, F. G. S. L. Brandao, D. A. Buell, et al., "Quantum supremacy using a programmable superconducting processor", Nature **574**, 505–510 (2019).

[11] H.-S. Zhong, H. Wang, Y.-H. Deng, M.-C. Chen, L.-C. Peng, Y.-H. Luo, J. Qin, D. Wu, X. Ding, Y. Hu, et al., "Quantum computational advantage using photons", Science **370**, 1460–1463 (2020).

[12] P. W. Shor, "Algorithms for quantum computation: discrete logarithms and factoring", in Proceedings of the 35th annual symposium on foundations of computer science, SFCS 94 (1994), 124–134.

[13] E. Diamanti, H.-K. Lo, B. Qi, and Z. Yuan, "Practical challenges in quantum key distribution", npj Quantum Information **2** (2016).

[14] P. W. Shor and J. Preskill, "Simple proof of security of the BB84 quantum key distribution protocol", Physical Review Letters **85**, 441–444 (2000).

[15] N. Gisin and R. Thew, "Quantum communication", Nature Photonics **1**, 165–171 (2007).

[16] H. J. Kimble, "The quantum internet", Nature **453**, 1023–1030 (2008).

[17] S. Wehner, D. Elkouss, and R. Hanson, "Quantum internet: a vision for the road ahead", Science **362**, eaam9288 (2018).

[18] C. Simon, "Towards a global quantum network", Nature Photonics (2017).

[19] H.-J. Briegel, W. Dür, J. I. Cirac, and P. Zoller, "Quantum repeaters: the role of imperfect local operations in quantum communication", Physical Review Letters **81**, 5932–5935 (1998).

[20] M. Mastriani and S. Iyengar, "Satellite quantum repeaters for a quantum internet", Quantum Engineering **2** (2020).

[21] B. Hensen, H. Bernien, A. E. Dréau, A. Reiserer, N. Kalb, M. S. Blok, J. Ruitenberg, R. F. Vermeulen, R. N. Schouten, C. Abellán, et al., "Loophole-free Bell inequality violation using electron spins separated by 1.3 kilometres", Nature **526**, 682–686 (2015).

[22] M. Giustina, M. A. M. Versteegh, S. Wengerowsky, J. Handsteiner, A. Hochrainer, K. Phelan, F. Steinlechner, J. Kofler, J.-A. Larsson, C. Abellán, et al., "Significant-loophole-free test of Bell's theorem with entangled photons", Physical Review Letters **115**, 250401 (2015).

[23] L. K. Shalm, E. Meyer-Scott, B. G. Christensen, P. Bierhorst, M. A. Wayne, M. J. Stevens, T. Gerrits, S. Glancy, D. R. Hamel, M. S. Allman, et al., "Strong loophole-free test of local realism", Physical Review Letters **115**, 250402 (2015).

[24] D. Rideout, T. Jennewein, G. Amelino-Camelia, T. Demarie, B. Higgins, A. Kempf, A. Kent, R. Laflamme, X. Ma, R. Mann, et al., "Fundamental quantum optics experiments conceivable with satellites - reaching relativistic distances and velocities", Classical and Quantum Gravity **29** (2012).

[25] V. Giovannetti, S. Lloyd, and L. Maccone, "Quantum metrology", Physical Review Letters **96**, 010401 (2006).

[26] V. Giovannetti, S. Lloyd, and L. Maccone, "Advances in quantum metrology", Physical Review Letters **96** (2011).

[27] C. L. Degen, F. Reinhard, and P. Cappellaro, "Quantum sensing", Reviews of Modern Physics **89**, 035002 (2017).

[28] G. Brida and I. Ruo Berchera, "Experimental realization of sub-shot-noise quantum imaging", Nature Photonics **4**, 227 (2010).

[29] L. Henriet, L. Beguin, A. Signoles, T. Lahaye, A. Browaeys, G.-O. Reymond, and C. Jurczak, "Quantum computing with neutral atoms", Quantum **4**, 327 (2020).

[30] C. D. Bruzewicz, J. Chiaverini, R. McConnell, and S. M. J., "Trapped-ion quantum computing: progress and challenges", Applied Physics Review **6**, 021314 (2019).

[31] J. I. Cirac and P. Zoller, "Quantum computations with cold trapped ions", Physical Review Letters **74**, 4091–4094 (1995).

[32] M. Kjaergaard, M. E. Schwartz, J. Braumüller, P. Krantz, J. I.-J. Wang, S. Gustavsson, and W. D. Oliver, "Superconducting qubits: current state of play", Annual Review of Condensed Matter Physics **11**, 369–395 (2020).

[33] M. W. Doherty, N. B. Manson, P. Delaney, F. Jelezko, J. Wrachtrup, and L. C. Hollenberg, "The nitrogen-vacancy colour centre in diamond", Physics Reports **528**, 1–45 (2013).

[34] G. Kurizki, P. Bertet, Y. Kubo, K. Molmer, D. Petrosyan, P. Rabl, and J. Schmiedmayer, "Quantum technologies with hybrid systems", Proceedings of the National Academy of Sciences **112**, 3866–3873 (2015).

[35] D. Istrati, Y. Pilnyak, J. Loredo, C. Antón, N. Somaschi, P. Hilaire, H. Ollivier, M. Esmann, L. Cohen, L. Vidro, et al., "Sequential generation of linear cluster states from a single photon emitter", Nature Communications **11**, 5501 (2020).

[36] D. E. Browne and T. Rudolph, "Resource-efficient linear optical quantum computation", Physical Review Letters **95**, 010501 (2005).

[37] P. Hilaire, E. Barnes, and S. E. Economou, "Resource requirements for efficient quantum communication using all-photonic graph states generated from a few matter qubits", Quantum **5**, 397 (2021).

[38] E. Meyer-Scott, C. Silberhorn, and A. Migdall, "Single-photon sources: approaching the ideal through multiplexing", Review of Scientific Instruments **91**, 041101 (2020).

[39] P. Grangier, G. Roger, and A. Aspect, "Experimental evidence for a photon anticorrelation effect on a beam splitter: a new light on single-photon interferences", Europhysics Letters (EPL) **1**, 173–179 (1986).

[40] P. Farrera, G. Heinze, B. Albrecht, M. Ho, M. Chavez, C. Teo, N. Sangouard, and H. de Riedmatten, "Generation of single photons with highly tunable wave shape from a cold atomic ensemble", Nature Communications **7**, 13556 (2016).

[41] A. Beveratos, R. Brouri, J.-P. Poizat, and P. Grangier, "Bunching and antibunching from single NV color centers in diamond", Kluwer Academic Publishers **4** (2000).

[42] B. Rodiek, M. López, H. Hofer, G. Porrovecchio, M. Smid, X.-L. Chu, S. Gotzinger, V. Sandoghdar, S. Lindner, C. Becher, and S. Kück, "Experimental realization of an absolute single-photon source based on a single nitrogen vacancy center in a nanodiamond", Optica **4**, 71 (2017).

[43] B. Lounis and W. E. Moerner, "Single photons on demand from a single molecule at room temperature", Nature **407**, 491–3 (2000).

[44] L. Zhang, Y.-J. Yu, L.-G. Chen, Y. Luo, B. Yang, F.-F. Kong, G. Chen, Y. Zhang, Q. Zhang, Y. Luo, J.-L. Yang, Z.-C. Dong, and J. G. Hou, "Electrically driven single-photon emission from an isolated single molecule", Nature Communications **8**, 580 (2017).

[45] P. Michler, A. Kiraz, C. Becher, W. V. Schoenfeld, P. M. Petroff, L. Zhang, E. Hu, and A. Imamoğlu, "A quantum dot single-photon turnstile device", Science **290**, 2282–2285 (2000).

[46] P. Senellart, G. Solomon, and A. White, "High-performance semiconductor quantum-dot single-photon sources", Nature Nanotechnology **12**, 1026 (2017).

[47] J. C. Loredo, C. Antón, B. Reznychenko, P. Hilaire, A. Harouri, C. Millet, H. Ollivier, N. Somaschi, L. De Santis, A. Lemaitre, I. Sagnes, L. Lanco, A. Auffèves, O. Krebs, and P. Senellart, "Generation of non-classical light in a photon-number superposition", Nature Photonics **13**, 803–808 (2019).

[48] A. Dousse, J. Suffczyński, A. Beveratos, O. Krebs, A. Lemaitre, I. Sagnes, J. Bloch, P. Voisin, and P. Senellart, "Ultrabright source of entangled photon pairs", Nature **466**, 217–220 (2010).

[49] I. Schwartz, D. Cogan, E. R. Schmidgall, Y. Don, L. Gantz, O. Kenneth, N. H. Lindner, and D. Gershoni, "Deterministic generation of a cluster state of entangled photons", Science **354**, 434–437 (2016).

[50] H. Wei and F.-G. Deng, "Scalable quantum computing based on stationary spin qubits in coupled quantum dots inside double-sided optical microcavities", Scientific Reports **4**, 7551 (2014).

[51] E. Schöll, L. Schweickert, L. Hanschke, K. D. Zeuner, F. Sbresny, T. Lettner, R. Trivedi, M. Reindl, S. F. Covre da Silva, R. Trotta, et al., "Crux of using the cascaded emission of a three-level quantum ladder system to generate indistinguishable photons", Physical Review Letters **125**, 233605 (2020).

[52] O. Benson, C. Santori, M. Pelton, and Y. Yamamoto, "Regulated and entangled photons from a single quantum dot", Physical Review Letters **84**, 2513–2516 (2000).

[53] N. Akopian, N. H. Lindner, E. Poem, Y. Berlatzky, J. Avron, D. Gershoni, B. D. Gerardot, and P. M. Petroff, "Entangled photon pairs from semiconductor quantum dots", Physical Review Letters **96**, 130501 (2006).

[54] J. Huwer, R. M. Stevenson, J. Skiba-Szymanska, M. B. Ward, A. J. Shields, M. Felle, I. Farrer, D. A. Ritchie, and R. V. Penty, "Quantum-dot-based telecommunication-wavelength quantum relay", Physical Review Applied **8**, 024007 (2017).

[55] F. Basso Basset, M. B. Rota, C. Schimpf, D. Tedeschi, K. D. Zeuner, S. F. Covre da Silva, M. Reindl, V. Zwiller, K. D. Jöns, A. Rastelli, and R. Trotta, "Entanglement swapping with photons generated on demand by a quantum dot", Physical Review Letters **123**, 160501 (2019).

[56] M. Zopf, R. Keil, Y. Chen, J. Yang, D. Chen, F. Ding, and O. G. Schmidt, "Entanglement swapping with semiconductor-generated photons violates Bell's inequality", Physical Review Letters **123**, 160502 (2019).

[57] S. Lloyd, M. S. Shahriar, J. H. Shapiro, and P. R. Hemmer, "Long distance, unconditional teleportation of atomic states via complete Bell state measurements", Physical Review Letters **87**, 167903 (2001).

[58] J. M. Gérard, B. Sermage, B. Gayral, B. Legrand, E. Costard, and V. Thierry-Mieg, "Enhanced spontaneous emission by quantum boxes in a monolithic optical microcavity", Physical Review Letters **81**, 1110–1113 (1998).

[59] M. Pelton, C. Santori, J. Vucković, B. Zhang, G. S. Solomon, J. Plant, and Y. Yamamoto, "Efficient source of single photons: a single quantum dot in a micropost microcavity", Physical Review Letters **89**, 233602 (2002).

[60] R. Uppu, H. Eriksen, H. Thyrrestrup, A. D. Ugurlu, W. Ying, S. Scholz, A. D. Wieck, A. Ludwig, M. C. Löbl, R. J. Warburton, P. Lodahl, and L. Midolo, "On-chip deterministic operation of quantum dots in dual-mode waveguides for a plug-and-play single-photon source", Nature Communications **11**, 1–6 (2020).

[61] J. Claudon, J. Bleuse, N. S. Malik, M. Bazin, P. Jaffrennou, N. Gregersen, C. Sauvan, P. Lalanne, and J.-M. Gérard, "A highly efficient single-photon source based on a quantum dot in a photonic nanowire", Nature Photonics **4**, 174–177 (2010).

[62] A. Tamada, Y. Ota, K. Kuruma, K. Watanabe, S. Iwamoto, and Y. Arakawa, "Single plasmon generation in an InAs/GaAs quantum dot in a transfer-printed plasmonic microring resonator", ACS Photonics **6**, 1106–1110 (2019).

[63] J. Liu, R. Su, Y. Wei, B. Yao, S. F. C. d. Silva, Y. Yu, J. Iles-Smith, K. Srinivasan, A. Rastelli, J. Li, and X. Wang, "A solid-state source of strongly entangled photon pairs with high brightness and indistinguishability", Nature Nanotechnology **14**, 586–593 (2019).

[64] A. Badolato, K. Hennessy, M. Atatüre, J. Dreiser, E. Hu, P. Petroff, and A. Imamoglu, "Deterministic coupling of single quantum dots to single nanocavity modes", Science **308**, 1158 (2005).

[65] K. Hennessy, A. Badolato, M. Winger, D Gerace, M. Atatüre, S Gulde, S Fält, E. Hu, and A Imamoğlu, "Quantum nature of a strongly coupled single quantum dot-cavity system", Nature **445**, 896 (2007).

[66] A. Dousse, L. Lanco, J. Suffczynski, E. Semenova, A. Miard, A. Lemaitre, I. Sagnes, C. Roblin, J. Bloch, and P. Senellart, "Controlled light-matter coupling for a single quantum dot embedded in a pillar microcavity using far-field optical lithography", Physical Review Letters **101**, 267404 (2008).

[67] O. Gazzano, S. Michaelis de Vasconcellos, C. Arnold, A Nowak, E. Galopin, I. Sagnes, L. Lanco, A. Lemaitre, and P. Senellart, "Bright solid-state sources of indistinguishable single photons", Nature Communications **4**, 1425 (2013).

[68] Y.-M. He, Y. He, Y.-J. Wei, D. Wu, M. Atatüre, C. Schneider, S. Höfling, M. Kamp, C.-Y. Lu, and J.-W. Pan, "On-demand semiconductor single-photon source with near-unity indistinguishability", Nature Nanotechnology **8**, 213–217 (2013).

[69] L. Monniello, A. Reigue, R. Hostein, A. Lemaitre, A. Martinez, R. Grousson, and V. Voliotis, "Indistinguishable single photons generated by a quantum dot under resonant excitation observable without postselection", Physical Review B **90**, 041303 (2014).

[70] N. Somaschi, V. Giesz, L. De Santis, J. C. Loredo, M. P. Almeida, G. Hornecker, S. L. Portalupi, T. Grange, C. Antón, J. Demory, et al., "Near-optimal single-photon sources in the solid state", Nature Photonics **10**, 340 (2016).

[71] J. C. Loredo, M. A. Broome, P. Hilaire, O. Gazzano, I. Sagnes, A. Lemaitre, M. P. Almeida, P. Senellart, and A. G. White, "Boson sampling with single-photon fock states from a bright solid-state source", Physical Review Letters **118**, 130503 (2017).

[72] H. Wang, Y. He, Y.-H. Li, Z.-E. Su, b. li, H.-L. Huang, X. Ding, M.-c. Chen, C. Liu, J. Qin, et al., "Multi-photon boson-sampling machines beating early classical computers", arXiv:1612.06956 (2016).

[73] H. Wang, W. Li, X. Jiang, Y.-M. He, Y.-H. Li, X. Ding, M.-C. Chen, J. Qin, C.-Z. Peng, C. Schneider, et al., "Toward scalable boson sampling with photon loss", Physical Review Letters **120**, 230502 (2018).

[74] H. Wang, J. Qin, X. Ding, M.-C. Chen, S. Chen, X. You, Y.-M. He, X. Jiang, L. You, Z. Wang, C. Schneider, J. J. Renema, S. Höfling, C.-Y. Lu, and J.-W. Pan, "Boson sampling with 20 input photons and a 60-mode interferometer in a 1014-dimensional Hilbert space", Physical Review Letters **123**, 250503 (2019).

[75] C. Antón, J. Loredo, G. Coppola, H. Ollivier, N. Viggianiello, A. Harouri, N. Somaschi, A. Crespi, I. Sagnes, A. Lemaitre, L. Lanco, R. Osellame, F. Sciarrino, and P. Senellart, "Interfacing scalable photonic platforms: solid-state based multi-photon interference in a reconfigurable glass chip", Optica **6**, 1471 (2019).

[76] H. Ollivier, I. Maillette de Buy Wenniger, S. Thomas, S. C. Wein, A. Harouri, G. Coppola, P. Hilaire, C. Millet, A. Lemaitre, I. Sagnes, et al., "Reproducibility of high-performance quantum dot single-photon sources", ACS Photonics **7**, 1050–1059 (2020).

[77] H. Ollivier, S. E. Thomas, S. C. Wein, I. M. de Buy Wenniger, N. Coste, J. C. Loredo, N. Somaschi, A. Harouri, A. Lemaitre, I. Sagnes, L. Lanco, C. Simon, C. Antón, O. Krebs, and P. Senellart, "Hong-ou-mandel interference with imperfect single photon sources", Physical Review Letters **126**, 063602 (2021).

[78] J. Y. Marzin, J. M. Gérard, A. Izraël, D. Barrier, and G. Bastard, "Photoluminescence of single InAs quantum dots obtained by self-organized growth on GaAs", Physical Review Letters **73**, 716–719 (1994).

[79] A. Baskaran and P. Smereka, "Mechanisms of Stranski-Krastanov growth", Journal of Applied Physics **111**, 044321 (2012).

[80] O. Madelung, *Semiconductors: data handbook* (Springer, 2004).

[81] P. Senellart, V. Giesz, and L. Lanco, "Ultrabright single-photon sources", Photoniques, 23–26 (2017).

[82] L. D. Santis, *Thesis: single photon generation and manipulation with semiconductor quantum dot devices* (Université Paris-Saclay COmUE, 2018).

[83] V. Giesz, *Thesis: cavity-enhanced photon-photon interactions with bright quantum dot sources* (Université Paris-Saclay COmUE, 2015).

[84] J. M. Gérard, I. Cabrol, J. Y. Marzin, N. Lebouché, and J. M. Moison, "Optical investigation of some statistic and kinetic aspects of the nucleation and growth of InAs islands on GaAs", Materials Science and Engineering: B **37**, 8–16 (1996).

[85] S. J. Xu, X. C. Wang, S. J. Chua, C. H. Wang, W. J. Fan, J. Jiang, and X. G. Xie, "Effects of rapid thermal annealing on structure and luminescence of self-assembled InAs/GaAs quantum dots", Applied Physics Letters **72**, 3335–3337 (1998).

[86] M. Fox, *Optical properties of solids*, Oxford Master Series in Condensed Matter Physics (Oxford University Press, 2001).

[87] R. Blümel, *Foundations of quantum mechanics: from photons to quantum computers* (Jones and Bartlett Publishers, 2010).

[88] H. Drexler, D. Leonard, W. Hansen, J. P. Kotthaus, and P. M. Petroff, "Spectroscopy of quantum levels in charge-tunable InGaAs quantum dots", Physical Review Letters **73**, 2252–2255 (1994).

[89] R. J. Warburton, C. Schäflein, D. Haft, F. Bickel, A. Lorke, K. Karrai, J. M. Garcia, W. Schoenfeld, and P. M. Petroff, "Optical emission from a charge-tunable quantum ring", Nature **405**, 926–929 (2000).

[90] P.-L. Ardelt, T. Simmet, K. Müller, C. Dory, K. A. Fischer, A. Bechtold, A. Kleinkauf, H. Riedl, and J. J. Finley, "Controlled tunneling-induced dephasing of Rabi rotations for high-fidelity hole spin initialization", Physical Review B **92**, 115306 (2015).

[91] P. Hilaire, C. Millet, J. C. Loredo, C. Antón, A. Harouri, A. Lemaitre, I. Sagnes, N. Somaschi, O. Krebs, P. Senellart, and L. Lanco, "Deterministic assembly of a charged-quantum-dot–micropillar cavity device", Physical Review B **102**, 195402 (2020).

[92] K. De Greve, D. Press, P. L. McMahon, and Y. Yamamoto, "Ultrafast optical control of individual quantum dot spin qubits", Reports on Progress in Physics **76**, 092501 (2013).

[93] G. Bastard, *Wave mechanics applied to semiconductor heterostructures*, Monographies de Physique (Wiley-Interscience, 1988).

[94] J. Marzin and J. Gerard, "Optical properties of some iii–v strained-layer superlattices", Superlattices and Microstructures **5**, 51–58 (1989).

[95] J.-W. Luo, G. Bester, and A. Zunger, "Long- and short-range electron-hole exchange interaction in different types of quantum dots", New Journal of Physics **11**, 123024 (2009).

[96] H. Fu, L.-W. Wang, and A. Zunger, "Excitonic exchange splitting in bulk semiconductors", Physical Review B **59**, 5568–5574 (1999).

[97] A. Franceschetti, L.-W. Wang, H. Fu, and A. Zunger, "Short-range versus long-range electron-hole exchange interactions in semiconductor quantum dots", Physical Review B **58**, R13367–R13370 (1998).

[98] P. Michler, *Single quantum dots, fundamentals, applications and new concepts*, Topics in Applied Physics (Springer, 2003).

[99] P. Lodahl, S. Mahmoodian, and S. Stobbe, "Interfacing single photons and single quantum dots with photonic nanostructures", Reviews of Modern Physics **87**, 347–400 (2015).

[100] S. L. Chuang, *Physics of optoelectronic devices* (Wiley–Blackwell, 1995).

[101] J. M. Luttinger and W. Kohn, "Motion of electrons and holes in perturbed periodic fields", Physical Review **97**, 869–883 (1955).

[102] Y. Léger, L. Besombes, L. Maingault, and H. Mariette, "Valence-band mixing in neutral, charged, and Mn-doped self-assembled quantum dots", Physical Review B **76**, 045331 (2007).

[103] M. Bayer, G. Ortner, O. Stern, A. Kuther, A. A. Gorbunov, A. Forchel, P. Hawrylak, S. Fafard, K. Hinzer, T. L. Reinecke, S. N. Walck, J. P. Reithmaier, F. Klopf, and F. Schäfer, "Fine structure of neutral and charged excitons in self-assembled In(Ga)As/(Al)GaAs quantum dots", Physical Review B **65**, 195315 (2002).

[104] D. Kiang and K. Young, "The angular momentum of photons in a circularly polarized beam", American Journal of Physics **76**, 1012–1014 (2008).

[105] Y. Léger, *Thèse : détection de spins individuels dans les boites quantiques magnétiques* (Université Joseph Fourier, Grenoble 1, 2007).

[106] T. Belhadj, T. Amand, A. Kunold, C.-M. Simon, T. Kuroda, M. Abbarchi, T. Mano, K. Sakoda, S. Kunz, X. Marie, and B. Urbaszek, "Impact of heavy hole-light hole coupling on optical selection rules in GaAs quantum dots", Applied Physics Letters **97**, 051111 (2010).

[107] E Moreau, I Robert, J. Gérard, I Abram, L Manin, and V Thierry-Mieg, "Single-mode solid-state single photon source based on isolated quantum dots in pillar microcavities", Applied Physics Letters **79**, 2865–2867 (2001).

[108] J. Beugnon, *Physique statistique quantique, notes de cours* (pour l'ENS Cachan (Phytem), LKB, www.lkb.upmc.fr/boseeinsteincondensates/beugnon, 2017).

[109] R. Loudon, *The quantum theory of light* (OUP Oxford, 2000).

[110] J.-M. Gerard and B. Gayral, "Strong purcell effect for inas quantum boxes in three-dimensional solid-state microcavities", Journal of Lightwave Technology **17**, 2089–2095 (1999).

[111] M. Fox, *Quantum optics: an introduction*, Oxford Master Series in Atomic, Optical and Laser Physics (Oxford University Press, 2006).

[112] E. M. Purcell, H. C. Torrey, and R. V. Pound, "Resonance absorption by nuclear magnetic moments in a solid", Physical Review **69**, 37–38 (1946).

[113] A. Auffèves, D. Gerace, J.-M. Gérard, M. Franca Santos, L. C. Andreani, and J.-P. Poizat, "Controlling the dynamics of a coupled atom-cavity system by pure dephasing", Physical Review B **81**, 245419 (2010).

[114] M. Munsch, *Thèse : etude du régime de purcell pour une boite quantique unique dans une microcavité semiconductrice : vers une non-linéarité optique géante* (Université de Grenoble 1, 2009).

[115] D. A. Steck, *Quantum and atom optics* (available online at http://steck.us/teaching (revision 0.13.4, 24 September 2020), 1988).

[116] C. C. Gerry and P. L. Knight, *Introductory quantum optics* (Cambridge University Press, 2004).

[117] E. T. Jaynes and F. W. Cummings, "Comparison of quantum and semiclassical radiation theories with application to the beam maser", Proceedings of the IEEE **51**, 89–109 (1963).

[118] A. K. Nowak, S. L. Portalupi, V. Giesz, O. Gazzano, C. Dal Savio, P.-F. Braun, K. Karrai, C. Arnold, L. Lanco, I. Sagnes, A. Lemaitre, and P. Senellart, "Deterministic and electrically tunable bright single-photon source", Nature Communications **5**, 3240 (2014).

[119] C. Antón, P. Hilaire, K. C. A., J. Demory, C. Gomez, A. Lemaitre, I. Sagnes, N. D. Lanzillotti-Kimura, O. Krebs, N. Somaschi, P. Senellart, and L. Lanco, "Tomography of the optical polarization rotation induced by a single quantum dot in a cavity", Optica **4**, 1326–1332 (2017).

[120] L. De Santis, C. Antón, B. Reznychenko, N. Somaschi, G. Coppola, J. Senellart, C. Gómez, A. Lemaitre, I. Sagnes, A. G. White, L. Lanco, A. Auffèves, and P. Senellart, "A solid-state single-photon filter", Nature Nanotechnology **12**, 663–667 (2017).

[121] L. De Santis, G. Coppola, C. Antón, N. Somaschi, C. Gómez, A. Lemaitre, I. Sagnes, L. Lanco, J. C. Loredo, O. Krebs, and P. Senellart, "Overcomplete quantum tomography of a path-entangled two-photon state", Physical Review A **99**, 022312 (2019).

[122] Y.-J. Wei, Y.-M. He, M.-C. Chen, Y.-N. Hu, Y. He, D. Wu, C. Schneider, M. Kamp, S. Höfling, C.-Y. Lu, and J.-W. Pan, "Deterministic and robust generation of single photons on a chip with 99.5% indistinguishability using rapid adiabatic passage", Nano Letters **14**, 6515–6519 (2014).

[123] P. Hilaire, C. Antón, C. Kessler, A. Lemaitre, I. Sagnes, N. Somaschi, P. Senellart, and L. Lanco, "Accurate measurement of a 96% input coupling into a cavity using polarization tomography", Applied Physics Letters **112**, 201101 (2018).

[124] V. Giesz, N. Somaschi, G. Hornecker, T. Grange, B. Reznychenko, L. De Santis, J. Demory, C. Gomez, I. Sagnes, A. Lemaitre, O. Krebs, N. D. Lanzillotti-Kimura, L. Lanco, A. Auffeves, and P. Senellart, "Coherent manipulation of a solid-state artificial atom with few photons", Nature Communications **7**, 11986 (2016).

[125] P. Kok, W. J. Munro, K. Nemoto, T. C. Ralph, J. P. Dowling, and G. J. Milburn, "Linear optical quantum computing with photonic qubits", Reviews of Modern Physics **79**, 135–174 (2007).

[126] N. Sangouard, C. Simon, J. Minar, H. Zbinden, H. de Riedmatten, and N. Gisin, "Long-distance entanglement distribution with single-photon sources", Physical Review A **76**, 050301 (2007).

[127] M. Müller, H. Vural, C. Schneider, A. Rastelli, O. G. Schmidt, S. Höfling, and P. Michler, "Quantum-dot single-photon sources for entanglement enhanced interferometry", Physical Review Letters **118**, 257402 (2017).

[128] R. Ghobadi, S. Wein, H. Kaviani, P. Barclay, and C. Simon, "Progress toward cryogen-free spin-photon interfaces based on nitrogen-vacancy centers and optomechanics", Physical Review A **99**, 053825 (2019).

[129] K. A. Fischer, R. Trivedi, V. Ramasesh, I. Siddiqi, and J. Vucković, "Scattering into one-dimensional waveguides from a coherently-driven quantum-optical system", Quantum **2**, 69 (2018).

[130] E. Knill, R. Laflamme, and G. J. Milburn, "A scheme for efficient quantum computation with linear optics", Nature **409**, 46–52 (2001).

[131] J. C. Loredo, N. A. Zakaria, N. Somaschi, C. Antón, L. de Santis, V. Giesz, T. Grange, M. A. Broome, O. Gazzano, G. Coppola, et al., "Scalable performance in solid-state single-photon sources", Optica **3**, 433–440 (2016).

[132] C. K. Hong, Z. Y. Ou, and L. Mandel, "Measurement of subpicosecond time intervals between two photons by interference", Physical Review Letters **59**, 2044–2046 (1987).

[133] A. Kiraz, M. Atatüre, and A. Imamoglu, "Quantum-dot single-photon sources: prospects for applications in linear optics quantum-information processing", Physical Review A **69**, 032305 (2004).

[134] I. E. Zadeh, A. W. Elshaari, K. D. Jöns, A. Fognini, D. Dalacu, P. J. Poole, M. E. Reimer, and V. Zwiller, "Deterministic Integration of Single Photon Sources in Silicon Based Photonic Circuits", Nano Letters **16**, 2289–2294 (2016).

[135] G. Kirsanske, H. Thyrrestrup, R. S. Daveau, C. L. Dreessen, T. Pregnolato, L. Midolo, P. Tighineanu, A. Javadi, S. Stobbe, R. Schott, et al., "Indistinguishable and efficient single photons from a quantum dot in a planar nanobeam waveguide", Physical Review B **96**, 165306 (2017).

[136] X. Ding, Y. He, Z.-C. Duan, N. Gregersen, M.-C. Chen, S. Unsleber, S. Maier, C. Schneider, M. Kamp, S. Höfling, C.-Y. Lu, and J.-W. Pan, "On-demand single photons with high extraction efficiency and near-unity indistinguishability from a resonantly driven quantum dot in a micropillar", Physical Review Letters **116**, 020401 (2016).

[137] R. Keil, M. Zopf, Y. Chen, B. Höfer, J. Zhang, F. Ding, and O. G. Schmidt, "Solid-state ensemble of highly entangled photon sources at rubidium atomic transitions", Nature Communications **8**, 15501 (2017).

[138] D. Huber, M. Reindl, Y. Huo, H. Huang, J. S. Wildmann, O. G. Schmidt, A. Rastelli, and R. Trotta, "Highly indistinguishable and strongly entangled photons from symmetric GaAs quantum dots", Nature Communications **8**, 15506 (2017).

[139] E. Schöll, L. Hanschke, L. Schweickert, K. D. Zeuner, M. Reindl, S. F. Covre da Silva, T. Lettner, R. Trotta, J. J. Finley, K. Müller, et al., "Resonance fluorescence of GaAs quantum dots with near-unity photon indistinguishability", Nano Letters **19**, 2404–2410 (2019).

[140] G. Juska, V. Dimastrodonato, L. O. Mereni, A. Gocalinska, and E. Pelucchi, "Towards quantum-dot arrays of entangled photon emitters", Nature Photonics **7**, 527–531 (2013).

[141] T. Grange, G. Hornecker, D. Hunger, J.-P. Poizat, J.-M. Gérard, P. Senellart, and A. Auffèves, "Cavity-funneled generation of indistinguishable single photons from strongly dissipative quantum emitters", Physical Review Letters **114**, 193601 (2015).

[142] J. Iles-Smith, D. P. S. McCutcheon, A. Nazir, and J. Mork, "Phonon scattering inhibits simultaneous near-unity efficiency and indistinguishability in semiconductor single-photon sources", Nature Photonics **11**, 521–526 (2017).

[143] M. Davanco, J. Liu, L. Sapienza, C.-Z. Zhang, J. V. D. M. Cardoso, V. Verma, R. Mirin, S. W. Nam, L. Liu, and K. Srinivasan, "Heterogeneous integration for on-chip quantum photonic circuits with single quantum dot devices", Nature Communications **8**, 889 (2017).

[144] Y.-M. He, J. Liu, S. Maier, M. Emmerling, S. Gerhardt, M. Davanco, K. Srinivasan, C. Schneider, and S. Höfling, "Deterministic implementation of a bright, on-demand single-photon source with near-unity indistinguishability via quantum dot imaging", Optica **4**, 802 (2017).

[145] P. Schnauber, A. Singh, J. Schall, S. I. Park, J. D. Song, S. Rodt, K. Srinivasan, S. Reitzenstein, and M. Davanco, "Indistinguishable photons from deterministically integrated single quantum dots in heterogeneous GaAs/Si3N4 quantum photonic circuits", Nano Letters **19**, 7164 (2019).

[146] H. Wang, Y.-M. He, T.-H. Chung, H. Hu, Y. Yu, S. Chen, X. Ding, M.-C. Chen, J. Qin, X. Yang, et al., "Towards optimal single-photon sources from polarized microcavities", Nature Photonics **13**, 770–775 (2019).

[147] B. Gayral, J. M. Gérard, B. Legrand, E. Costard, and V. Thierry-Mieg, "Optical study of GaAs/AlAs pillar microcavities with elliptical cross section", Applied Physics Letters **72**, 1421–1423 (1998).

[148] D. F. Walls and G. J. Milburn, *Quantum optics* (Springer, 1994).

[149] C. Y. Hu, A. Young, J. L. O'Brien, W. J. Munro, and J. G. Rarity, "Giant optical faraday rotation induced by a single-electron spin in a quantum dot: applications to entangling remote spins via a single photon", Physical Review B **78**, 085307 (2008).

[150] A. Auffèves, J.-M. Gérard, and J.-P. Poizat, "Pure emitter dephasing: a resource for advanced solid-state single-photon sources", Physical Review A **79**, 053838 (2009).

[151] H. P. Breuer and F. Petruccione, *The theory of open quantum systems* (Oxford University Press, Great Clarendon Street, 2002).

[152] R. A. Bertlmann, W. Grimus, and B. C. Hiesmayr, "Open-quantum-system formulation of particle decay", Physical Review A **73**, 054101 (2006).

[153] T. H. Stievater, X. Li, D. G. Steel, D. Gammon, D. S. Katzer, D. Park, C. Piermarocchi, and L. J. Sham, "Rabi oscillations of excitons in single quantum dots.", Physical Review Letters **87**, 133603 (2001).

[154] K. A. Fischer, L. Hanschke, J. Wierzbowski, T. Simmet, C. Dory, J. J. Finley, J. Vucković, and K. Müller, "Signatures of two-photon pulses from a quantum two-level system", Nature Physics **13**, 649 (2017).

[155] T. Grange, N. Somaschi, C. Antón, L. De Santis, G. Coppola, V. Giesz, A. Lemaitre, I. Sagnes, A. Auffèves, and P. Senellart, "Reducing phonon-induced decoherence in solid-state single-photon sources with cavity quantum electrodynamics", Physical Review Letters **118**, 253602 (2017).

[156] R. Trotta, J. Martín-Sánchez, I. Daruka, C. Ortix, and A. Rastelli, "Energy-tunable sources of entangled photons: a viable concept for solid-state-based quantum relays", Physical Review Letters **114**, 150502 (2015).

[157] S. C. Wein, J.-W. Ji, Y.-F. Wu, F. Kimiaee Asadi, R. Ghobadi, and C. Simon, "Analyzing photon-count heralded entanglement generation between solid-state spin qubits by decomposing the master-equation dynamics", Physical Review A **102**, 033701 (2020).

[158] J. Quilter, A. Brash, F. Liu, M. Glässl, A. Barth, V. Axt, M. Skolnick, and A. Fox, "Phonon-assisted population inversion of a single InGaAs/GaAs quantum dot by pulsed laser excitation", Physical Review Letters **114**, 137401 (2015).

[159] M. Reindl, J. H. Weber, D. Huber, C. Schimpf, S. F. Covre da Silva, S. L. Portalupi, R. Trotta, P. Michler, and A. Rastelli, "Highly indistinguishable single photons from incoherently excited quantum dots", Physical Review B **100**, 155420 (2019).

[160] M. Cosacchi, F. Ungar, M. Cygorek, A. Vagov, and V. M. Axt, "Emission-frequency separated high quality single-photon sources enabled by phonons", Physical Review Letters **123**, 017403 (2019).

[161] C. Gustin and S. Hughes, "Efficient pulse-excitation techniques for single photon sources from quantum dots in optical cavities", Advanced Quantum Technologies **3**, 1900073 (2019).

[162] S. E. Thomas, M. Billard, N. Coste, S. C. Wein, Priya, H. Ollivier, O. Krebs, L. Tazaïrt, A. Harouri, A. Lemaitre, et al., "Bright polarized single-photon source based on a linear dipole", Physical Review Letters, accepted (2021).

[163] T. H. Au, S. Buil, X. Quelin, J.-P. Hermier, and N. Lai, "Coupling of a single photon source based on a colloidal semiconductor nanocrystal into polymer-based photonic structures", in (May 2018), p. 114.

[164] T. Nguyen, Q. Tong, I. Ledoux-Rak, and N. Lai, "One-step fabrication of submicrostructures by low one-photon absorption direct laser writing technique with local thermal effect", Journal of Applied Physics **119**, 013101 (2016).

[165] M. Billard, *Thèse : vers des sources semi-conductrices de photons uniques et indiscernables, efficaces et faciles à utiliser, pour des applications quantiques* (Université Paris Saclay, 2021).

[166] L.-M. Duan, M. D. Lukin, J. I. Cirac, and P. Zoller, "Long-distance quantum communication with atomic ensembles and linear optics", Nature **414**, 413–418 (2001).

[167] N. Sangouard, C. Simon, H. de Riedmatten, and N. Gisin, "Quantum repeaters based on atomic ensembles and linear optics", Reviews of Modern Physics **83**, 33–80 (2011).

[168] E. Knill, R. Laflamme, and G. J. Milburn, "A scheme for efficient quantum computation with linear optics", Nature **409**, 46–52 (2001).

[169] J. L. OBrien, "Optical quantum computing", Science **318**, 1567–1570 (2007).

[170] K. A. Fischer, R. Trivedi, and D. Lukin, "Particle emission from open quantum systems", Physical Review A **98**, 023853 (2018).

[171] R. Trivedi, K. A. Fischer, J. Vučković, and K. Müller, "Generation of non-classical light using semiconductor quantum dots", Advanced Quantum Technologies **3**, 1900007 (2020).

[172] A. B. U'Ren, C. Silberhorn, J. L. Ball, K. Banaszek, and I. A. Walmsley, "Characterization of the nonclassical nature of conditionally prepared single photons", Physical Review A **72**, 021802 (2005).

[173] A. J. Bennett, R. B. Patel, C. A. Nicoll, D. A. Ritchie, and A. J. Shields, "Interference of dissimilar photon sources", Nature Physics **5**, 715–717 (2009).

[174] S. V. Polyakov, A. Muller, E. B. Flagg, A. Ling, N. Borjemscaia, E. Van Keuren, A. Migdall, and G. S. Solomon, "Coalescence of single photons emitted by disparate single-photon sources: the example of InAs quantum dots and parametric down-conversion sources", Physical Review Letters **107**, 157402 (2011).

[175] T. Huber, M. Prilmüller, M. Sehner, G. S. Solomon, A. Predojević, and G. Weihs, "Interfacing a quantum dot with a spontaneous parametric down-conversion source", Quantum Science and Technology **2**, 034016 (2017).

[176] N. Tomm, A. Javadi, N. Antoniadis, D. Najer, M. Löbl, A. Korsch, R. Schott, S. Valentin, A. Wieck, A. Ludwig, and R. Warburton, "A bright and fast source of coherent single photons", Nature Nanotechnology **16** (2021).

[177] K. A. Fischer, L. Hanschke, M. Kremser, J. J. Finley, K. Müller, and J. Vucković, "Pulsed rabi oscillations in quantum two-level systems: beyond the area theorem", Quantum Science and Technology **3**, 014006 (2017).

[178] M. Bayer, G. Ortner, O. Stern, A. Kuther, A. A. Gorbunov, A. Forchel, P. Hawrylak, S. Fafard, K. Hinzer, T. L. Reinecke, S. N. Walck, J. P. Reithmaier, F. Klopf, and F. Schäfer, "Fine structure of neutral and charged excitons in self-assembled In(Ga)As/(Al)GaAs quantum dots", Physical Review B **65**, 195315 (2002).

[179] A. S. Lenihan, M. V. Gurudev Dutt, D. G. Steel, S. Ghosh, and P. K. Bhattacharya, "Raman coherence beats from entangled polarization eigenstates in InAs quantum dots", Physical Review Letters **88**, 223601 (2002).

[180] K. Zielnicki, K. Garay-Palmett, D. Cruz delgado, H. Cruz-Ramirez, M. O'Boyle, B. Fang, V. Lorenz, A. U'Ren, and P. Kwiat, "Joint spectral characterization of photon-pair sources", Journal of Modern Optics **65**, 1141–1160 (2018).

[181] S. Lloyd, M. S. Shahriar, J. H. Shapiro, and P. R. Hemmer, "Long distance, unconditional teleportation of atomic states via complete Bell state measurements", Physical Review Letters **87**, 167903 (2001).

[182] J. D. Plumhof, R. Trotta, A. Rastelli, and O. G. Schmidt, "Experimental methods of post-growth tuning of the excitonic fine structure splitting in semiconductor quantum dots", Nanoscale Research Letters **7**, 336 (2012).

[183] R. J. Young, R. M. Stevenson, A. J. Shields, P. Atkinson, K. Cooper, D. A. Ritchie, K. M. Groom, A. I. Tartakovskii, and M. S. Skolnick, "Inversion of exciton level splitting in quantum dots", Physical Review B **72**, 113305 (2005).

[184] J. D. Plumhof, V. Krápek, F. Ding, K. D. Jöns, R. Hafenbrak, P. Klenovský, A. Herklotz, K. Dörr, P. Michler, A. Rastelli, and O. G. Schmidt, "Strain-induced anticrossing of bright exciton levels in single self-assembled gaas/al x ga 1- x as and in x ga 1- x as/gaas quantum dots", Physical Review B **83**, 121302 (2011).

[185] K. Kowalik, *Thesis: symmetry effects in optical properties of single semiconductor quantum dots* (Warsaw University, Université Paris VI, 2007).

[186] B. Gerardot, S. Seidl, P. Dalgarno, R. Warburton, D. Granados, J. García, K. Kowalik-Seidl, O. Krebs, K. Karrai, A. Badolato, and P. Petroff, "Manipulating exciton fine-structure in quantum dots with a lateral electric field", Applied Physics Letters **90**, 041101 (2007).

[187] S. Seidl, M. Kroner, A. Hogele, and K. Karrai, "Effect of uniaxial stress on excitons in a self-assembled quantum dot", Applied Physics Letters **88** (2006).

[188] C. Kuklewicz, R. Malein, P. Petroff, and B. Gerardot, "Electro-elastic tuning of single particles in individual self-assembled quantum dots", Nano Letters **12**, 3761 (2012).

[189] R. Trotta, E. Zallo, C. Ortix, P. Atkinson, J. D. Plumhof, J. van den Brink, A. Rastelli, and O. G. Schmidt, "Universal recovery of the energy-level degeneracy of bright excitons in InGaAs quantum dots without a structure symmetry", Physical Review Letters **109**, 147401 (2012).

[190] R. Trotta, J. Wildmann, E. Zallo, O. Schmidt, and A. Rastelli, "Highly entangled photons from hybrid piezoelectric-semiconductor quantum dot devices", Nano Letters **14**, 3439–3444 (2014).

[191] R. M. Stevenson, A. J. Hudson, A. J. Bennett, R. J. Young, C. A. Nicoll, D. A. Ritchie, and A. J. Shields, "Evolution of entanglement between distinguishable light states", Physical Review Letters **101**, 170501 (2008).

[192] C. Santori, D. Fattal, M. Pelton, G. S. Solomon, and Y. Yamamoto, "Polarization-correlated photon pairs from a single quantum dot", Physical Review B **66**, 045308 (2002).

[193] R. M. Stevenson, R. M. Thompson, A. J. Shields, I. Farrer, B. E. Kardynal, D. A. Ritchie, and M. Pepper, "Quantum dots as a photon source for passive quantum key encoding", Physical Review B **66**, 081302 (2002).

[194] S. Ulrich, S. Strauf, P. Michler, G. Bacher, and A. Forchel, "Triggered polarization-correlated photon pairs from a single cdse quantum dot", Applied Physics Letters **83**, 1848–1850 (2003).

[195] R. Young, R. Stevenson, P. Atkinson, K. Cooper, D. Ritchie, and A. Shields, "Improved fidelity of triggered entangled photons from single quantum dots", New Journal of Physics **8**, 29 (2006).

[196] A. J. Hudson, R. M. Stevenson, A. J. Bennett, R. J. Young, C. A. Nicoll, P. Atkinson, K. Cooper, D. A. Ritchie, and A. J. Shields, "Coherence of an entangled exciton-photon state", Physical Review Letters **99**, 266802 (2007).

[197] R. Hafenbrak, S. Ulrich, P Michler, L Wang, A. Rastelli, and O. Schmidt, "Triggered polarization-entangled photon pairs from a single quantum dot up to 30 K", New Journal of Physics **9**, 315 (2007).

[198] A. Muller, W. Fang, J. Lawall, and G. S. Solomon, "Creating polarization-entangled photon pairs from a semiconductor quantum dot using the optical Stark effect", Physical Review Letters **103**, 217402 (2009).

[199] R. M. Stevenson, C. L. Salter, J. Nilsson, A. J. Bennett, M. B. Ward, I. Farrer, D. A. Ritchie, and A. J. Shields, "Indistinguishable entangled photons generated by a light-emitting diode", Physical Review Letters **108**, 040503 (2012).

[200] T. Flissikowski, A. Betke, I. A. Akimov, and F. Henneberger, "Two-photon coherent control of a single quantum dot", Physical Review Letters **92**, 227401 (2004).

[201] G Weihs, H Jayakumar, A Predojević, T Huber, T Kauten, and G. Solomon, "Deterministic photon cascade from resonant two-photon excitation of a single inas quantum dot", in (IEEE, 2012), pp. 674–675.

[202] M. Muller, S. Bounouar, K. D. Jons, and P. Michler, "On-demand generation of indistinguishable polarization-entangled photon pairs", Nature Photonics **8**, 224–228 (2014).

[203] D. Huber, M. Reindl, S. F. Covre da Silva, C. Schimpf, J. Martín-Sánchez, H. Huang, G. Piredda, J. Edlinger, A. Rastelli, and R. Trotta, "Strain-tunable GaAs quantum dot: a nearly dephasing-free source of entangled photon pairs on demand", Physical Review Letters **121**, 033902 (2018).

[204] H. Wang, H. Hu, T.-H. Chung, J. Qin, X. Yang, J.-P. Li, R.-Z. Liu, H.-S. Zhong, Y.-M. He, X. Ding, et al., "On-demand semiconductor source of entangled photons which simultaneously has high fidelity, efficiency, and indistinguishability", Physical Review Letters **122**, 113602 (2019).

[205] R. Stevenson, R Young, P Atkinson, K Cooper, D. Ritchie, and A Shields, "A semiconductor source of triggered entangled photon pairs", Nature **439**, 179 (2006).

[206] Y. Huo, A. Rastelli, and O. Schmidt, "Ultra-small excitonic fine structure splitting in highly symmetric quantum dots on GaAs (001) substrate", Applied Physics Letters **102**, 152105 (2013).

[207] T. Mano, M. Abbarchi, T. Kuroda, B. McSkimming, A. Ohtake, K. Mitsuishi, and K. Sakoda, "Self-assembly of symmetric GaAs quantum dots on (111)a substrates: suppression of fine-structure splitting", Applied Physics Express **3**, 065203 (2010).

[208] M. Abbarchi, T. Kuroda, T. Mano, and K. Sakoda, "Fine structure splitting reduction in droplet epitaxy GaAs quantum dots grown on (111)a surface", in, Vol. 245, Journal of Physics Conference Series (Sept. 2010), p. 012049.

[209] D. Ellis, R. Stevenson, R. Young, A. Shields, P. Atkinson, and D. Ritchie, "Control of fine-structure splitting of individual InAs quantum dots by rapid thermal annealing", Applied Physics Letters **90**, 011907 (2007).

[210] A. Bennett, M. Pooley, R. Stevenson, M. Ward, R. Patel, A. Giroday, N. Sköld, I. Farrer, C. Nicoll, D. Ritchie, and A. Shields, "Electric-field-induced coherent coupling of the exciton states in a single quantum dot", Nature Physics **6**, 947–950 (2010).

[211] K. Kowalik, O. Krebs, A. Lemaitre, S. Laurent, P. Senellart, P. Voisin, and J. A. Gaj, "Influence of an in-plane electric field on exciton fine structure in InAs-GaAs self-assembled quantum dots", Applied Physics Letters **86**, 041907 (2005).

[212] M. Zeeshan, N. Sherlekar, A. Ahmadi, R. L. Williams, and M. E. Reimer, "Proposed scheme to generate bright entangled photon pairs by application of a quadrupole field to a single quantum dot", Physical Review Letters **122**, 227401 (2019).

[213] M. Gong, W. Zhang, G.-C. Guo, and L. He, "Exciton polarization, fine-structure splitting, and the asymmetry of quantum dots under uniaxial stress", Physical Review Letters **106**, 227401 (2011).

[214] R. Trotta, J. Martín-Sánchez, J. Wildmann, G. Piredda, M. Reindl, C. Schimpf, E. Zallo, S. Stroj, J. Edlinger, and A. Rastelli, "Wavelength-tunable sources of entangled photons interfaced with atomic vapours", Nature Communications **7**, 10375 (2016).

[215] M. Moczała, Dusanowski, S. Gerhardt, Y. He, M. Reindl, A. Rastelli, R. Trotta, N. Gregersen, S. Höfling, and C. Schneider, "Strain-tunable single-photon source based on a quantum dot–micropillar system", ACS Photonics **6**, 2025–2031 (2019).

[216] T. Hiroshima, "Electric field induced refractive index changes in GaAs-AlxGa1-xAs quantum wells", Applied Physics Letters **50**, 968–970 (1987).

[217] J. A. Frey, H. J. Snijders, J. Norman, A. C. Gossard, J. E. Bowers, W. Loffler, and D. Bouwmeester, "Electro-optic polarization tuning of microcavities with a single quantum dot", Opt. Lett. **43**, 4280–4283 (2018).

[218] S. Strauf, N. Stoltz, M. Rakher, L. Coldren, P. Petroff, and D. Bouwmeester, "High-frequency single-photon source with polarization control", Nature Photonics **1**, 704–708 (2007).

[219] A. I. Tartakovskii, M. N. Makhonin, I. R. Sellers, J. Cahill, A. D. Andreev, D. M. Whittaker, J. P. R. Wells, A. M. Fox, D. J. Mowbray, M. S. Skolnick, K. M. Groom, M. J. Steer, H. Y. Liu, and M. Hopkinson, "Effect of thermal annealing and strain engineering on the fine structure of quantum dot excitons", Physical Review B **70**, 193303 (2004).

[220] W. Langbein, P. Borri, U. Woggon, V. Stavarache, D. Reuter, and A. D. Wieck, "Control of fine-structure splitting and biexciton binding in InxGa1-xAs quantum dots by annealing", Physical Review B **69**, 161301 (2004).

[221] E. Moreau, *Thèse : etude d'une source solide monomode de photons uniques constituée par une boite quantique semi-conductrice dans une microcavité optique* (Physique atomique, Université Pierre et Marie Curie - Paris VI, 2002).

[222] F. Meier and B. Zakharchenya, *Optical orientation*, Vol. 8, Modern Problems in Condensed Matter Sciences (1984).

[223] K. D. Jöns, P. Atkinson, M. Müller, M. Heldmaier, S. M. Ulrich, O. G. Schmidt, and P. Michler, "Triggered indistinguishable single photons with narrow line widths from site-controlled quantum dots", Nano Letters **13**, 126–130 (2013).

[224] M. E. Reimer, G. Bulgarini, A. Fognini, R. W. Heeres, B. J. Witek, M. A. M. Versteegh, A. Rubino, T. Braun, M. Kamp, S. Höfling, D. Dalacu, J. Lapointe, P. J. Poole, and V. Zwiller, "Overcoming power broadening of the quantum dot emission in a pure wurtzite nanowire", Physical Review B **93**, 195316 (2016).

[225] M. Reindl, K. Jöns, D. Huber, C. Schimpf, Y. Huo, V. Zwiller, A. Rastelli, and R. Trotta, "Phonon-assisted two-photon interference from remote quantum emitters", Nano Letters **17**, 4090–4095 (2017).

[226] W. Gao, P. Fallahi, E. Togan, A. Delteil, Y. Chin, J. Miguel-Sánchez, and A. Imamoglu, "Quantum teleportation from a propagating photon to a solid-state spin qubit.", Nature communications **4**, 2744 (2013).

[227] J. Cha, L. Howard, A. Tranter, M. Su, M. P. Almeida, and A. G. White, "A toolbox for improving the performance of a solid-state single-photon source, abstract b12.07", in Korean physical society meeting (2020).

[228] G. Bacher, R. Weigand, J. Seufert, V. D. Kulakovskii, N. A. Gippius, A. Forchel, K. Leonardi, and D. Hommel, "Biexciton versus exciton lifetime in a single semiconductor quantum dot", Physical Review Letters **83**, 4417–4420 (1999).

[229] O. Gazzano, S. Michaelis de Vasconcellos, K. Gauthron, C. Symonds, P. Voisin, J. Bellessa, A. Lemaitre, and P. Senellart, "Single photon source using confined tamm plasmon modes", Applied Physics Letters **100**, 232111 (2012).

[230] S. Michaelis de Vasconcellos, A. Calvar, A. Dousse, J. Suffczyński, N. Dupuis, A. Lemaitre, I. Sagnes, J. Bloch, P. Voisin, and P. Senellart, "Spatial, spectral, and polarization properties of coupled micropillar cavities", Applied Physics Letters **99**, 101103 (2011).

[231] S. Wein, N. Lauk, R. Ghobadi, and C. Simon, "Feasibility of efficient room-temperature solid-state sources of indistinguishable single photons using ultrasmall mode volume cavities", Physical Review B **97**, 205418 (2018).

[232] Y.-M. He, H. Wang, S. Gerhardt, K. Winkler, J. Jurkat, Y. Yu, M.-C. Chen, X. Ding, S. Chen, J. Qian, et al., "Polarized indistinguishable single photons from a quantum dot in an elliptical micropillar", arXiv:1809.10992 (2018).

# Appendices

# Appendix A

# Appendix: group theory

The symmetry of quantum dots greatly impacts its emission properties. In this appendix, we give the definitions of the different symmetries mentioned in the main text.

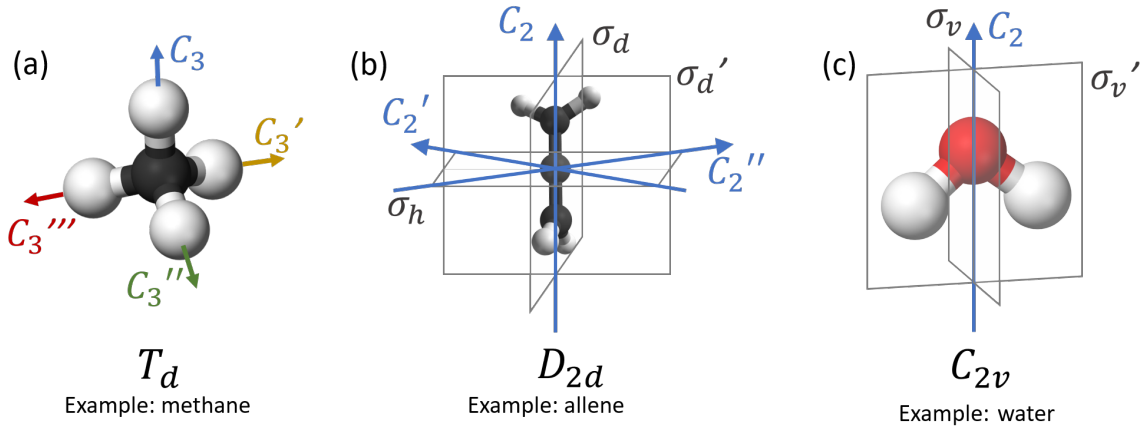


Figure A.1: (a) Illustration of the cubic ($T_d$) symmetry. (b) Tetragonal ($D_{2d}$) symmetry. (c) Orthorhombic ($C_{2v}$) symmetry.

- The cubic ($T_d$) symmetry defines geometries that are invariant by: $8C_3$ (rotations by 120° around axes $C_3$, $C_3'$, $C_3''$ and $C_3'''$), $3C_2$ (rotations by 180° around the axes that are halfway between $C_3$ and $C_3'$, between $C_3$ and $C_3''$ and halfway between $C_3$ and $C_3'''$ that I did not draw for the sake of clarity), $6\sigma_d$ (reflections by the $\sigma_d$ planes defined by the couples of axes $\{C_3; C_3'\}$, $\{C_3; C_3''\}$, $\{C_3; C_3'''\}$, $\{C_3'; C_3''\}$, $\{C_3'; C_3'''\}$, $\{C_3''; C_3'''\}$) and finally $6S_4$ operations (rotation by 90° around the axis bisecting $C_3$ and $C_3'$ followed by a reflection by the plane that is perpendicular to that axis, and 5 similar actions but with the couples of axes $\{C_3; C_3''\}$, $\{C_3; C_3'''\}$, $\{C_3'; C_3''\}$, $\{C_3'; C_3'''\}$ and $\{C_3''; C_3'''\}$). An example of molecule belonging to this symmetry group is the methane molecule $CH_4$, as shown on figure A.1(a).

- The tetragonal ($D_{2d}$) symmetry is a lower symmetry than $T_d$. It defines geometries that are invariant by: $C_2$ (rotation by 180° around the axis named $C_2$), $2C_2'$ (rotations by 180° around axes $C_2'$ and $C_2''$), $2\sigma_d$ (reflections by the $\sigma_d$ and $\sigma_d'$) and $2S_4$ (clockwise and

anticlockwise rotations by 180° around axis $C_2$ followed by a reflection by the plane $\sigma_h$. Planes $\sigma_d$ are defined as planes that bisect the angle between two adjacent $C_2$ rotation axes. An example of molecule belonging to this symmetry group is the allene molecule $C_3H_4$, as shown on figure A.1(b).

- The orthorhombic ($C_{2v}$) symmetry: it is an even lower symmetry than $D_{2d}$. It defines geometries that are invariant by: $C_2$ (rotation by 180° around the axis named $C_2$) and $2\sigma_v$ (reflection by the planes $\sigma_v$ and $\sigma'_v$). An example of molecule belonging to this symmetry group is the water molecule $H_2O$, as shown on figure A.1(c).

# Appendix B

# Appendix: derivation of the brightness for an exciton-based single-photon source in a cross-polarization setup

In the main part of the thesis, I have shown that the maximum brightness one can get from an exciton-based source in a cross-polarized setup, in the bad-cavity regime, and with a symmetric cavity, is equal to 1/2. In this appendix, we present the model developed by S. Wein to derive an expression of the brightness coming out from an exciton-based single-photon source, without making the bad-cavity assumption, as function of the different parameters involved. I use an inversion of the Bloch equations, which allows me to find the brightness without making any assumption about the relative magnitude of the parameters.

## B.1 Optical Bloch Equations

From the master equation 2.15, we can derive a set of 16 coupled linear differential optical Bloch equations that describe the dynamics of the 16 expectation values:

$$\begin{aligned} &\langle \hat{x}^\dagger \hat{x} \rangle , \langle \hat{x}^\dagger \hat{y} \rangle , \langle \hat{y}^\dagger \hat{x} \rangle , \langle \hat{y}^\dagger \hat{y} \rangle , \langle \hat{x}^\dagger \hat{h} \rangle , \langle \hat{x}^\dagger \hat{v} \rangle , \langle \hat{x} \hat{h}^\dagger \rangle , \langle \hat{x} \hat{v}^\dagger \rangle , \\ &\langle \hat{y}^\dagger \hat{h} \rangle , \langle \hat{y}^\dagger \hat{v} \rangle , \langle \hat{y} \hat{h}^\dagger \rangle , \langle \hat{y} \hat{v}^\dagger \rangle , \langle \hat{h}^\dagger \hat{h} \rangle , \langle \hat{h}^\dagger \hat{v} \rangle , \langle \hat{v}^\dagger \hat{h} \rangle , \langle \hat{v}^\dagger \hat{v} \rangle . \end{aligned} \tag{B.1}$$

### B.1.1 Derivation of the equation of motion for an example

We outline how to compute the optical Bloch equations using $\langle \hat{x}^\dagger \hat{x} \rangle$ as a case example. The population in the state $|x\rangle$ is given by the equation of motion

$$\begin{aligned} \frac{d}{dt} \langle \hat{x}^\dagger \hat{x} \rangle &= \frac{d}{dt} \mathrm{Tr} \left( \hat{x}^\dagger \hat{x} \hat{\rho}(t) \right) = \mathrm{Tr} \left( \hat{x}^\dagger \hat{x} \frac{d}{dt} \hat{\rho}(t) \right) \\ &= -i \mathrm{Tr} \big( \hat{x}^\dagger \hat{x} \big[ \hat{H}, \hat{\rho}(t) \big] \big) + \gamma_x \mathrm{Tr} \left( \hat{x}^\dagger \hat{x} \mathcal{D}(\hat{x}) \hat{\rho}(t) \right) + \cdots \end{aligned} \tag{B.2}$$

**Homogeneous term**

The homogeneous term can be solved by first rearranging the commutation using the linear and cyclic properties of the trace:

$$\mathrm{Tr}\big(\hat{x}^\dagger\hat{x}\hat{H}\hat{\rho} - \hat{x}^\dagger\hat{x}\hat{\rho}\hat{H}\big) = \mathrm{Tr}\big(\hat{x}^\dagger\hat{x}\hat{H}\hat{\rho} - \hat{H}\hat{x}^\dagger\hat{x}\hat{\rho}\big) = \mathrm{Tr}\big(\big[\hat{x}^\dagger\hat{x}, \hat{H}\big]\hat{\rho}(t)\big). \tag{B.3}$$

Then the commutation can be computed from equation 2.10:

$$\begin{aligned}\big[\hat{x}^\dagger\hat{x}, \hat{H}\big] =& \delta_x\big[\hat{x}^\dagger\hat{x}, \hat{x}^\dagger\hat{x}\big] + \delta_y\big[\hat{x}^\dagger\hat{x}, \hat{y}^\dagger\hat{y}\big] + \delta_h\big[\hat{x}^\dagger\hat{x}, \hat{h}^\dagger\hat{h}\big] + \delta_v\big[\hat{x}^\dagger\hat{x}, \hat{v}^\dagger\hat{v}\big] \\ &+ g_{xh}\left(\big[\hat{x}^\dagger\hat{x}, \hat{x}^\dagger\hat{h}\big] + \big[\hat{x}^\dagger\hat{x}, \hat{x}\hat{h}^\dagger\big]\right) + g_{xv}\left(\big[\hat{x}^\dagger\hat{x}, \hat{x}^\dagger\hat{v}\big] + \big[\hat{x}^\dagger\hat{x}, \hat{x}\hat{v}^\dagger\big]\right) \\ &+ g_{yh}\left(\big[\hat{x}^\dagger\hat{x}, \hat{y}^\dagger\hat{h}\big] + \big[\hat{x}^\dagger\hat{x}, \hat{y}\hat{h}^\dagger\big]\right) + g_{yv}\left(\big[\hat{x}^\dagger\hat{x}, \hat{y}^\dagger\hat{v}\big] + \big[\hat{x}^\dagger\hat{x}, \hat{y}\hat{v}^\dagger\big]\right)\end{aligned} \tag{B.4}$$

Some useful commutation relations for the three-level system are:

$$\begin{aligned}&\big[\hat{x}^\dagger\hat{x}, \hat{x}^\dagger\big] = \hat{x}^\dagger, \qquad &&\big[\hat{x}^\dagger\hat{x}, \hat{x}\big] = -\hat{x}, \qquad &&\big[\hat{x}^\dagger\hat{x}, \hat{y}^\dagger\big] = 0, \qquad &&\big[\hat{x}^\dagger\hat{x}, \hat{y}\big] = 0, \\ &\big[\hat{x}^\dagger\hat{y}, \hat{x}^\dagger\big] = 0, \qquad &&\big[\hat{x}^\dagger\hat{y}, \hat{x}\big] = -\hat{y}, \qquad &&\big[\hat{x}^\dagger\hat{y}, \hat{y}^\dagger\big] = \hat{x}^\dagger, \qquad &&\big[\hat{x}^\dagger\hat{y}, \hat{y}\big] = 0.\end{aligned} \tag{B.5}$$

Using symmetry of $\hat{x}$ and $\hat{y}$, the other commutation relations can easily be obtained.
We also have the following rules about the full system:

$$\big[\hat{x}^\dagger\hat{x}, \hat{h}\big] = 0, \qquad \big[\hat{x}^\dagger\hat{x}, \hat{h}^\dagger\big] \ = 0, \qquad \big[\hat{x}^\dagger\hat{x}, \hat{v}\big] = 0, \qquad \big[\hat{x}^\dagger\hat{x}, \hat{v}^\dagger\big] \ = 0. \tag{B.6}$$

Then, we have:

$$\begin{aligned}&\big[\hat{x}^\dagger\hat{x}, \hat{x}^\dagger\hat{x}\big] = 0 \\ &\big[\hat{x}^\dagger\hat{x}, \hat{y}^\dagger\hat{y}\big] = \hat{y}^\dagger\big[\hat{x}^\dagger\hat{x}, \hat{y}\big] + \big[\hat{x}^\dagger\hat{x}, \hat{y}^\dagger\big]\hat{y} = 0 \\ &\big[\hat{x}^\dagger\hat{x}, \hat{h}^\dagger\hat{h}\big] = \hat{h}^\dagger\big[\hat{x}^\dagger\hat{x}, \hat{h}\big] + \big[\hat{x}^\dagger\hat{x}, \hat{h}^\dagger\big]\hat{h} = 0 \\ &\big[\hat{x}^\dagger\hat{x}, \hat{v}^\dagger\hat{v}\big] = \hat{v}^\dagger\big[\hat{x}^\dagger\hat{x}, \hat{v}\big] + \big[\hat{x}^\dagger\hat{x}, \hat{v}^\dagger\big]\hat{v} = 0 \\ &\big[\hat{x}^\dagger\hat{x}, \hat{x}^\dagger\hat{h}\big] = \hat{x}^\dagger\big[\hat{x}^\dagger\hat{x}, \hat{h}\big] + \big[\hat{x}^\dagger\hat{x}, \hat{x}^\dagger\big]\hat{h} = \hat{x}^\dagger\hat{h} \\ &\big[\hat{x}^\dagger\hat{x}, \hat{x}\hat{h}^\dagger\big] = \hat{x}\big[\hat{x}^\dagger\hat{x}, \hat{h}^\dagger\big] + \big[\hat{x}^\dagger\hat{x}, \hat{x}\big]\hat{h}^\dagger = -\hat{x}\hat{h}^\dagger \\ &\big[\hat{x}^\dagger\hat{x}, \hat{x}^\dagger\hat{v}\big] = \hat{x}^\dagger\big[\hat{x}^\dagger\hat{x}, \hat{v}\big] + \big[\hat{x}^\dagger\hat{x}, \hat{x}^\dagger\big]\hat{v} = \hat{x}^\dagger\hat{v} \\ &\big[\hat{x}^\dagger\hat{x}, \hat{x}\hat{v}^\dagger\big] = \hat{x}\big[\hat{x}^\dagger\hat{x}, \hat{v}^\dagger\big] + \big[\hat{x}^\dagger\hat{x}, \hat{x}\big]\hat{v}^\dagger = -\hat{x}\hat{v}^\dagger \\ &\big[\hat{x}^\dagger\hat{x}, \hat{y}^\dagger\hat{h}\big] = \hat{y}^\dagger\big[\hat{x}^\dagger\hat{x}, \hat{h}\big] + \big[\hat{x}^\dagger\hat{x}, \hat{y}^\dagger\big]\hat{h} = 0 \\ &\big[\hat{x}^\dagger\hat{x}, \hat{y}\hat{h}^\dagger\big] = \hat{y}\big[\hat{x}^\dagger\hat{x}, \hat{h}^\dagger\big] + \big[\hat{x}^\dagger\hat{x}, \hat{y}\big]\hat{h}^\dagger = 0 \\ &\big[\hat{x}^\dagger\hat{x}, \hat{y}^\dagger\hat{v}\big] = \hat{y}^\dagger\big[\hat{x}^\dagger\hat{x}, \hat{v}\big] + \big[\hat{x}^\dagger\hat{x}, \hat{y}^\dagger\big]\hat{v} = 0 \\ &\big[\hat{x}^\dagger\hat{x}, \hat{y}\hat{v}^\dagger\big] = \hat{y}\big[\hat{x}^\dagger\hat{x}, \hat{v}^\dagger\big] + \big[\hat{x}^\dagger\hat{x}, \hat{y}\big]\hat{v}^\dagger = 0\end{aligned} \tag{B.7}$$

Finally:

$$\big[\hat{x}^\dagger\hat{x}, \hat{H}\big] = g_{xh}(\hat{x}^\dagger\hat{h} - \hat{x}\hat{h}^\dagger) + g_{xv}\left(\hat{x}^\dagger\hat{v} - \hat{x}\hat{v}^\dagger\right). \tag{B.8}$$

**Inhomogeneous terms**

The inhomogeneous (dissipative) part can be obtained by using the cyclic properties of the trace and some commutation relations:

$$\begin{aligned}\gamma_x \mathrm{Tr}\big(\hat{x}^\dagger\hat{x}\mathcal{D}(\hat{x})\hat{\rho}\big) &= \gamma_x \mathrm{Tr}\big(\hat{x}^\dagger\hat{x}\big(\hat{x}\hat{\rho}\hat{x}^\dagger - \hat{x}^\dagger\hat{x}\hat{\rho}/2 - \hat{\rho}\hat{x}^\dagger\hat{x}/2\big)\big) \\ &= \gamma_x \mathrm{Tr}\big(\big(\hat{x}^\dagger\hat{x}^\dagger\hat{x}\hat{x} - \hat{x}^\dagger\hat{x}\hat{x}^\dagger\hat{x}/2 - \hat{x}^\dagger\hat{x}\hat{x}^\dagger\hat{x}/2\big)\hat{\rho}\big) \\ &= -\gamma_x \mathrm{Tr}\big([\hat{x}^\dagger\hat{x}, \hat{x}^\dagger]\hat{x}\hat{\rho}\big) = -\gamma_x \mathrm{Tr}\big(\hat{x}^\dagger\hat{x}\hat{\rho}\big) = -\gamma_x \left\langle \hat{x}^\dagger\hat{x}\right\rangle .\end{aligned} \tag{B.9}$$

It is useful to note that if $\left[\hat{O}, \hat{A}^\dagger\right] = 0$ and $\left[\hat{O}, \hat{A}\right] = 0$, then $\mathrm{Tr}\big(\hat{O}\mathcal{D}(\hat{A})\hat{\rho}\big) = 0$. This can be proven:

$$\begin{aligned}\mathrm{Tr}\left(\hat{O}\mathcal{D}(\hat{A})\hat{\rho}\right) &= \gamma_x \mathrm{Tr}\left(\hat{O}\left(\hat{A}\hat{\rho}\hat{A}^\dagger - \hat{A}^\dagger\hat{A}\hat{\rho}/2 - \hat{\rho}\hat{A}^\dagger\hat{A}/2\right)\right) \\ &= \gamma_x \mathrm{Tr}\left(\left(\hat{A}^\dagger\hat{O}\hat{A} - \hat{O}\hat{A}^\dagger\hat{A}/2 - \hat{A}^\dagger\hat{A}\hat{O}/2\right)\hat{\rho}\right) \\ &= \gamma_x \mathrm{Tr}\left(\hat{O}\left(\hat{A}^\dagger\hat{A} - \hat{A}^\dagger\hat{A}/2 - \hat{A}^\dagger\hat{A}/2\right)\hat{\rho}\right) = 0.\end{aligned} \tag{B.10}$$

Then since $\left[\hat{x}^\dagger\hat{x}, \hat{y}\right] = 0$ and $\left[\hat{x}^\dagger\hat{x}, \hat{y}^\dagger\right] = 0$, we have $\mathrm{Tr}\big(\hat{x}^\dagger\hat{x}\mathcal{D}(\hat{y})\hat{\rho}\big) = 0$. In the same way, $\left[\hat{x}^\dagger\hat{x}, \hat{h}\right] = 0$ and $\left[\hat{x}^\dagger\hat{x}, \hat{h}^\dagger\right] = 0$ so $\mathrm{Tr}\big(\hat{x}^\dagger\hat{x}\mathcal{D}(\hat{h})\hat{\rho}\big) = 0$ and finally $\left[\hat{x}^\dagger\hat{x}, \hat{v}\right] = 0$ and $\left[\hat{x}^\dagger\hat{x}, \hat{v}^\dagger\right] = 0$ imply that $\mathrm{Tr}\big(\hat{x}^\dagger\hat{x}\mathcal{D}(\hat{v})\hat{\rho}\big) = 0$.

**Conclusion**

We have all the elements to write the equation of motion:

$$\frac{d}{dt}\left\langle \hat{x}^\dagger\hat{x}\right\rangle = -ig_{xh}(\left\langle \hat{x}^\dagger\hat{h}\right\rangle - \left\langle \hat{x}\hat{h}^\dagger\right\rangle) - ig_{xv}\left(\left\langle \hat{x}^\dagger\hat{v}\right\rangle - \left\langle \hat{x}\hat{v}^\dagger\right\rangle\right) - \gamma_x \left\langle \hat{x}^\dagger\hat{x}\right\rangle . \tag{B.11}$$

This equation is the first of 16 equations that are needed. It also gives the next 4 that should be derived. Namely, those for $\langle \hat{x}^\dagger\hat{h}\rangle$, $\langle \hat{x}\hat{h}^\dagger\rangle$, $\langle \hat{x}^\dagger\hat{v}\rangle$, and $\langle \hat{x}\hat{v}^\dagger\rangle$. Luckily, due to the symmetry between $x$ and $y$, and also between $h$ and $v$, it is possible to derive only 5 equations and then obtain the remaining ones by symmetry and conjugation. To identify $x$–$y$ symmetries, it is easier to have the Hamiltonian defined in the QD $x$–$y$ basis instead of in the QD $h$–$v$ basis like in [124].

For example, from $\langle \hat{x}^\dagger\hat{x}\rangle$ we can easily obtain the equation of motion for $\langle \hat{y}^\dagger\hat{y}\rangle$:

$$\frac{d}{dt}\left\langle \hat{y}^\dagger\hat{y}\right\rangle = -ig_{yh}(\left\langle \hat{y}^\dagger\hat{h}\right\rangle - \left\langle \hat{y}\hat{h}^\dagger\right\rangle) - ig_{yv}\left(\left\langle \hat{y}^\dagger\hat{v}\right\rangle - \left\langle \hat{y}\hat{v}^\dagger\right\rangle\right) - \gamma_y \left\langle \hat{y}^\dagger\hat{y}\right\rangle . \tag{B.12}$$

**Single-excitation approximation**

Deriving some of the equations requires using the single-excitation approximation, meaning that we limit ourselves to the subspace $\{|000\rangle, |x00\rangle, |y00\rangle, |010\rangle, |001\rangle\}$, as explained in paragraph 2.3.1. Let us apply it on an example to make it more concrete. When calculating the equation of motion for $\langle \hat{x}^\dagger\hat{h}\rangle$, we need to calculate:

$$\left[\hat{x}^\dagger\hat{h}, \hat{x}\hat{h}^\dagger\right] = \hat{x}^\dagger\hat{x}\left[\hat{h}, \hat{h}^\dagger\right] + \left[\hat{x}^\dagger, \hat{x}\right]\hat{h}^\dagger\hat{h} = \hat{x}^\dagger\hat{x} + \hat{x}^\dagger\hat{x}\hat{h}^\dagger\hat{h} - \hat{x}\hat{x}^\dagger\hat{h}^\dagger\hat{h} \tag{B.13}$$

where I used that $\left[\hat{h}, \hat{h}^\dagger\right] = 1$. In the single-excitation approximation, this term is equal to $\hat{x}^\dagger\hat{x} - \hat{h}^\dagger\hat{h}$.

Indeed, the operator $\hat{x}^\dagger\hat{x}\hat{h}^\dagger\hat{h}$ vanishes since $\hat{h}$ would give a nonzero operator only if the state it acts on is $|010\rangle$, but then it would be cancelled by $\hat{x}$. The only states that would give a non zero result are the states $|xkk'\rangle$ with $k, k' \in \mathbf{N}$ which is not part of the subspace we take into account in the single-excitation approximation.

And, about the term $\hat{x}\hat{x}^\dagger\hat{h}^\dagger\hat{h}$: in the same way, $\hat{h}$ would give a nonzero operator only if the state it acts on is $|010\rangle$. Since, $\hat{x}\hat{x}^\dagger|010\rangle = |010\rangle$, we can say that $\hat{x}\hat{x}^\dagger\hat{h}^\dagger\hat{h} = \hat{h}^\dagger\hat{h}$ in the single-excitation approximation.
In other words, in the single-excitation approximation we have $[\hat{x}, \hat{x}^\dagger\hat{A}] = \hat{A}$.

Luckily, using $x$–$y$ and $h$–$v$ symmetries and conjugation, it is possible to obtain all 16 equations from only the following set of 5 equations of motion:

$$
\begin{aligned}
\frac{d}{dt}\langle\hat{x}^\dagger\hat{x}\rangle &= -ig_{xh}(\langle\hat{x}^\dagger\hat{h}\rangle - \langle\hat{x}\hat{h}^\dagger\rangle) - ig_{xv}\left(\langle\hat{x}^\dagger\hat{v}\rangle - \langle\hat{x}\hat{v}^\dagger\rangle\right) - \gamma_x\langle\hat{x}^\dagger\hat{x}\rangle\,,\\
\frac{d}{dt}\langle\hat{x}^\dagger\hat{y}\rangle &= i(\delta_x - \delta_y)\langle\hat{x}^\dagger\hat{y}\rangle + ig_{xh}\langle\hat{y}\hat{h}^\dagger\rangle + ig_{xv}\langle\hat{y}\hat{v}^\dagger\rangle - ig_{yh}\langle\hat{x}^\dagger\hat{h}\rangle - ig_{yv}\langle\hat{x}^\dagger\hat{v}\rangle - \frac{1}{2}(\gamma_x + \gamma_y)\langle\hat{x}^\dagger\hat{y}\rangle\,,\\
\frac{d}{dt}\langle\hat{h}^\dagger\hat{h}\rangle &= ig_{xh}\left(\langle\hat{x}^\dagger\hat{h}\rangle - \langle\hat{x}\hat{h}^\dagger\rangle\right) + ig_{yh}\left(\langle\hat{y}^\dagger\hat{h}\rangle - \langle\hat{y}\hat{h}^\dagger\rangle\right) - \kappa_h\langle\hat{h}^\dagger\hat{h}\rangle\,,\\
\frac{d}{dt}\langle\hat{x}^\dagger\hat{h}\rangle &= i(\delta_x - \delta_h)\langle\hat{x}^\dagger\hat{h}\rangle - ig_{xh}\left(\langle\hat{x}^\dagger\hat{x}\rangle - \langle\hat{h}^\dagger\hat{h}\rangle\right)\\
&\qquad + ig_{xv}\langle\hat{v}^\dagger\hat{h}\rangle - ig_{yh}\langle\hat{x}^\dagger\hat{y}\rangle - \frac{1}{2}(\gamma_x + \kappa_h)\langle\hat{x}^\dagger\hat{h}\rangle\,,\\
\frac{d}{dt}\langle\hat{v}^\dagger\hat{h}\rangle &= -i(\delta_h - \delta_v)\langle\hat{v}^\dagger\hat{h}\rangle - ig_{xh}\langle\hat{x}\hat{v}^\dagger\rangle + ig_{xv}\langle\hat{x}^\dagger\hat{h}\rangle\\
&\qquad - ig_{yh}\langle\hat{y}\hat{h}^\dagger\rangle + ig_{yv}\langle\hat{y}^\dagger\hat{h}\rangle - \frac{1}{2}(\kappa_h + \kappa_v)\langle\hat{v}^\dagger\hat{h}\rangle\,.
\end{aligned}
\tag{B.14}
$$

The remaining 11 equations can all by obtained by exchanging $x$ with $y$ and/or $h$ with $v$ and/or by taking the complex conjugate.

To derive this system of equations, it is necessary to make the single-excitation approximation, described in 2.3.1. It means that the system of equations B.14 describes the dynamics of the subsystem of only 5 states, that I gave before in 2.13: $|00\rangle$, $|x0\rangle$, $|y0\rangle$, $|0h\rangle$, and $|0v\rangle$. This is necessary to truncate the number of coupled equations.

## B.2 Matrix differential equation

The system of linear differential equations B.14 can be expressed as a matrix differential equation in the basis given by equation (B.1). Let $\mathbf{u}$ be a 16-vector of the expectation values, so that $u_1 = \langle\hat{x}^\dagger\hat{x}\rangle$, $u_2 = \langle\hat{x}^\dagger\hat{y}\rangle$, and so on. Also, let $\mathbf{e}_k$ represent the unit vectors associated with $u_k$ so that $\mathbf{u} = \sum_k \mathbf{e}_k u_k$. Then the system can be written $\dot{\mathbf{u}} = \mathbf{M}\mathbf{u}$, where $\mathbf{M}$ is a

$16 \times 16$ matrix. The solution for any initial state $\mathbf{u}_0$ is then given by $\mathbf{u}(t) = e^{\mathbf{M}t}\mathbf{u}_0$ and the $k^{\text{th}}$ expectation value can be obtained by the scalar product $\mathbf{e}_k \cdot \mathbf{u}(t)$.

### B.2.1 Initial state

For any initial QD state $|\psi_0\rangle$ in the single-excitation approximation, there is a corresponding initial vector $\mathbf{u}_0$. For example, in our current case where $|\psi_0\rangle = |v0\rangle$, the corresponding vector is

$$\mathbf{u}_0 = \left(\sin^2\theta, -\sin\theta\cos\theta, -\sin\theta\cos\theta, \cos^2\theta, 0, 0, \cdots, 0\right)^{\mathrm{T}}. \tag{B.15}$$

That is $\langle\hat{x}^\dagger(0)\hat{x}(0)\rangle = \langle v0|\hat{x}^\dagger\hat{x}|v0\rangle = \sin^2\theta$, $\langle\hat{x}^\dagger(0)\hat{y}(0)\rangle = \langle v0|\hat{x}^\dagger\hat{y}|v0\rangle = -\sin\theta\cos\theta$, and so on. Since we assume that the cavity modes are in the vacuum state, all the expectation values involving cavity modes $\hat{h}$ and $\hat{v}$ (or their conjugates) will vanish.

### B.2.2 Final state

If we are collecting the single photon from the $H$ mode of the cavity, which is orthogonal to the excitation polarization, then we are interested in knowing the cavity population in the $H$-polarized mode. This corresponds to $\langle\hat{h}^\dagger\hat{h}\rangle = u_{13}$ and it is represented by the unit vector $\mathbf{e}_{13}$ in the basis ordering given by equation (B.1).

## B.3 Derivation of the brightness

Here again, like in the last section, we start from the general formula of the brightness $\beta = \kappa_h \int_0^\infty \langle\hat{h}^\dagger\hat{h}\rangle\, dt$. For an initially prepared state of $|\psi_0\rangle$ at $t = 0$ corresponding to $\mathbf{u}_0$, the brightness from the $H$-polarized cavity mode is given by

$$\begin{aligned}\beta &= \kappa_h \int_0^\infty \langle\hat{h}^\dagger\hat{h}\rangle\, dt = \kappa_h \int_0^\infty \mathbf{e}_{13}e^{\mathbf{M}t}\mathbf{u}_0 dt = \kappa_h\mathbf{e}_{13}\int_0^\infty e^{\mathbf{M}t}dt\mathbf{u}_0 \\ &= \kappa_h\mathbf{e}_{13}\,\mathbf{M}^{-1}e^{\mathbf{M}t}\Big|_0^\infty \mathbf{u}_0 = -\kappa_h\mathbf{e}_{13}\mathbf{M}^{-1}\mathbf{u}_0,\end{aligned} \tag{B.16}$$

where we have used that $\mathbf{M}$ is invertible and that $\lim_{t\to\infty} e^{\mathbf{M}t} = 0$, which holds so long as the system reaches a dark state such as $|00\rangle$. This is true when the system is only driven by pulses of light far-separated in time relative to the decay rates. The result from equation (B.16) is plotted in figure B.1. That expression means it is possible to solve the brightness without solving the complicated time dynamics—instead we only need to invert the matrix $\mathbf{M}$ [231]. In addition, this method does not require any assumptions about the magnitudes of the parameters, it only relies on the single-excitation approximation. Thus it can be used even if the cavity-emitter system is on the boundary of the bad-cavity regime where the Purcell enhancement saturates.

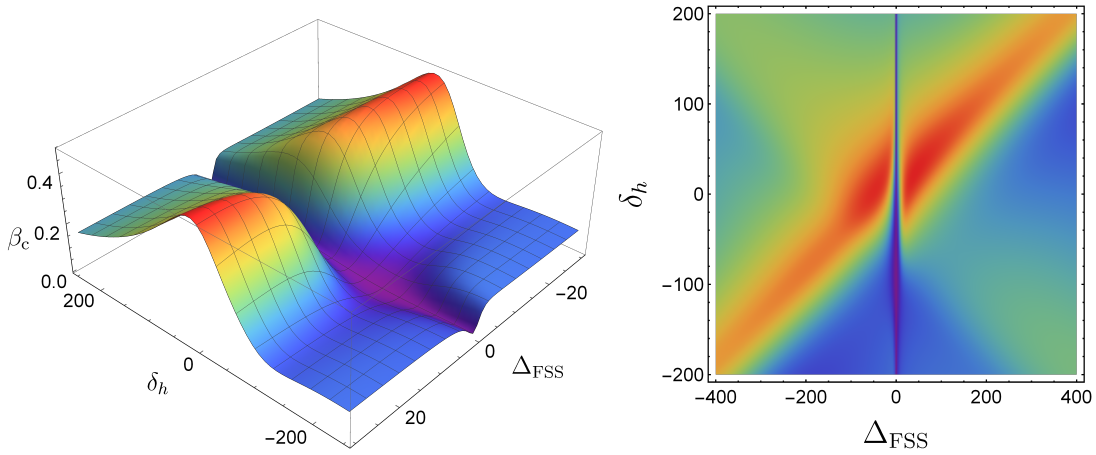


Figure B.1: Collection probability $\beta_c = \beta$ as a function of FSS $\omega_{xy}$ and $\delta_h$ for a large but fixed $\delta_v - \delta_h = 100$ computed numerically using the inverse method. The other parameters are $g = 20$, a relatively small $\kappa = 100$, $\gamma = 0.5$, and $\theta = \pi/8$. The units for all rates are $\mu$eV and are chosen to demonstrate the method and shape of the solution.

### B.3.1 Result and interpretation

Let us now assume that the cavity modes have roughly the same linewidths $\kappa = \kappa_h = \kappa_v$, that both dipoles dissipate equally $\gamma = \gamma_x = \gamma_y$, and that the cavity linewidths are much larger than the bare QD linewidth $\kappa \gg \gamma$. Under these conditions, the inverse of $\mathbf{M}$ can be analytically computed. In particular, in the case where the cavity modes are degenerate and equally detuned from both QD dipole resonances ($\delta_h = \delta_v = 0$), and the Purcell factor $R/\gamma > 1$, the emission brightness takes a simple form

$$\beta = \frac{1}{2}\omega_{xy}^2 \frac{(\kappa^2 + R^2 + \omega_{xy}^2 + \kappa R)}{(\kappa^2 + \omega_{xy}^2)(R^2 + \omega_{xy}^2)} \sin^2(2\theta), \tag{B.17}$$

where $R = 4g^2/\kappa$ is the effective rate of population exchange between the QD and cavity [150] in the limit of $\kappa \gg \gamma$. This function is maximized for arbitrary $R$ and $\kappa$ when $\omega_{xy} = \sqrt{\kappa R + (\kappa + R)\sqrt{\kappa R}}$. Interestingly, $\beta$ can exceed $1/2$ when $\omega_{xy}^2 > \kappa R$ and can reach a maximum value of $9/16$ when $R = \kappa$, implying $\omega_{xy} = \sqrt{3}\kappa$. Hence, the fundamental upper-bound on brightness for an exciton in a cross-polarization setup with degenerate cavity modes is $9/16$, and this occurs exactly on the boundary of the strong cavity coupling regime (when $\kappa = 2g$).

It seems counterintuitive to be able to exceed a probability of $1/2$ in a cross-polarization setup, but the coherent dynamics in the exciton excited state can be exploited to optimize the population transfer through the orthogonal cavity mode by competing with the Purcell effect. This becomes more clear when considering that the condition $\omega_{xy}^2 > \kappa R$ to exceed $1/2$ efficiency implies $\omega_{xy}/2 > g$. The coupling rate between $|v\rangle$ and $|h\rangle$ is $\omega_{xy}\cos(\theta+\phi)\sin(\theta+\phi)$, which maximizes at $\omega_{xy}/2$ for $\theta = \pi/4$, so when exciting with a polarization at $\pi/4$ from $|x0\rangle$ and $|y0\rangle$. When the FSS coupling exceeds the coupling to the cavity, population is more quickly transferred from $|v0\rangle$ to $|h0\rangle$ than from $|v0\rangle$ to $|0v\rangle$.

This 9/16 limit can be exceeded if there is a cavity mode splitting. If the mode splitting is larger than the cavity linewidth, the different detunings can cause unequal decay rates for $|x0\rangle$ and $|y0\rangle$, which can be engineered to favor decay from $|0h\rangle$. For example, suppose that $\delta_h = 0$, but $\delta_v = \delta \gg \kappa, \omega_{xy}$ and $\omega_{xy} > R$. Then the limit to brightness becomes $\beta = 1 - (\kappa^2 + \omega_{xy}^2)/(4\delta^2)$, which approaches unity as $\delta$ is increased. A similar regime has been recently utilized using a charged exciton by Jian-Wei Pan's group [232], where they hint at a similar scaling. However, a cavity mode splitting such as this necessarily requires a stronger excitation pulse. The detuning between the excitation laser and the quantum dot being bigger, the coupling between the cavity mode used to excite the quantum dot and the quantum dot itself is smaller. Then the required power to excite the quantum dot is higher, which may degrade other qualities of the single-photon source.

Alternatively, brightness can be improved if fast dynamic control of $\omega_{xy}$ is available. The simplest example would be to quickly turn off the FSS interaction at some time $t_c$ after excitation. If for $t < t_c$ we have $\omega_{xy} > g$ and for $t > t_c$ we have $\omega_{xy} \ll R$, then this can trap population in the $|0h\rangle$ state and improve emission into the $h$-mode of the cavity. For example, turning off an FSS of $\omega_{xy} = 40\mu$eV at $t_c = \pi/\omega_{xy}$ can increase the maximum brightness from $\sim 50\%$ to $\sim 77\%$ for a system with $g = 20\mu$eV, $\kappa = 200\mu$eV, and no cavity mode splitting. Doing so would require FSS switching on the ps timescale.

# Appendix C

# Appendix: $g^{(2)}$ and HOM histograms

## C.1 Second-order correlation histograms

All the figures of this document contain on the left side the second-order correlation histogram $g^{(2)}(\tau)$ as a function of the delay between two detectors, and on the right side the second-order correlation in a Hong-Ou-Mandel two-photon interference experiment.

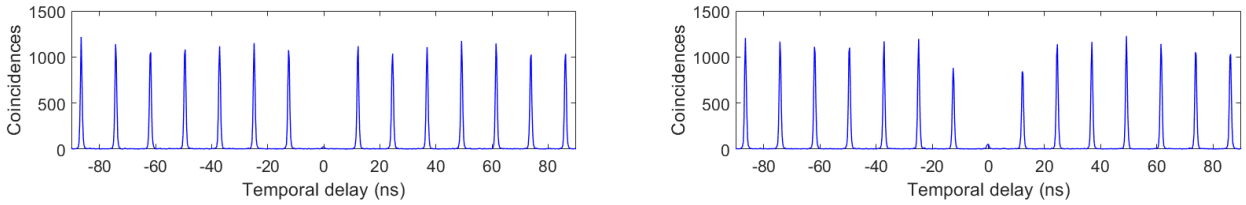


(a) Source S1.

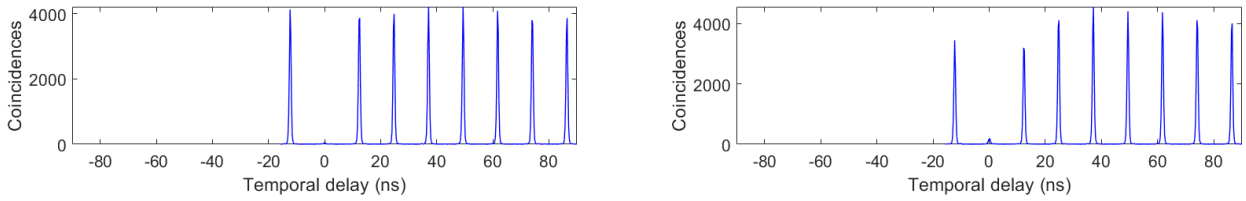


(b) Source S2.

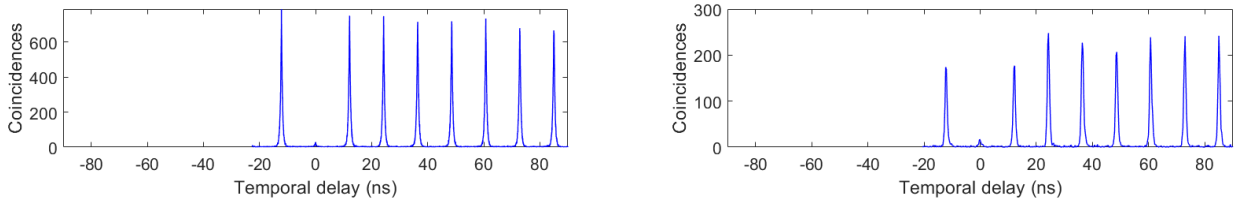


(c) Source S3.

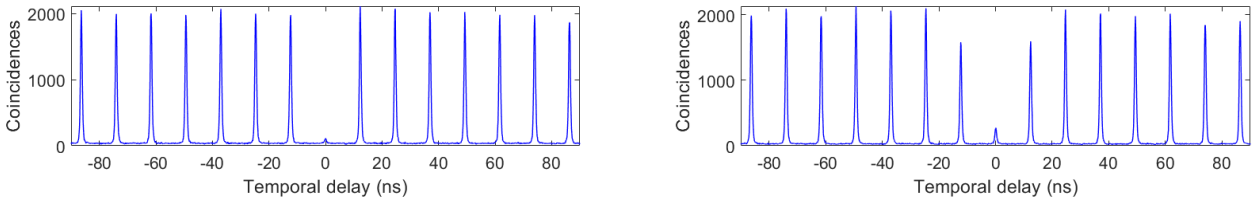


(a) Source S4.

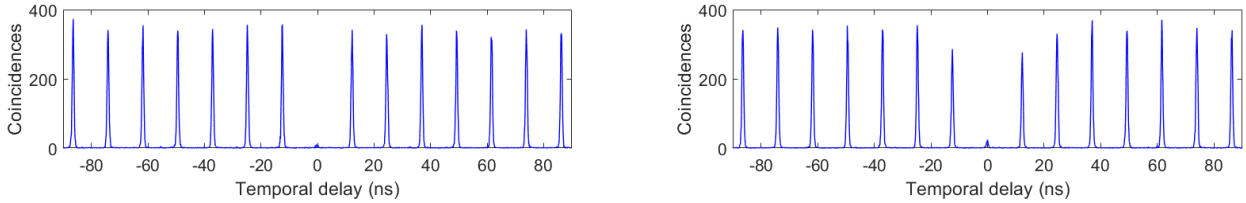


(b) Source S5.

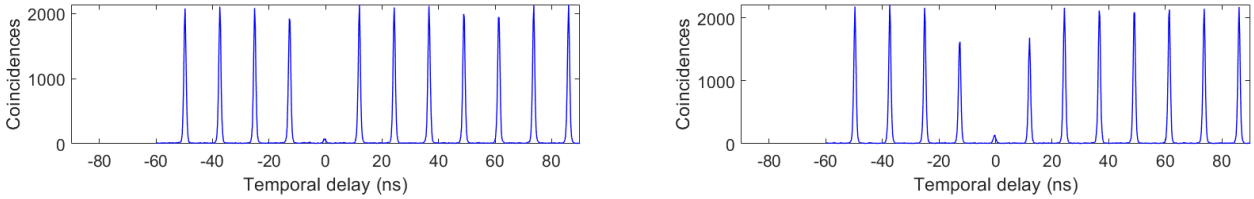


(c) Source S6.

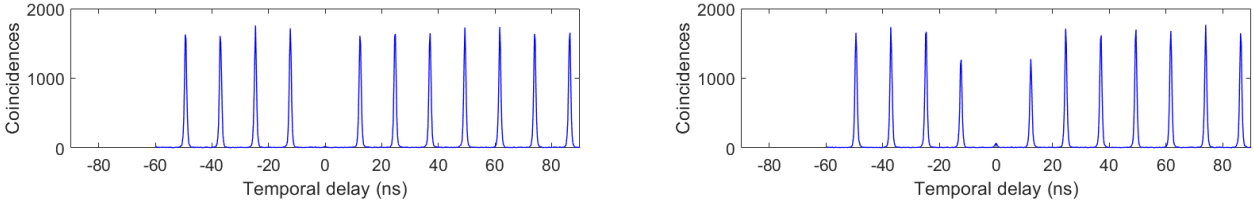


(d) Source S7.

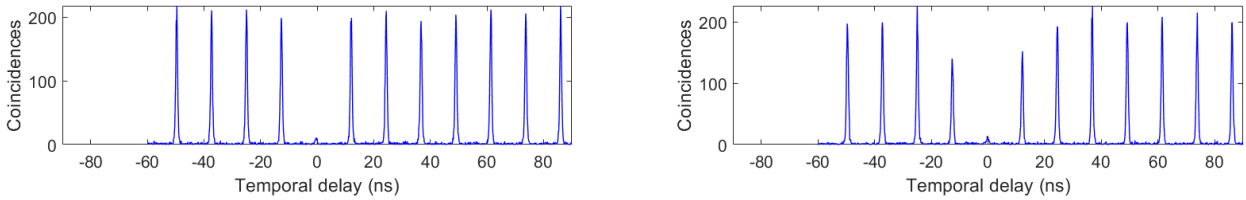


(e) Source S8.

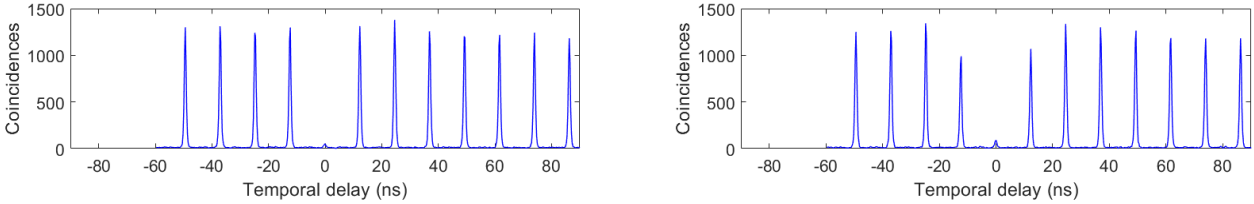


(f) Source S9.

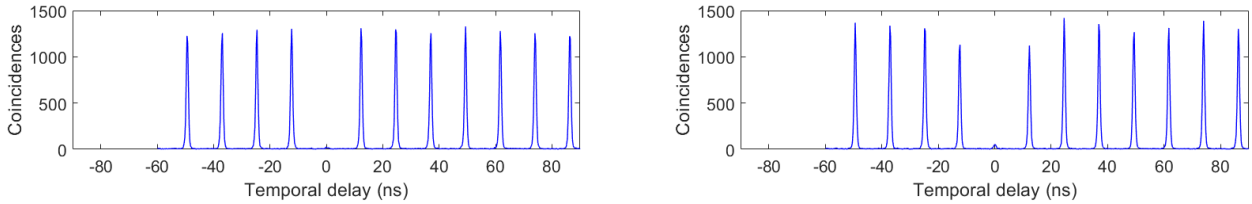


(a) Source S10.

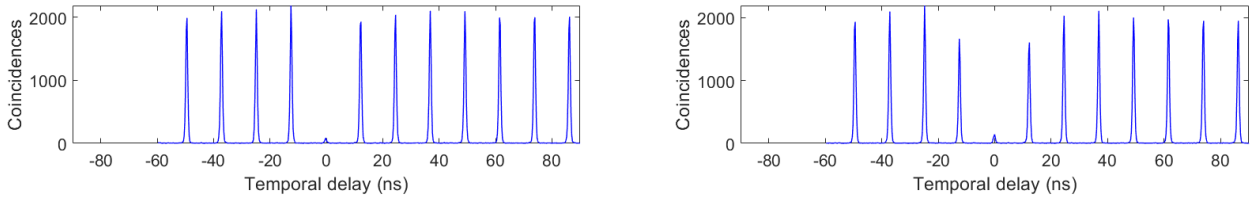


(b) Source S11.

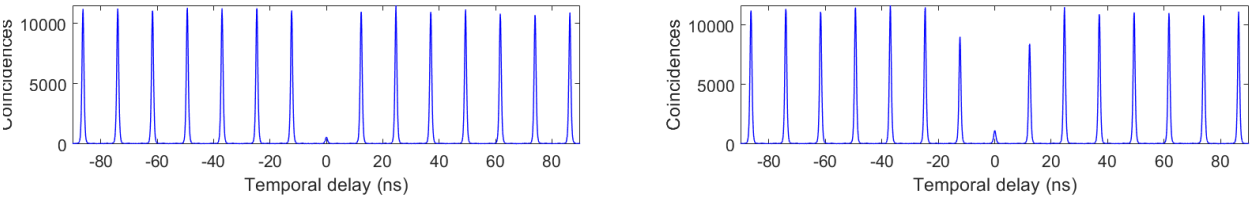


(c) Source S12.

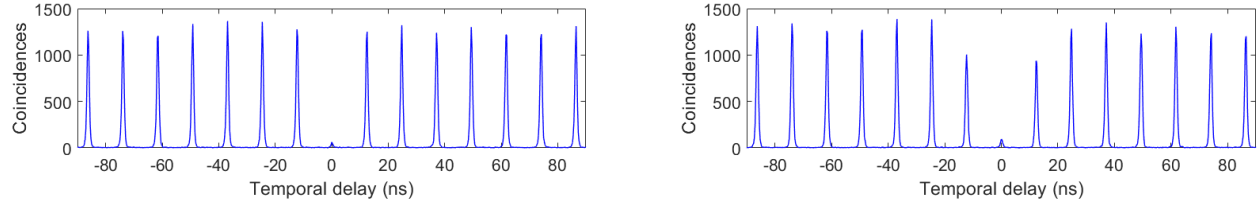


(d) Source S13.

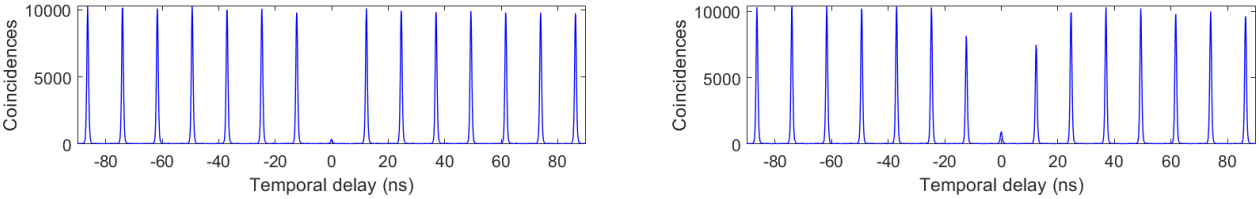


(e) Source S14.

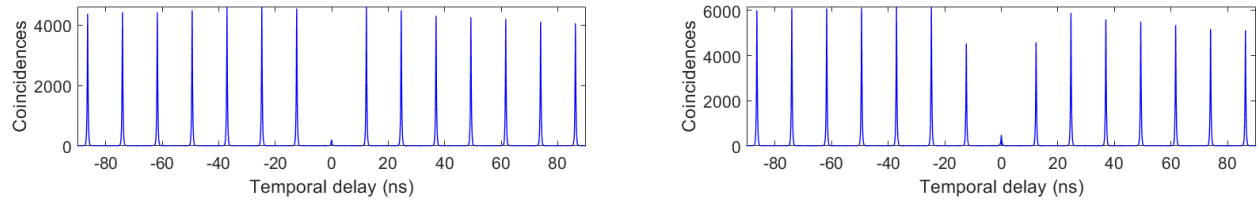


(f) Source S15.

# List of publications

- **Bright polarized single-photon source based on a linear dipole**
  S. E. Thomas, M. Billard, N. Coste, S. C. Wein, Priya, H. Ollivier, O. Krebs, L. Tazaïrt, A. Harouri, A. Lemaitre, I. Sagnes, C. Anton, L. Lanco, N. Somaschi, J. C. Loredo, and P. Senellart
  *Phys. Rev. Lett.* **126**, 233601 (2021)

- **Hong-Ou-Mandel Interference with Imperfect Single Photon Sources**
  H. Ollivier, S. E. Thomas, S. C. Wein, I. Maillette de Buy Wenniger, N. Coste, J. C. Loredo, N. Somaschi, A. Harouri, A. Lemaitre, I. Sagnes, L. Lanco, C. Simon, C. Anton, O. Krebs, and P. Senellart
  *Phys. Rev. Lett.* **126**, 063602 (2021)

- **Reproducibility of High-Performance Quantum Dot Single-Photon Sources**
  H. Ollivier, I. Maillette de Buy Wenniger, S. Thomas, S. C. Wein, A. Harouri, G. Coppola, P. Hilaire, C. Millet, A. Lemaître, I. Sagnes, O. Krebs, L. Lanco, J. C. Loredo, C. Antón, N. Somaschi*, and P. Senellart
  *ACS Photonics* **7**, 4, 1050-1059 (2020)

- **Sequential generation of linear cluster states from a single photon emitter**
  D. Istrati, Y. Pilnyak, J. C. Loredo, C. Antón, N. Somaschi, P. Hilaire, H. Ollivier, M. Esmann, L. Cohen, L. Vidro, C. Millet, A. Lemaître, I. Sagnes, A. Harouri, L. Lanco, P. Senellart and H. S. Eisenberg
  *Nature Communications* **11**, 5501 (2020)

- **Generation of non-classical light in a photon-number superposition**
  J. C. Loredo, C. Antón, B. Reznychenko, P. Hilaire, A. Harouri, C. Millet, H. Ollivier, N. Somaschi, L. De Santis, A. Lemaître, I. Sagnes, L. Lanco, A. Auffèves, O. Krebs and P. Senellart
  *Nature Photonics* **13**, 803–808 (2019)

- **Interfacing scalable photonic platforms: solid-state based multi-photon interference in a reconfigurable glass chip**
  C. Antón, J. C. Loredo, G. Coppola, H. Ollivier, N. Viggianiello, A. Harouri, N. Somaschi, A. Crespi, I. Sagnes, A. Lemaître, L. Lanco, R. Osellame, F. Sciarrino, and P. Senellart
  *Optica* **6**, 12, 1471-1477 (2019)

université PARIS-SACLAY

ÉCOLE DOCTORALE
Ondes et matière
(EDOM)

**Titre:** Pureté quantique et contrôle de symétrie de sources de photons uniques à base de boîtes quantiques semiconductrices

**Mots clés:** Boîte quantique, Photons uniques, Semiconducteur

**Résumé:** Les boîtes quantiques sont des éléments clés pour le développement des technologies quantiques car elles peuvent générer des photons uniques et des paires de photons intriqués. La fabrication déterministe de sources à base de boîtes quantiques en cavité ouvre la voie vers leur utilisation à grande échelle : nous montrons ainsi pour la première fois qu'il est possible d'obtenir des propriétés homogènes, en étudiant en détails 15 de nos sources. Chacune des caractéristiques de l'émission des boîtes quantiques est mesurée avec un montage expérimental spécifique. Parmi celles-ci, l'indiscernabilité est accessible via la visibilité de l'interférence de Hong-Ou-Mandel. Nous étudions comment cette dernière quantité est affectée par la présence de photons additionnels, selon la nature de ce bruit. Nous dérivons ainsi une formule pour déduire la vraie indiscernabilité des photons uniques à partir de la visibilité mesurée, et nous l'appliquons à nos sources. Enfin, les propriétés de l'émission des boîtes quantiques sont profondément liées à leur état de charge et à leur symétrie. Nous proposons une nouvelle façon de contrôler le dédoublement de structure fine de l'exciton en appliquant trois tensions électriques via une structure de contact déporté. Cette étude expérimentale ouvre la voie à la génération reproductible de paires de photons intriqués avec une grande brillance, ainsi que de qubits encodés en fréquence.

**Title:** Quantum purity and symmetry control of single-photon sources based on semiconductor quantum dots

**Keywords:** Quantum dots, Single photons, Semiconductor

**Abstract:** Quantum dots are a key building block for quantum technologies as they are able to generate single photons or entangled photon pairs. The deterministic fabrication of sources based on quantum dots in cavities paves the way towards scalability: we show for the first time that it is possible to obtain homogeneous properties, by studying in detail 15 of our sources. Each characteristic of the quantum dots' emission is measured with a specific setup. Among them, the indistinguishability is accessible through the visibility of the Hong-Ou-Mandel interference. We study how this latter quantity is affected by the presence of additional photons, depending on the nature of that noise. We thus derive a formula to deduce the true single-photon indistinguishability from the measured visibility and apply it to our sources. Finally, the properties of the emission from quantum dots is deeply related to their charge state and symmetry. We propose a new way to control the exciton's symmetry by applying three voltages via a specific structure. This experimental study opens the way to the reproducible generation of entangled photon pairs with a high brightness as well as frequency-encoded qubits.

Université Paris-Saclay
Espace Technologique / Immeuble Discovery
Route de l'Orme aux Merisiers RD 128 / 91190 Saint-Aubin, France